

MANIPULATING STATES OF LIGHT IN OPTICAL RING
RESONATORS

KATHLEEN MCGARVEY

A THESIS
IN
THE DEPARTMENT
OF
PHYSICS

PRESENTED IN PARTIAL FULFILLMENT OF THE REQUIREMENTS
FOR THE DEGREE OF DOCTOR OF PHILOSOPHY (PHYSICS)
CONCORDIA UNIVERSITY
MONTRÉAL, QUÉBEC, CANADA

MARCH 2021

© KATHLEEN MCGARVEY, 2021

CONCORDIA UNIVERSITY
School of Graduate Studies

This is to certify that the thesis prepared

By: **Kathleen McGarvey**

Entitled: **Manipulating states of light in optical ring resonators**

and submitted in partial fulfillment of the requirements for the degree of

Doctor of Philosophy (Physics)

complies with the regulations of this University and meets the accepted standards with respect to originality and quality.

Signed by the final examining committee:

Chair _____
Galia Dafni, Ph.D.

External Examiner _____
David V. Plant, Ph.D., McGill University

Examiner _____
Saurabh Maiti, Ph.D.

Examiner _____
Mariana Frank, Ph.D.

Supervisor _____
Pablo Bianucci, Ph.D.

Approved _____
Valter Zazubovits, Ph.D., Graduate Program Director

November 17, 2020 _____

Pascale Sicotte, Ph.D., Dean
Faculty of Arts and Sciences

Abstract

Manipulating states of light in optical ring resonators

Kathleen McGarvey, Ph.D.

Concordia University, 2021

An optical ring resonator is a fundamental element of an integrated photonic circuit due to its ability to confine optical waves. Composed of a dielectric waveguide closed in a loop, the periodic geometry of the ring allows for the build-up of high-intensity electric fields at particular wavelengths of light known as resonances. These resonances can be used for applications in fields such as non-linear optics, biosensing, and high-precision spectroscopy. The intended operation of a ring resonator is often limited by the underlying material dispersion of the ring's waveguide. To counteract these effects, the dispersion of the waveguide can be designedly engineered via precise geometric patterning of the material. In this work, several dispersion engineering methods are proposed. In particular, condensed matter theories including Bloch's theorem, the Su-Schrieffer-Heeger model, and synthetic dimensions are applied to the periodic dielectric function of the ring. Using these principles, photonic analogs of band structures, topologically-protected edge states, coupled degenerate two-level systems, and a synthetic modal dimension in an optical ring resonator will be shown.

Acknowledgments

The past five years of my life have strengthened bonds with women that I consider my sisters. Meryem Benghalem and Alexis Dang, I have benefited so much from your friendship. I never in a million years thought a girl from Montana would end up so close with a Dubai princess and a Parisien badass, but our differences have enhanced our relationship and I'm so grateful for you two. Thank you for the hours and hours of gossip text chains, pictures of the beautiful Mai Anh, and (Meryem hold on to your chair) the shared appreciation for Hugh Jackman's talents. I can't wait to see your faces again someday. And I'm sure Alexis will agree with me when I say, Meryem you owe us a name ... Debora Militzer, Amanda Szpylkyn, Mihaela Iordanova, and Melize Ferrus you all have been rockstars during a time of my life that really sucked. I've been on the receiving end of dinners, wine and cheese picnics, birthday cakes, plants, workouts that made me puke, terrifying camping trips with ridiculously smart raccoons, sleepovers, and hours of laughter. You all have embraced my children and I'm grateful for the attention you gave them when I felt exhausted.

I'd like to thank all of the members of the Bianucci research group that I've had the opportunity to work with, including Tabassom Hamidfar, Mathieu Couillard, Mohammad Javad Safdari, Amir Hassanpour, Rajni Bagga, Alexis Hotte-Kilburn, Mohammed Mirjalili, Samar Deep, Kevin Sohn, George Williams, Joshua Lilliman, Erin Stigall, Jeffrey Morais, and Amalia Sanabria Lopez-Silvero. I've also greatly appreciated fellow graduate students faring the Concordia physics department, including Marc Collette, Simeon Hanks, and Gareth Melin for Sunday afternoon D and D sessions, and Ozer Ozdal and Jack Araz for getting me through QFT.

There would be no Bianucci Research Group without Professor Pablo Bianucci. Pablo, I wish I could work for you for the rest of my life. I don't believe I would have dragged myself across the doctorate finish line with two kids in tow without the encouragement and understanding you've given me during the past seven years. I've always respected you as a scientist, but I also deeply respect the culture you have built in your lab. It has been empowering and affirming to work for you and I cannot say thank you enough.

Best. Supervisor. Ever.

Yannick D’Mello, you’re a buddy for life. I only wish we had more conferences together to build our crew. Thank you for parties at your house, picnics with surprise appearances from Jesus Christ himself, and fondue/brownie sessions. You also are responsible for bringing the wonderful and magnificent Evi into my life, who is the first person who ever made me feel like I was good at keeping plants alive. It’s a rare gift when you can share a thought with a person without saying a word, however I feel that Evi and I have shared this experience many times during one of Yannick’s lovely, yet long-winded, stories.

Thank you to Jeremie for kitchen window time, enduring my plant tours, fixing the stuff you broke, banana wars, Joe Exotic and Koh Lanta binges, Rik Instagram time, and for all the coffee. Especially the coffee part. You are a very gracious loser when we play Smash and I feel confident that you’ll get better if you just keep practicing.

Thanks to my family, including my parents, sisters, brother-in-laws, and nieces and nephews, who have always encouraged my goal of becoming a crazy scientist. Getting a phone call from my four-year-old niece about her desire to become a chemist was somewhat challenging, however I believe I still have time to bring her into the physics fold.

Arthur and Adele, you are the greatest gift in my life. You have challenged me and pushed me to my limits, but being your mom is the best experience I could have ever imagined. Your humor, strength, love, and compassion have fueled me every single day of this PhD. David, I will always be indebted to you for these awesome kids and I’m so happy that we will get to share the experience of watching them grow up.

Thank you to Serguei for still hanging around - your first month of knowing me, I was a astronaut mess trying to finish my thesis. Instead of getting scared off, you made cakes (not pies) and bought me beer. You’d be a perfect companion if you could play Crash, but I guess you can’t have everything. (I’m sure its my big ears and ridiculously long arms that give me the edge). Thanks for the BEST COFFEE EVER, jars of love, walks, and (most importantly) access to midnight snacks.

Finally, there is one person that I owe my existence to (both figuratively and literally). Valeri McGarvey, it has always been difficult for me to express the depth of my love for you. Since I was a little girl, you have been a pillar of beauty, grace, kindness, intelligence, humility, and love. There is no relationship in my life that I have worked harder for or that I am more proud of. Thank you for the hours that you spent listening to me complain, cry, worry, and rage. Thank you for caring for my children (and me) when I felt like I couldn’t. Thank you for countless packages, affirmative texts, trips to

Montreal, and lengthy video chats with my son while he stared lovingly at you through the camera without saying a word. You are the person that got me through this PhD, but I feel like you would respond with ‘No Kathleen, you got yourself through it’, which says it all. I love you Mom.

Obituary for my headphones



Figure 1: Kathleen’s headphones 2016 - 2020 RIP

Admittedly not a traditional part of a PhD thesis, I feel like things would not be complete if I did not take the time to pay tribute to my beloved headphones. The happiest times of my life in the past five years have been spent with you. I know it’s time for you to retire so thanks for the good times. Finally, thanks to all of the artists that made my headphone times so happy, including:

Abra, Alabama Shakes, Alex G, Alt-J, Amadou & Mariam, Anderson Paak, Angel Olsen, Animal Collective, Arcade Fire, Architecture in Helsinki, Bas, Bat for Lashes, Beach House, Beastie Boys, Beirut, Beyonce, Big Thief, Billie Eilish, Bjork, Black Pumas, Blood Orange, Bombay Bicycle Club, Bon Iver, Brittany Howard, Brockhampton, Caleb Landry Jones, Car Seat Headrest, Cardi B, Caribou, Carly Rae Jepsen, Cate Le Bon, Cautious Clay, Chance the Rapper, Charli XCX, Charlotte Gainsbourg, Childish Gambino, Christine and the Queens, Clairo, Clap Your Hands Say Yeah, The Clash, Cosmo Pyke, Courtney Barnett, Crosby, Stills, and Nash, Crumb, Deerhoof, Deerhunter, Destroyer, Digable Planets, Disclosure, Discovery, Dizzy, Emily Wells, Father John Misty,

Fiona Apple, First Aid Kit, FKA twigs, Fleet Foxes, Fleetwood Mac, Florence + the Machine, Flying Lotus, Foals, Frank Ocean, Fugees, Grimes, Grizzly Bear, H.E.R., HAIM, Half Waif, Ian Chang, Ibeyi, Ife, The Internet, Jai Paul, J. Cole, James Blake, Jamie XX, Jamila Woods, Jane's Addiction, Janelle Monae, Jay Rock, Jay Som, Jay-Z, Jeff Buckley, Jenny Hval, Jeremy Dutcher, Jessie Ware, Jidenna, Jorja Smith, Joseph, July Talk, Jungle, Kacey Musgraves, Kali Uchis, Kanye West, Karen O. & Danger Mouse, Kassa Overall, Kate Bush, Kendrick Lamar, Khalid, Khruangbin, Kiiara, Kids see Ghosts, King Princess, Labrinth, Ladytron, Lana Del Rey, Lauryn Hill, LCD Soundsystem, Let's Eat Grandma, Lifafa, Little Dragon, Little Simz, Lizzo, Lorde, Lykke Li, M.I.A., M83, Mac Miller, Manu Chao, Maren Morris, Mariah the Scientist, Marina and the Diamonds, Mark Morrison, Massive Attack, Maxo Kream, Men I Trust, MGMT, Michael Kiwanuka, Miike Snow, Miles Davis, Missy Elliott, Mitski, MorMor, Moses Sumney, N.E.R.D., The National, Nilufer Yanya, Noname, The Notorious B.I.G., Okay Kaya, OSHUN, Outkast, Panda Bear, Passion Pit, Perfume Genius, Peter Cat Recording Co., Phantogram, Phoenix, Photay, Pink Floyd, Porches, The Postal Service, Pusha T, Radiohead, Ramones, Robyn, Rosalia, RyX, Safe, Santigold, Sex Pistols, Shame, Sharon Van Etten, She & Him, Sheer Mag, Sigur Ros, Sky Ferreira, Smashing Pumpkins, Snail Mail, Snoop Dogg, SOAK, Soccer Mommy, Solange, St.Vincent, Stella Donnelly, Stromae, Sufjan Stevens, Superorganism, Sylvan Esso, SZA (!!), Tame Impala, Taylor Swift, Terry Lynn, Thom Yorke, Tierra Whack, Travis Scott, A Tribe Called Quest, Tune-Yards, Tyler the Creator, A Tribe Called Red, Vampire Weekend, Waxahatchee, The Weeknd, Weyes Blood, Woodkid, The XX, Young Fathers, 100 gees (and thanks to Sander Mann for contributing to this list)

Contribution of Authors

Chapter 4: K.M. and P.B. conceived the presented idea. P.B. developed the theory and K.M. performed the computational analysis. K.M. designed the fabricated devices. Fabrication was performed by the IMEC Silicon Photonics foundry. D.P, L.X, T.H., and K.M. carried out the experimental characterization of the devices. K.M. analyzed the experimental results and prepared the manuscript for publication.

Publication: Kathleen McGarvey-Lechable, Tabassom Hamidfar, David Patel, Luhua Xu, David V. Plant, and Pablo Bianucci, "Slow light in mass-produced, dispersion-engineered photonic crystal ring resonators," *Opt. Express* 25, 3916-3926 (2017)

Chapter 5: K.M. and P.B. conceived the presented idea. K.M. performed the computational analysis and designed the devices for fabrication. Fabrication of devices will be performed by Applied NanoTools Inc.

Chapter 6: K.M. and P.B. conceived the presented idea. K.M. developed the analytical model and performed the computational analysis. Fabrication and characterization of devices was performed by AEAPONYX Inc. K.M. analyzed the experimental results and prepared the manuscript for publication.

Publication: McGarvey-Lechable, Kathleen, and Pablo Bianucci. "Bloch-floquet waves in optical ring resonators." *Physical Review B* 97.21 (2018): 214204.

Chapter 7: K.M. and P.B. conceived the presented idea. K.M. performed the computational analysis and designed devices for fabrication.

Contents

List of Figures	xii
List of Tables	xv
Abbreviations	xvi
Glossary	xviii
1 Introduction	1
2 Maxwell's equations in an optical ring resonator	4
2.1 Maxwell's equations for optical materials	4
2.1.1 Boundary conditions at a dielectric interface	9
2.2 Optical waveguides	11
2.2.1 Polarization	14
2.3 Ring resonators	14
3 Silicon-based optical devices	19
3.1 The silicon-on-insulator fabrication platform	19
3.2 CMOS-compatible fabrication methods	21
3.3 Drawbacks of silicon-on-insulator optical devices	23
3.4 Alternative integrated photonics platforms	24
3.4.1 Silicon nitride	24
3.4.2 Lithium niobate	25
4 Photonic crystal ring resonators	27
4.1 Light propagation in periodic dielectric structures	27
4.2 Photonic crystal lattices in ring resonators	31
4.3 Design method and computational results	32
4.3.1 Computation of ring's dispersion relation	32

4.3.2	Selection of ring’s geometric parameters	34
4.3.3	Computational characterization of slow light resonances	35
4.4	Fabrication and experimental characterization	36
4.5	Experimental results	36
4.5.1	Experimental determination of ring’s dispersion relation	39
4.6	Conclusion	41
5	Topological edge states in photonic crystal ring resonators	43
5.1	Topological photonics	43
5.2	Symmetries of topological insulators	44
5.3	Topological photonic crystal ring resonators	45
5.3.1	The Su-Schrieffer-Heeger model	45
5.3.2	Symmetries of the dimerized lattice	47
5.3.3	The Zak phase and topological edge states	50
5.3.4	The SSH model in a one-dimensional photonic crystal lattice	51
5.3.5	Computational results	53
5.4	Proposed experimental verification	57
5.5	Generalized result for unit cells of $L = 3$ and 4	57
5.6	Conclusions	63
6	Bloch waves in optical ring resonators	64
6.1	Theoretical prediction	64
6.1.1	Quantitative Fourier analysis of modal splitting	66
6.2	Computational results	70
6.2.1	Frequency-domain eigenmode solver simulations	70
6.2.2	Finite-difference time-domain simulations	71
6.3	Experimental results	72
6.4	Conclusion	75
7	Ring resonators as synthetic dimension platforms	78
7.1	Synthetic dimensions in photonics	78
7.2	Synthetic dimensions in spatially modulated ring resonators	81
7.3	Computational results	83
7.4	Proposed experimental method	85
7.5	Conclusions	87
8	Conclusions and outlook	88

Bibliography	91
A Python scripts for frequency-domain eigenmode simulations	104
B Python scripts for finite-difference-time-domain simulations	109
B.1 Photonic crystal ring resonator	109
B.2 Bloch waves in ring resonators	124
C Photonic crystal rings GDS library	139
D Dimerized photonic crystal rings GDS library	149
E Python scripts for the SSH model	166
E.1 Dimerized lattice	166
E.2 Trimer lattice	167
E.3 Tetramer lattice	169
F Bloch-Floquet rings GDS library	172
G Synthetic dimensions rings GDS library	174

List of Figures

1	Kathleen’s headphones 2016 - 2020 RIP	vi
2	Total internal reflection in dielectric materials	10
3	The electric field profiles of dielectric waveguides	13
4	The effective refractive indices of dielectric waveguides.	13
5	The electric field profiles of TE and TM modes in a dielectric waveguide.	15
6	An optical ring resonator.	16
7	An optical ring resonator and its transmission spectrum.	18
8	The silicon-on-insulator material platform.	20
9	Examples of various geometries employed for silicon photonic waveguides and their electric field profiles	21
10	Fabrication of silicon photonic devices via deep-UV optical lithography.	22
11	Transparency windows of various integrated photonics materials.	26
12	A photonic crystal waveguide.	29
13	The first two photonic bands of a TE-polarized, silicon photonic crystal waveguide.	30
14	A photonic crystal ring resonator.	31
15	The dispersion relation of a photonic crystal waveguide and the phase matching conditions of an optical ring resonator.	33
16	Scanning electron microscope images of SOI photonic crystal ring resonators.	37
17	Scanning electron microscope image of the coupling region of a photonic crystal ring resonator.	37
18	The experimental setup employed for the characterization of on-chip devices.	38
19	The normalized transmission spectrum of a 20- μm -radius photonic crystal ring resonator.	39
20	The normalized transmission spectrum of a 20- μm -radius standard ring resonator.	40
21	The experimental dispersion relation of a 10- μm -radius photonic crystal ring resonator.	41

22	The experimental group index of a 10- μm -radius photonic crystal ring resonator.	42
23	A dimerized atomic chain.	47
24	The bulk energy dispersion relation of the SSH model.	48
25	The SSH model implemented in a photonic crystal waveguide	51
26	A topological phase transition occurs at the interface between a topological and trivial dimerized photonic crystal waveguide.	52
27	A dimerized photonic crystal ring with two topologically-protected cavities.	53
28	The computational dispersion relation of a one-dimensional photonic crystal waveguide with a trivial Zak phase.	55
29	The computational dispersion relation of a one-dimensional photonic crystal waveguide with a non-trivial Zak phase.	56
30	The 2D-FDTD computational optical spectrum of a dimerized photonic crystal ring resonator.	57
31	The 2D-FDTD computational optical spectrum of a dimerized photonic crystal ring with coupled edge states.	58
32	A trimerized atomic chain.	60
33	The bulk energy dispersion relation for a 1D atomic lattice and a 1D trimerized atomic lattice.	60
34	A tetramer atomic chain.	62
35	The bulk energy dispersion relation for a 1D atomic lattice and a 1D tetramer atomic lattice.	62
36	An optical ring resonator with point surface scatterers.	66
37	The photonic dispersion relation of an optical ring resonator in the reduced zone scheme.	67
38	The numerical prediction of Equation 134 as compared to FDE and FDTD computational results.	71
39	The dielectric profiles of ring resonators with periodic perturbations of various magnitudes.	72
40	The 2D FDTD computational spectra of optical ring resonators with periodic perturbations of various magnitudes.	73
41	The dielectric profiles of ring resonators with periodic perturbations of various spatial periods.	74
42	The 2D FDTD computational spectrum of an optical ring resonator with multiple periodic perturbations of various spatial periods.	74

43	The experimental transmission spectrum of a silicon-nitride ring resonator with multiple periodic perturbations of various spatial periods.	76
44	Scanning electron microscope image of a periodically-perturbed, silicon-nitride optical ring resonator.	77
45	Photonic arrays composed of optical ring resonators.	79
46	A 1D synthetic array of an optical ring resonator with nearest-neighbor coupling between adjacent resonances.	80
47	A ring resonator of radius R with a width modulation of spatial period $2\pi R$	83
48	2D FDTD computational transmission spectra of spatially-modulated optical ring resonator coupled to an external waveguide (thickest to thinnest width of ring).	84
49	2D FDTD computational transmission spectra of spatially-modulated optical ring resonator coupled to an external waveguide (thinnest to thickest width of ring).	84
50	The dispersion relation of the 1D synthetic ring array.	86
51	The proposed experimental setup for measurement of a 1D synthetic dimension in a spatially modulated optical ring resonator.	86

List of Tables

3	Comparison of the non-linear properties of several integrated photonic materials.	25
4	Comparison of the properties of Maxwell's equations and Schrödinger's equation formulated as hermitian eigenvalue problems	28
5	The ten symmetry classes of topological insulators. [96]	45
6	Comparison of synthetic dimensions in frequency and modal space.	82

Abbreviations

CMOS Complementary-metal-oxide-semiconductor

FDE Frequency-domain eigenmode solver

FDE Finite-difference eigenmode solver

FEM Finite-element method

FSR Free spectral range

FWHM Full-width-half-maximum

FWM Four-wave-mixing

LiNbO₃ Lithium niobate

MEEP MIT Electromagnetic Equation Propagation

MPB MIT Photonic Bands

OPL Optical path length

PhC Photonic crystal

PhCRR Photonic crystal

Q Quality factor

RR Ring resonator

Si	Silicon
Si ₃ N ₄	Silicon nitride
SOI	Silicon-on-insulator
SSH	Su-Schrieffer-Heeger
TE	Transverse-electric
TM	Transverse-magnetic
TPA	Two-photon absorption

Glossary

Description	Symbol	Units
Angular frequency	ω	rad/sec
Annihilation (creation) operator	a_n (a_n^\dagger)	
Charge-conjugation operator	\mathcal{C}	
Chiral-symmetry operator	\mathcal{S}	
Complex conjugation operator	γ	
Coupling waveguide width	W	m
Critical angle	θ_c	
Effective refractive index	n_{eff}	
Electric charge density	ρ	C/m ³
Electric current density	\mathbf{J}	A/m ²
Electric displacement	\mathbf{D}	C/m ²
Electric field	\mathbf{E}	V/m
Energy	E	J
Evanescant coupling gap	g	m
Fourier coefficients of ring's dielectric profile	κ_l	
Full width half maximum	$\delta\lambda$	m
Group index	n_g	

Description	Symbol	Units
Group velocity	v_g	m/s
Hamiltonian operator	H	
Imaginary portion of ϵ_r	ϵ''	
Intercell hopping parameter	b	
Intracell hopping parameter	a	
Inversion-symmetry operator	\mathcal{P}	
Localization length	δ	m
Magnetic field	\mathbf{H}	A/m
Magnetic induction	\mathbf{B}	Wb/m ²
Magnetic susceptibility	χ_m	
Magnetization	\mathbf{M}	A/m
Particle wavefunction	Ψ	
Pauli matrices	σ_i	
Phase velocity	v_p	m/s
Photonic crystal degree of dimerization	dd	
Photonic crystal reciprocal lattice vector	q	m ⁻¹
Photonic crystal unit cell	l	m
Polarization	\mathbf{P}	C/m ²
Propagation constant	β	m ⁻¹
Real portion of ϵ_r	ϵ'	
Refractive index	n	
Relative permeability	μ_r	
Relative permittivity	ϵ_r	
Ring radius	R	m
Ring's perimeter	P	m

Description	Symbol	Units
Time-symmetry operator	\mathcal{T}	
Vacuum wavenumber	k_0	m^{-1}
Wavelength	λ	m
Wavenumber	k	m^{-1}
Wavevector	\mathbf{k}	m^{-1}
Zak phase	Z	

Chapter 1

Introduction

All-optical control of light on an integrated chip has persisted as an overarching theme in 21st-century photonics research. The ability to manipulate on-chip light propagation has been a long-held goal of the community, leading to the development of integrated devices such as optical waveguides [1], mode-size converters [2], grating couplers [3], polarizer converters [4], and directional couplers [5]. A variety of integrated optical cavities, including optical microdisks [6], microtoroids [7], and three-dimensional micropillars [8], have likewise emerged as devices capable of confining light to compact footprints.

Within the scope of capturing light on a chip, few devices have proved as versatile as the optical ring resonator. Composed of a dielectric waveguide closed in a loop, a ring resonator confines light to its core via the mechanism of total internal reflection. Certain wavelengths of light, known as the ‘resonances’ or ‘modes’ of the ring, satisfy phase matching conditions imposed by the ring’s geometry. A resonance will constructively interfere with itself as it makes multiple circuits around the ring, resulting in the build-up of high intensity electric fields [9]. The compact scale of a ring resonator, in addition to the resonant accumulation of light within its material, has allowed the ring resonator to serve as the platform for a multitude of research areas.

State-of-the-art fabrication techniques, such as electron-beam [10] and optical lithography [11], have enabled the on-chip integration of ring resonators. Specifically, the well-developed technologies of the electronics industry have been leveraged to advance the burgeoning field of integrated silicon photonics [12]. The excellent optical properties of silicon, in addition to the nanometer-scale precision of existing lithography techniques, have allowed for the development of micron-scale ring resonators operating at optical frequencies [13]. On-chip rings have been used to explore fundamental physics phenomena, such as generation of multi-photon entangled states [14], topologically-protected photonic

edge states [15], and dissipative Kerr solitons [16]. Ring resonators have additionally been used for more practical purposes in fields like telecommunications, biosensing, and high-precision spectroscopy. Silicon-based, integrated rings interface easily with existing optical communications networks and have been used as optical filters [17], power-efficient, all optical switches [18], and dense wavelength multiplexers [19]. The sharp spectral features of the ring have also been used for label-free biosensing [20,21] and refractive index sensing [22]. Within the context of high-precision spectroscopy, the equidistantly spaced resonances of a ring have enabled the generation of octave-spanning optical frequency combs [23–25]. The versatility of its optical features has thus solidified the ring resonator as a fundamental building block in photonic integrated circuits.

To enhance control over the performance of ring-resonator-based optical devices, it is often desirable to engineer the dispersion of the ring. The intrinsic dispersion of the ring’s material can lead to deleterious effects, such as non-equidistant spacing of adjacent resonances [26] and temporal broadening of optical pulses [27], that can limit a device’s bandwidth. While the material properties of the ring are fixed for a given wavelength, the underlying geometric dispersion of the waveguide can be manipulated using various degrees of freedom. To date, current dispersion engineering techniques include geometric tailoring of the waveguide cross section [27–29], multi-resonator systems [30,31], modal coupling [32,33], and layer deposition schemes [34,35].

The aim of this work is to build upon existing dispersion engineering techniques to obtain finer control over light propagation in an optical ring resonator. Drawing inspiration from condensed matter systems, the periodic nature of the ring’s dielectric profile will be utilized to generate photonic crystal lattices and band gaps that provide a high degree of control over the ring’s dispersion relation. The proposed dispersion engineering methods will then be utilized to describe coupled degenerate two-level systems, non-trivial topological geometric phases, and synthetic dimensions in optical ring resonators.

To begin, a theoretical framework for this work will be laid through a discussion of Maxwell’s equations in an optical ring resonator. Key concepts related to dielectric waveguides and ring resonators will be detailed. A discussion on material platforms is then offered in Chapter 3 and the choice of silicon photonics is motivated.

The first of the dispersion engineering techniques offered will overview photonic crystal lattices in optical ring resonators. The theory of light propagation in periodic dielectric materials will be discussed and parallels between Maxwell’s equations and Schrödinger’s equations will be drawn. Using these parallels, the photonic equivalent of a material band gap will be shown both computationally and experimentally. Additionally, the slow light

nature of the ring's resonances will be demonstrated and a method for direct measurement of the ring's dispersion will be given.

The concepts of photonic crystal lattices in ring resonators are extended in Chapter 5. The Su-Schrieffer-Heeger model is applied to a dimerized photonic crystal lattice superimposed onto a ring resonator. Discussion of geometric phases in a diatomic photonic crystal lattice will be given. The dimerization of the photonic crystal lattice and the appearance of a topologically-protected edge state will be demonstrated computationally. Additionally, experimental verification of topological edge states in dimerized photonic crystal lattices will be proposed.

Chapter 6 reframes the geometry of the optical ring resonator to consider it as an infinitely-long dielectric waveguide. It will be shown that perturbations of the ring's material imposes a periodicity of lattice constant P to the infinitely-long waveguide. Through application of a Fourier analysis, it will be demonstrated theoretically, computationally, and experimentally that a frequency-degenerate pair of resonances can be designedly coupled through periodic patterning of the material. To conclude, the concepts of Chapter 6 will be applied to a spatially modulated ring resonator to demonstrate how a synthetic dimension can be projected along the ring's modal degree of freedom.

Chapter 2

Maxwell's equations in an optical ring resonator

2.1 Maxwell's equations for optical materials

The general form of Maxwell's equations is given by [36]:

$$\begin{aligned}\nabla \cdot \mathbf{E} &= \frac{\rho}{\epsilon_0} & \nabla \times \mathbf{E} &= -\frac{\partial \mathbf{B}}{\partial t} \\ \nabla \cdot \mathbf{B} &= 0 & \nabla \times \mathbf{B} &= \mu_0 \mathbf{J} + \frac{1}{c^2} \frac{\partial \mathbf{E}}{\partial t}\end{aligned}\tag{1}$$

In these equations, \mathbf{E} is the electric field, \mathbf{B} is the magnetic induction, ρ is the electric charge density, and \mathbf{J} is the electric current density. ϵ_0 and μ_0 are the vacuum permittivity and permeability, respectively, which are related to the speed of light by $c = \frac{1}{\sqrt{\epsilon_0 \mu_0}}$. These equations encompass the information required to describe the propagation of an electric field in a material.

When selecting a material to serve as the basis for an optical device, several assumptions about the material properties can be made. These conditions simplify the form of Maxwell's equations, yet are sufficient to describe the operation of a large class of devices. These conditions include [36]:

1. **The material has no charge or current sources.**

In the absence of charge or current sources (i.e. $\rho = \mathbf{J} = 0$), Maxwell's equations can be reduced to:

$$\begin{aligned}\nabla \cdot \mathbf{E} &= 0 & \nabla \times \mathbf{E} &= -\frac{\partial \mathbf{B}}{\partial t} \\ \nabla \cdot \mathbf{B} &= 0 & \nabla \times \mathbf{B} &= \frac{1}{c^2} \frac{\partial \mathbf{E}}{\partial t}\end{aligned}\tag{2}$$

2. The polarization of the material is linearly proportional to the electric field.

The non-linear response of a material can be described by expanding the material's dielectric polarization in a Taylor series. This form of the polarization relates the response of a dielectric material to an externally applied electric field. The coefficients of the Taylor series are given by the i -th order electric susceptibilities of the material, $\chi^{(i)}$:

$$\mathbf{P}(t) = \epsilon_0[\chi^{(1)}\mathbf{E}(t) + \chi^{(2)}\mathbf{E}^2 + \chi^{(3)}\mathbf{E}^3 + \dots] \quad (3)$$

If the electric field intensities are low enough, the higher-order terms of the expansion can be neglected, resulting in a linear relation between the polarization and the applied electric field:

$$\mathbf{P}(t) = \epsilon_0\chi^{(1)}\mathbf{E}(t) \quad (4)$$

A great many optical devices operate in the linear regime of a material, and thus the approximation is valid for much of this work. However, it should be highlighted that many optical materials offer interesting non-linear properties (e.g. non-trivial i^{th} -order susceptibilities) which can be utilized for applications that depend on photon-photon interactions.

The electric displacement of an electromagnetic field in a material is given by:

$$\mathbf{D} = \epsilon_0\mathbf{E} + \mathbf{P} \quad (5)$$

Combining 4 and 5:

$$\begin{aligned} \mathbf{D} &= \epsilon_0\mathbf{E} + \mathbf{P} \\ &= \epsilon_0\mathbf{E} + \epsilon_0\chi^{(1)}\mathbf{E} \\ &= \epsilon_0\epsilon_r\mathbf{E} \end{aligned} \quad (6)$$

where the relative permittivity of the material has been defined as $\epsilon_r = 1 + \chi^{(1)}$.

A similar relationship can be derived for the magnetic fields. A linear relation is assumed for the magnetization, \mathbf{M} , of the material:

$$\mathbf{M}(t) = \chi_m\mathbf{H}(t) \quad (7)$$

where χ_m is the magnetic susceptibility of the material and \mathbf{H} is the magnetic field. The magnetic induction can then be represented as:

$$\begin{aligned}\mathbf{B} &= \mu_0(\mathbf{H} + \mathbf{M}) \\ &= \mu_0\mathbf{H} + \mu_0\chi_m\mathbf{H} \\ &= \mu_0\mu_r\mathbf{H}\end{aligned}\tag{8}$$

where $\mu_r = 1 + \chi_m$ is the relative permeability of the material. Equations 6 and 8 represent the electromagnetic constitutive relations which detail the response of a material to an externally applied electric or magnetic field.

3. The material is isotropic.

When considering the relative permittivity of the material, it is necessary to determine whether the material is iso- or anisotropic in nature. In an anisotropic material, the relative permittivity can be represented as a tensor to account for optical properties such as birefringence. Alternatively, the relative permittivity of an isotropic material is a frequency-dependent scalar, $\epsilon_r(\omega)$.

4. The material has no magnetic susceptibility

For many optical materials, the magnetic susceptibility is negligible, implying that the relative permeability of the material is:

$$\mu_r = 1 + \chi_m = 1\tag{9}$$

and the magnetic induction of the material will behave as in vacuum.

5. The material is transparent for the wavelength ranges of interest.

To maximize the efficiency of a device, optical losses due to material absorption must be minimized. This is achieved by selecting materials that have transparency windows with large bandwidths. To determine where these transparency windows lie, the relative permittivity of a material can be decomposed into its real and imaginary components:

$$\epsilon_r = \epsilon' - i\epsilon''\tag{10}$$

The real portion of ϵ_r indicates the degree of phase lag between the driving electric field, $E(t)$, and the response frequency of the material. The imaginary component of the relative permittivity acts as a damping coefficient; as light propagates through the material the amplitude of the field will be attenuated due to material absorption losses. The rate of this attenuation is given by ϵ'' . A material is said to be “transparent” if it possess a negligible ϵ'' over a particular range of wavelengths. Within

this window, the relative permittivity of the material can be approximated as real-valued. Thus, the performance of an optical device can be optimized by designing its operating wavelength to fall within a transparency window of a material.

6. The material has negligible dispersion

In an isotropic material, the relative permittivity of the material is treated as a scalar quantity. Near absorption features of the material, the frequency-dependency of the permittivity plays a crucial role in describing the behavior of the material. However, away from these features, the permittivity of the material can often be approximated as a constant, namely:

$$\epsilon_r(\omega) = \epsilon_r \quad (11)$$

Using the above assumptions, Maxwell's equations can be reduced into a set of second-order partial differential equations [36]. Inserting Eqs. 4 and 7 into Eq. 2 and applying the vector identity $\nabla(\nabla \cdot \mathbf{A}) - \nabla^2 \mathbf{A} = \nabla \times \nabla \times \mathbf{A}$ yields:

$$\nabla^2 \mathbf{E} = \frac{1}{v^2} \frac{\partial^2 \mathbf{E}}{\partial t^2} \quad (12)$$

$$\nabla^2 \mathbf{B} = \frac{1}{v^2} \frac{\partial^2 \mathbf{B}}{\partial t^2} \quad (13)$$

Maxwell's equations in this form indicate that photons propagate as waves with a phase velocity of $v_p = \frac{1}{\sqrt{\epsilon_0 \mu_0}} \frac{1}{\sqrt{\epsilon_r \mu_r}}$. Recalling the definition of the speed of light in vacuum, the phase velocity becomes:

$$v_p = \frac{c}{\sqrt{\epsilon_r \mu_r}} = \frac{c}{n} \quad (14)$$

Here the refractive index of the material, n , has been defined in terms of the relative permittivity and permeability. Because the magnetic susceptibility of the material is assumed to be negligible (i.e. $\mu_r = 1$), the refractive index is approximately equal to the square root of its relative permittivity.

The wave equation can be decomposed into a pair of coupled ordinary differential equations by first assuming a solution of the form $\mathbf{E}(\mathbf{r}, t) = \mathbf{X}(\mathbf{r})T(t)$:

$$\begin{aligned} \nabla^2 \mathbf{X}T &= \frac{1}{v^2} \frac{\partial^2}{\partial t^2} (\mathbf{X}T) \\ \implies \frac{\nabla^2 \mathbf{X}}{\mathbf{X}} &= \frac{1}{v^2} \frac{T''}{T} \end{aligned} \quad (15)$$

As the left and right hand sides of the equations depend on separate variables, both sides of the equation can be set equal to a constant:

$$\frac{\nabla^2 \mathbf{X}}{\mathbf{X}} = k^2 = \frac{1}{v^2} \frac{T''}{T} \quad (16)$$

The time-dependent portion of Equation 16 is satisfied by harmonic, time-oscillating complex exponentials of the form:

$$\mathbf{T}(t) = e^{i\omega t} \quad (17)$$

where $\omega = kv_p = \frac{ck}{n}$ is the angular frequency of the field. Using this definition, it is evident that the constant k must have dimensions of inverse length. This quantity thus represents the wavenumber of the field. The angular frequency of the field also yields the material's dispersion relation, allowing for formal definitions of the the electromagnetic wave's phase and group velocities [36]:

$$v_p = \frac{\omega}{k} = \frac{c}{n} \quad (18)$$

$$v_g = \frac{d\omega}{dk} = \frac{c}{n_g} \quad (19)$$

where n_g is referred to as the group refractive index. Provided the dispersion relation is linear (i.e. n is a constant), the phase and group velocities are equivalent.

In the context of Eq. 17, the wave number is a scalar given by the amplitude of its vector components:

$$k = |\mathbf{k}| = \sqrt{k_x^2 + k_y^2 + k_z^2} \quad (20)$$

However, the full vectorial nature of \mathbf{k} must be taken into account when considering the spatial component of \mathbf{E} . The spatial differential equation can be recognized as Helmholtz's equation,

$$\nabla^2 \mathbf{X} - k^2 \mathbf{X} = 0 \quad (21)$$

which is likewise satisfied by complex exponentials:

$$\mathbf{X}(\mathbf{r}) = e^{-i\mathbf{k}\cdot\mathbf{r}} \quad (22)$$

The final solutions for the fields are given by [36]:

$$\mathbf{E}(\mathbf{r}, t) = \mathbf{E}_0(\mathbf{r})e^{-i(\mathbf{k}\cdot\mathbf{r}-\omega t)} \quad (23)$$

$$\mathbf{B}(\mathbf{r}, t) = \mathbf{B}_0(\mathbf{r})e^{-i(\mathbf{k}\cdot\mathbf{r}-\omega t)} \quad (24)$$

In an homogeneous medium, this equation describes a plane wave with an amplitude of $\mathbf{E}_0(\mathbf{r})$. With no spatial restrictions on the wavevector, \mathbf{k} acts as a continuous variable.

With the above assumptions in place, a photon can be understand as an electromagnetic wave whose propagation is modified by the presence of a material. The dielectric response of the material acts as a retarding force which slows the vacuum speed of a photon by a factor of n .

2.1.1 Boundary conditions at a dielectric interface

With an understanding of how the propagation of light is modified in a material, it is now worth exploring how light will behave at a dielectric interface. At the boundary between two dielectric materials (Figure 2a), a propagating wave must satisfy the following boundary conditions [36]:

$$\mathbf{E}_{i\parallel} = \mathbf{E}_{t\parallel} \quad (25)$$

$$\mathbf{H}_{i\parallel} = \mathbf{H}_{t\parallel} \quad (26)$$

$$D_{i\perp} = D_{t\perp} \quad (27)$$

$$B_{i\perp} = B_{t\perp} \quad (28)$$

where \parallel and \perp represent the tangential and normal components of the fields, respectively. These equations, along with Eqs. 23 and 24, can be used to compute reflection and transmission coefficients for the interface. Additionally, they provide information concerning the relative angle between an incident and transmitted wave. Applying Eq. 25 to 23:

$$\begin{aligned} e^{i\mathbf{k}_i \cdot \mathbf{r}_{\parallel}} &= e^{i\mathbf{k}_t \cdot \mathbf{r}_{\parallel}} \\ \implies \mathbf{k}_{i\parallel} &= \mathbf{k}_{t\parallel} \\ \implies |\mathbf{k}_i| \sin \theta_i &= |\mathbf{k}_t| \sin \theta_t \end{aligned} \quad (29)$$

Using $|\mathbf{k}_i| = k_0 n_i$ and $|\mathbf{k}_t| = k_0 n_t$, where $k_0 = \frac{2\pi}{\lambda}$ is the vacuum wavenumber, Equation 29 becomes [36]:

$$n_i \sin \theta_i = n_t \sin \theta_t \quad (30)$$

This relation is known as the law of refraction and dictates the behavior of transmitted light at a material interface.

An interesting feature of this equation occurs when the transmitted beam has an angle of $\theta_t = \frac{\pi}{2}$ (Figure 2b). The corresponding incident angle which permits a transmitted beam parallel to the interface is given by:

$$\theta_c = \arcsin n_t/n_i \quad (31)$$

Known as the ‘critical angle’, θ_c has two conditions. If $n_t > n_i$, n_t/n_i is outside the domain of the arcsine function and no critical angle exists. If $n_t < n_i$, the phenomenon of total internal reflection can be observed. Not only does the critical angle have a finite value, but light with an incident angle satisfying $\theta_i > \theta_c$ will be totally internally reflected at the interface, ensuring that 100% of the incident light is retained in the n_i material

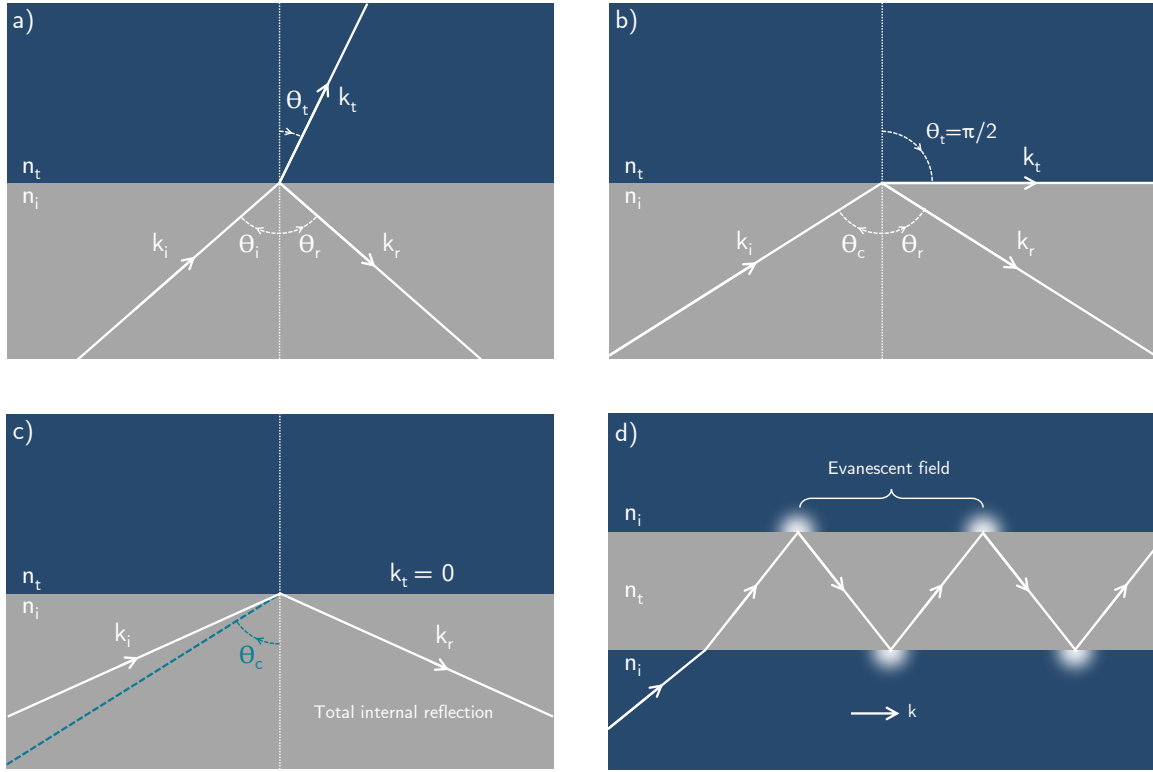


Figure 2: (a) An incident ray of light with wavenumber k_i is incident on a dielectric interface between two materials with refractive indices of n_i and n_t . The reflected and refracted beams are indicated by wavenumbers k_r and k_t , respectively. (b) When light is incident on the interface at the critical angle, the transmitted beam has an angle of $\theta_t = \pi/2$, implying the transmitted beam is parallel to the dielectric interface. (c) When θ_i exceeds the critical angle, the incident beam is totally internally reflected at the interface. (d) Multiple reflections occur in a three layer dielectric stack, forming a waveguide.

(Figure 2c). Although no power is transferred to the n_t material, there remains an imaginary portion of the perpendicular component of \mathbf{k}_t . Correspondingly, an exponentially decaying electric field can be found in the n_t medium. Known as the ‘evanescent’ field, it provides the primary mechanism for coupling between photonic devices on a chip.

Light which is totally internally reflected will undergo a phase shift. For an input electric field which is perpendicular to the plane of incidence, the phase shift can be written as [36]:

$$\phi_{\perp} = \arctan \left[\sqrt{\sin^2(\theta_i) - (n_t/n_i)^2} / \cos(\theta_i) \right] \quad (32)$$

For an incident wave which is parallel to the plane of incidence, the phase shift becomes [36]:

$$\phi_{\parallel} = \arctan \left[(n_i/n_t)^2 \sqrt{\sin^2(\theta_i) - (n_t/n_i)^2} / \cos(\theta_i) \right] \quad (33)$$

2.2 Optical waveguides

Conveniently, the simple concept of total internal reflection is sufficient to provide the primary light-guiding mechanism for photonic circuits. Placing a layer of high refractive index material between two lower index cladding layers allows for multiple total reflections (Figure 2d). These reflections can be utilized to guide light in a particular direction and form the basis for a device fittingly referred to as a ‘waveguide’. Guided modes in optical waveguides can be found through a simple geometric analysis. Considering a plane wave that enters an interface at an angle θ , the wavevector in the direction of propagation can be written as:

$$\beta = k_0 n_t \sin \theta \quad (34)$$

Applying a simple vector analysis, the phase shift obtained by the light along the axis perpendicular to the direction of propagation becomes:

$$k_{t\perp} = \sqrt{(k_0 n_t)^2 - \beta^2} \quad (35)$$

In order for light to be guided within the high refractive index core of the waveguide, the light must undergo a total transverse phase shift of $\Phi = 2\pi n$ where $n \in \mathbb{Z}$ upon reflection at the top and bottom interfaces of the waveguide. The condition for a guided mode becomes:

$$\Phi = 2k_{t\perp} t - 4\phi = 2\pi n \quad (36)$$

where t is the thickness of the high refractive index core and ϕ can be determined utilizing Equations 32 and 33.

The wavevector of light in the waveguide now contains contributions from both material properties and the geometry of the waveguide. As such, it is common to define an effective refractive index for the waveguide which encompasses both effects [36]:

$$n_{\text{eff}} = \frac{\beta}{k_0} \quad (37)$$

The effective index plays a key role in the design of a waveguide. While the material index is fixed by the operating temperature and wavelength of the device, the effective index can easily be varied by changing the waveguide configuration. As a result, the dispersion of the waveguide can be engineered through careful design of the waveguide's geometry.

The effective refractive index can be found computationally using a finite-difference-eigenmode solver (FDE) [37] or finite-element methods (FEM) [38] to solve Maxwell's equations over a cross section of the waveguide. In particular, Equation 21 is solved using eigenequation mode solvers. The eigenvalues of the equation yield the allowed propagation constants in the waveguide with corresponding eigenfunctions composed of the transverse electric field profiles. These field profiles are referred to as the 'modes' of the waveguide. If the dimensions of the waveguide are large enough, multiple solutions to the eigenequation exist, resulting in a 'multi-mode' waveguide (Figure 3). Single-mode waveguides can likewise be engineered by reducing the dimensions of the waveguide cross-section so that it supports a single transverse-mode [36].

An example of dispersion engineering is shown in Figure 4. A eigenmode solver [38] is used to compute the effective refractive indices of several different waveguide configurations. For a one-dimensional planar waveguide, the geometry of the guiding layer is isotropic. If the thickness of the guiding layer is larger than the wavelength of light under consideration, the effective and material indices are approximately equivalent. However, as the layer thickness approaches λ , geometric effects effect the propagation of the wave and the effective refractive index decreases (Figure 4a). A similar, yet more pronounced, effect occurs in a two-dimensional, rectangular waveguide. The guiding material is now discrete in two dimensions. Both the waveguide width and layer thickness influence the effective refractive index of the waveguide, providing greater control over engineering the dispersion of the waveguide (Figure 4b).

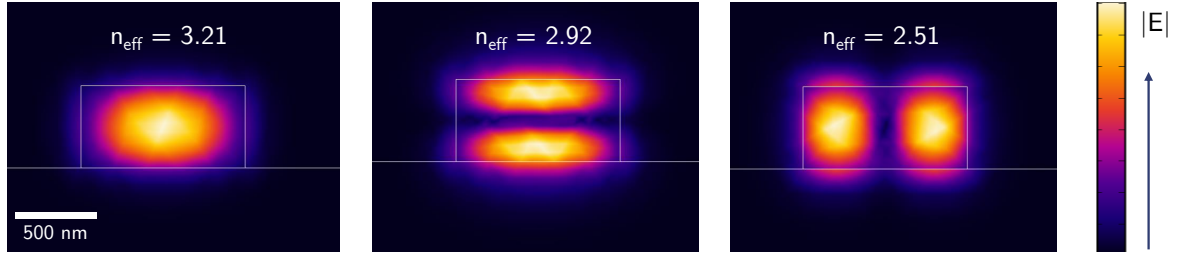


Figure 3: The normalized electric field profile of the modes of a rectangular optical waveguide. The field profiles were calculated on a cross-section of the waveguide using finite-element computational methods. The waveguide has a width of $w = 1 \mu\text{m}$ and a layer thickness of $t = 0.5 \mu\text{m}$. The confining layer has a refractive index of $n_{core} = 3.5$ and is clad with a low index material of $n_{clad} = 1.45$. The waveguide can support multiple modes, as can be seen in the increasing number of nodes in the transverse electric field profile. The effective refractive indices vary depending on the electric field profiles of the mode.

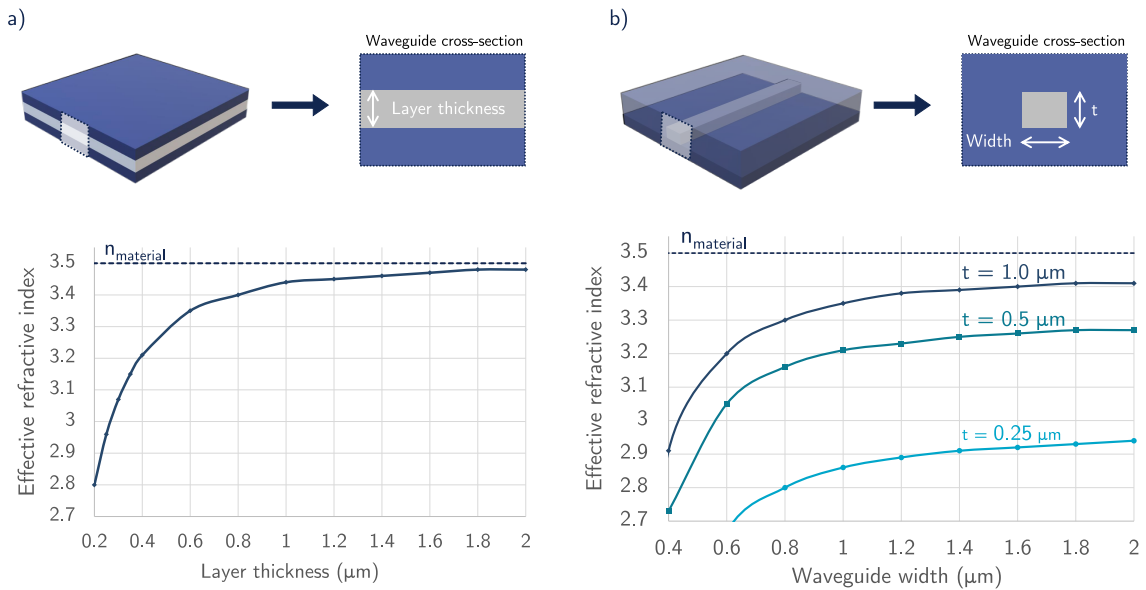


Figure 4: (a) The geometry of a planar waveguide, the cross section of the waveguide used for effective refractive index computations, and the effective refractive index as a function of the layer thickness. (b) The geometry of a rectangular waveguide, the cross section of the waveguide used for effective refractive index computations, and the effective refractive index as a function of the layer thickness and waveguide width.

2.2.1 Polarization

An additional degree of freedom for waveguide dispersion engineering is provided by a propagating wave's polarization. In a planar waveguide, the material is isotropic in two-dimensions, implying that the modal profiles of the waveguide must be invariant when transformed about the two symmetry axes of the system. These conditions restrict the orientations of the fields in the waveguide, allowing for two different polarizations [36]:

$$\text{Transverse magnetic (TM) mode} \quad E_x, E_z, \text{ and } H_y = 0 \quad (38)$$

$$\text{Transverse electric (TE) mode} \quad H_x, H_z, \text{ and } E_y = 0 \quad (39)$$

These polarizations are only valid in a planar waveguide, however can be applied to rectangular waveguides under certain conditions. Typically the polarization of light in a rectangular waveguide forms a hybrid mode composed of both TE and TM fields. As the thickness of the waveguide layer is reduced to below that of the operating wavelength of the waveguide, the electric/magnetic fields oriented along that direction become very small. As a result, it is common to refer to modes in a rectangular waveguide with a thin core layer as 'quasi'-TE or -TM.

The boundary conditions given by Eqs. 25 - 28 yield different modal configurations for TE or TM modes and can be utilized to alter the effective refractive index of the waveguide (Figure 5). TE modes are well-confined to the core of the waveguide and thus have a higher refractive index. In comparison, the TM modes have discontinuous electric fields at the dielectric boundaries of the waveguide, lowering its index and making it more susceptible to optical losses due to imperfections found on the dielectric interface. Thus, a single waveguide can support two different polarizations that possess distinct dispersion relations.

2.3 Ring resonators

While optical waveguides provide control over the direction of light propagation on a chip, another essential element of a photonic circuit is the ability to confine light. A large class of optical cavities is available for this purpose. While the confinement mechanisms of these cavities vary, all share a resonant, intra-cavity buildup of light at certain wavelengths due to constructive interference effects. These resonances occur when the wavelength of light in the cavity can be related to the optical path length (OPL) as [13]:

$$\text{Optical path length} = m\lambda \quad (40)$$

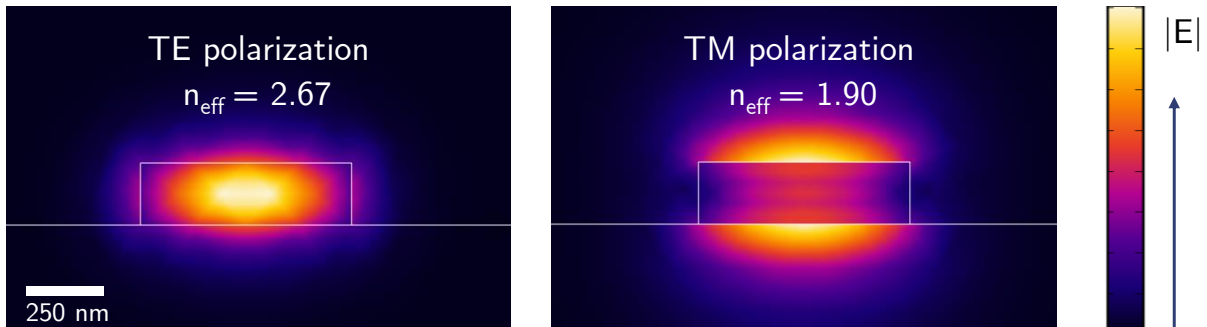


Figure 5: The normalized electric field profile of the TE and TM modes of a rectangular optical waveguide. The field profiles were calculated on a cross-section of the waveguide using finite-element computational methods. The waveguide has a width of $w = 0.75 \mu\text{m}$ and a layer thickness of $t = 0.22 \mu\text{m}$. The confining layer has a refractive index of $n_{core} = 3.5$ and is clad with a low index material of $n_{clad} = 1.45$. The transverse electric mode is tightly confined to the waveguide core, while the transverse magnetic mode has large overlap of its electric fields with the dielectric boundaries of the waveguide. Due to their different field configurations, the TE and TM modes have widely different refractive indices, despite sharing the same waveguide geometry.

where $m \in \mathbb{Z}$ is a discrete variable. Thus at the wavelengths of light satisfying Equation 40, the cavity will support the build-up of high-intensity electric fields. A common figure of merit used to quantify the losses of the optical cavity is the quality (Q) factor, defined as [13]:

$$Q = \frac{\lambda}{\delta\lambda} \quad (41)$$

$\delta\lambda$ represents the full-width-half-maximum (FWHM) of a resonance centered on λ . The width of the resonance depends on the losses of the ring due to absorption, scattering, and radiative processes. In the time domain, the quality factor is proportional to the lifetime of a photon in the cavity.

The ring resonator (RR) is a commonly-used optical cavity formed by closing a waveguide in a loop. The geometry of the cavity ensures discrete translational symmetry along the direction of light propagation, imposing phase matching conditions on the wavevectors in the ring. Equation 40 becomes:

$$\beta = \frac{m}{R} \quad (42)$$

where R is the radius of the ring. The spacing between adjacent resonances is given by the ring's free spectral range (FSR). Using Equation 42 the spacing between the allowed

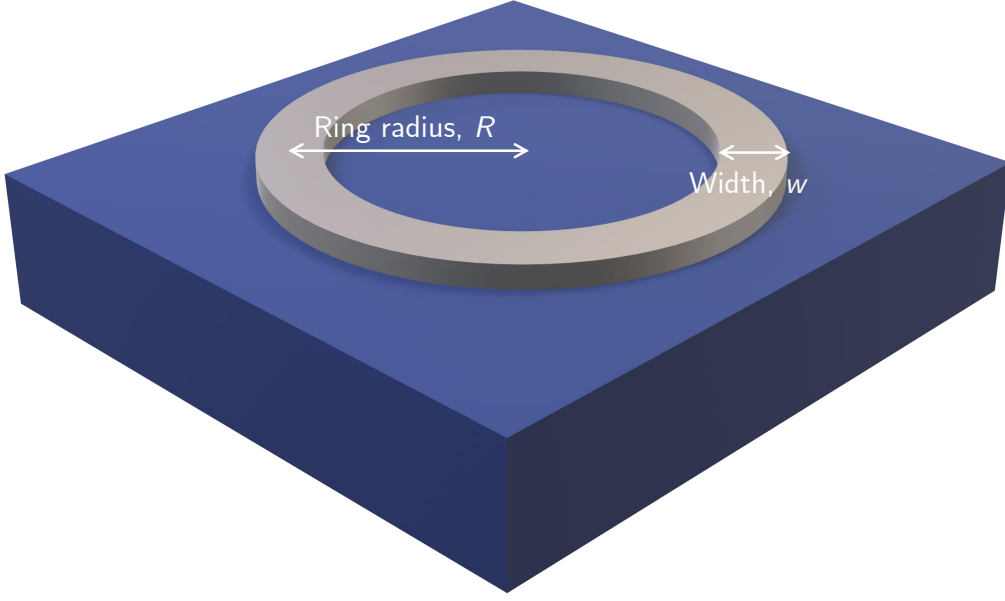


Figure 6: A ring resonator of radius R is formed by closing a waveguide of width w in a loop.

wavevectors in the ring is:

$$\Delta\beta = \beta_{m+1} - \beta_m = \frac{m+1}{R} - \frac{m}{R} = \frac{1}{R} \quad (43)$$

The wavelength-dependence of the free spectral range of the ring can be found by expanding $\beta = n_{\text{eff}}k_0$ in a Taylor series in λ [9]:

$$\frac{\partial\beta}{\partial\lambda} = -\frac{\beta}{\lambda} + k_0 \frac{\partial n_{\text{eff}}}{\partial\lambda} \quad (44)$$

Provided the effective refractive index of the ring is constant (i.e. $\frac{\partial n_{\text{eff}}}{\partial\lambda} = 0$), the free spectral range becomes [9]:

$$\Delta\lambda = -\frac{1}{R} \left(\frac{\partial\beta}{\partial\lambda} \right)^{-1} \approx \frac{\lambda^2}{2\pi n_{\text{eff}} R} \quad (45)$$

Equation 45 describes an optical spectrum composed of evenly spaced resonances which scale inversely with the perimeter of the ring. Thus for applications requiring large spacing between adjacent resonances, tight bend radii on the order of tens of micron are needed. While these tight bend radii enable dense integration of devices on a chip, the propagating light must be tightly confined to the core of the ring's waveguide to ensure

low optical losses around sharp bends. To maximize this confinement and reduce losses, a material platform possessing a high refractive index contrast can be used.

Characterization of an optical ring resonator often occurs in an basic two-port configuration consisting of a coupling waveguide and a ring resonator. Light propagating through the waveguide is evanescently coupled to the ring and the transmission of the waveguide is monitored at the other end. The ring is considered to support a single, uni-directional mode with a single polarization and lossless coupling parameters. Under these assumptions, the complex modal amplitudes of the fields can be found using the matrix formalization [9]:

$$\begin{bmatrix} E_{t1} \\ E_{t2} \end{bmatrix} = \begin{bmatrix} t & \kappa \\ -\kappa^* & t^* \end{bmatrix} \begin{bmatrix} E_{i1} \\ E_{i2} \end{bmatrix} \quad (46)$$

Here κ and t represent the coupling parameters in the ring and waveguide, E_{t1} is the transmitted field at the output port of the coupling waveguide, and E_{t2} is the circulating field in the ring (see Figure 7). The transmitted power of the configuration can be found by solving Equation (46) and taking the squared magnitude of the fields. To simplify the equation, E_{t1} is set equal to 1. The modal amplitude of the field after a single round trip in the ring is given by [9]:

$$E_{i2} = \alpha e^{i\theta} E_{t2} \quad (47)$$

where α represents the loss coefficient of the ring and θ gives the phase change accumulated during a round trip [9]:

$$\theta = \beta * 2\pi R = \frac{4\pi^2 n_{\text{eff}} R}{\lambda} \quad (48)$$

Finally, the time-reversal symmetry of the system requires the reciprocity condition [9]:

$$|\kappa^2| + |t^2| = 1 \quad (49)$$

Using Equations 46-49, the transmitted power in the coupling waveguide is:

$$P_{t1} = |E_{t1}|^2 = \frac{\alpha^2 + |t|^2 - 2\alpha|t| \cos(\theta + \phi_t)}{1 + \alpha^2|t|^2 - 2\alpha|t| \cos(\theta + \phi_t)} \quad (50)$$

and the circulating power in the ring is given by:

$$P_{i2} = |E_{i2}|^2 = \frac{\alpha^2(1 - |t|^2)}{1 + \alpha^2|t|^2 - 2\alpha|t| \cos(\theta + \phi_t)} \quad (51)$$

where ϕ_t is the phase introduced by the coupler and $t = |t|e^{i\phi_t}$. The relative values of α

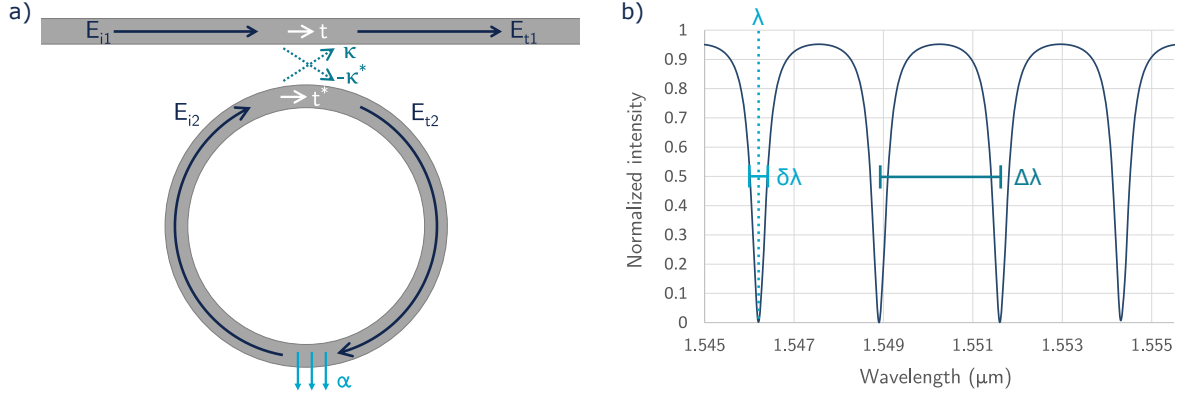


Figure 7: (a) A ring resonator evanescently coupled to an optical waveguide in a point coupler configuration. The coupling between the complex modal amplitudes of the two-port configuration are given by the parameters κ and t , which can be tuned by changing the evanescent gap between the input waveguide and the ring. The losses of the ring are denoted by α . (b) The transmission spectrum of a ring with $n_{\text{neff}} = 2.83$, $R = 50 \mu\text{m}$, and $\alpha = t = 0.8$.

and t define three different coupling regimes for the ring-waveguide system [13]:

$$\begin{aligned}
 \alpha > |t| & \quad \text{Overcoupled} \\
 \alpha < |t| & \quad \text{Undercoupled} \\
 \alpha = |t| & \quad \text{Critically coupled}
 \end{aligned}$$

When the ring is critically coupled, the transmitted power goes to zero on resonance. Equation 50 is plotted in Figure 7b for a critically coupled ring of radius $R = 50 \mu\text{m}$, $n_{\text{eff}} = 2.83$, and $\alpha = t = 0.8$. Wavelengths of light meeting the resonant phase matching conditions of the ring's geometry (i.e. $(\theta + \phi_t) = 2\pi m$) correspond to dips in transmission at the drop port of the waveguide.

Utilizing the concepts detailed in this chapter, a suitable material platform must now be selected. The following chapter will highlight several commonly used optical materials and motivate the choice of silicon photonics for this work.

Chapter 3

Silicon-based optical devices

3.1 The silicon-on-insulator fabrication platform

Silicon-based integrated devices have long been the powerhouse of the electronics industry. A readily available natural resource, silicon (Si) has been widely used for the fabrication of low-cost, integrated electronic circuits. Its semiconductor properties have been utilized to construct fundamental electronic components such as diodes and transistors, the latter of which have formed the foundation for modern electronics. Decades of research have culminated in mature fabrication processes compatible with high throughput manufacturing of devices via wafer-scale processes. It is thus logical to leverage the groundwork laid by the silicon electronics industry when choosing a platform for integrated photonics.

Silicon incidentally possesses excellent optical properties when considering the intended operation of an integrated photonic circuit. It has a high refractive index ($n = 3.5^1$) which results in strong modal confinement when clad with a low index material such as air or silica ($n = 1.44$) [39]. This confinement allows for tight bend radii on the order of microns, essential for the compact integration of optical components. It is transparent in the infrared ($\sim 1.1 - 7 \mu\text{m}$) [40] and is thus compatible with existing fiber-optics communications networks, making silicon-based photonic devices attractive candidates for optical filters [17], buffers [41], and wavelength (de)multiplexers [42]. Additionally, its nonlinear properties have proven useful for optical parametric oscillators, wherein the large Kerr non-linearity of the material can be utilized for frequency generation via the process of four-wave-mixing (FWM) [43]. This effect has also been employed for Kerr frequency combs [44], which use a continuous-wave pump laser in an optical cavity to create a cascade of coherent frequency generation. The evenly spaced 'teeth' of the frequency

¹Unless otherwise specified, the given refractive indices in this chapter are at 1550 nm

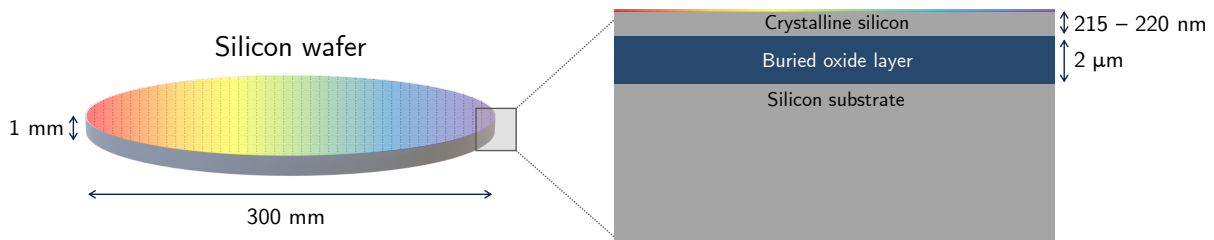


Figure 8: The silicon-on-insulator platform utilizes a standard silicon wafer for fabrication of photonic devices. A 2- μm -thick layer of silica is deposited on the surface of the wafer, followed by a 220-nm-thick layer of silicon. Photonic devices can be monolithically integrated into the surface of the chip via lithography processes.

comb can serve for optical metrology or high-precision spectroscopy purposes [45].

To integrate these applications on a silicon chip, the silicon-on-insulator (SOI) platform is commonly employed. A 220-nm-thick layer of silicon is deposited on top of a 2- μm -thick silica layer. A standard silicon wafer, typically 300-450 mm in diameter, is used as the substrate for the platform (see Figure 8). Fabrication of photonic devices is achieved using complementary-metal-oxide-semiconductor (CMOS) methods to monolithically integrate photonic devices into the surface of the thin layer of silicon. The precision of the CMOS fabrication processes allow for feature sizes down to tens of nanometers, giving an ultra-high degree of control over the on-chip geometry of devices.

This precision plays a crucial role in the design and operation of photonic systems-on-a-chip. Many applications depend heavily upon the ability to engineer the underlying dispersion of the device. Through precise modification of the waveguide’s dimensions, different effective refractive indices can be engineered that meet the requirements of a given application.

Modification of waveguide geometry can additionally alter the electric field mode profiles of a propagating wave. Subwavelength grating waveguides (Figure 9b) demonstrate strong overlap of the electric field with the surfaces of the waveguide which can be utilized to increase the sensitivity of biosensing devices [46–48]. Strip waveguides (Figure 9c) offer compact integration of devices to the tight confinement of the optical mode and are thus well suited for telecommunication applications [49, 50]. Slot waveguides (Figure 9d) concentrate the electric field in a channel which can be filled with active materials [51] or a non-linear organic cladding [52]. Overall, the versatility of the SOI platform, along

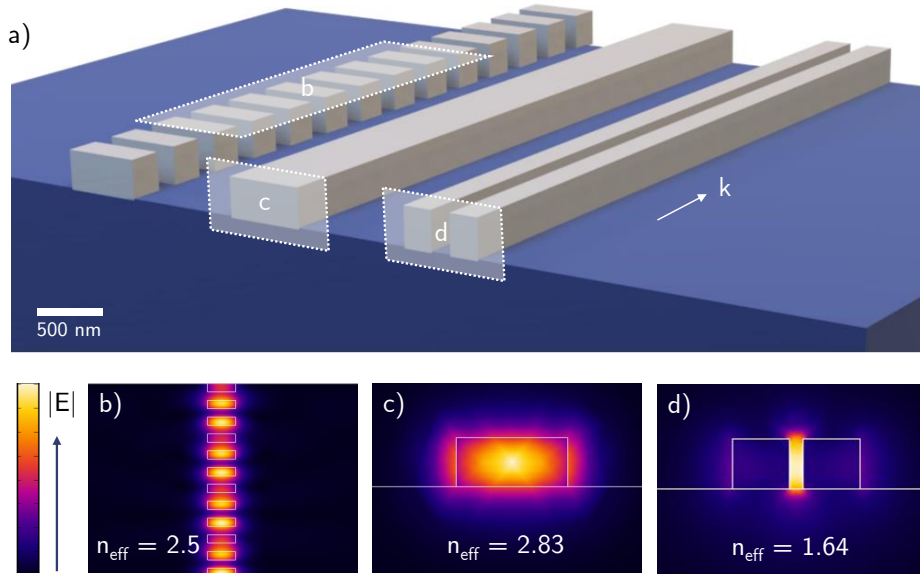


Figure 9: .

(a) Examples of the various geometries employed for silicon photonic waveguides. (b) The electric field modal profile of a latitudinal cross section of a subwavelength grating waveguide. (c) The electric field modal profile of a longitudinal cross-section of a standard strip waveguide. (d) The electric field modal profile of a longitudinal cross-section of a slot waveguide.

with its precise, foundry-scale processes, portend its potential to extend the success of silicon electronics to the photonics industry.

3.2 CMOS-compatible fabrication methods

Dense integration of photonic devices depends on the ability to pattern a silicon chip with sub-micron precision. Commonly employed patterning technologies for the SOI platform use electron-beam or optical deep-UV lithography. The underlying principles of the fabrication techniques are similar: the silicon device layer is covered with a electro-(photo-)sensitive resist and then exposed to a pattern. The solubility of the resist changes depending on the exposure dose of the electron beam (light), allowing for patterning of the silicon via etching techniques (see Figure 10). However, the exposure methods of each technique lead to differences in resolution and production yields.

Electron-beam lithography utilizes a ‘direct-write’ technique, wherein an electron-beam is used to directly pattern the resist. This method allows for fine feature sizes (~ 10 nm) [10], making it the most precise of the two techniques. However, the direct-write

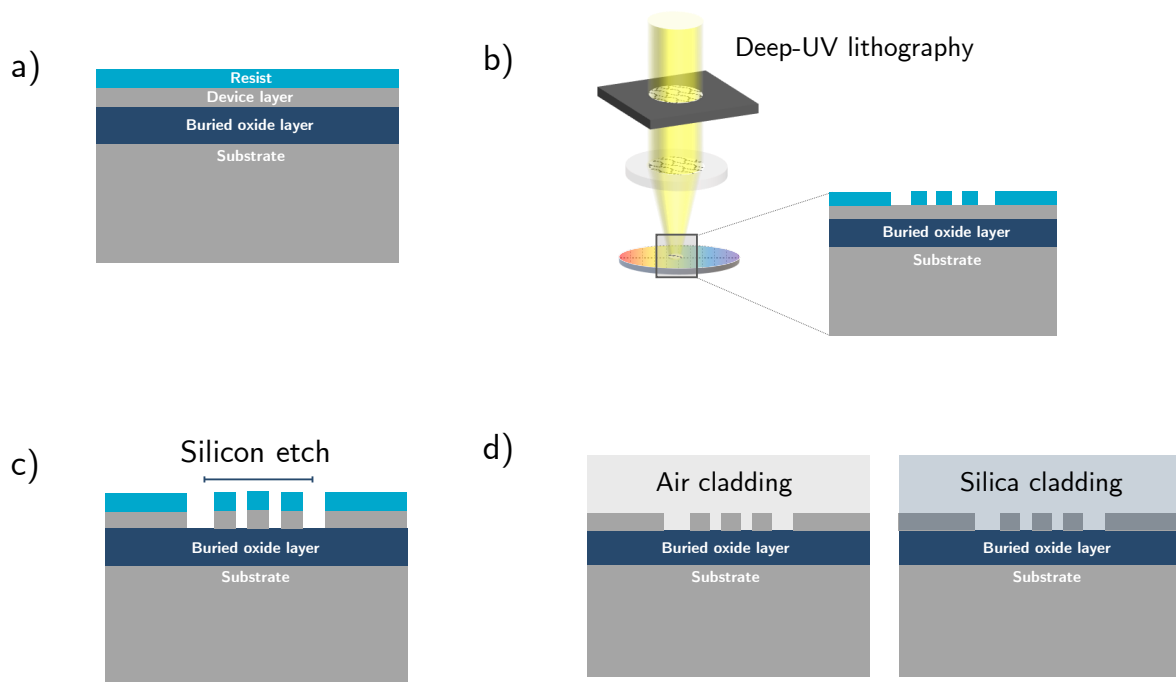


Figure 10: Fabrication of silicon photonic devices via deep-UV optical lithography (a) A silicon-on-insulator chip with a photosensitive resist layered on top. (b) The chip is exposed to a pattern using deep-UV light. The light passes through a patterned mask and is then focused with a lens onto the chip. Repeated exposure of this pattern on different regions of the wafer allow for high throughput fabrication of devices. (c) The devices are formed by etching the 220-nm-thick layer of silicon underlying the exposed resist. (c) The remaining photoresist is removed and the devices are clad with a low-refractive index material.

method limits the production yields of devices, making it incompatible with wafer-scale commercial manufacturing. Conversely, optical lithography uses a mask pre-patterned with the desired device geometries. The resist is then exposed to deep-UV light through the mask. This method increases the allowable resolutions to tens of nanometers, yet allows for high throughput of photonic devices. As deep-UV lithography advances, optical sources with varying wavelengths can offer a higher degree of precision. State-of-the-art lithography processes currently use 193-nm deep-UV light [53], allowing for on-chip dimensions of ~ 150 nm. Optical lithography has the potential to move to the extreme-UV, where light sources with wavelengths of 13 nm can push the allowed dimensions of photonic devices to those that are comparable with electron-beam lithography [11]. Overall, both lithography processes provide a high degree of control over on-chip device dimensions which can be utilized to engineer the dispersion of devices.

3.3 Drawbacks of silicon-on-insulator optical devices

Optical losses due to two photon absorption (TPA) are one of the main limitations of silicon photonics. The process of TPA frequently occurs at high optical intensities where two energy-matched photons are absorbed by the material to create free carriers. This effect introduces both unwanted heat and non-linear losses that can limit the performance of a device [54]. Silicon also lacks a native χ_2 non-linearity due to the centrosymmetry of its crystalline structure. Although this property limits the potential of silicon photonic devices as electro-optic modulators, it has been shown that induced strain to the crystalline structure can create a second-order non-linearity in the system [55].

Another major roadblock to silicon photonics is fabrication-induced sidewall surface roughness. During fabrication, small scatterers are formed on the dielectric interfaces between a silicon device and its surrounding cladding material. The strong refractive index contrast of the SOI platform results in large optical losses when the confined electric field overlaps with these interfaces. Engineering of a waveguide's cross section can be used to reduce the overlap of a propagating field with the sidewalls. Additionally, the polarization degree of freedom can be exploited; TM-polarized modes are typically more sensitive to sidewall roughness due to their modal profile. As a result, TE-polarized modes are frequently employed for low-loss propagation in silicon waveguides.

Despite the fact that the transparency window of silicon extends into the mid-IR, the typical bandwidth of SOI devices are limited by the material absorption of silica; losses due to leaking of light into the buried oxide layer occur above ~ 4 μm . However, it is

possible to extend the operating bandwidth of SOI devices by underetching the silica layer in post-processing steps [56]. These steps would allow SOI devices to be utilized in the mid-IR, where many absorption bands of chemical and biological molecules lie. Such devices could be utilized for atmospheric sensing or precise probing of molecular transitions [40]. Finally, silicon’s lack of direct band gap has limited the integration of on-chip laser sources. Proposals for integration of active III-IV materials into the SOI platform have provided promising options for on-chip light sources which can allow for full optical control of light on a chip [57].

3.4 Alternative integrated photonics platforms

While the silicon-on-insulator platform is known for the maturity of its fabrication methods, several alternative platforms for integrated optical devices have arisen in recent years (Table 3). Most notably, the silicon-nitride and lithium-niobate platforms have been utilized to advance the monolithic integration of novel optical devices due to their distinct non-linear material properties.

3.4.1 Silicon nitride

Silicon nitride (Si_3N_4) is a CMOS-compatible material which has a moderate refractive index ($n = 1.98$) and a large transparency window ranging from the visible to mid-IR (0.45 - 4.0 μm) [56] (Figure 11). The low material absorption of the material over a large range of wavelengths makes it an attractive candidate for wide-bandwidth linear optical devices. The platform is also compatible with foundry-scale fabrication processes, giving a large degree of control over the dispersion engineering of Si_3N_4 waveguides. In particular, high-aspect-ratio integrated silicon nitride waveguides have been engineered to reduce the overlap of the confined mode with the surface roughness of the waveguide sidewalls, resulting in ultra low propagation losses (0.045 ± 0.04 dB/m) [58].

While silicon nitride is a promising material for linear devices, it is perhaps best known for its non-linear properties. The material has a third-order Kerr non-linearity of $n_2 = 2.4 \times 10^{-15}$ cm²/W, making it suitable for ultra-fast non-linear devices. As opposed to silicon, Si_3N_4 also possesses a wide energy band gap resulting in negligible two-photon absorption. The silicon nitride platform thus holds a major advantage over the SOI platform in regards to non-linear device operation [59].

Enhancement of the non-linear response of the system can be achieved via use of low-aspect-ratio waveguides which tightly confine the modal profile to the silicon nitride

	χ_2 (pm/V)	Kerr coefficient (cm^2/W)	TPA coefficient (cm/GW)
Silicon	0	6.3×10^{-14} [60]	0.614 [60]
Silicon dioxide	0	2.3×10^{-16} [61]	negligible
Silicon nitride	0	2.4×10^{-15} [59]	negligible
Lithium niobate	30 [62]	9.0×10^{-16} [63]	0.38 [63]

Table 3: Comparison of the non-linear properties of several integrated photonic materials.

core. Fabrication of such waveguides has been limited by tensile-stress-induced cracking of silicon nitride layers thicker than 250 nm [64]. However, recent improvements in fabricating 500-700-nm-thick layers of silicon nitride have enabled the low aspect ratios required for non-linear device operation [59, 65]. This advancement has opened the door to the development of on-chip optical parametric oscillators requiring sub-mW powers [66] and broadband, coherent optical frequency combs [16].

3.4.2 Lithium niobate

Similar to silicon nitride, lithium niobate (LiNbO_3) possesses a relatively high refractive index ($n = 2.2$) and low material absorption in the telecommunications window ($\lambda = 0.35 - 5 \mu\text{m}$). In addition, the material notably has a large second-order non-linearity ($\chi_2 = 30 \text{ pm}/\text{V}$), making the material an excellent candidate for devices such as electro-optic modulators [62]. Today, the electro-optic response of lithium niobate is widely used to reduce the effects of dispersion in fiber-optics communications systems [67]. However, current fabrication techniques limit the miniaturization of a LiNbO_3 waveguide to the centimeter-scale, restricting the potential for compact, on-chip integration of devices [68].

To enable dense integration of LiNbO_3 -based optical devices, several different fabrication methods have been proposed. Firstly, a hybrid technique combines the fabrication capabilities of the SOI platform with the second-order susceptibility of high-quality LiNbO_3 thin films. Nanopatterning of a silicon wafer using standard lithography techniques is then followed by deposition of a thin layer of LiNbO_3 , resulting in integrated LiNbO_3 -on-SOI optical devices. This method has been utilized to fabricate micron-scale ring resonator and Mach-Zender modulators [69, 70]. The second promising fabrication technique for lithium niobate is monolithic, relying on direct etching of LiNbO_3 thin films. While technologically challenging, the monolithic technique has been shown to produce

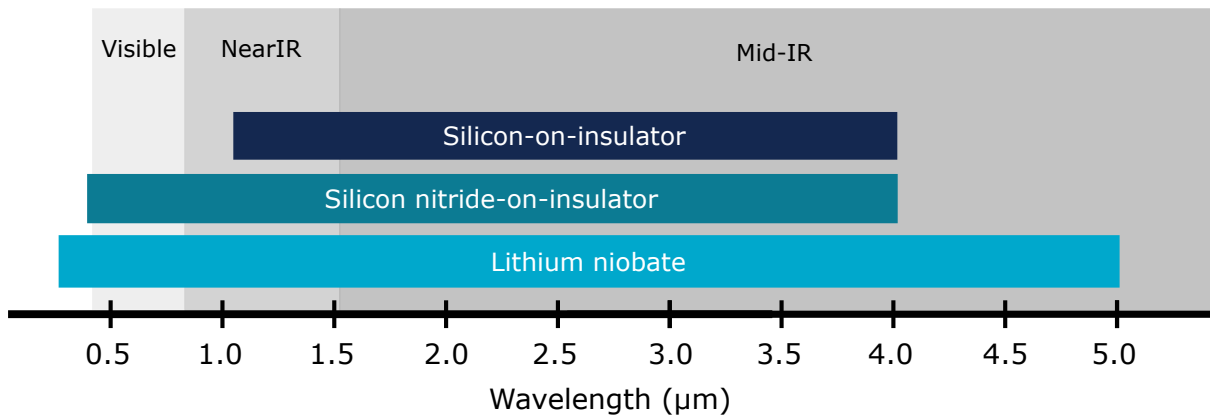


Figure 11: Transparency windows of various integrated photonics materials. [56, 62]

LiNbO₃ waveguides with losses as low as 2.7 ± 0.3 dB/m [62]. This technique has enabled the on-chip integration of devices such as LiNbO₃ Kerr frequency combs [71] and a “photonic molecule” which can be programmed via gigahertz microwave signals [72]. The advancement of lithium niobate fabrication techniques has opened a wide-range of possibilities for on-chip integration of wide-bandwidth electro-optic modulators compatible with optical telecommunication networks. When applied to standard on-chip photonic devices, lithium niobate has the potential to revolutionize microwave-addressable photonics.

Chapter 4

Photonic crystal ring resonators

The first of the dispersion engineering techniques explored in this work will focus on photonic crystals. The following sections will detail how slow light can be implemented in a standard ring resonator via periodic patterning of the material. Computational and experimental confirmation of the highly dispersive nature of the ring will be offered.

4.1 Light propagation in periodic dielectric structures

To examine the behavior of a periodically patterned dielectric waveguide, it is useful to reframe Maxwell's equations as a hermitian eigenvalue problem [73].

$$\nabla \times \left(\frac{1}{\epsilon(\mathbf{r})} \nabla \times \mathbf{H}(\mathbf{r}) \right) = \left(\frac{\omega}{c} \right)^2 \mathbf{H}(\mathbf{r}) \quad (52)$$

Defining the differential hermitian operator as $\hat{\Theta} = \nabla \times \frac{1}{\epsilon(\mathbf{r})} \nabla \times$, Equation 52 becomes:

$$\hat{\Theta} \mathbf{H}(\mathbf{r}) = \left(\frac{\omega}{c} \right)^2 \mathbf{H}(\mathbf{r}) \quad (53)$$

Here, the differential operator acts on the magnetic field, yielding eigenvalues of $\left(\frac{\omega}{c} \right)^2$ [73].

Due to the hermicity of $\hat{\Theta}$, many parallels between electrodynamics and quantum mechanics can be drawn (Table 4). Schrödinger's equation describes the behavior of a particle propagating through a potential energy landscape. Similarly, Maxwell's equations dictate the motion of a photon, where the dielectric function of the medium acts as the 'potential energy' of the equation. This correspondence sheds light on how light propagates through a periodic dielectric material, known as a photonic crystal (PhC) [74, 75].

	Maxwell's equations	Schrödinger's equation
Hermitian operator	$\hat{\Theta} = \nabla \times \frac{1}{\epsilon(\mathbf{r})} \nabla \times$	$\hat{H} = -\frac{\hbar^2}{2m} \nabla^2 + V(\mathbf{r})$
Field	$\mathbf{H}(\mathbf{r}, t) = \mathbf{H}(\mathbf{r})e^{-i\omega t}$	$\Psi(\mathbf{r}, t) = \Psi(\mathbf{r})e^{-iEt/\hbar}$
Eigenvalues	$\left(\frac{\omega}{c}\right)^2$	E

Table 4: Comparison of the properties of Maxwell's equations and Schrödinger's equation formulated as hermitian eigenvalue problems

The dielectric function of a material possessing discrete translational symmetry in one-dimension (e.g. the \hat{x} -direction) is given by:

$$\varepsilon(x) = \varepsilon(x + l) \quad (54)$$

where l is the lattice constant of the dielectric function. An example of an one-dimensional photonic crystal can be seen in Figure 12. An optical waveguide is perforated with holes of radius r with a spacing of l between adjacent holes. The holes introduce a periodicity to the waveguide that imposes restrictions on the allowed wavevectors in the material. These constraints can be found by applying Bloch's theorem [76]. Bloch states are most commonly used in condensed matter systems to describe the behavior of an electron in an atomic lattice. The periodicity of the potential energy function of the lattice results in the condition [77]:

$$\Psi_k(x) = u_k(x)e^{ik_x \cdot x} \quad (55)$$

where

$$u_k(x) = u_k(x + l) \quad (56)$$

Correspondingly, the magnetic fields in a material possessing a dielectric function described by Equation 54 must satisfy:

$$\mathbf{H}(\mathbf{r}) \propto u_k(x)e^{ik_x \cdot x} \quad (57)$$

where $u_k(x)$ is given by Equation 56.

As a result of Bloch's theorem, an electromagnetic eigenvector of the periodic system is invariant when a wavevector undergoes a translation of the form:

$$k_x = k_x + pq \quad (58)$$

where $q = \frac{2\pi}{l}$ is the reciprocal lattice vector of the system and $p \in \mathbb{Z}$. Consequently, the eigenfrequencies corresponding to each allowed wavevector must satisfy:

$$\omega(k_x) = \omega(k_x + pq) \quad (59)$$

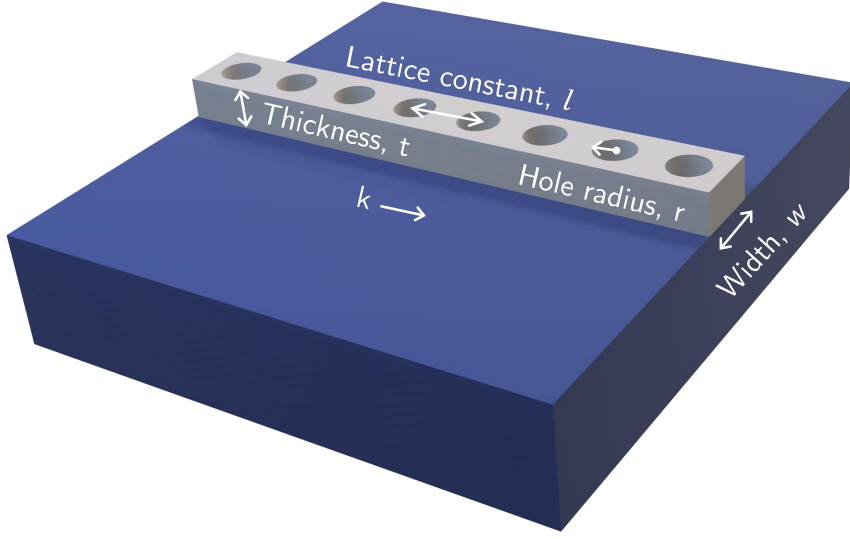


Figure 12: A photonic crystal waveguide of thickness t and width w . The filling factor of the photonic crystal is given by the ratio of the hole radius r to the lattice constant l .

The nonredundant wavevectors in reciprocal space (i.e. $-\frac{\pi}{l} \leq k_x \leq +\frac{\pi}{l}$) form the first Brillouin zone of the system. At the Brillouin zone edge, the eigenvalues become two-fold degenerate and the frequency levels split. This results in the formation of a photonic band structure (Figure 13a). The allowed frequencies of light in the photonic crystal waveguide can possess only certain values; any light of a frequency falling within a band gap of the system is forbidden from propagating in the material.

The physical mechanism of the formation of photonic band gaps can be understood by examining the band-edge field configurations. In a two-fold degenerate system, a perturbation couples the degenerate states of the system. Two new eigenvectors are formed through symmetric and anti-symmetric linear combinations of the original states of the non-perturbed system. If $\mathbf{H}_a^0(\mathbf{r})$ and $\mathbf{H}_b^0(\mathbf{r})$ are the original degenerate eigenvectors of Equation 52, the new eigenvectors of the system are given by:

$$\mathbf{H}_{\pm}(\mathbf{r}) = \alpha_{\pm}\mathbf{H}_a^0(\mathbf{r}) + \beta_{\pm}\mathbf{H}_b^0(\mathbf{r}) \quad (60)$$

where $\alpha_{+(-)}$ and $\beta_{+(-)}$ are normalized constants for the symmetric (anti-symmetric) field configuration. Because the new eigenvectors of the system are distinct, they necessarily oscillate at different frequencies, resulting in the splitting of frequencies at the photonic band edge [73].

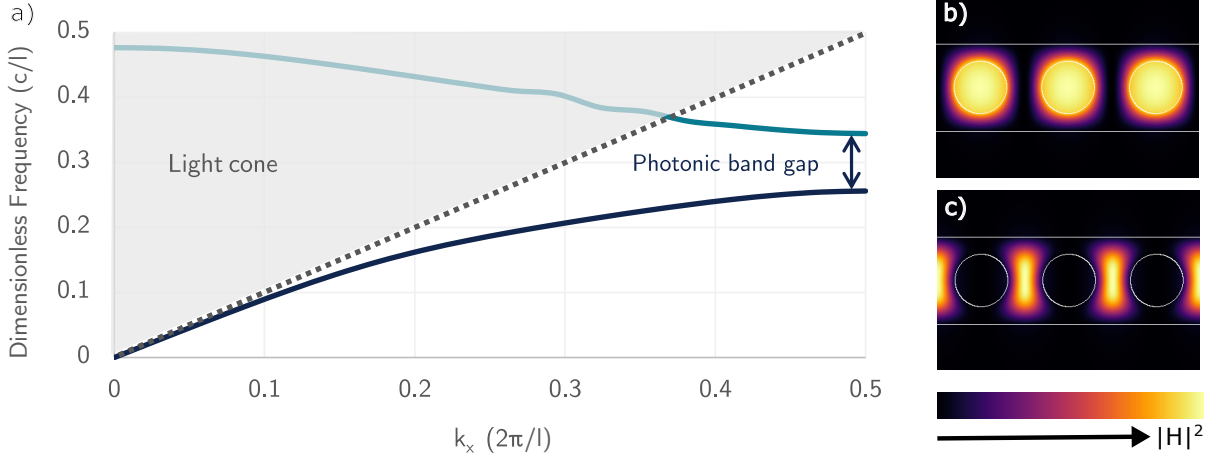


Figure 13: The first two photonic bands of a TE-polarized photonic crystal waveguide with $n_{\text{eff}} = 2.83$, $w = 1.0l$ and $f = 0.3l$. The states lying in the light cone are considered 'leaky' modes of the waveguide. A photonic band gap is formed due to the periodicity of the waveguide's dielectric function. The magnetic-field energy density of the first (b) and second (c) photonic bands at $k_x = 0.5 \left(\frac{\pi}{l}\right)$.

Breaking the continuous translational symmetry of an optical waveguide provides a new degree of freedom for dispersion engineering. As described in Chapter 2, the dispersion relation of a waveguide is approximately linear, with a slope of $v_g = \frac{c}{n_g} \approx \frac{c}{n_{\text{eff}}}$. In a photonic crystal waveguide, frequency splitting at the photonic band edge causes the dispersion relation to flatten out as it approaches $k_x = \frac{\pi}{l}$. Recalling Equation 19, the group velocity of a wave in a photonic crystal waveguide becomes:

$$v_g = \frac{d\omega}{dk} = \frac{c}{n_{\text{eff}}} + ck \frac{\partial n_{\text{eff}}}{\partial k} \quad (61)$$

An additional term appears in the expression due to the wavelength-dependence of the effective index of the waveguide. The effect of this term is most prominent near the photonic band edge; the slope of the dispersion relation approaches zero, resulting in a wave with a negligible group velocity. Such states are referred to as 'slow light' modes of the photonic crystal waveguide. Thus, through periodic, geometric patterning of a standard optical waveguide, the velocity of a propagating wave can be finely-tuned to meet the requirements of a given application.



Figure 14: A photonic crystal ring resonator composed of a standard ring resonator with an overlying photonic crystal lattice.

4.2 Photonic crystal lattices in ring resonators

The optical features of a standard ring resonator can be modified by utilizing the slow light properties of a photonic crystal. A photonic crystal ring resonator (PhCRR) is a hybrid device composed of a ring resonator with an overlying photonic crystal lattice (Figure 14) [78]. The dispersive properties of the photonic crystal lattice alter the propagation of the ring's modes, resulting in resonances which possess low group velocities [79,80]. Slow-light resonances can exhibit properties such as enhanced light-matter interactions [81] and improved microcavity lifetimes [82], both effects of which can be highly desirable for non-linear optics and biosensing applications.

In order to maximize the slow-light effect of a photonic crystal in a ring resonator, a precise design method is required. The following section details a clear-cut method which ensures a ring resonance found exactly at the photonic band edge of the PhC lattice, where the slow-light effect is at its greatest [83]. Additionally, the design method accounts for the feasibility of integrating such a device on a chip by considering geometric parameters which can be manufactured using CMOS-compatible fabrication techniques on the silicon-on-insulator material platform.

4.3 Design method and computational results

To reduce the group velocity of a given ring resonance, the phase matching conditions of the resonance must be selected so as to correspond with the non-linear region of the PhC's dispersion relation. The slow-light effect is maximized at the photonic band edge, where $k_x = \frac{\pi}{l}$. Inserting this value into the phase matching conditions imposed by the ring (Equation 42) yields:

$$m_{BE} = \frac{\pi R}{l} \quad (62)$$

To ensure discreteness of the photonic crystal lattice, an integer number of unit cells must fit within the perimeter of the ring:

$$Nl = 2\pi R \quad (63)$$

where $N \in \mathbb{Z}$. The photonic band edge mode number of a PhCRR can be found by combining Equations 62 and 63:

$$m_{BE} = \frac{N}{2} \quad (64)$$

This equation indicates that a slow-light resonance placed directly at the photonic band edge (i.e. where $v_g = 0$) can occur in any ring possessing an even number of unit cells.

Away from the photonic band edge, the group velocity of the ring resonances will be determined by the finite slope of the dispersion relation. Variations in the waveguide width, filling factor, and effective index of the photonic crystal are degrees of freedom which can be utilized to modify the dispersion relation. The following section details how computational methods can be employed to calculate the dispersion relation of a photonic crystal ring and in turn design slow light resonances in PhCRRs.

4.3.1 Computation of ring's dispersion relation

To model the dispersion relation of the photonic crystal ring, it is first assumed that the radius of curvature of the ring is much larger than the wavelength of light in the material:

$$R \gg \frac{\lambda}{n_{\text{eff}}} \quad (65)$$

Under this approximation, the radius of curvature can be neglected and the ring can be modeled as an infinitely-long photonic crystal waveguide of width w , filling factor f , and effective index n_{eff} .

To compute the dispersion relation of the PhC waveguide, the MIT Photonic Bands (MPB) frequency-domain eigenmode solver is used [84] (Appendix A). The effective refractive index is set depending on the geometry of the material platform under consideration. The PhC waveguide geometry is then defined by fixing the waveguide width and

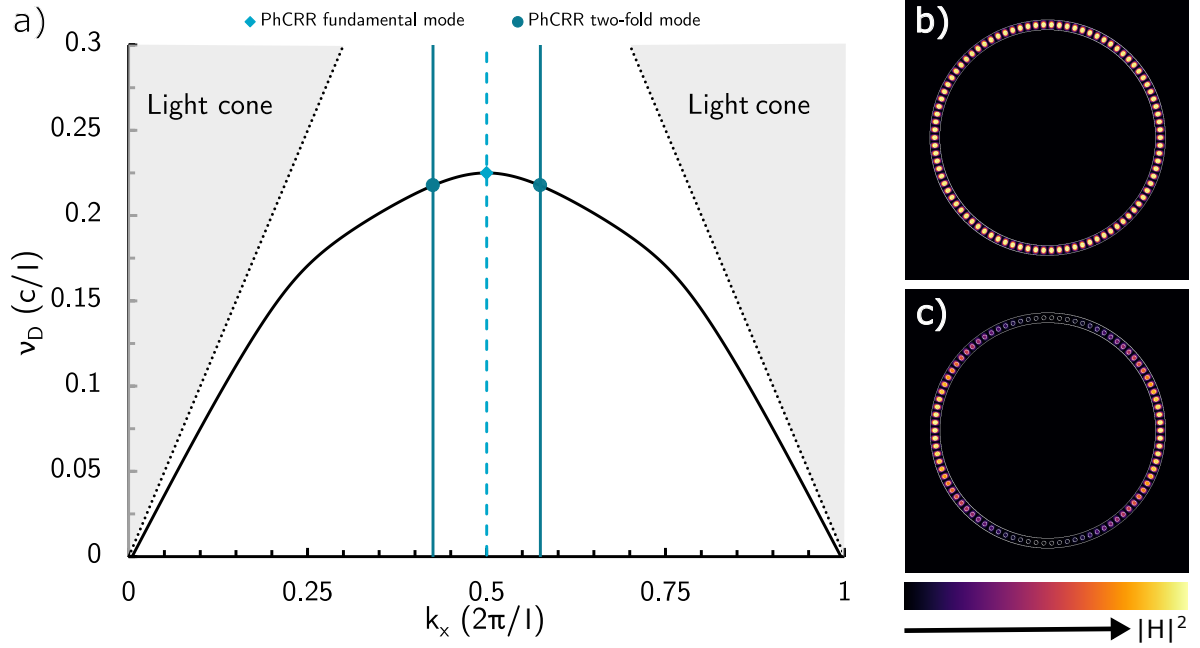


Figure 15: (a) The photonic dispersion relation of an infinitely long, photonic crystal waveguide of parameters $w = 1.3l$, $f = 0.243l$, and $n_{\text{eff}} = 2.83$. The vertical lines denote the phase matching conditions imposed by the ring's geometry. Every intersection between the PhC waveguide's dispersion relation and the ring's phase matching conditions correspond to a resonance of the photonic crystal ring resonator. The magnetic field densities of the (b) fundamental and (c) dipole mode of a PhCRR with $R = 4.985 \mu\text{m}$, $l = 348 \text{ nm}$, $w = 452 \text{ nm}$, $r = 85 \text{ nm}$, $N = 90$ and $n_{\text{eff}} = 2.83$

filling factor. While a wider waveguide can lower optical losses by reducing overlap of the mode with the waveguide sidewalls, the width is restricted to allow for propagation of a single radial mode. Finally, the filling factor of the waveguide is selected based on the minimum feature resolution of the chosen fabrication method.

The solid black line in Figure 15a shows the first photonic band of a TE-polarized, 1D photonic crystal of parameters $w = 1.3l$, $f = 0.243l$, and $n_{\text{eff}} = 2.83$. The dispersion relation is computed in two-dimensions due to computational constraints. The chosen effective refractive index corresponds to the silicon-on-insulator platform described in Chapter 3, while the filling factor and waveguide width are chosen to fall within the fabrication tolerances of 193-nm deep-UV lithography.

4.3.2 Selection of ring's geometric parameters

To find the resonant modes of the ring, the phase matching conditions given by Equation 42 are imposed on the dispersion relation of the 1-D photonic crystal waveguide. Graphically, these phase matching conditions are represented as the vertical lines in Figure 15a; each intersection between the phase matching conditions and the PhC's dispersion relation corresponds to a resonance of the ring. Thus the phase matching conditions of the spatially-bound RR structure serve the purpose of discretizing the continuous dispersion relation of the infinitely long PhC waveguide.

The band-edge, or 'fundamental', mode of the system is indicated by the light blue diamond in Figure 15a. Because the mode falls directly at the band-edge, this resonance will possess a zero group velocity. Moving away from the band edge, the resonant modes become two-fold frequency-degenerate due to the symmetry of the photonic crystal's band structure about the edge of the first Brillouin zone (the green circles in Figure 15a). The wavenumbers of the resonances found away from the photonic band edge are given by:

$$k_x = \frac{m_{BE} \pm j}{R} \quad (66)$$

where $j \in \mathbb{Z}$. Recalling Equation 19, the finite slope of the dispersion relation close to the band edge indicates that the frequency-degenerate modes will possess a non-trivial, yet low, group velocity. This implies that the group velocity of resonances around the band edge can be varied by changing the radius of the ring to ensure that the phase matching conditions intersect the dispersion relation at a particular point.

To select the final geometric parameters for a photonic crystal ring possessing slow light resonances, the design wavelength of the system is specified and the dimensionless frequency of the photonic band edge resonance is scaled to the proper dimensions. MPB

accounts for the scale invariance of Maxwell's equations by computing the dispersion relation in dimensionless frequency units of ν_D ($\frac{c}{l}$). Resultingly, the wavelength of the PhC waveguide modes can be scaled by changing the magnitude of the lattice constant l :

$$\lambda = \frac{l}{\nu_D} \quad (67)$$

Once the lattice constant is set, an approximate ring radius is chosen and inserted into Equation 63. N is scaled to the closest even integer yielded by Equation 63 and the final radius of the ring is in turn recomputed.

4.3.3 Computational characterization of slow light resonances

Upon selection of the PhCRR's geometric parameters, the time evolution of slow light resonances in a ring can be found by performing finite-difference, time-domain simulations using the MIT Electromagnetic Equation Propagation (MEEP) software [85] (Appendix B.1). For a TE-polarized mode, the fields can be expressed as:

$$H_z(x, y) = H_0(y)e^{ik_x x} \quad (68)$$

Correspondingly, a broadband Gaussian dipole source is used to excite the z -component of the magnetic fields and a time monitor measures the field evolution as a function of time. A Fourier transform of these fields yields the ring's optical spectrum. Once the optical spectrum of a ring is determined, a narrowband Gaussian dipole source is centered on each slow light resonance to characterize the magnetic field configurations of the mode.

Figure 15b shows the magnetic field density of the band-edge fundamental mode for a ring of radius $R = 4.985 \mu\text{m}$, $l = 348 \text{ nm}$, $w = 452 \text{ nm}$, $r = 85 \text{ nm}$, $N = 90$ and $n_{\text{eff}} = 2.83$. These particular dimensions are chosen to ensure slow light resonances falling on the first photonic band of the PhC with a design wavelength of $\lambda_0 = 1550 \text{ nm}$. The magnetic field is concentrated in the holes of the ring, consistent with the fields computed for the first photonic band of a TE-polarized photonic crystal waveguide in Figure 13b. The 'dipole' mode possesses a similar field configuration, yet exhibits spatial beating with two nodes around the ring. This beating is due to the degeneracy of the modes about the photonic band edge. The dipole mode of the system is composed of a linear combination of the original frequency-degenerate modes with wavevectors $k_x = \frac{m_{BE} \pm 1}{R}$. Inserting this expression into Equation 68, the magnetic field configuration for the dipole mode becomes:

$$H_z \propto e^{i\frac{(m_{BE}+1)}{R}x} + e^{i\frac{(m_{BE}-1)}{R}x} = e^{i\frac{\pi}{l}x} \cos\left(\frac{2\pi}{Nl}x\right) \quad (69)$$

As a consequence of the cosine function in the expression for H_z , two nodes appear in the magnetic field configuration of the two-fold mode. For higher-order modes (i.e. for $j > 1$) the cosine function will oscillate at a higher frequency:

$$H_z \propto e^{i\frac{\pi}{a}x} \cos\left(\frac{2\pi j}{Nl}x\right) \quad (70)$$

While this particular ring was designed to operate on the first photonic band of the PhC, the result can easily be generalized so as to target resonances falling on the second band of the PhC lattice, where the resonances focus the magnetic field strength in the material of the PhC [86].

4.4 Fabrication and experimental characterization

To verify the validity of the proposed design method, PhCRRs are fabricated on the silicon-on-insulator platform using 193-nm deep-UV lithography (IMEC Silicon Photonics Platform). Design biases are added to the dimensions of the resist mask to ensure correspondence of the on-chip dimensions of the waveguide width and PhC hole radius to the geometric parameters computed above. The resulting mask dimensions of these parameters are thus $w = 462$ nm and $r = 120$ nm. A full etch of the silicon layer is used for the photonic crystal lattice and an air cladding is used to maximize the refractive index contrast of the material platform (Figures 16 and 17).

Photonic crystal ring resonators of radii $R = 10.081$ and 19.939 μm (corresponding to $N = 182$ and 360 , respectively) are fabricated and characterized. Standard ring resonators of similar sizes are placed on the chip for comparative purposes. Each ring is evanescently coupled to a strip waveguide of width $W = 450$ nm with an evanescent gap of $g = 150$ nm (see Appendix C). A standard SMF-28 optical fiber is used to input light from a tunable C-band laser via an input grating coupler. A second optical fiber is placed at the output grating coupler and a power meter is utilized to monitor the rings' transmission spectrum (Figure 18)

4.5 Experimental results

The mean band-edge wavelength of the thirty measured PhCRRs is 1546.2 ± 5.8 nm, a variation of 0.2% from the target design wavelength of 1550 nm [87]. The spectral characteristics of a PhCRR can be seen in Figure 19. The experimental transmission spectrum of a 20- μm -radius PhCRR is indicated in black. The vertical lines indicate

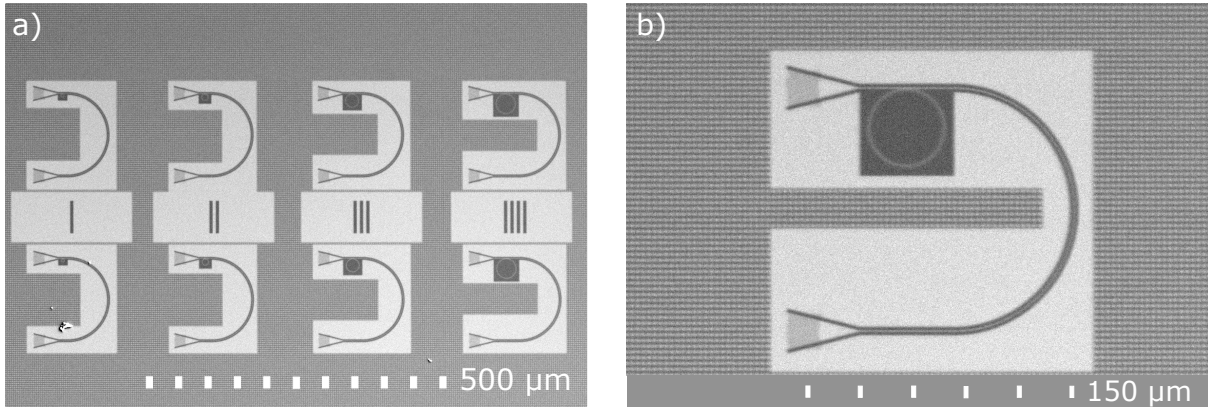


Figure 16: (a) Scanning electron microscope image of photonic crystal ring resonators and standard ring resonators integrated on a silicon chip. (b) The on-chip configuration of a ring, the input and output grating couplers, and the coupling waveguide.

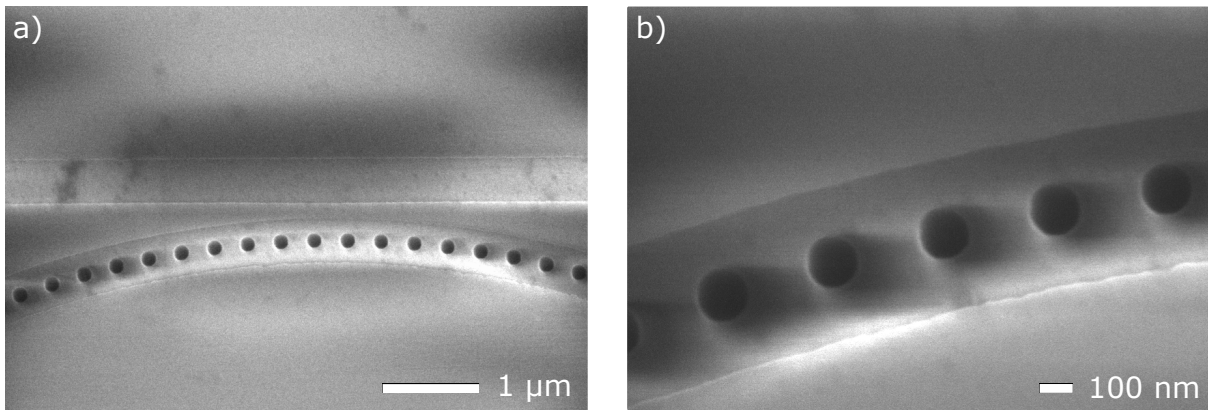


Figure 17: (a) Scanning electron microscope image of the evanescent coupling region between the input waveguide and a photonic crystal ring resonator. (b) The photonic crystal lattice of a PhCRR.

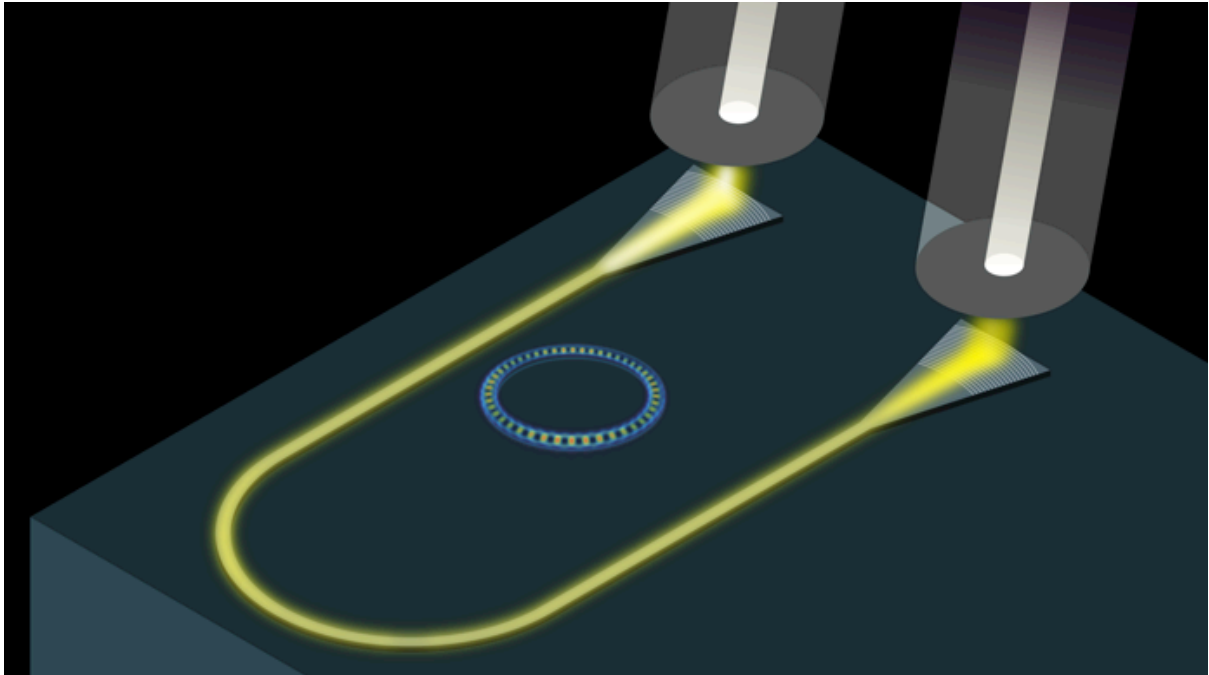


Figure 18: The experimental setup employed for the characterization of on-chip devices. An optical fiber inputs light from a tunable C-Band laser onto the chip via a grating coupler. Each ring is evanescently coupled to a strip waveguide and the transmission spectrum is monitored via an output grating coupler.

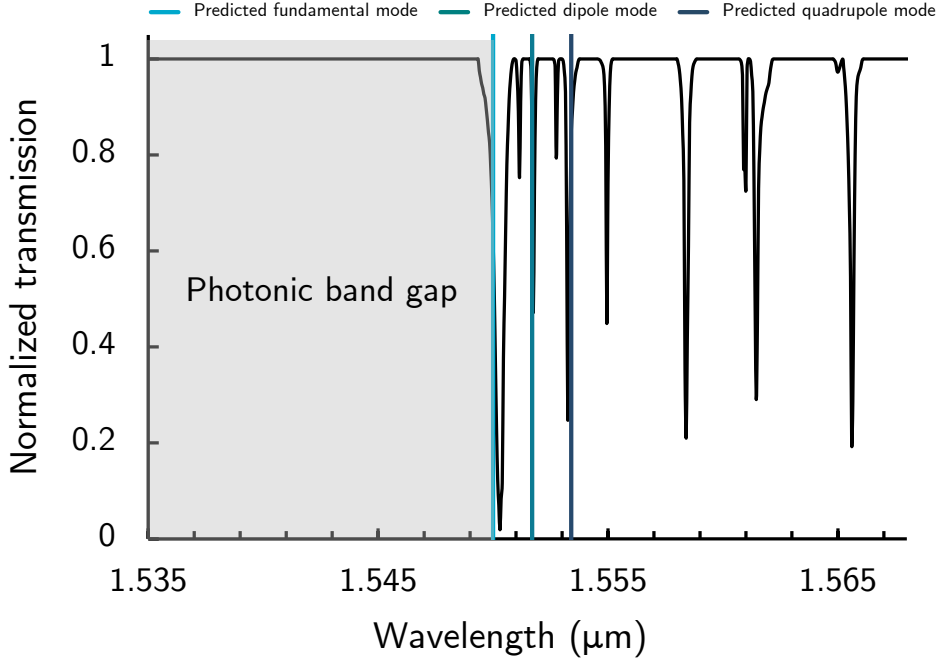


Figure 19: The normalized transmission spectrum of a 20- μm -radius photonic crystal ring resonator. The photonic band gap is indicated by the shaded grey region. The vertical lines denote the wavelengths of fundamental, dipole, and quadrupole modes predicted using the design method detailed above.

the wavelengths of the fundamental ($j = 0$), dipole ($j = 1$), and quadrupole ($j = 2$) modes predicted using the above design method, showing strong agreement between the experimental and computational results. The PhCRR possesses a large photonic band gap, within which no resonances of the ring can be found. Additionally, the PhCRR displays non-equidistant spacing between adjacent resonances which can be attributed to the strong dispersion of the PhC lattice. Splittings of several slow light resonances is observed due to coupling of degenerate propagating and counter-propagating resonances in the ring. In comparison, the transmission spectrum of a 20- μm -radius standard ring resonator (Figure 20) displays no photonic band gap and possesses a constant free spectral range between adjacent resonances.

4.5.1 Experimental determination of ring's dispersion relation

The unique characteristics of a PhCRR allow for experimental determination of the underlying dispersion relation of the PhC waveguide [87]. Each resonance of the PhCRR is assigned a mode number according to its proximity to the photonic band edge using

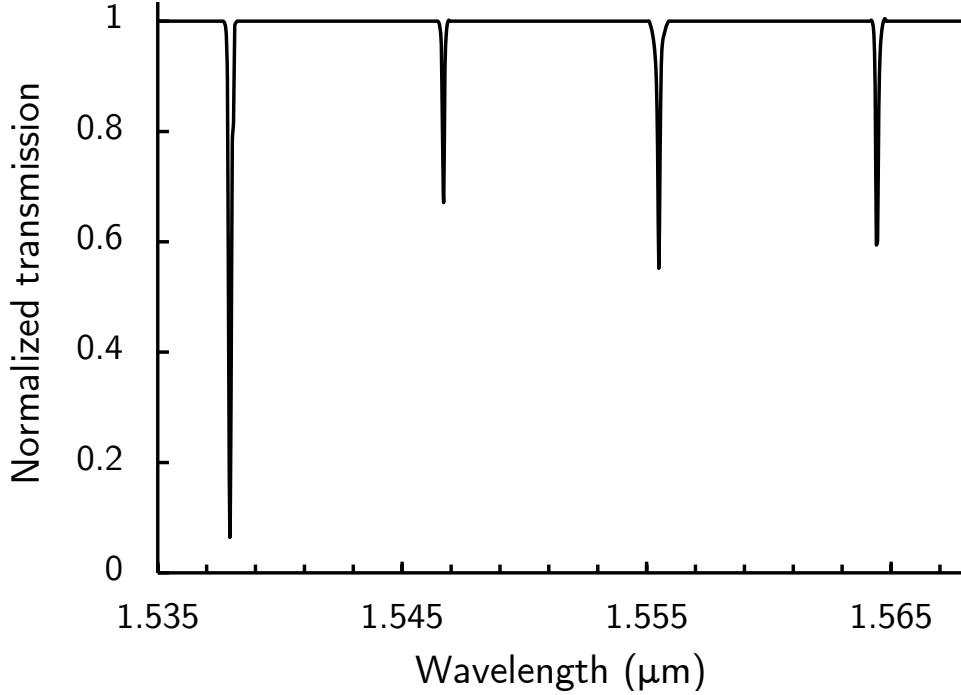


Figure 20: The normalized transmission spectrum of a 20- μm -radius standard ring resonator.

Equation 64. The corresponding wavevector of each mode is then computed using Equation 66. The dimensionless frequency of each mode is found by inserting the resonant wavelength of each mode and the lattice constant of the PhC obtained from scanning-electron-microscope images into Equation 67. Figure 21 compares the experimentally determined dispersion relation of a 10- μm -radius ring to the 2D computational dispersion relation calculated using MPB, showing strong agreement. The non-linearity of the dispersion relation demonstrates the strong dispersion of the PhC lattice near the photonic band edge.

The group index of each resonance is computed using the relation

$$n_g = \frac{c}{v_g} = c \left(\frac{d\omega}{dk} \right)^{-1} \quad (71)$$

Figure 22 shows the experimental group index of a 10- μm -radius ring compared to the computational group index, again showing strong agreement. At the photonic band edge, the group index is ≈ 23.4 , nearly an order of magnitude greater than the effective index of a standard silicon ring resonator. The experimental group index of the dipole mode is noticeably larger than the predicted group index derived from computational results. This could potentially be attributed to fabrication-induced splitting of frequency-degenerate modes. If the mode splitting is comparable to the free spectral range between adjacent

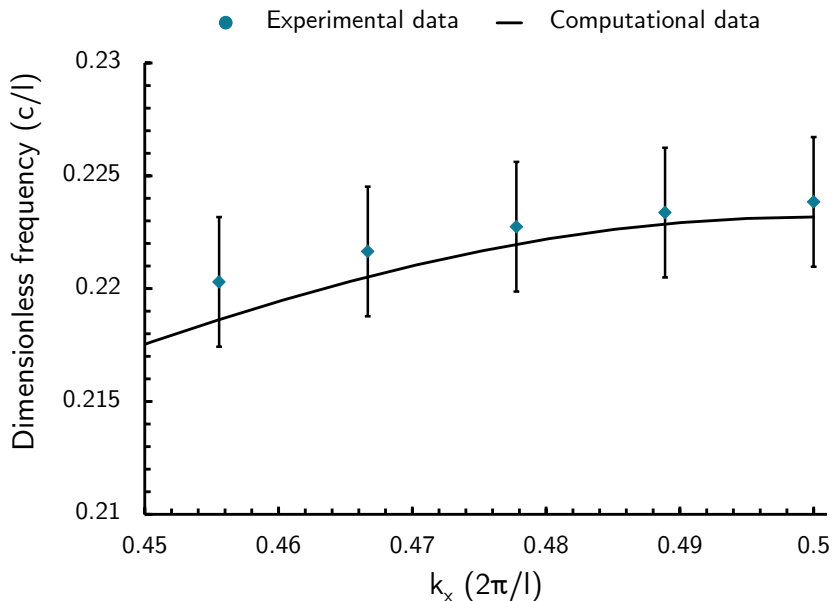


Figure 21: The experimental dispersion relation of a 10- μm -radius photonic crystal ring resonator compared to the dispersion relation of an infinitely long photonic crystal waveguide computed using the MIT Photonic Bands software.

modes, the splitting may contribute to modal interactions resulting in flat-band regions of the dispersion relation found away from the photonic band edge. This effect can provide an additional degree of freedom in engineering the dispersion relation of the PhC lattice.

4.6 Conclusion

In summary, the dispersion relation of a standard optical ring resonator can be engineered via periodic patterning of the material. The resultant photonic crystal lattice is highly dispersive, resulting in slow light regions of the photonic band structure. The phase matching conditions of the ring can be finely tuned to correspond directly with the photonic band edge of the PhC lattice via precise design of the ring's geometric parameters.

The proposed design method has been applied to rings fabricated on the silicon-on-insulator platform via CMOS-compatible 193-nm deep-UV lithography. The optical spectrum of a photonic crystal ring exhibits a photonic band gap and nonequidistant spacing between adjacent resonances. The unique features of the PhCRR allow for experimental determination of the ring's dispersion relation. Using this method, the highly

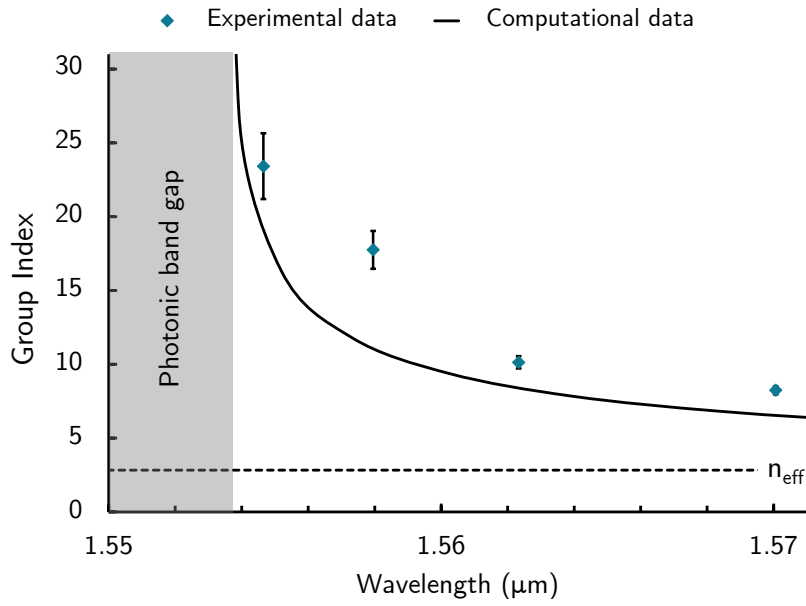


Figure 22: The experimental group index of a 10- μm -radius photonic crystal ring resonator compared to the group index of an infinitely long photonic crystal waveguide computed using the MIT Photonic Bands software.

dispersive nature of a PhCRR has been shown with a maximum calculated group index of ~ 23.6 .

In the next chapter, the principles related to photonic crystal ring resonators will be extended into engineering non-trivial topological geometric phases in dimerized photonic crystal lattices.

Chapter 5

Topological edge states in photonic crystal ring resonators

5.1 Topological photonics

The discovery of the integer quantum Hall effect (QHE) has offered interesting insights into the topological properties of low-dimensional electron gases [88]. Experimental verification of the integer QHE in room-temperature graphene has further intensified exploration of geometric phases in crystalline structures [89]. Intriguingly, the mathematical principles underpinning the quantum Hall effect can be extended to electromagnetic fields. A proposal of an optical quantum Hall effect in a photonic crystal lattice possessing broken time-reversal symmetry [90, 91], followed by experimental observation of microwave photonic edge states in a magneto-optic photonic crystal [92, 93], opened the field of topological photonics. However, extending these concepts to optical frequencies has been hindered by the lack of materials possessing magneto-optic properties.

To overcome this challenge, the geometry of a photonic crystal can be engineered so as to possess non-trivial topology [94, 95]. This method reduces the need for an external-magnetic field and is highly compatible with the tight fabrication resolutions of state-of-the-art lithography processes. The following sections will explore the topological features of various one-dimensional photonic crystal lattices. Different crystal bases (dimer, trimer, and tetramer) are applied to the one-dimensional PhC lattice and the topological characteristics of each lattice are classified using symmetry operators. Additionally, the dimerized PhC lattice is mapped to an optical ring using the concepts of Chapter 4 and computational results demonstrate the appearance of topological edge states in the photonic band gap of the dimerized PhCRR.

5.2 Symmetries of topological insulators

All topological insulators can be sorted into one of ten different symmetry classes via a classification scheme known as the “ten-fold way” [96]. These classes are distinguished by the transformation of a topological insulator’s irreducible, single-particle Hamiltonian under three generic symmetry operators:

1. Time-reversal symmetry

All time-reversal symmetric Hamiltonians satisfy:

$$\mathcal{T}H\mathcal{T}^{-1} = +H \quad (72)$$

where \mathcal{T} is the anti-unitary time-symmetry operator. If the Hamiltonian is time-reversal symmetric, the corresponding topological insulator is assigned a value of either +1 ($\mathcal{T}^2 = +1$) or -1 ($\mathcal{T}^2 = -1$). In the absence of time-reversal symmetry, the insulator is given a value of 0.

2. Charge conjugation symmetry

All charge-conjugation symmetric Hamiltonians satisfy:

$$\mathcal{C}H\mathcal{C}^{-1} = -H \quad (73)$$

where \mathcal{C} is the charge conjugation operator. As in the case of time-symmetry, a Hamiltonian can be assigned a value of either $\mathcal{C} = 1$ ($\mathcal{C}^2 = 1$), -1 ($\mathcal{C}^2 = -1$), or 0.

3. Chiral symmetry

In select cases, a Hamiltonian is found to be invariant after combined application of the \mathcal{T} and \mathcal{C} operators. Such Hamiltonians are categorized as chirally symmetric and satisfy:

$$\mathcal{S}H\mathcal{S}^{-1} = -H \quad (74)$$

where \mathcal{S} is the chiral-symmetry operator defined as:

$$\mathcal{S} = \mathcal{T}\mathcal{C} \quad (75)$$

Hamiltonians are assigned a value of either 0 (no chiral symmetry) or +1 (chiral symmetry). Hamiltonians that possess chiral symmetry can be written in the form:

$$H(k) = \begin{pmatrix} 0 & h^\dagger(k) \\ h(k) & 0 \end{pmatrix} \quad (76)$$

Considering all possible combination of the above symmetries results in a total of ten different symmetry classes. This classification provides useful information concerning the topological invariant of an insulator. For each symmetry class, the spatial dimensionality of the system determines whether the topology of the system is trivial or possesses a \mathbb{Z} or \mathbb{Z}_2 topological invariant (Table 5). Within the context of photonic systems, the ten-fold way can be used to categorize optical systems which possess non-trivial topology. The following section will detail the application of the Su-Schreefer-Heeger model to a one-dimensional photonic crystal. Classification of the SSH model via the ten-fold way will be used to categorize the topology of the system.

5.3 Topological photonic crystal ring resonators

5.3.1 The Su-Schrieffer-Heeger model

The energy band structure of a dimerized atomic lattice can be found through application of the Su-Schreefer-Heeger (SSH) model, which considers particles ‘hopping’ in a periodic potential composed of two sublattices, A and B [97]. Hopping parameters a and b represent the probabilities that a particle will move from one sublattice to the next

Cartan label	\mathcal{T}	\mathcal{C}	\mathcal{S}	$d = 0$	$d = 1$	$d = 2$	$d = 3$
A (unitary)	0	0	0	\mathbb{Z}	0	\mathbb{Z}	0
AI (orthogonal)	+1	0	0	\mathbb{Z}	0	0	0
AII (symplectic)	-1	0	0	$2\mathbb{Z}$	0	\mathbb{Z}_2	\mathbb{Z}_2
AIII (ch. unit.)	0	0	1	0	\mathbb{Z}	0	\mathbb{Z}
BDI (ch. orth.)	+1	1	1	\mathbb{Z}_2	\mathbb{Z}	0	0
CII (ch. sympl.)	-1	-1	1	0	$2\mathbb{Z}$	0	\mathbb{Z}_2
D (BdG)	0	-1	0	\mathbb{Z}_2	\mathbb{Z}_2	\mathbb{Z}	0
C (BdG)	0	-1	0	0	0	$2\mathbb{Z}$	0
DIII (BdG)	-1	+1	1	0	\mathbb{Z}_2	\mathbb{Z}_2	\mathbb{Z}
CI (BdG)	+1	-1	1	0	0	0	$2\mathbb{Z}$

Table 5: The ten symmetry classes of topological insulators. [96]

(Figure 23). The Hamiltonian for a dimerized lattice can be written as [98]:

$$H = a \sum_{n=1}^N \left(|n, A\rangle \langle n, B| + h.c. \right) + b \sum_{n=1}^{N-1} |n+1, A\rangle \langle n, B| + h.c. \quad (77)$$

where n denotes the unit cell index, N is the number of unit cells in the chain, and A and B are the sublattice indices. It is convenient to decompose the Hamiltonian describing the system into a tensor product of its internal (the sublattice index) and external (unit cell index) degrees of freedom:

$$H = \mathcal{H}_{external} \otimes \mathcal{H}_{internal} \quad (78)$$

$$\Rightarrow \langle n, A| = \langle n| \otimes \langle A| \quad (79)$$

The Hamiltonian can now be written in terms of the Pauli matrices, σ_i :

$$H = a \sum_{n=1}^N \left(|n\rangle \langle n| \otimes \sigma_x + h.c. \right) + b \sum_{n=1}^{N-1} \left(|n+1\rangle \langle n| \otimes \frac{\sigma_x + i\sigma_y}{2} + h.c. \right) \quad (80)$$

where the Pauli matrices are defined as:

$$\sigma_0 = \begin{pmatrix} 1 & 0 \\ 0 & 1 \end{pmatrix}; \quad \sigma_x = \begin{pmatrix} 0 & 1 \\ 1 & 0 \end{pmatrix}; \quad \sigma_y = \begin{pmatrix} 0 & -i \\ i & 0 \end{pmatrix}; \quad \sigma_z = \begin{pmatrix} 1 & 0 \\ 0 & -1 \end{pmatrix} \quad (81)$$

If the length of the bulk dimer chain approaches infinity, Born-van Karman boundary conditions can be imposed [77]:

$$\Psi(x) = \Psi(x + Nl) \quad (82)$$

where l is the length of dimer unit cell. Due to the periodicity of the bulk dimer chain, Bloch wave eigenstates of the Hamiltonian can be used:

$$|\Psi_m(k)\rangle = |k\rangle \otimes |u_m(k)\rangle \quad (83)$$

where $|u_m(k)\rangle = a_m(k)|A\rangle + b_m(k)|B\rangle$ are the internal DOF eigenstates of the bulk momentum-space Hamiltonian and $|k\rangle$ are a basis of plane wave states defined as:

$$|k\rangle = \frac{1}{\sqrt{N}} \sum_{n=1}^N e^{ink} |n\rangle \quad (84)$$

The bulk momentum-space Hamiltonian can be found by taking the Fourier transform of Equation 80:

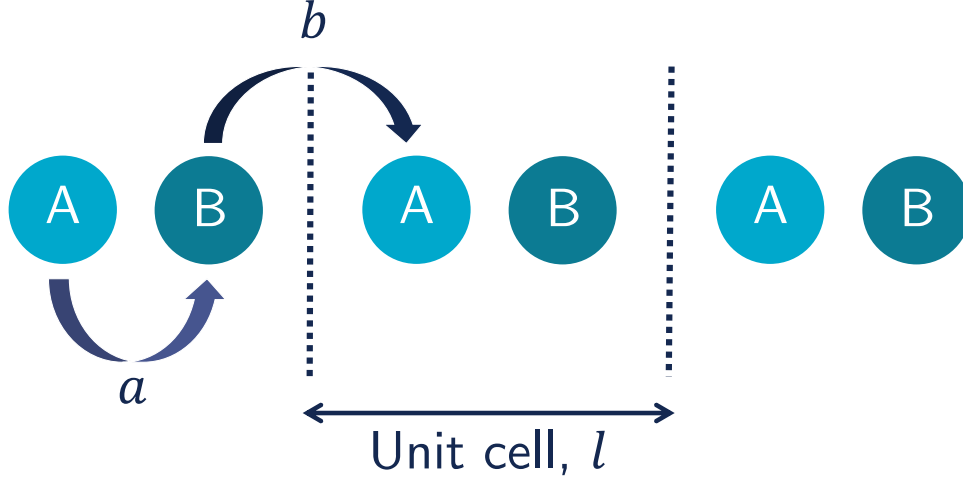


Figure 23: A dimerized atomic chain of lattice constant l and two sublattices, A and B . The probabilities of a particle hopping from one sublattice to the other are denoted by a and b .

$$H(k) = \langle k|H|k\rangle \quad (85)$$

$$= \begin{pmatrix} 0 & a + be^{-ik} \\ a + be^{ik} & 0 \end{pmatrix} \quad (86)$$

Schrödinger's equation now reads:

$$H(k) \begin{pmatrix} a(k) \\ b(k) \end{pmatrix} = E(k) \begin{pmatrix} a(k) \\ b(k) \end{pmatrix} \quad (87)$$

The energy eigenvalues, $E(k)$, of Schrödinger's equation can be found by taking the determinant of Equation 86. The energy spectrum as a function of wavevector k across the first Brillouin zone of the dimer unit cell's reciprocal lattice is plotted in Figure 24. Depending on the values of the hopping parameters, a and b , the energy spectrum of the bulk dimer chain will either be continuous (Figure 24a) or gapped (Figure 24b). This implies that dimerization of a one-dimensional atomic chain converts the bulk properties of the material from conductive to insulating.

5.3.2 Symmetries of the dimerized lattice

To classify the topology of a dimerized atomic lattice, the mathematical framework of the ten-fold way can be applied to the Hamiltonian of the system. The time reversal symmetry operator can be defined as:

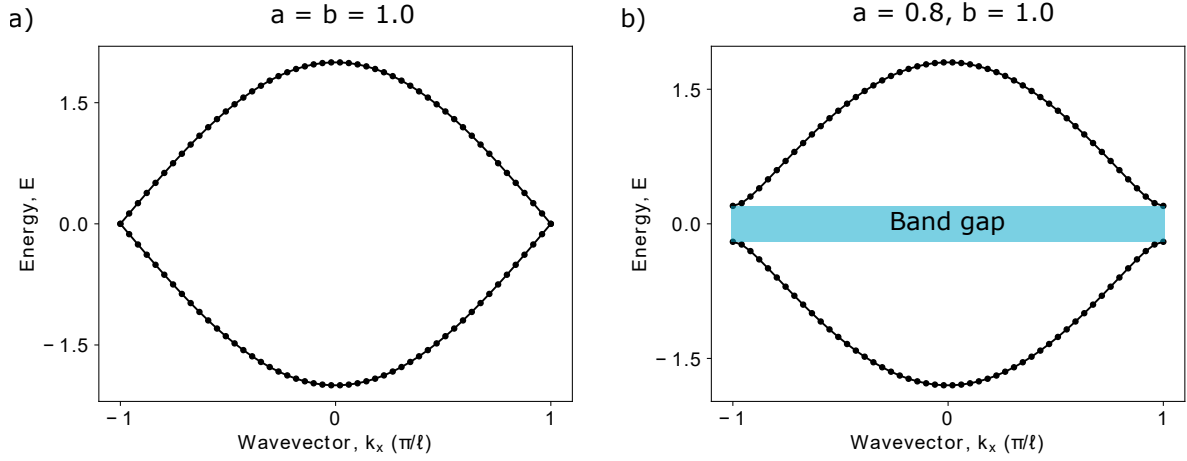


Figure 24: The bulk energy dispersion relation of the SSH model for (a) a one-dimensional atomic lattice with $a = b = 1.0$ and (b) a one-dimensional dimerized atomic lattice with $a = 0.8$ and $b = 1.0$.

$$\mathcal{T} = \gamma \begin{pmatrix} 1 & 0 \\ 0 & 1 \end{pmatrix} \quad (88)$$

where γ indicates the complex conjugation operator (i.e. $\gamma i = -i, \gamma^2 = 1$). Applying this operator to the dimerized Hamiltonian (Equation 86) yields:

$$\mathcal{T}H\mathcal{T}^{-1} = \gamma \begin{pmatrix} 1 & 0 \\ 0 & 1 \end{pmatrix} \begin{pmatrix} 0 & a + be^{-ik} \\ a + be^{+ik} & 0 \end{pmatrix} \gamma \begin{pmatrix} 1 & 0 \\ 0 & 1 \end{pmatrix} \quad (89)$$

$$= \gamma \begin{pmatrix} 1 & 0 \\ 0 & 1 \end{pmatrix} \begin{pmatrix} 0 & a + be^{+ik} \\ a + be^{-ik} & 0 \end{pmatrix} \quad (90)$$

$$= \begin{pmatrix} 0 & a + be^{-ik} \\ a + be^{+ik} & 0 \end{pmatrix} = +H \quad (91)$$

This result indicates that the dimerized Hamiltonian is time-reversal symmetric and can be assigned a value of $\mathcal{T} = \pm 1$. To determine the sign of \mathcal{T} , the value of \mathcal{T}^2 is computed:

$$\mathcal{T}^2 = \gamma \begin{pmatrix} 1 & 0 \\ 0 & 1 \end{pmatrix} \gamma \begin{pmatrix} 1 & 0 \\ 0 & 1 \end{pmatrix} = \gamma^2 \mathbf{1} = \mathbf{1}^2 \quad (92)$$

Hence, \mathcal{T} for a dimerized lattice is 1.

The chiral operator is defined as:

$$\mathcal{S} = \begin{pmatrix} \mathbb{1} & 0 \\ 0 & -\mathbb{1} \end{pmatrix} = \sigma_z \quad (93)$$

The chirality of the dimer chain is found by applying \mathcal{S} to the dimer bulk momentum-space Hamiltonian:

$$\mathcal{S}H\mathcal{S}^{-1} = \begin{pmatrix} 1 & 0 \\ 0 & -1 \end{pmatrix} \begin{pmatrix} 0 & a + be^{-ik} \\ a + be^{+ik} & 0 \end{pmatrix} \begin{pmatrix} 1 & 0 \\ 0 & -1 \end{pmatrix} = \begin{pmatrix} 0 & -a - be^{-ik} \\ -a - be^{+ik} & 0 \end{pmatrix} = -H \quad (94)$$

The Hamiltonian is chirally symmetric and is thus assigned a value of $\mathcal{S} = 1$.

With knowledge of the form of the time-symmetry and chiral symmetry operators, the charge-conjugation operator can be constructed:

$$\mathcal{S} = \sigma_z = \mathcal{T}\mathcal{C} \quad (95)$$

$$\Rightarrow \sigma_z = (\gamma \cdot \mathbb{1})\mathcal{C} \quad (96)$$

The charge-conjugation symmetry operator is necessarily:

$$\mathcal{C} = \gamma\sigma_z \quad (97)$$

Applying this operator to the dimer bulk Hamiltonian yields:

$$\mathcal{C}H\mathcal{C}^{-1} = \gamma \begin{pmatrix} 1 & 0 \\ 0 & -1 \end{pmatrix} \begin{pmatrix} 0 & a + be^{-ik} \\ a + be^{+ik} & 0 \end{pmatrix} \gamma \begin{pmatrix} 1 & 0 \\ 0 & -1 \end{pmatrix} \quad (98)$$

$$= \gamma \begin{pmatrix} 1 & 0 \\ 0 & -1 \end{pmatrix} \begin{pmatrix} 0 & -(a + be^{+ik}) \\ a + be^{-ik} & 0 \end{pmatrix} \quad (99)$$

$$= \begin{pmatrix} 0 & -(a + be^{-ik}) \\ -(a + be^{+ik}) & 0 \end{pmatrix} = -H \quad (100)$$

This result implies that the dimer chain has charge-conjugation symmetry. To determine the sign of \mathcal{C} , the charge-conjugation operator is squared:

$$\mathcal{C}^2 = \gamma \begin{pmatrix} 1 & 0 \\ 0 & -1 \end{pmatrix} \gamma \begin{pmatrix} 1 & 0 \\ 0 & -1 \end{pmatrix} = \mathbb{1} \quad (101)$$

Accordingly, the total classification of the dimer Bulk Hamiltonian is $(\mathcal{T}, \mathcal{C}, \mathcal{S}) = +1, +1, 1$, corresponding to the BDI symmetry group. As the dimer chain has a spatial dimension of $d = 1$, the system will possess a \mathbb{Z} topological invariant.

5.3.3 The Zak phase and topological edge states

To quantify the topological phase of the dimer bulk Hamiltonian, the Berry connection is integrated over the first Brillouin zone of the system. This topological invariant, known as the Zak phase, is defined as [99]:

$$\mathcal{Z} = \frac{i}{\pi} \oint dk \langle u_k | \partial_k u_k \rangle \quad (102)$$

where u_k are the Bloch wave functions. Due to the dimerization of the photonic crystal lattice, the Zak phase can take one of two distinct values:

$$\mathcal{Z} = \begin{cases} 0, & a > b \quad \text{Trivial} \\ 1, & a < b \quad \text{Topological} \end{cases} \quad (103)$$

It can be shown that in the large M limit, \mathcal{Z} can be related to the number of bulk states as [100]:

$$M_{\text{bulk}} = \begin{cases} 2N & \text{when } \mathcal{Z} = 0 \\ 2N - 1 & \text{when } \mathcal{Z} = 1 \end{cases} \quad (104)$$

This equation highlights the bulk-edge correspondence of the SSH model. A dimerized atomic lattice with $a < b$ will possess a state localized on the edges of the chain. This edge state represents the bulk state that has been pulled into the band gap of the insulator to allow for the topological phase transition that occurs at the edge of the atomic chain.

In general, the number of edge states found in the insulating gap is determined by the difference in topological invariant in the two bulk materials. In the case of the SSH model, the interface of the trivial and topological bulk materials will support one edge state [100]:

$$\text{number of edge states} = \mathcal{Z}_{\text{topo}} - \mathcal{Z}_{\text{trivial}} = 1 \quad (105)$$

The confinement of the edge state is determined by the contrast of the intra- and intercell hopping parameters [100]:

$$\frac{a}{b} \approx \exp\left(\frac{l}{\delta}\right) \quad (106)$$

where δ is the edge state's localization length. Spectrally, the edge state will be found precisely mid band gap.

Topologically-protected edge states are highly robust to perturbations. The confinement of the edge state can be attributed to the topological phase transition occurring at the interface between two bulk materials of different invariants. Perturbations to the material are insufficient to alter the topological invariant of each bulk lattice. As a result, the confinement of the edge state is largely unaffected by small perturbations found in the bulk.

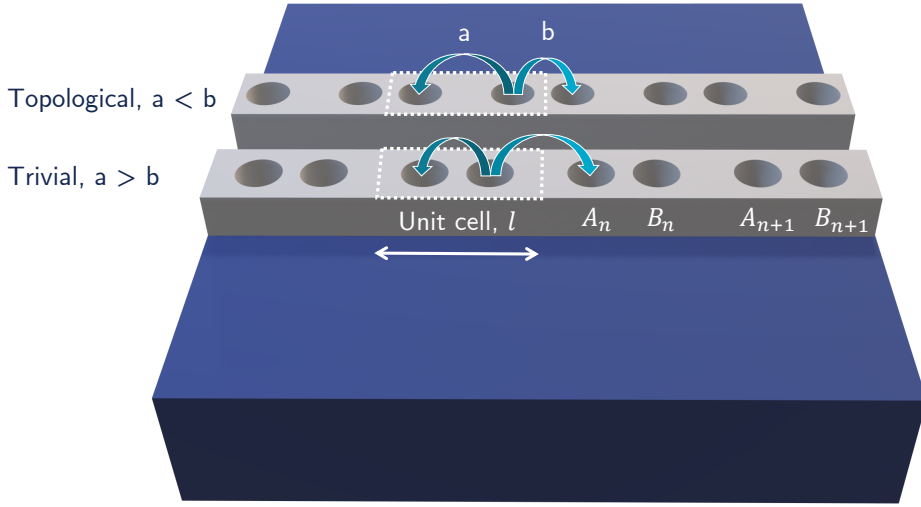


Figure 25: The SSH model implemented in a photonic crystal waveguide. The lattice is dimerized by varying the intra and intercell spacing, denoted as a and b respectively. When the intracell spacing is larger than the intercell spacing (i.e. $a < b$), the Zak phase of the dimer PhC bulk is $\mathcal{Z} = 1$.

5.3.4 The SSH model in a one-dimensional photonic crystal lattice

The SSH model can be implemented in a one-dimensional photonic crystal via dimerization of the PhC lattice (Figure 25). The degree of dimerization in the PhC crystal is controlled by changing the spacing between two adjacent holes. Decreasing the distance between two holes corresponds to a stronger coupling parameter between the two sites. This method introduces a new degree of freedom for engineering the dispersion relation of a waveguide. Recalling Equation 106, the size of the system's band gap is directly related to the contrast of the intra- and intercell hopping parameters. As a result, the band gap of the photonic crystal can be engineered by tuning the lattice's intra- and intercell spacing.

A photonic, topologically-protected edge state can be realized by interfacing the two dimerized PhC bulk chains (Figure 26). The photonic edge state forms a basis for a photonic crystal cavity which is robust against perturbations to the photonic crystal lattice. Photonic crystal cavities have proven interesting platforms for the study of light-matter interactions and cavity quantum electrodynamics due to their low modal volumes and high quality factors [101, 102]. Typical one-dimensional photonic crystal cavities

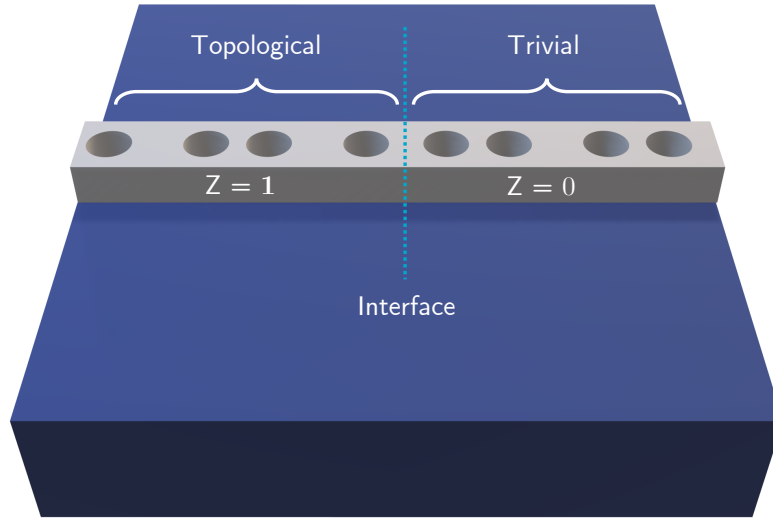


Figure 26: A topological phase transition occurs at the interface between a topological and trivial dimerized photonic crystal waveguide. A topologically-protected edge state will form at the interface between the bulk materials.

are formed through an adiabatic tapering of the PhC hole size [103]. While effective in creating high-Q cavities, this method is susceptible to fabrication imperfections that perturb the taper profile of the PhC holes. Alternatively, a topologically-protected photonic edge state is highly robust against perturbations to the bulk PhC lattice. As a result, edge states in PhC lattices are interesting candidates for highly robust photonic crystal cavities.

To examine the dispersion relation of the dimerized photonic crystal lattice and the presence of photonic edge states, the concepts of Chapter 4 can be applied. By mapping the dimerized photonic crystal lattice onto a ring resonator, the ring's phase matching conditions allows for direct calculation of the dimerized photonic crystal's underlying dispersion. Additionally, the geometry of the ring allows for the design of two topologically-protected edge states formed at the interfaces of the trivial and topological dimerized bulk PhC lattices (Figure 27) which can be easily accessed via evanescent coupling to the ring.

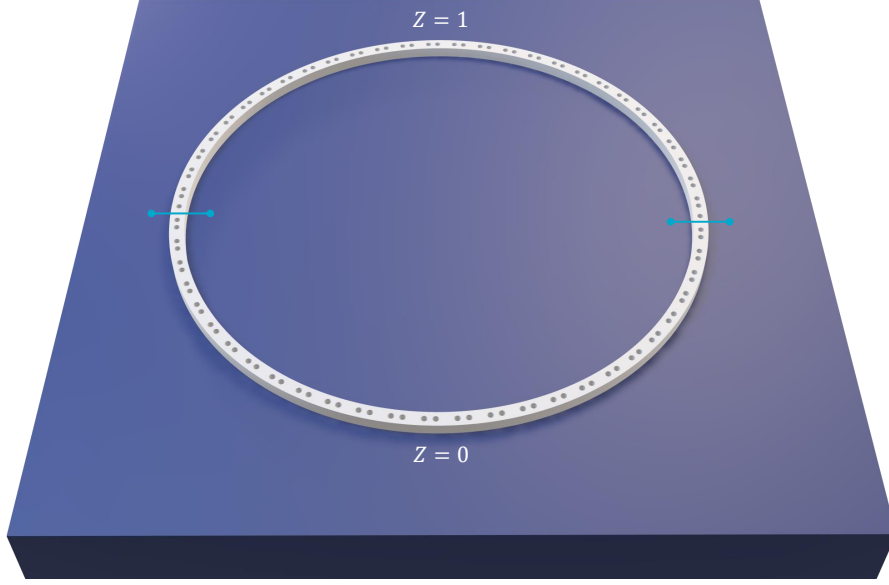


Figure 27: A dimerized photonic crystal ring with two topologically-protected cavities. The ring has parameters $R = 4.991 \mu\text{m}$, $l = 560 \text{ nm}$, $w = 280 \text{ nm}$, $r = 56 \text{ nm}$, and $dd = 0.15l$. The topological edge states will be localized at the interfaces (blue lines) between the trivial ($\mathcal{Z} = 0$) and topological ($\mathcal{Z} = 1$) bulk dimerized PhC lattices.

5.3.5 Computational results

Frequency-domain eigenmode solver simulations

2D-FDE simulations [84] are performed on an infinitely-long, one-dimensional photonic crystal waveguide of effective refractive index $n_{\text{eff}} = 2.83$, $w = \frac{l}{2}$, and PhC hole radius $r = 0.15l$ (Appendix A). Only the TE-polarized, fundamental mode of the waveguide is considered. The degree of dimerization of the lattice, dd , is varied by changing the spacing between the two holes in the simulation's unit cell.

Simulations are run for the parameters $dd = 0, \pm 0.05$ and $\pm 0.1 (l)$. When $dd = 0$, the unit cell is equivalent to a standard photonic crystal waveguide. For $dd > 0$, the Zak phase of the bulk Hamiltonian is trivial, while $dd < 0$ corresponds to a Zak phase of $\mathcal{Z} = 1$. Figure 28 shows the computational dispersion relation of the trivial dimerized photonic crystal lattice. As dd increases, a photonic band gap opens at the point $k_x = \frac{\pi}{l}$. Unlike the theoretical results of the SSH model shown in Figure 24, the bands of the photonic dispersion relation are asymmetric about the photonic band gap. This can be attributed to material dispersion effects which reduce the slope of the dispersion relation in the second band. Figure 29 shows the results for $dd < 0$. Similar to the dispersion relations for $dd > 0$, dimerization of the PhC lattice results in the appearance of a photonic band

gap.

Finite difference time-domain simulations

Following the method detailed in Chapter 4, the dimerized PhC lattice is mapped on to an optical ring resonator. Half of the lattice is dimerized in the trivial ($dd > 0$) configuration, while the second half is dimerized with $dd < 0$. At the interfaces of the two bulk chains, the dimerized photonic crystal ring resonator can support topologically-protected edge states.

To probe the time evolution of the topologically-protected PhC cavities, 2D-FDTD simulations [85] are performed on a ring of parameters $R = 9.90 \mu\text{m}$, $l = 622 \text{ nm}$, $w = 467 \text{ nm}$, $r = 78 \text{ nm}$, $dd = 0.15l$, and $n_{\text{eff}} = 1.786$ (Appendix B.1). A Gaussian dipole source is centered on $\lambda = 1550 \text{ nm}$ with a width of $1 \mu\text{m}$ and the resultant fields are monitored in time. Figure 30a shows the optical spectrum of the ring. As predicted, the ring possesses a photonic band gap due to the dimerization of the lattice. Additionally, a photonic edge state is found at the center of the band gap at a value of $\lambda = 1547 \text{ nm}$. A Gaussian dipole source centered on $\lambda = 1547 \pm 15 \text{ nm}$ is used to characterize the fields of the edge state. As seen in Figure 30b, the field is localized about one of the interfaces between the trivial and topological PhC waveguides and decays exponentially into the bulk lattice. Additionally, the field is localized on a single sub-lattice, consistent with the predictions of the SSH model [98]. By reducing the spacing between the topological interfaces, coupling between the photonic edge states can be induced. The degree of coupling between the states depends on the overlap of the frequency-degenerate wave functions. By reducing the number of unit cells of the trivial dimerized PhC bulk waveguide, N_{triv} , the overlap of the edge state fields increases. This coupling can be observed in the optical spectrum of the ring as splitting of the edge state found in the center of the photonic band gap. Figure 31 demonstrates this effect; the number of unit cells between the two topological interfaces is decreased from (a) $N_{\text{triv}} = 45$, (b) $N_{\text{triv}} = 40$, and (c) $N_{\text{triv}} = 35$. As the overlap of the edge states increases, the computational optical spectra demonstrate symmetric splitting of the degenerate edge state about the center of the photonic band gap. This effect could prove useful for engineering coupled photonic cavities. The topological protection of the edge states ensures the modes will be frequency degenerate; as a result, topologically-protected photonic nanocavities can be coupled without the need for any external tuning of the resonances.

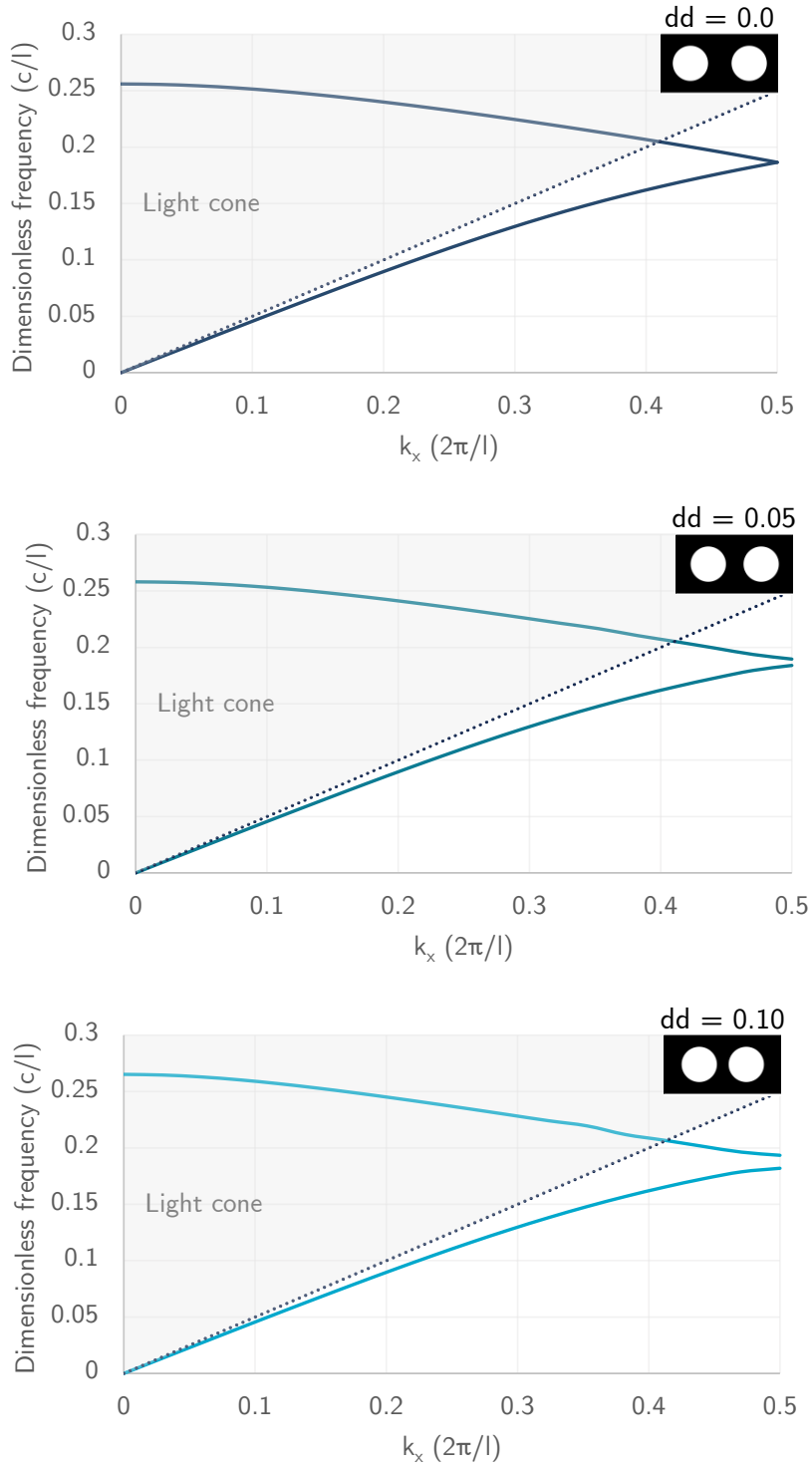


Figure 28: The computational dispersion relation of a one-dimensional photonic crystal waveguide with $w = 0.5l$, $r = 0.15l$, and $n_{\text{eff}} = 2.83$. The degree of dimerization is given in units of the lattice constant l . As the dimerization of the lattice increases, a photonic band gap opens at the point $k_x = \frac{\pi}{l}$. The dimerized unit cell corresponds to a bulk topological Zak phase of $\mathcal{Z} = 0$.

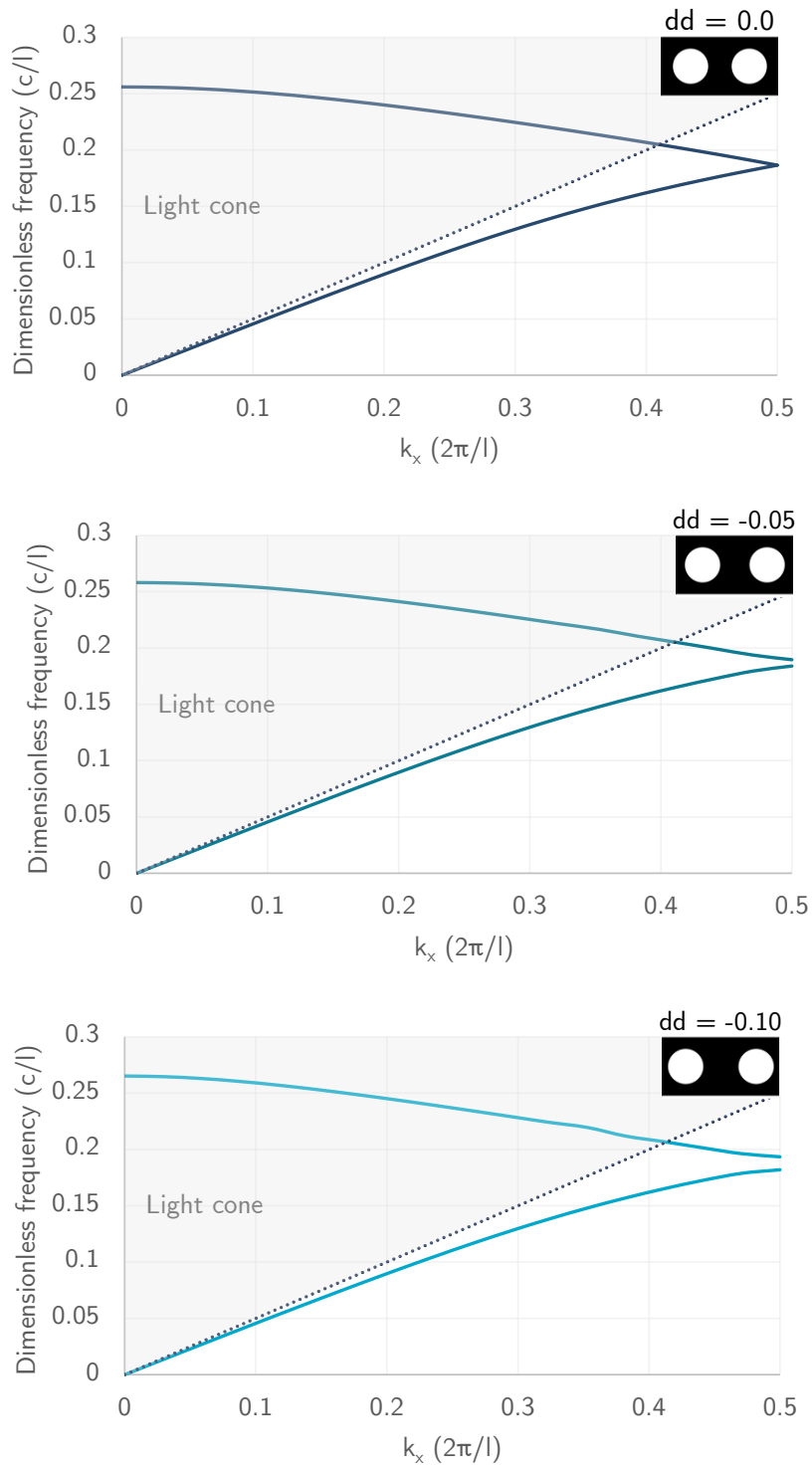


Figure 29: The computational dispersion relation of a one-dimensional photonic crystal waveguide with $w = 0.5l$, $r = 0.15l$, and $n_{\text{eff}} = 2.83$. The dimerized unit cell corresponds to a bulk topological Zak phase of $\mathcal{Z} = 1$.

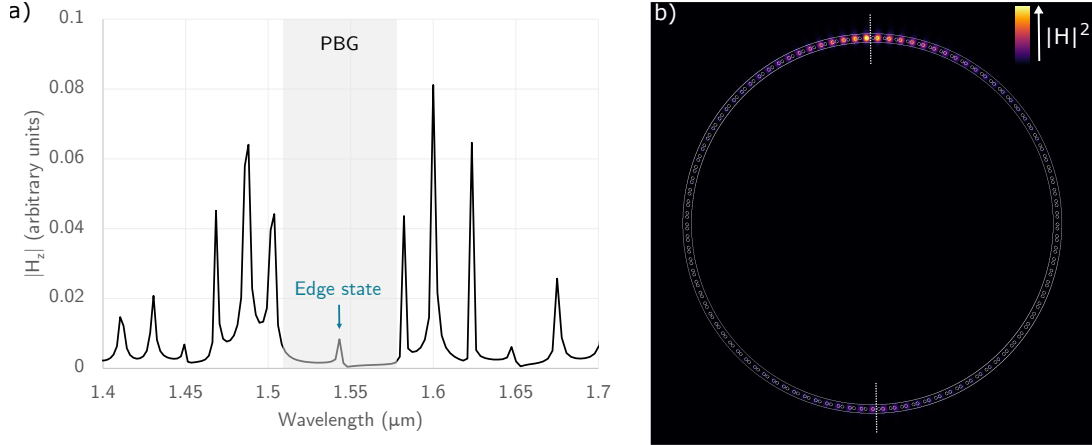


Figure 30: (a) The 2D-FDTD computational optical spectrum of a dimerized photonic crystal ring of parameters $R = 9.90 \mu\text{m}$, $l = 622 \text{ nm}$, $w = 467 \text{ nm}$, $r = 78 \text{ nm}$, $dd = 0.15l$, and $n_{\text{eff}} = 1.786$. The photonic band gap of the ring is shaded in grey. The photonic edge state can be found in the center of the band gap. (b) The magnetic field density of the photonic edge state. The field strength is localized about the bulk-bulk interface (white line) and decays exponentially into the surrounding material.

5.4 Proposed experimental verification

The degree of dimerization of the photonic crystal lattice depends on the spacing between two holes in a unit cell. In practice, the maximum degree of dimerization is limited by the resolution of the fabrication processes ($\sim 50 - 150 \text{ nm}$). To optimize the degree of dimerization, we have chosen to fabricate dimerized photonic crystal rings on silicon nitride via electron beam lithography. The reduced refractive index contrast of the material platform, in combination with the tight fabrication resolution of the e-beam process, allows for sufficient dimerization of the PhC lattice. Devices fabricated with ANT Technologies are currently being characterized (see Appendix D)

5.5 Generalized result for unit cells of $L = 3$ and 4

The SSH model can easily be extended to consider nearest-neighbor hopping in a unit cell of L sites. In particular, the Hamiltonian for a trimerized lattice ($L = 3$) is given as:

$$H = a \sum_{n=1}^N \left(|n, A\rangle \langle n, B| + h.c. \right) + b \sum_{n=1}^N \left(|n, B\rangle \langle n, C| + h.c. \right) + c \sum_{n=1}^{N-1} \left(|n+1, A\rangle \langle n, C| + h.c. \right) \quad (107)$$

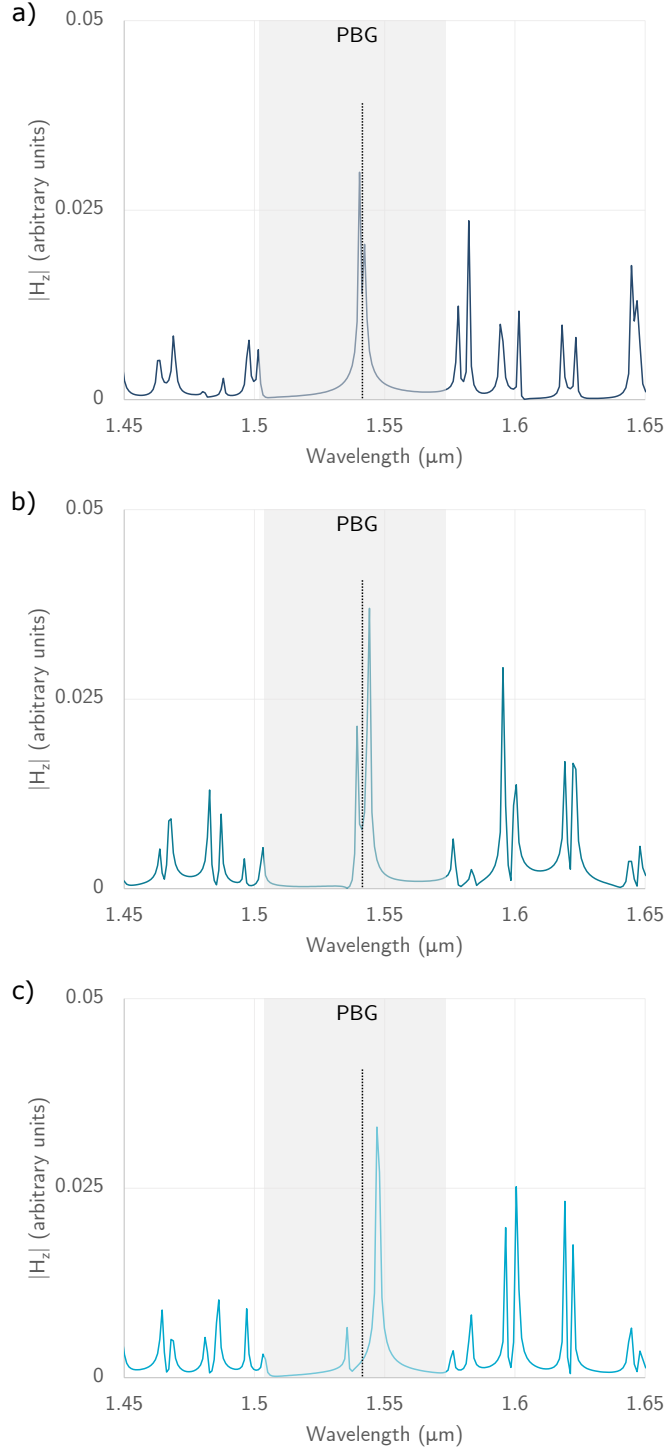


Figure 31: The 2D-FDTD computational optical spectrum of a dimerized photonic crystal ring of parameters $R = 9.90 \mu\text{m}$, $l = 622 \text{ nm}$, $w = 467 \text{ nm}$, $r = 78 \text{ nm}$, $dd = 0.15l$, and $n_{\text{eff}} = 1.786$. The number of unit cells between the two topological interfaces is decreased from (a) $N_{\text{triv}} = 45$, (b) $N_{\text{triv}} = 40$, and (c) $N_{\text{triv}} = 35$ unit cells. The photonic band gap of the ring is shaded in grey. The splitting of the coupled photonic edge states is symmetric about the center of the band gap (dotted black line) and increases with decreasing N_{triv} .

where n denotes the unit cell index, N is the number of unit cells in the chain, and A , B , and C are the sublattice indices (Figure 32).

Following the same method as in Section 5.3¹, the bulk-momentum space Hamiltonian for the trimer unit cell is [105]:

$$H = \begin{pmatrix} 0 & a & ce^{-ik} \\ a & 0 & b \\ ce^{ik} & b & 0 \end{pmatrix} \quad (108)$$

Plotting the eigenvalues of Equation 108 across the first Brillouin zone of the trimer unit cell demonstrates the features of the lattice. As compared to a standard photonic crystal lattice (Figure 33a), a trimerized lattice with $a = b = 0.8$ and $c = 1$ (Figure 33b) possesses two photonic band gaps.

It can be shown that this Hamiltonian again possesses time-reversal symmetry with a \mathcal{T}^2 value of +1. However, it is evident that the trimer Hamiltonian cannot be written in off-diagonal form (i.e. in the form of Equation 76), indicating the trimer chain is not chirally-symmetric. As a result, it is not expected that the trimer chain will support topologically-protected edge states.

However, the geometry of the system allows for definition of a new symmetry operator. When $|a| = |b|$, the unit cell possesses inversion symmetry about its midpoint, which can be characterized by the operator, \mathcal{P} , where [105]:

$$\mathcal{P} = \begin{pmatrix} 0 & 0 & 1 \\ 0 & 1 & 0 \\ 1 & 0 & 0 \end{pmatrix} \quad (109)$$

¹The Hilbert space of the single-particle Hamiltonian is now 3-dimensional. The results of Section 5.3 can be generalized to three dimensions by using the Gell-Mann matrices [104], defined as:

$$\begin{aligned} \lambda_1 &= \begin{pmatrix} 0 & 1 & 0 \\ 1 & 0 & 0 \\ 0 & 0 & 0 \end{pmatrix} & \lambda_2 &= \begin{pmatrix} 0 & -i & 0 \\ i & 0 & 0 \\ 0 & 0 & 0 \end{pmatrix} & \lambda_3 &= \begin{pmatrix} 1 & 0 & 0 \\ 0 & -1 & 0 \\ 0 & 0 & 0 \end{pmatrix} \\ \lambda_4 &= \begin{pmatrix} 0 & 0 & 1 \\ 0 & 0 & 0 \\ 1 & 0 & 0 \end{pmatrix} & \lambda_5 &= \begin{pmatrix} 0 & 0 & -i \\ 0 & 0 & 0 \\ i & 0 & 0 \end{pmatrix} \\ \lambda_6 &= \begin{pmatrix} 0 & 0 & 0 \\ 0 & 0 & 1 \\ 0 & 1 & 0 \end{pmatrix} & \lambda_7 &= \begin{pmatrix} 0 & 0 & 0 \\ 0 & 0 & -i \\ 0 & i & 0 \end{pmatrix} & \lambda_8 &= \frac{1}{\sqrt{3}} \begin{pmatrix} 1 & 0 & 0 \\ 0 & 1 & 0 \\ 0 & 0 & -2 \end{pmatrix} \end{aligned}$$

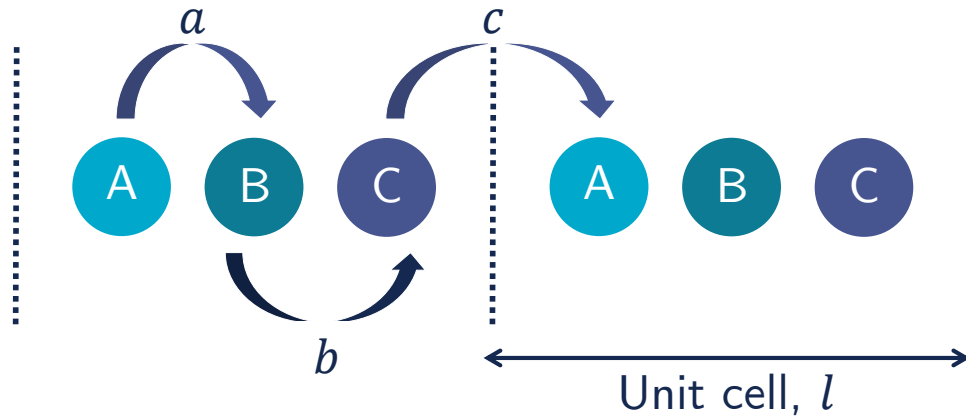


Figure 32: A trimerized atomic chain of lattice constant l and three sublattices, A , B , and C . The probabilities of a particle hopping from one sublattice to the other are denoted by a , b , and c .

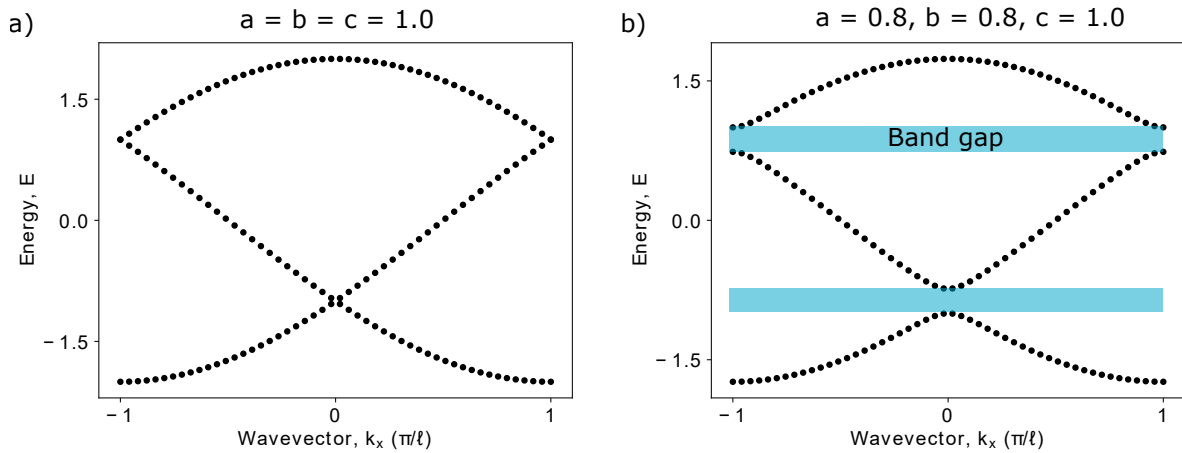


Figure 33: The bulk energy dispersion relation for (a) a one-dimensional atomic lattice with $a = b = c = 1.0$ and (b) a one-dimensional trimerized atomic lattice with $a = 0.8$, $b = 0.8$, and $c = 1.0$.

Similar to chiral symmetry in the SSH model, the topological properties of a one-dimensional bulk Hamiltonian possessing inversion symmetry can be determined via calculation of the Zak phase. In particular, the Zak phase for the trimer phase is defined as [105]:

$$\mathcal{Z} = \begin{cases} 0, & |a| = |b| > |c| \\ 1, & |a| = |b| < |c| \end{cases} \quad (110)$$

While the trivial configuration of the trimer cell does not exhibit any topological properties, the nontrivial configuration will possess a topologically-protected edge state. As opposed to the dimer edge state which is found at both ends of the chain, the trimer edge state is localized at a single bulk-bulk interface. It has additionally been proposed that trimer chains with broken inversion symmetry can also support edge states, provided the hopping amplitudes satisfy certain conditions [105, 106].

For $L = 4$, chirality is returned to the system. The Hamiltonian for a tetramized lattice is given as:

$$\begin{aligned} \hat{H} = & a \sum_{n=1}^N \left(|n, A\rangle \langle n, B| + h.c. \right) + b \sum_{n=1}^N \left(|n, B\rangle \langle n, C| + h.c. \right) \\ & + c \sum_{n=1}^N \left(|n, C\rangle \langle n, D| + h.c. \right) + d \sum_{n=1}^{N-1} \left(|n+1, A\rangle \langle n, D| + h.c. \right) \end{aligned} \quad (111)$$

where n denotes the unit cell index, N is the number of unit cells in the chain, and A , B , C , and D are the sublattice indices (Figure 34). The bulk momentum-space Hamiltonian becomes:

$$\hat{H}(k) = \begin{pmatrix} 0 & 0 & a & de^{-ik} \\ 0 & 0 & b & c \\ a & b & 0 & 0 \\ de^{ik} & c & 0 & 0 \end{pmatrix} \quad (112)$$

The Hamiltonian of the tetramer unit cell has been returned to block off-diagonal form. Application of the chiral operator indicates that the tetramer Hamiltonian possesses chiral symmetry:

$$\mathcal{S}\hat{H}\mathcal{S}^{-1} = \begin{pmatrix} \mathbb{1} & 0 \\ 0 & -\mathbb{1} \end{pmatrix} \begin{pmatrix} 0 & h^\dagger(k) \\ h(k) & 0 \end{pmatrix} \begin{pmatrix} \mathbb{1} & 0 \\ 0 & -\mathbb{1} \end{pmatrix} = \begin{pmatrix} 0 & -h^\dagger(k) \\ -h(k) & 0 \end{pmatrix} = -\hat{H} \quad (113)$$

where $h(k) = \begin{pmatrix} a & b \\ de^{ik} & c \end{pmatrix}$. The chirality of the tetramer chain is evidenced in its dispersion relation (Figure 35b), which displays a symmetric energy spectrum about the zero-energy

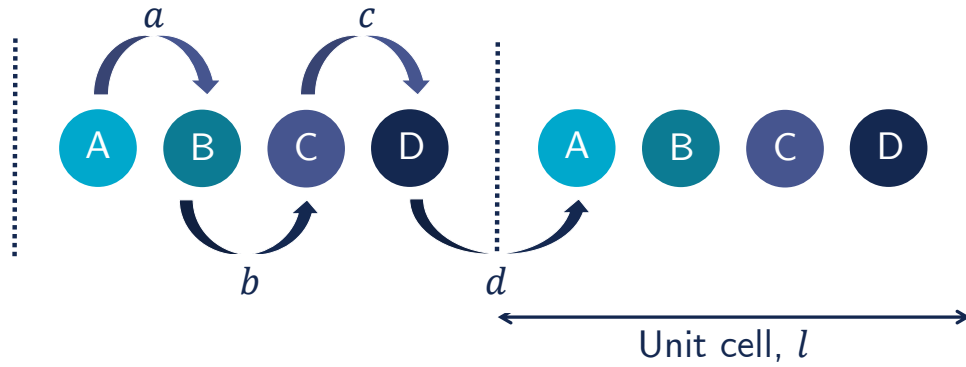


Figure 34: A tetramer atomic chain of lattice constant l and four sublattices, A , B , C , and D . The probabilities of a particle hopping from one sublattice to the other are denoted by a , b , c , and d .

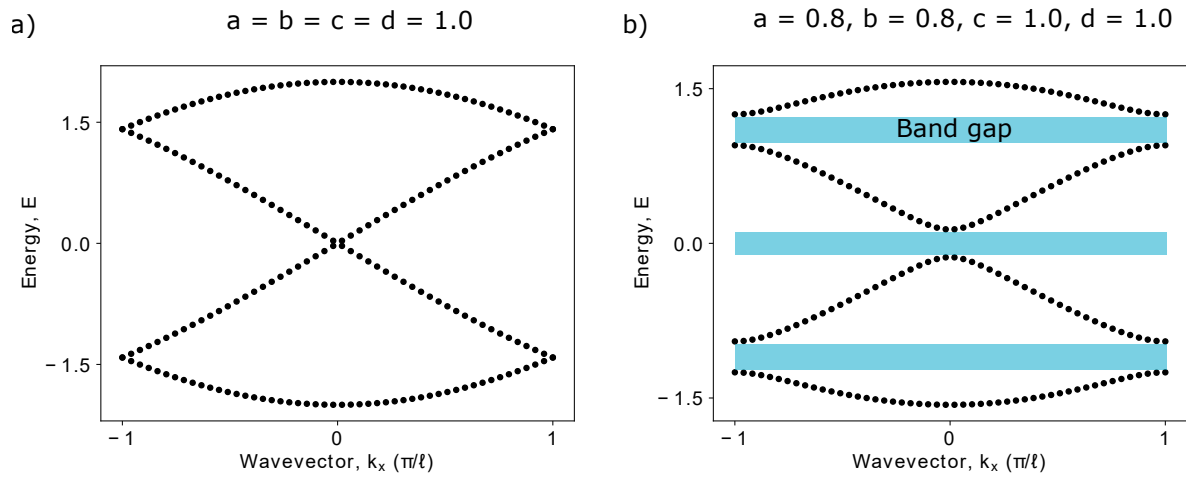


Figure 35: The bulk energy dispersion relation for (a) a one-dimensional atomic lattice with $a = b = c = d = 1.0$ and (b) a one-dimensional tetramer atomic lattice with $a = 0.8$, $b = 0.8$, $c = 1.0$, and $d = 1.0$.

point of the system. Similar to the dimer, the tetramer unit cell belongs to the BDI symmetry class and possesses non-trivial topological features quantified by the Zak phase. Beyond the chirality of the Hamiltonian, the increased parameter space of the tetramer unit cell opens the door for exploration of additional symmetries that may lead to non-trivial topology in the bulk.

5.6 Conclusions

In conclusion, the Su-Schrieffer-Heeger model has been discussed and applied to a one-dimensional photonic crystal waveguide. The lattice is dimerized via variation of the spacing between two adjacent PhC holes. FDE simulations confirm the appearance of a photonic band gap as the PhC lattice is dimerized.

The dimerized 1D photonic crystal lattice is mapped to an optical ring resonator. FDTD simulations are used to verify the dispersion relation of the dimerized PhC lattice. Additionally, the appearance of a photonic edge state found precisely midgap is observed. Coupling of edge states in the ring can be achieved by reducing the number of unit cells in the trivial PhC bulk lattice. As the fields of the edge states overlap, the coupled edge states split symmetrically about the center of the photonic band gap.

The realization of dimerized photonic crystal ring resonators possessing topological edge states on silicon nitride is proposed. Finally, the ten-fold way is applied to the SSH Hamiltonian and the results are generalized to consider non-trivial topology in unit cells of $L = 3$ and $L = 4$.

Chapter 6

Bloch waves in optical ring resonators

In Chapter 4, modal splitting was observed in the transmission spectrum of a photonic crystal ring resonator. This effect can be attributed to backscattering of a clockwise propagating mode into a frequency-degenerate, counterclockwise propagating mode. This scattering occurs due to fabrication-induced disorder on the dielectric surfaces of the ring, resulting in modal coupling which lifts the degeneracy of the resonances. This phenomenon has been well-described via several different approaches, including temporal coupled mode theory [17, 107–111], steady-state loop equations [112], and the transfer-matrix method [113, 114]. While these methods are robust, they are generally restricted to analyzing the splitting of a single mode.

The following chapter will reframe the problem of modal splitting in a ring resonator by mapping the ring’s structure to an equivalent, condensed-matter-inspired system. Specifically, the dielectric profile of the ring is considered as an infinitely-long, periodic dielectric structure and application of Bloch-Floquet theory is utilized to quantify the modal splitting of an arbitrary resonance of the ring. Additionally, this analysis will be extended to show how disorder can be purposefully integrated into the system in order to modify the dispersion of the ring.

6.1 Theoretical prediction

The theoretical analysis of the problem begins with Maxwell’s equations in the form given by Equation 21, where the fields are considered to be harmonic in time (i.e. $\mathbf{E}(\mathbf{r}, t) = \mathbf{E}(\mathbf{r})e^{i\omega t}$) [115]. Several assumptions can now be made which simplify the form of Equation

21. As in Chapter 4, the radius of curvature of the ring is considered to be much larger than the wavelength of light under consideration (Equation 65), allowing the ring to be considered as an infinitely long waveguide with a dielectric function of:

$$\varepsilon(\mathbf{r}) = \varepsilon(x) \quad (114)$$

In such a system, the wavevector of the ring can be written as:

$$\mathbf{k}(\mathbf{r}) = k(x) \quad (115)$$

Finally, it is assumed that the electric field is linearly polarized, reducing the electric field to $\mathbf{E}(\mathbf{r}) = E(x)\hat{y}$. The above assumptions, in combination with the linear dispersion relation $\omega = \frac{ck}{n_{\text{eff}}}$, yield a one-dimensional Helmholtz equation of the form:

$$\varepsilon^{-1}(x) \frac{\partial^2 E}{\partial x^2} = -\left(\frac{\omega}{c}\right)^2 E(x) \quad (116)$$

This equation is analogous in form to the time-independent Schrödinger's equation and thus allows for direct comparison between the dielectric function of an optical ring resonator and a periodic potential energy landscape in a solid state system.

While this analysis is similar to the discussion of photonic crystals in Chapter 4, a crucial difference lies in the defined lattice constant of the system. In a standard PhC, the lattice constant of the crystal is engineered into the system and its dimensions are on the order of the wavelength of light propagating through the material. Conversely, the periodicity of the ring is innate to the structure, with a lattice constant equal to its perimeter $P = 2\pi R$ (Figure 36). This allows Equation 114 to be written as:

$$\varepsilon(x) = \varepsilon(x + 2\pi R) \quad (117)$$

Applying the Bloch-Floquet theorem to Equation 116, it can be shown [116] that the fields propagating in the ring must satisfy:

$$E(x) = E(x + 2\pi R) \quad (118)$$

The periodicity of the ring results in the formation of Bragg planes at the points of symmetry in the reciprocal lattice of the ring, given by:

$$k_x = \pm \frac{n\pi}{P} = \pm \frac{n}{2R} \quad (119)$$

where $n \in \mathbb{Z}$. At these symmetry points, the frequency-degeneracy of the propagating and counterpropagating modes of the ring is lifted, resulting in the appearance of photonic

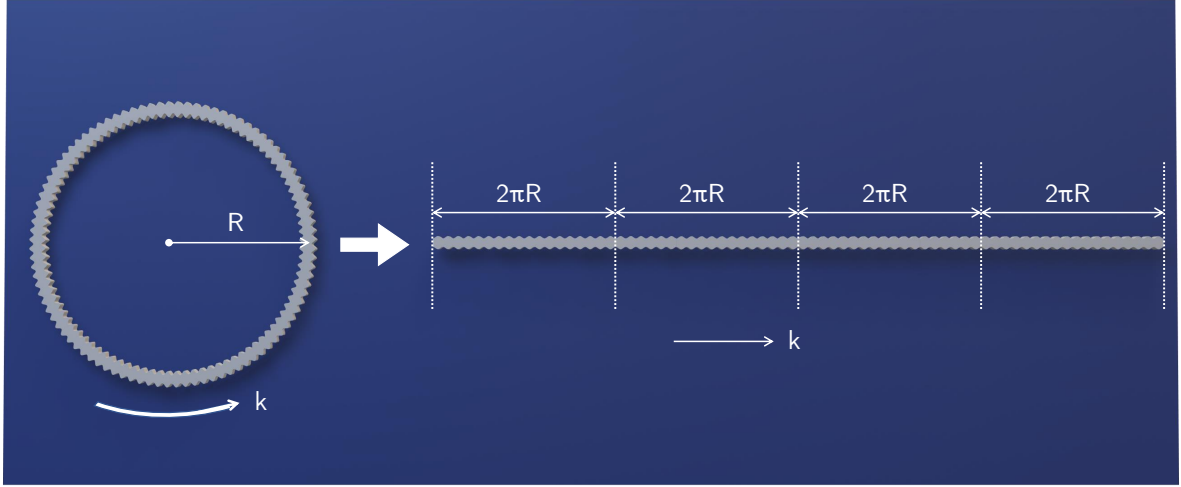


Figure 36: A standard ring resonator of radius R with point surface scatterers represented as an infinitely long dielectric waveguide.

band gaps in the ring's dispersion relation. The relation between the ring's Bragg planes and the ring's resonances is found by applying the phase matching conditions required by the ring's geometry. Combining Equations 42 and 119, it is found that a resonance of the ring coincides with a Bragg plane whenever $n = \{2m : m \in \mathbb{Z}\}$. Figure 37 depicts the ring's first Brillouin zone in reciprocal space. In the reduced zone scheme of the ring's dispersion relation, only the $m = 0$ phase matching condition is applicable. The $n = 0$ Bragg plane aligns with this phase matching condition, resulting in resonances which are susceptible to modal splitting.

6.1.1 Quantitative Fourier analysis of modal splitting

The magnitude of this splitting can be determined via a Fourier analysis of the ring's dielectric profile. Due to the periodicity of the ring, the dielectric profile can be decomposed into a Fourier series [115]. More specifically, the inverse dielectric profile can be written as:

$$\varepsilon^{-1}(x) = \sum_{l=-\infty}^{\infty} \kappa_l e^{i2\pi lx} \quad (120)$$

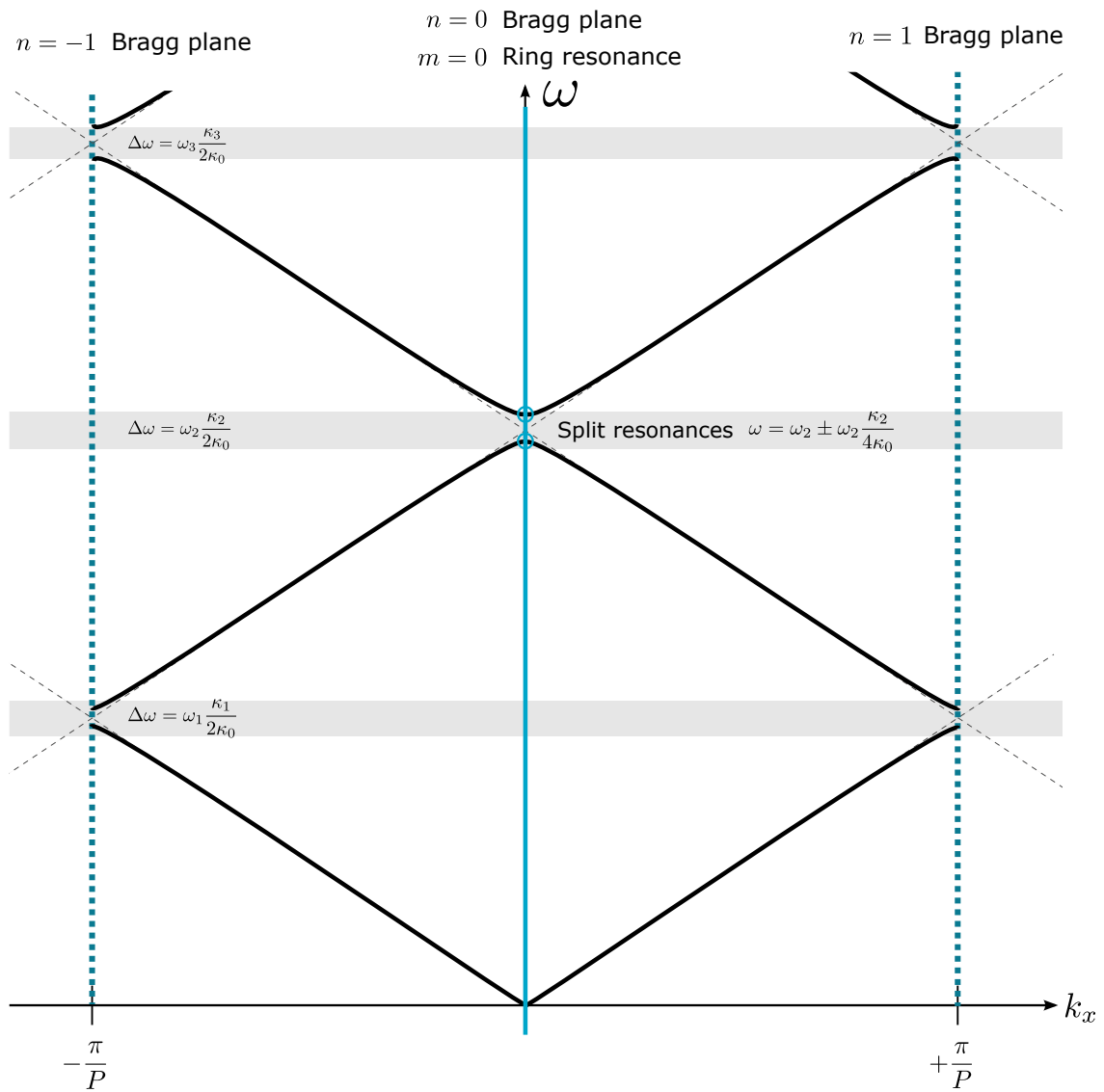


Figure 37: The photonic dispersion relation of a ring resonator in the reduced zone scheme (assuming linear waveguide dispersion). A resonance of the ring is found wherever the phase matching boundary conditions intersect with dispersion relation of the infinitely-long waveguide. (solid green line at $k_x = 0$). Phase matching conditions are separated by one reciprocal-lattice vector ($k_x = \frac{2\pi}{P}$); as a result, only the $m = 0$ boundary condition represents a physically distinct state in the reduced zone scheme.

where $l \in \mathbb{Z}$ and κ_l are the dielectric function's Fourier coefficients. Similarly, Bloch-Floquet theory allows the electric fields to be expressed as:

$$E(x) = \sum_{l=-\infty}^{\infty} E_l e^{i(k_x + 2\pi l/P)x} \quad (121)$$

Following the derivation detailed in Reference [116], it is first assumed that the Fourier expansion of the inverse dielectric function is dominated by the $l = 0$ and $l = \pm n$ components, where n is an arbitrary integer. Under this assumption the inverse dielectric function becomes:

$$\varepsilon^{-1}(x) = \kappa_0 + \kappa_n e^{i2\pi n x/P} + \kappa_{-n} e^{-i2\pi n x/P} \quad (122)$$

Equations 121 and 122 are now inserted into the 1D Helmholtz equation given by Equation 116:

$$\begin{aligned} & - \sum_{p=-1}^1 \sum_{l=-\infty}^{\infty} \kappa_{n \times p} e^{i \frac{2\pi(n \times p)x}{P}} E_l e^{i(k + \frac{2\pi l}{P})x} \left(k + \frac{2\pi l}{P} \right)^2 = - \left(\frac{\omega}{c} \right)^2 \sum_{l=-\infty}^{\infty} E_l e^{i(k + \frac{2\pi l}{P})x} \\ \Rightarrow & - \sum_{l=-\infty}^{\infty} \kappa_{-n} E_{l+n} e^{-i \frac{2\pi n x}{P}} e^{i \frac{2\pi(l+n)x}{P}} \left[k + \frac{2\pi(l+n)}{P} \right]^2 - \kappa_n E_{l-n} e^{i \frac{2\pi n x}{P}} e^{i \frac{2\pi(l-n)x}{P}} \left[k + \frac{2\pi(l-n)}{P} \right]^2 \\ & = \sum_{l=-\infty}^{\infty} \left[\kappa_0 \left(k + \frac{2\pi l}{P} \right)^2 - \left(\frac{\omega}{c} \right)^2 \right] E_l e^{i \frac{2\pi l}{P} x} \\ \Rightarrow & \sum_{l=-\infty}^{\infty} \kappa_{-n} \left[k + \frac{2\pi(l+n)}{P} \right]^2 E_{l+n} + \kappa_n \left[k + \frac{2\pi(l-n)}{P} \right]^2 E_{l-n} \\ & = \sum_{l=-\infty}^{\infty} \left[\left(\frac{\omega}{c} \right)^2 - \kappa_0 \left(k + \frac{2\pi l}{P} \right)^2 \right] E_l \end{aligned} \quad (123)$$

When $l = 0$, Equation 123 becomes:

$$\begin{aligned} & \kappa_{-n} \left(k + \frac{2\pi n}{P} \right)^2 E_n + \kappa_n \left(k - \frac{2\pi n}{P} \right)^2 E_{-n} = \left[\left(\frac{\omega}{c} \right)^2 - \kappa_0 k^2 \right] E_0 \\ \Rightarrow & E_0 \simeq \frac{1}{\left(\frac{\omega}{c} \right)^2 - \kappa_0 k^2} \left[\kappa_{-n} \left(k + \frac{2\pi n}{P} \right)^2 E_n + \kappa_n \left(k - \frac{2\pi n}{P} \right)^2 E_{-n} \right] \end{aligned} \quad (124)$$

Likewise, for $l = -n$:

$$\begin{aligned} & \kappa_{-n} k^2 E_0 + \kappa_n \left(k - \frac{4\pi n}{P} \right)^2 E_{-2n} = \left[\left(\frac{\omega}{c} \right)^2 - \kappa_0 \left(k - \frac{2\pi n}{P} \right)^2 \right] E_{-n} \\ \Rightarrow & E_{-n} \approx \frac{1}{\left(\frac{\omega}{c} \right)^2 - \kappa_0 \left(k - \frac{2\pi n}{P} \right)^2} \left[\kappa_n \left(k - \frac{4\pi n}{P} \right)^2 E_{-2n} + \kappa_{-n} k^2 E_0 \right] \end{aligned} \quad (125)$$

For a linear dispersion relation, the terms given by Equations 124 and 125 will dominate the Fourier series of the electric field whenever $k \approx \pm \frac{2\pi n}{P}$. Near these symmetry points of the ring's dispersion relation, Equations 124 and 125 are reduced to a coupled set of linear equations:

$$\begin{aligned} \left[\left(\frac{\omega}{c} \right)^2 - \kappa_0 k^2 \right] E_0 - \kappa_n \left(k - \frac{2\pi n}{P} \right)^2 E_{-n} &= 0 \\ \kappa_{-n} k^2 E_0 + \left[\left(\frac{\omega}{c} \right)^2 - \kappa_0 \left(k - \frac{2\pi n}{P} \right)^2 \right] E_{-n} &= 0 \end{aligned} \quad (126)$$

The solutions to the coupled equations can be found by taking the determinant of the resultant coefficient matrix:

$$\begin{vmatrix} \left(\frac{\omega}{c} \right)^2 - \kappa_0 k^2 & -\kappa_n \left(k - \frac{2\pi n}{P} \right)^2 \\ \kappa_{-n} k^2 & \left(\frac{\omega}{c} \right)^2 - \kappa_0 \left(k - \frac{2\pi n}{P} \right)^2 \end{vmatrix} = 0 \quad (127)$$

Defining $h = k - \frac{\pi n}{P}$, Equation 127 can be rewritten as:

$$\begin{vmatrix} \left(\frac{\omega}{c} \right)^2 - \kappa_0 \left(h + \frac{\pi n}{P} \right)^2 & -\kappa_n \left(h - \frac{\pi n}{P} \right)^2 \\ -\kappa_{-n} \left(h + \frac{\pi n}{P} \right)^2 & \left(\frac{\omega}{c} \right)^2 - \kappa_0 \left(h - \frac{\pi n}{P} \right)^2 \end{vmatrix} = 0 \quad (128)$$

$$\Rightarrow \left[\left(\frac{\omega}{c} \right)^2 - \kappa_0 \left(h + \frac{\pi n}{P} \right)^2 \right] \left[\left(\frac{\omega}{c} \right)^2 - \kappa_0 \left(h - \frac{\pi n}{P} \right)^2 \right] - \kappa_n^2 \left(h + \frac{\pi n}{P} \right)^2 \left(h - \frac{\pi n}{P} \right)^2 = 0 \quad (129)$$

Because the dispersion relation for the ring is approximately linear, only the terms $\propto h^0$ and h^4 are considered, yielding an approximate solution to Equation 129:

$$\left(\frac{\omega}{c} \right)^4 \simeq h^4 \left(\kappa_0^2 - \kappa_n^2 \right) + \left(\frac{\pi n}{2P} \right)^4 \left(\kappa_0^2 - \kappa_n^2 \right) \quad (130)$$

Near the photonic band edge (i.e. the RR phase matching condition $h = 0$), the dispersion relation is determined by the intercept of Equation 130:

$$\begin{aligned} \left(\frac{\omega}{c} \right)^4 &\simeq \left(\frac{\pi n}{2P} \right)^4 \kappa_0^2 \left(1 - \frac{\kappa_n^2}{\kappa_0^2} \right) \\ \Rightarrow \omega^2 \pm &\simeq \frac{\omega_n^2}{4} \sqrt{1 - \frac{\kappa_n^2}{\kappa_0^2}} \end{aligned} \quad (131)$$

where $\omega_n \equiv \frac{cn\sqrt{\kappa_0}}{2P}$ (s^{-1}) = $\frac{n\sqrt{\kappa_0}}{2} \left(\frac{c}{P} \right)$. For a small perturbation to the ring (i.e. for $\kappa_n \ll \kappa_0$), a Taylor expansion of Equation 131 yields:

$$\omega^2 = \begin{cases} + \frac{\omega_n^2}{4} \left(1 \pm \frac{\kappa_n^2}{2\kappa_0^2} \right), & \text{positive roots} \\ - \frac{\omega_n^2}{4} \left(1 \pm \frac{\kappa_n^2}{2\kappa_0^2} \right), & \text{negative roots} \end{cases} \quad (132)$$

Imposing realness on the frequency eigenvalues of the system, the negative eigenvalues of Equation 132 are discarded, while the positive eigenvalues are used to solve for $\Delta\omega$:

$$\begin{aligned}\Delta\omega^2 &= \frac{\omega_n^2}{4} + \frac{1}{2}\left(\frac{\omega_n\kappa_n}{2\kappa_0}\right)^2 - \frac{\omega_n^2}{4} - \frac{-1}{2}\left(\frac{\omega_n\kappa_n}{2\kappa_0}\right)^2 \\ &= \left(\frac{\omega_n\kappa_n}{2\kappa_0}\right)^2\end{aligned}\quad (133)$$

Thus, a small perturbation to the ring of magnitude κ_n and spatial period $T = \frac{2\pi R}{n}$ will result in the formation of a photonic band gap of magnitude:

$$\Delta\omega = \omega_n \frac{\kappa_n}{2\kappa_0} \quad (134)$$

As this photonic band gap corresponds to the phase matching conditions for the $m = \frac{n}{2}$ resonance of the ring, frequency splitting determined by Equation 134 will occur in the ring's optical spectrum (Figure 37).

6.2 Computational results

To verify the theoretical prediction of 6.1, simulations are performed on an example device with the aim of designedly splitting the $m = 48$ resonance of a $5\text{-}\mu\text{m}$ -radius SOI ring resonator [115]. Both a frequency-domain eigenmode solver (FDE) and a finite-difference-time-domain approach are utilized and compared.

6.2.1 Frequency-domain eigenmode solver simulations

2D-FDE simulations [84] are used to compute the effect of a small dielectric perturbation on the 1D dispersion relation of an infinitely-long, 2D SOI waveguide of width $w = 0.45\ \mu\text{m}$. The effective index of the SOI waveguide is computed assuming an air cladding, yielding a value of $n_{\text{eff}} = 2.83$. Only the fundamental, TE polarized mode of the waveguide is considered.

To induce modal coupling of the $m = 48$ resonance, a perturbation whose periodicity matches the modal order is turned on. The inverse dielectric function of the waveguide in real space can be defined as:

$$\epsilon^{-1}(x) = \kappa_0 + \sum_{2m:m \in \mathbb{Z}} \kappa_m \cos\left(\frac{2\pi mx}{P}\right) \quad (135)$$

where $\kappa_0 = \frac{1}{n_{\text{eff}}^2}$. Thus, the effective index of the waveguide is varied with a modulation of period $T = \frac{2\pi \cdot 5\ \mu\text{m}}{96}$, corresponding to a physical modulation of lattice constant $a =$

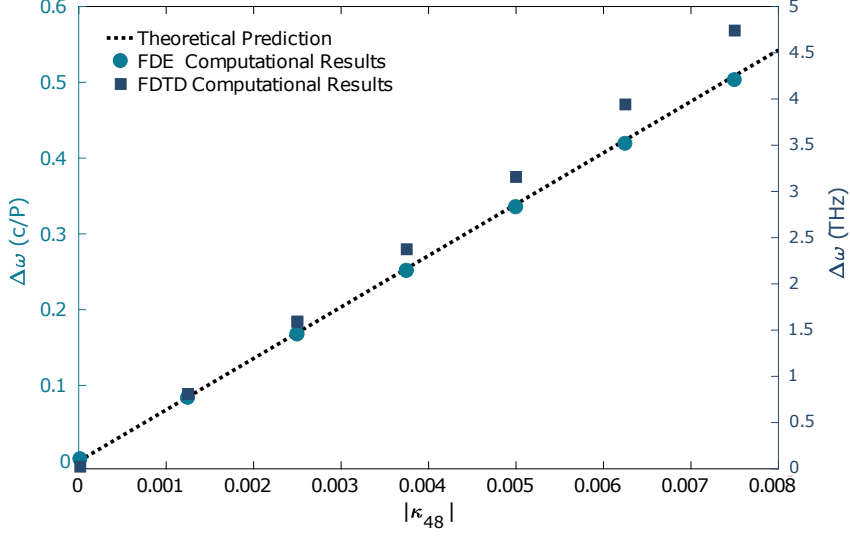


Figure 38: The numerical prediction of Equation 134 as compared to FDE and FDTD computational results for various values of κ_{48} . The dimensionless frequency of the FDE results has been scaled to the characteristic length unit for the system, the ring’s perimeter P , while the FDTD results are given in THz.

0.33 μm . In this particular work, it is proposed that the refractive index of the ring can be perturbed by varying the width of the ring’s waveguide, resulting in a slight change in the effective index due to waveguide dispersion effects. Because the material is assumed to be lossless, $\epsilon^{-1}(x)$ is considered to be entirely real. Additionally, the Fourier expansion of $\epsilon^{-1}(x)$ is independent of frequency and therefore does not account for material dispersion. To simplify the definition of the simulation’s geometry, a material function is defined which periodically varies the strength of the dielectric function in a one-dimensional waveguide with periodic boundary conditions. Simulations are run for the parameters $\kappa_{48} = 0, 0.00125, 0.0025, 0.00375, 0.005, 0.00625, \text{ and } 0.0075$. The results are seen in Figure 38, showing good agreement with the prediction given by Equation 134.

6.2.2 Finite-difference time-domain simulations

2D-FDTD simulations [85] are used to probe the time evolution of the coupled modes (Appendix B.2). A SOI ring resonator of radius 5.042 μm and a width modulation of period $T = \frac{2\pi R}{48}$ is simulated in two dimensions. A broadband Gaussian dipole source centered at 1550 nm is used to excite the modes of the ring. The fields are measured in time and a Fourier transform yields the optical spectrum of the ring. As the magnitude

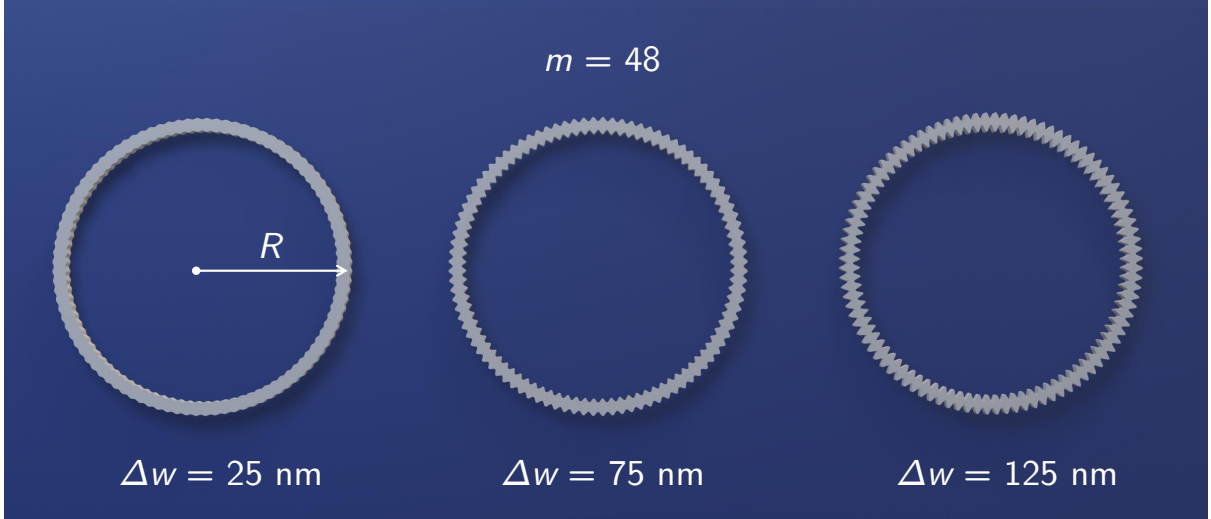


Figure 39: The dielectric profile of three ring resonators of radius $R = 5 \mu\text{m}$ with perturbations of magnitude $\kappa_{48} = 0.015$ ($\Delta w = 25 \text{ nm}$), 0.003 ($\Delta w = 75 \text{ nm}$), and 0.0045 ($\Delta w = 125 \text{ nm}$).

of κ_{48} is increased (Figure 39), splitting of the 48^{th} resonance is observed (Figure 40), corresponding well with the linear prediction of Equation 134. No frequency splitting in the $m \neq 48$ resonances is observed, indicating that all $l \neq m$ -resonances are unaffected by a m^{th} -order perturbation. However, the computational results show a higher slope than predicted (Figure 38). This could potentially be attributed to curvature effects which were not considered in the theoretical model.

6.3 Experimental results

In the previous section, the computational analysis was restricted to SOI optical ring resonators. In practice, the waveguide width modulations required to split the resonances of a $5\text{-}\mu\text{m}$ -radius SOI ring are on the order of $5\text{-}10 \text{ nm}$. Such a small modulation is outside of the fabrication resolutions of either optical or electron-beam lithography. Alternatively, the reduced refractive index contrast of the silicon nitride platform requires waveguide width modulations on the order of $50\text{-}100 \text{ nm}$, which are easily fabricated using standard lithography techniques. As a result, the silicon nitride platform was chosen for the experimental portion of this work.

Rings of radii $\sim 20 \mu\text{m}$ were fabricated on a silicon nitride chip via electron beam

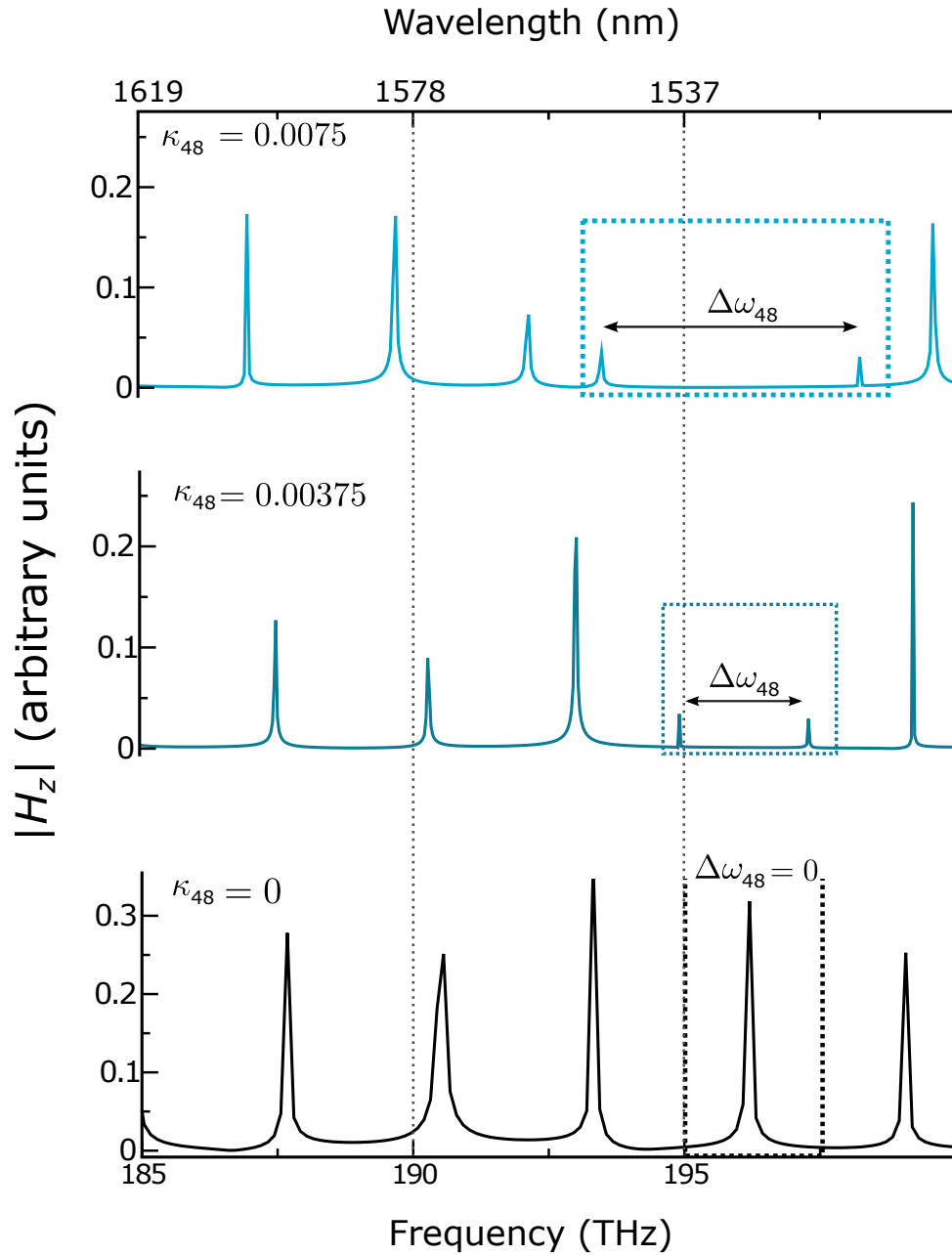


Figure 40: The computational spectra of 5 μm SOI rings with various magnitudes of κ_{48} obtained using 2D finite-difference time-domain simulations. A standard ring resonator (lower spectrum, $\kappa_{48} = 0$) exhibits no splitting in the $m = 48$ resonance. As κ_{48} increases, splitting of the 48th resonance is observed. If κ_{48} is large enough, the split modes will begin to interact with the resonances found directly adjacent. (top spectrum)

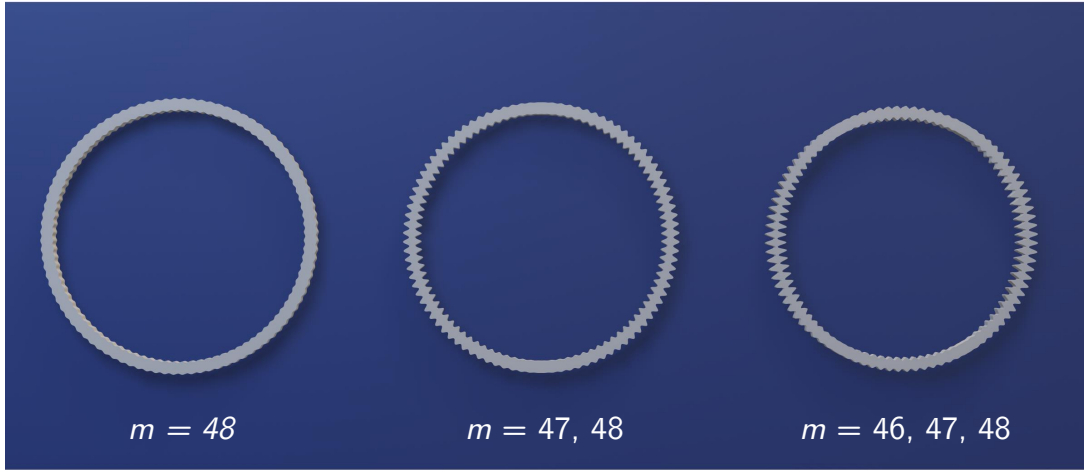


Figure 41: The dielectric profile of three ring resonators of radius $R = 5 \mu\text{m}$ with perturbations of order $m = 46$, $m = 46$ and 47 , and $m = 46, 47$, and 48 .

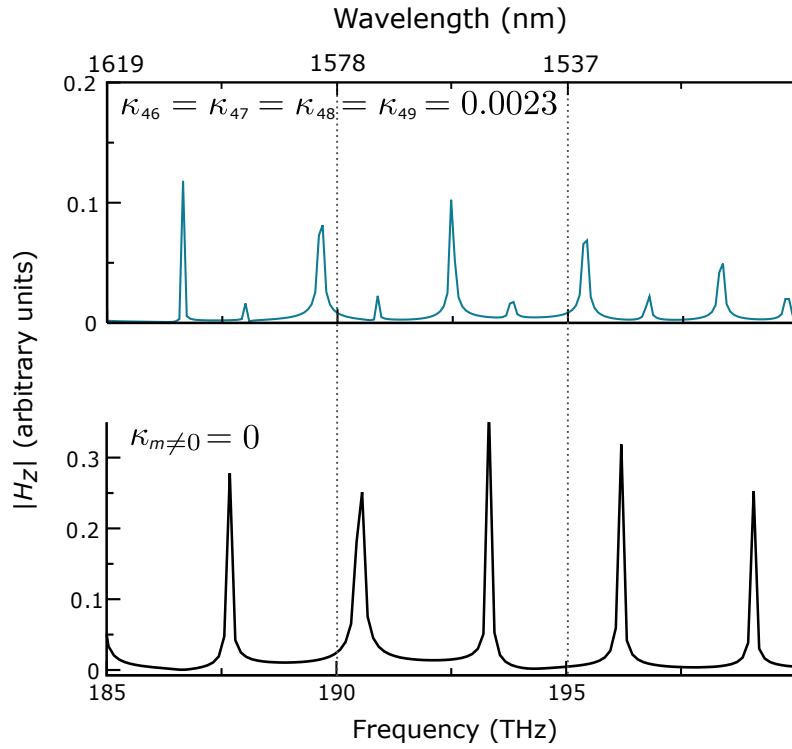


Figure 42: The computational spectra of $5\text{-}\mu\text{m}$ SOI ring with multiple perturbations obtained using 2D finite-difference time-domain simulations. A standard ring resonator (lower spectrum, $\kappa_{48} = 0$) exhibits no splitting in the $m = 48$ resonance. By adding four modulations to the ring's dielectric function ($\kappa_{46} = \kappa_{47} = \kappa_{48} = \kappa_{49} = 0.0023$), the free spectral range of the device is halved.

lithography (AEPONYX) and evanescently coupled to a waveguide and grating coupler for characterization (Appendix F). The rings were characterized via a tunable-C-band laser. Figure 43 shows a transmission spectrum of a 20.282- μm -radius-ring that has been modulated with periodic perturbations of order $m = 122, 123,$ and 124 and waveguide width modulations of 100, 90, and 90 nm, respectively. The experimental normalized transmission spectrum is seen in black, with the analytically-derived transmission spectrum of a standard 20- μm -radius ring resonator denoted as a dotted green line. The resonances with $\lambda < 1550$ nm are unaffected by the waveguide width modulations and correspond well with the theoretical prediction for a standard ring resonator. They are equidistantly spaced, with an average free spectral range of 9 nm.

The four resonances found above 1550 nm demonstrate resonance splitting. The waveguide width modulations were designed so as to split the $m = 122, 123,$ and 124 resonances a value of $\Delta\lambda \sim 4.5$ nm. The resonances in question experimentally demonstrated splittings of $\Delta\lambda_{122} = 8.0$ nm, $\Delta\lambda_{123} = 6.0$ nm, and $\Delta\lambda_{124} = 4.5$ nm. Additionally, the $n = 125$ resonance exhibits slight splitting. While the ring in question was not designed to split the $n = 125$ resonance, it is possible that the waveguide width modulations of the ring are large enough that they can no longer be considered as a small perturbation to the ring's dielectric profile. Reducing the amplitude of the modulations in future fabrications may diminish this effect.

6.4 Conclusion

The above chapter proposes selective modal coupling of frequency-degenerate, counter-propagating modes via periodic waveguide width modulations. The magnitude of splitting between the coupled modes has been theoretically shown to scale proportionally with the mode's corresponding coefficient in the Fourier expansion of the ring's dielectric function. Frequency-domain and finite-difference-time-domain computations both show correspondence with the linear prediction of the theoretical model.

The proposed dispersion engineering method has been applied to rings fabricated on the silicon nitride platform via electron-beam lithography. The transmission spectrum of a 20- μm -radius ring exhibits multiple modal splittings induced by waveguide modulations that correspond well to the theoretical predictions. These modal splittings effectively reduce the free spectral range of the ring in a targeted wavelength range.

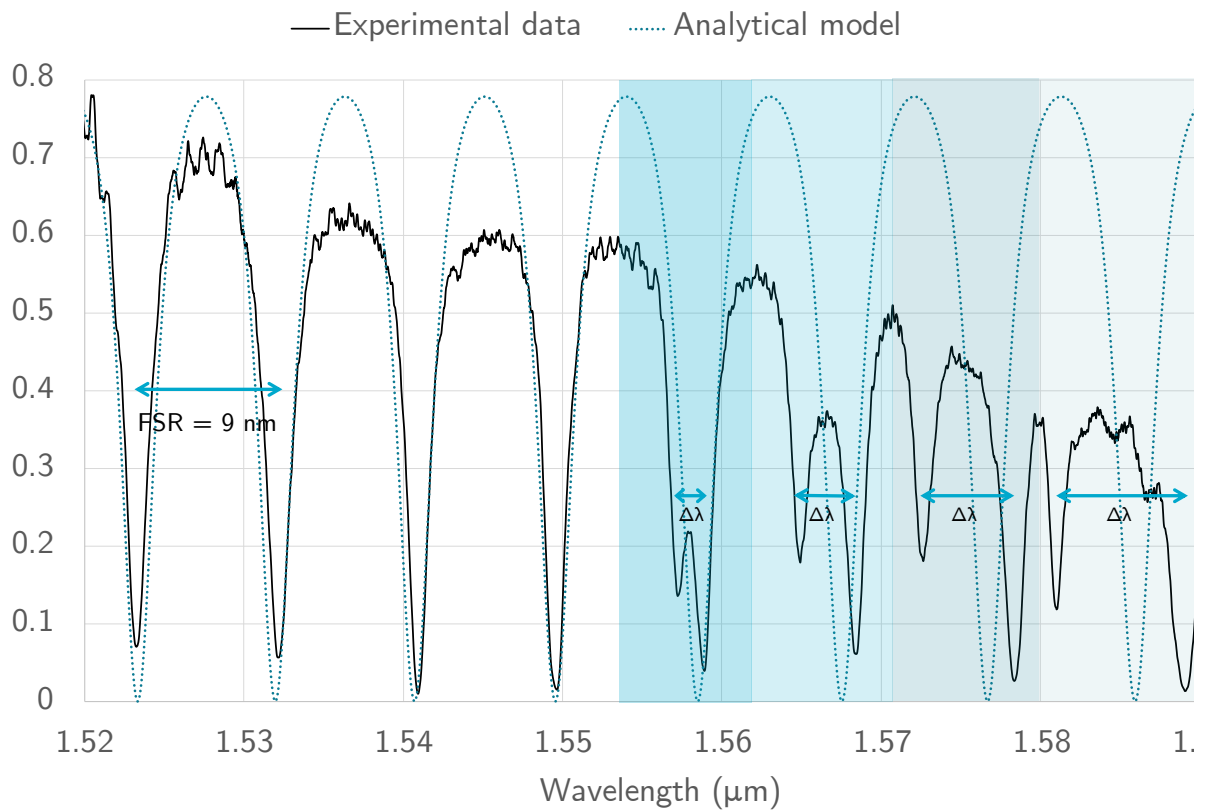


Figure 43: The transmission spectrum of a 20.282- μm -radius silicon-nitride ring resonator modulated with periodic perturbations of order $m = 122$, 123, and 124 and waveguide width modulations of 100, 90, and 90 nm, respectively.

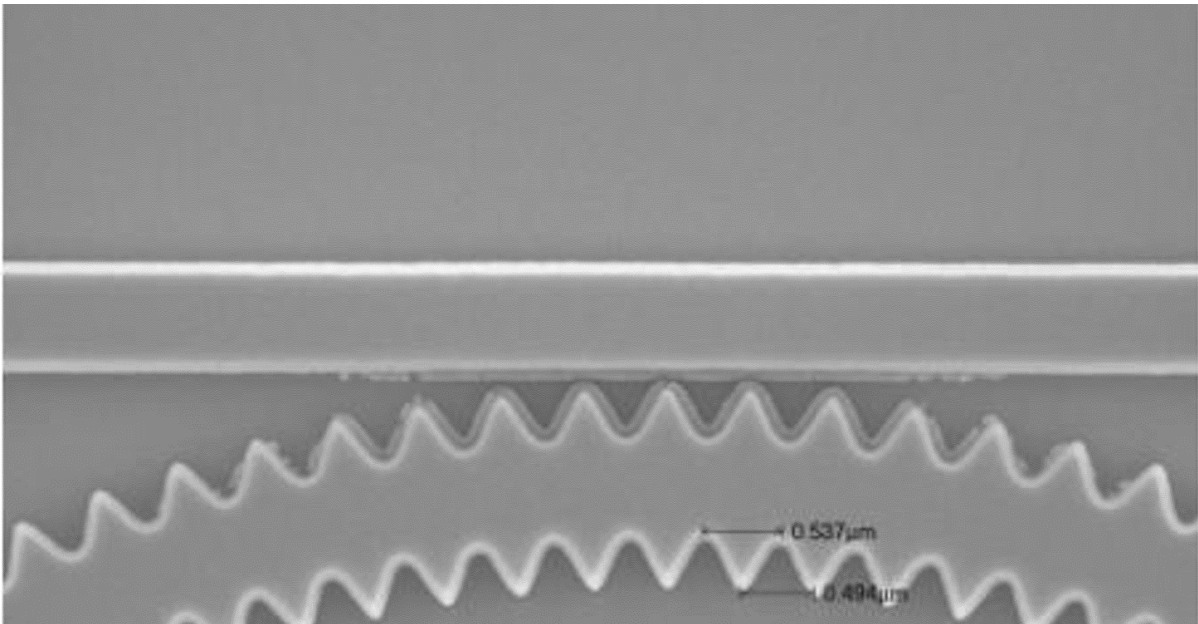


Figure 44: Scanning electron microscope image of a $20\ \mu\text{m}$ -radius ring resonator with a $m = 123$ modulation added.

Chapter 7

Ring resonators as synthetic dimension platforms

In Chapter 5, non-trivial geometric phases were engineered into photonic crystals via dimerization of the PhC lattice. This method was introduced as an alternative to using photonic crystals with broken time reversal symmetry due to the lack of materials possessing magneto-optic properties at optical frequencies. An additional technique to overcome this roadblock involves engineering photonic gauge potentials that can generate an effective magnetic field for photons [117].

A fine degree of control can be obtained over engineered gauge fields through use of a synthetic dimension. Synthetic dimensions utilize internal degrees of freedom (e.g. particle spin [118], orbital angular momentum [119], or frequency [120]) to simulate a spatial dimension. This technique allows for exploration of high-dimensional physics and facilitates generation of complex couplings that may be difficult to achieve in real-space lattices. The following chapter will apply the concepts of synthetic dimensions to a single ring resonator and demonstrate how the dimensionality of the system can be increased by projecting a synthetic axis along the ring's propagation axis.

7.1 Synthetic dimensions in photonics

Synthetic gauge fields were first introduced in cold-atom lattices [118, 121] and have recently been extended to photonics systems [119, 120]. In particular, arrays of ring resonators have proven interesting platforms for exploration of synthetic dimensions [122–124]. A single ring resonator represents a 0D system, with light propagation confined to the high refractive index of the core (Figure 45a). The dimensionality of the system is

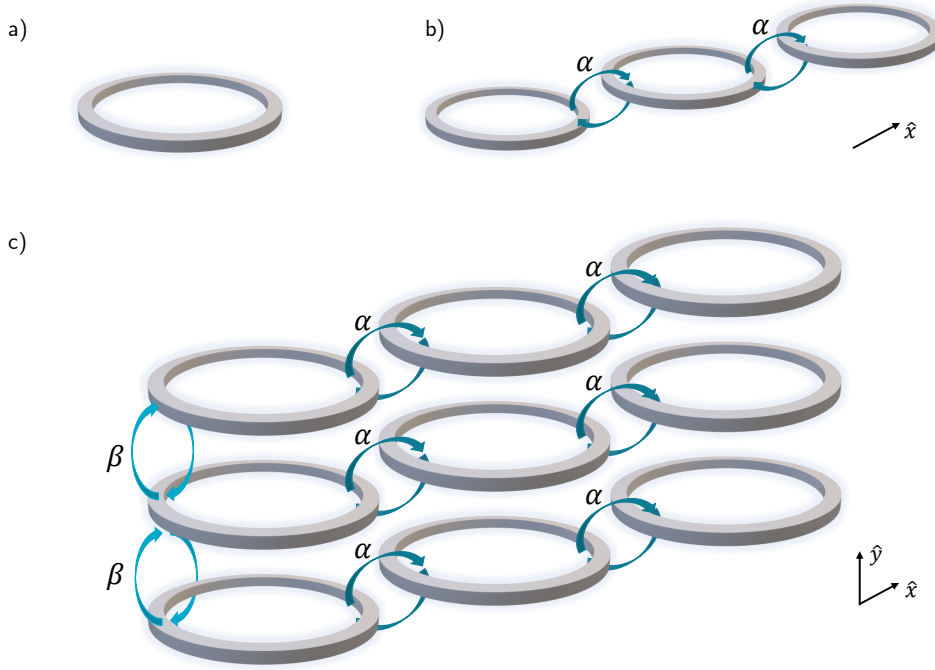


Figure 45: (a) A 0D optical array, consisting of a single ring resonator. (b) A 1D array of ring resonators. The strength of the evanescent coupling between adjacent rings is denoted by the hopping parameter α . (c) A 2D array of ring resonators. Evanescent coupling occurs along both the \hat{x} and \hat{y} axes, denoted by the hopping parameters α and β , respectively.

increased by creating a linear array of ring resonators evanescently coupled to each other (Figure 45b). The tight-binding Hamiltonian for the system can be written as [120]:

$$H = \sum_l \omega_m a_l^\dagger a_l + \alpha (a_l^\dagger a_{l+1} + a_{l+1}^\dagger a_l) \quad (136)$$

where a_l (a_l^\dagger) is the annihilation (creation) operator for the m^{th} resonance of the l^{th} ring, α is the hopping parameter between adjacent rings, and ω_m is the frequency of the ring's m^{th} -resonance. Similar Hamiltonians can be written in 2- or 3-dimensions (Figure 45c), however the order of the array is ultimately restricted by the dimensions of physical space.

This limitation can be overcome by utilizing an alternative degree of freedom upon which to project a synthetic axis. For instance, the frequency axis of a single ring resonator can be used as a synthetic dimension by inducing coupling between adjacent resonances of the ring [120]. The coupling enables a photon to ‘hop’ from one resonance to the next along the frequency axis (Figure 46). The ring is assumed to have equidistantly spaced

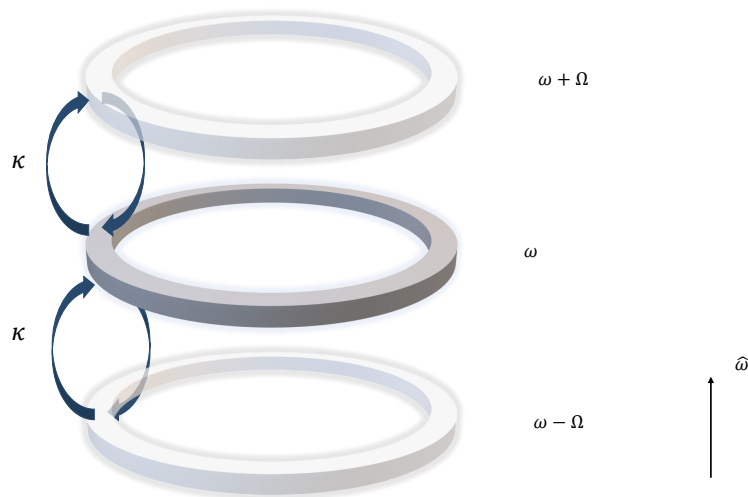


Figure 46: A 1D synthetic array consisting of a single ring resonator. Nearest-neighbor hopping between adjacent resonances of the ring ($\omega \rightarrow \omega \pm \Omega$) is induced with a hopping amplitude of κ . The resultant coupling along the frequency axis of the system increases the dimensions of the 0D physical array to a 1D synthetic array.

resonances, such that the frequency of a given mode can be written as:

$$\omega_m = \omega_0 + m\Omega \quad (137)$$

where Ω is the free spectral range of the ring. When the ring is modulated at the frequency Ω , coupling between adjacent resonances of the ring is induced. The resultant Hamiltonian of the system is [120]:

$$H = \sum_m \omega_m a_m^\dagger a_m + 2\kappa \cos(\Omega t + \phi)(a_{m+1}^\dagger a_m + a_m^\dagger a_{m+1}) \quad (138)$$

where a_m (a^\dagger) is the annihilation (creation) operator for the m^{th} -resonance of the ring, κ is the hopping amplitude between adjacent resonances, and ϕ is the phase of the modulation. Similar in form to Equation 136, the Hamiltonian demonstrates nearest neighbor coupling along the synthetic frequency axis. The hopping parameters of the system can be controlled through variation of the modulation's amplitude. Additionally, the phase factor of the modulation can be utilized to implement a photonic gauge in the system [120]. Experimentally, 1- and 2-dimensional synthetic frequency spaces have been engineered in 0D ring resonators [124, 125].

Synthetic dimensions in photonics have similarly been achieved by utilizing a waveguide's modal degree of freedom. Arrays of waveguides possessing spatial modulations can

effectively couple light along a modal synthetic axis. This effect can be attributed to the close correspondence between Schrödinger’s equation and Maxwell’s equations under the paraxial waveguide approximation. Provided the refractive index contrast between the waveguide’s core and cladding is low, Maxwell’s equations can be written as:

$$i\partial_x\psi(x, y, z) = -\frac{1}{2k_0}\nabla^2\psi(x, y, z) - \frac{k_0\Delta n(x, y, z)}{n_0}\psi(x, y, z) \quad (139)$$

where $\psi(x, y, z)$ is the envelope function of the electric field ($\mathbf{E}(x, y, z) = \psi(x, y, z)e^{ik_0x - i\omega t}\hat{z}$) and k_0 is the wavenumber of the light in a material of refractive index n_0 . The \hat{x} -axis is defined as the direction of light propagation and the Laplacian operator ∇^2 is restricted to the transverse $y - z$ plane. This equation is alike in form to the time-dependent Schrödinger’s equation, where the propagation axis of the waveguide serves as the time axis and the change in refractive index $\Delta n(x, y, z)$ acts as an effective potential for the electromagnetic fields. Modal synthetic dimensions in waveguides have led to the experimental realization of photonic Floquet topological insulators and topologically-protected edge states in modal space [126, 127].

7.2 Synthetic dimensions in spatially modulated ring resonators

The optical Schrödinger’s equation can be applied to a weakly guiding optical ring resonator through application of the concepts described in Chapter 6. The ring’s geometry allows the dielectric profile to be represented as an infinitely-long waveguide. Perturbations to the ring’s dielectric material imposes a periodicity on the system, with a lattice constant of $l = P = 2\pi R$. The ring can thus be considered as a synthetic, one-dimensional chain of ring resonators. The optical Schrödinger’s equation implies that a photon with propagation constant β can be coupled to its nearest neighbor, provided the ring is given a spatial modulation whose period matches the periodicity of the ring (i.e. $T = 2\pi R$). Figure 47 shows the dielectric profile of the proposed ring’s geometry. A single modulation of the ring’s width creates a synthetic axis where a photon’s propagation constant can be coupled to the propagation constant of its nearest neighbor.

Using a one-dimensional tight binding model, the Hamiltonian of the system can be written as:

$$H = \sum_n \beta_m a_n^\dagger a_n - \kappa(a_{n+1}^\dagger a_n + a_n^\dagger a_{n+1}) \quad (140)$$

where a_n (a_n^\dagger) is the annihilation (creation) operator for the ring’s m^{th} -mode with propagation constant β_m on the n^{th} circuit of the ring’s perimeter, κ is the hopping amplitude

Synthetic axis		
	Frequency space	Modal space
Eigenvalue	ω	β
Modulation period	$T = \Omega$	$T = 2\pi R$
Synthetic wavenumber	k_t (s)	k_θ (m ⁻¹)
First Brillouin zone	$k_t \in \left[-\frac{\pi}{2\Omega}, +\frac{\pi}{2\Omega}\right]$	$k_\theta \in \left[-\frac{\pi}{2P}, +\frac{\pi}{2P}\right]$

Table 6: Comparison of synthetic dimensions in frequency and modal space.

between adjacent rings along the synthetic axis, and the summation over n is dependent on the losses of the optical ring resonator. To transform the Hamiltonian into momentum-space, the summation is rewritten over nearest neighbors. Considering only the second term, the Hamiltonian becomes:

$$H_{tb} = -\kappa \sum_n \sum_q (a_n^\dagger a_{n+q} + a_{n+q}^\dagger a_n) \quad (141)$$

where q is summed over the nearest neighbor vectors of the system (i.e. $q = \pm P$) and a_{n+q} (a_{n+q}^\dagger) is the annihilation (creation) operator for the ring's m^{th} -mode with propagation constant β_m and position $x_n + q$. The creation and annihilation operators are now rewritten in momentum space [128]:

$$a_n^\dagger = \frac{1}{\sqrt{N}} \sum_k e^{-ikx_n} a_k^\dagger \quad (142)$$

$$a_n = \frac{1}{\sqrt{N}} \sum_k e^{+ikx_n} a_k \quad (143)$$

where $k = k_x$. The momentum space operators transform the tight-binding Hamiltonian to:

$$H_{tb} = -\frac{\kappa}{N} \sum_{n,q} \sum_{k,k'} e^{-ikx_n} e^{+ik'(x_n+q)} a_k^\dagger a_{k'} + e^{-ik'(x_n+q)} e^{+ikx_n} a_k^\dagger a_{k'} \quad (144)$$

$$= -\kappa \sum_{q,k} \left(e^{+ikq} + e^{-ikq} \right) a_k^\dagger a_k \quad (145)$$

$$= -2\kappa \sum_{q,k} \cos(kq) a_k^\dagger a_k \quad (146)$$

which yields a synthetic space dispersion relation of:

$$\beta(k) = -2\kappa \sum_q \cos(kq) \quad (147)$$

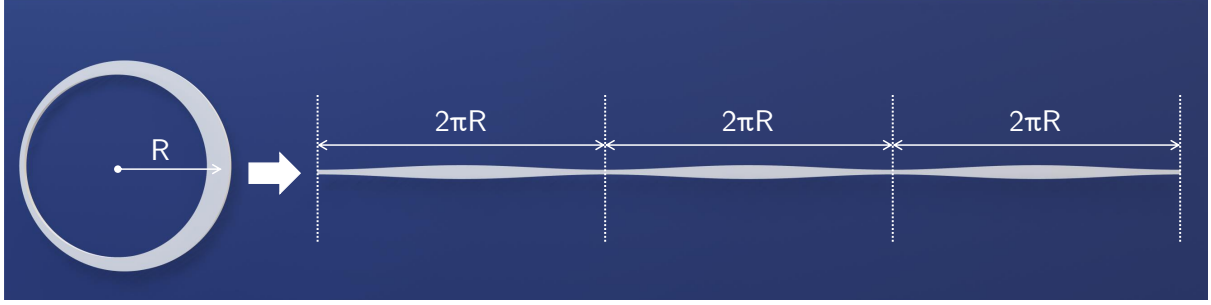


Figure 47: A ring resonator of radius R with a width modulation of spatial period $2\pi R$. Provided the ring's dimensions satisfy $R \gg n_{\text{eff}}\lambda$, the ring can be represented as a periodic, infinitely-long dielectric waveguide.

The two reciprocal lattice vectors of the system are:

$$q_1 = 2\pi R \quad \text{and} \quad q_2 = -2\pi R \quad (148)$$

Inserting Equation 148 into Equation 147 gives a final dispersion relation of:

$$\beta(k) = -4\kappa \cos(kP) \quad (149)$$

This result implies that a 0D ring resonator can possess a 1D dispersion relation in synthetic momentum space. The dispersion relation can be measured by probing the propagation constant of the ring across the first Brillouin zone of the system.

7.3 Computational results

To confirm the theoretical prediction of Equation 149, 2D FDTD simulations [85] are used to measure the time evolution of a spatially modulated ring (Appendix B.2). A ring resonator of radius $50 \mu\text{m}$ is simulated in two dimensions. With consideration of the weakly-guiding waveguide approximation used in the optical Schrödinger's equation, a silica waveguide of cross section of $1 \mu\text{m} \times 1 \mu\text{m}$ and an air cladding is chosen, corresponding to an effective index of $n_{\text{eff}} = 1.208$. The ring is given a width modulation with period $T = 2\pi R$, corresponding to nearest neighbor coupling along the synthetic axis.

To probe the local propagation constant of the ring at a particular point, the ring is placed next to a $1 \mu\text{m}$ wide silica waveguide of effective index $n_{\text{eff}} = 1.208$ in a point coupler configuration (Figure 7). The evanescent coupling gap between the input waveguide and the ring is set to $g = 0 \text{ nm}$. A broadband Gaussian dipole source centered at 1550 nm of width $\delta\lambda = 100 \text{ nm}$ is placed at the input port of the coupling waveguide and the

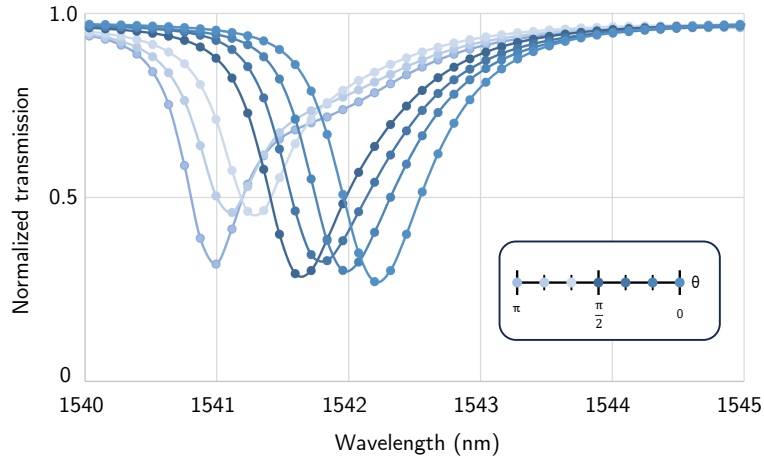


Figure 48: 2D finite-difference time-domain computational transmission spectra of a 50- μm -radius, spatially-modulated silica ring rotated from $\theta = 0$ to π w.r.t. the thinnest portion of the ring. The ring's modulation has an amplitude of 250 nm and a spatial period of $T = 2\pi R$. As the ring is rotated, the effective index of the ring evanescently coupled to the input waveguide increases. As a result, the resonance of the ring is blueshifted.

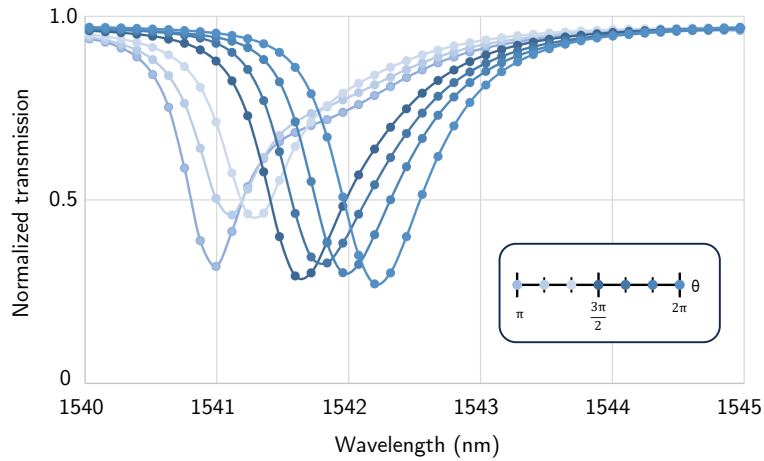


Figure 49: 2D finite-difference time-domain computational transmission spectra of a 50- μm -radius, spatially-modulated silica ring rotated from $\theta = \pi$ to 2π radians with respect to the thinnest portion of the ring. The ring's modulation has an amplitude of 250 nm and a spatial period of $T = 2\pi R$. The effective index of the ring evanescently coupled to the input waveguide now decreases, resulting in a redshift of the ring's resonance.

transmission spectrum of the ring is monitored at the output port. A single, TE-polarized mode of the ring is characterized.

Figure 48 shows the computational transmission spectrum of a silica ring with a width modulation of 250 nm. The thinnest portion of the ring ($w = 150$ nm) is aligned next to the coupling waveguide and the transmission spectrum of the ring is measured. The ring is then rotated π radians by steps of $\theta = \frac{\pi}{6}$ about its center axis and the simulation is repeated. As the ring rotates, the local effective index of the ring at the point of coupling increases. As a result, the resonant wavelength coupled into the ring is blueshifted. The simulation is then repeated for the angles $\theta = \pi$ to 2π . The spatial modulation of the ring is symmetric about its center axis, thus the local effective index of the ring now decreases, resulting in a redshifted resonance (Figure 49).

The resonant wavelength computed in the FDTD simulations can be related to the propagation constant of the mode using Equation 37:

$$\beta = n_{\text{eff}}k_0 = \frac{2\pi n_{\text{eff}}}{\lambda} \quad (150)$$

Applying Equation 150 to the simulated resonant wavelengths, the dispersion relation of the one-dimensional synthetic space can be computed. Figure 50 shows the results of simulations for three different width modulation amplitudes, $\Delta w = 0.25, 0.50,$ and 1.0 μm . The dispersion relation for the ring's propagation constant corresponds well with the prediction of Equation 149. The result also indicates that the strength of the hopping parameter between nearest neighbors along the synthetic axis can be tuned by changing the amplitude of the ring's width modulation.

7.4 Proposed experimental method

To experimentally determine the synthetic dispersion relation, a spatially modulated optical ring resonator can be fabricated on an undercut silica chip, resulting in a silica ring with an air cladding. The proposed ring is supported by a silica pedestal and spokes designed to minimize opto-mechanical effects within the ring. The ring is coupled to a tapered optical fiber and characterized using a tunable laser. The tapered fiber can be fabricated from a standard SMF-28 optical fiber which has been tapered using a flame-brushing technique [129]. The pulled fiber possess a large evanescent field at its thinnest portion and is thus highly suitable to coupling to an undercut silica ring [130]. Once a transmission spectrum is obtained, the ring is rotated utilizing a high-precision rotational stage, the tapered fiber is recoupled to the ring, and a new transmission spectrum is obtained. GDS files for the proposed devices can be found in Appendix G.

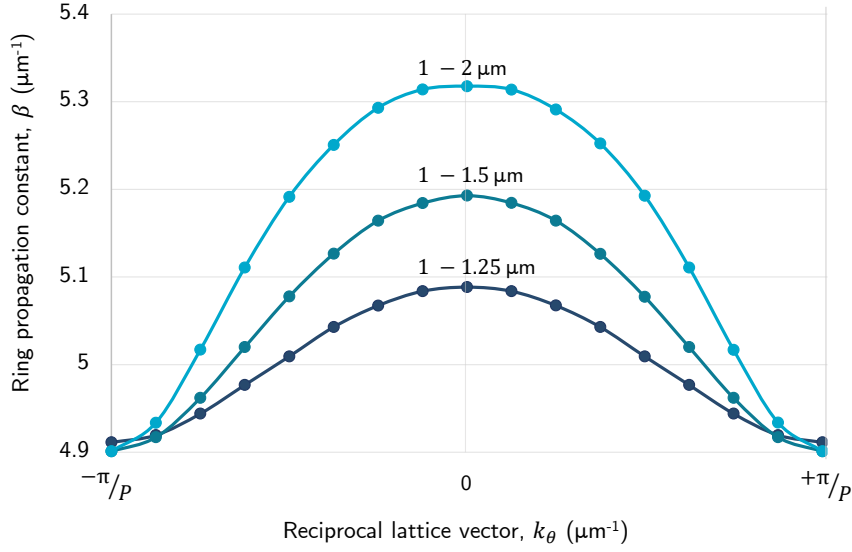


Figure 50: The dispersion relation of the 1D synthetic ring array. The propagation constant β is calculated using the resonant wavelengths from the FDTD computational spectra and the effective index of the ring at the coupling point. As the amplitude of the waveguide width modulation increases, the strength of nearest neighbor hopping along the synthetic axis increases.

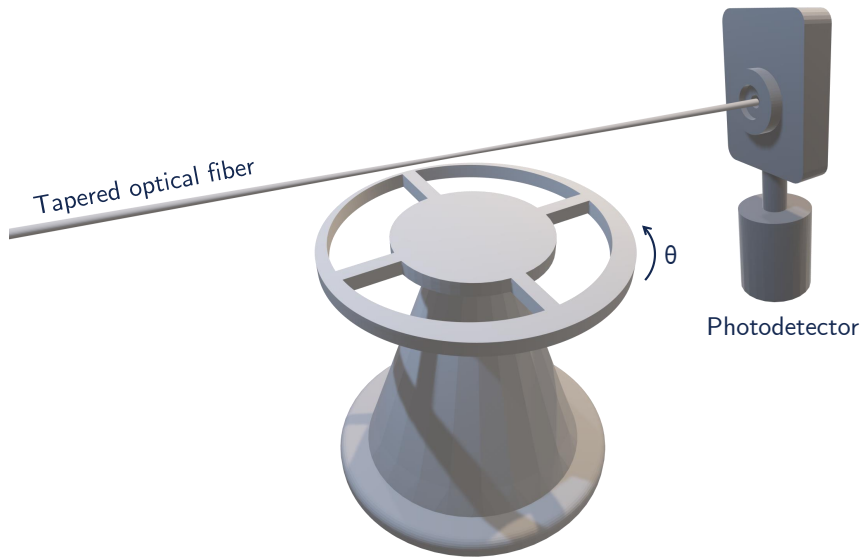


Figure 51: The proposed experimental setup for measurement of a 1D synthetic dimension in a spatially modulated optical ring resonator. The ring is rotated in the θ direction and the optical spectrum of the ring is characterized via evanescent coupling to a tapered optical fiber.

7.5 Conclusions

In summary, optical ring resonators can be engineered to possess a synthetic dimension by utilizing the periodicity of the ring's material. This allows the ring to be represented as an infinitely long chain of coupled resonators separated by a lattice constant of $l = P = 2\pi R$. The optical Schrödinger equation is applied to the ring's waveguide and the axis of propagation is cast as the 'time' axis of the system. A modulation of the refractive index creates an effective potential for the electromagnetic fields. If the spatial period of the ring's modulation matches the perimeter of the ring, the 0D ring resonator can be represented using the 1D tight binding model for a chain of coupled resonators in synthetic space.

The theoretical prediction of the tight binding model is confirmed using FDTD simulations. The transmission of a 50- μm -radius silica ring with a width modulation of period $T = 2\pi R$ in a point coupler configuration is simulated. As the ring is rotated about its center axis, the resonant wavelength of a particular mode shifts as a function of the local effective index of the ring. The dispersion relation of the propagation constant of the ring is then plotted, showing good agreement with theory. Additionally, a proposal for the experimental observation of synthetic modal dimensions in optical ring resonators is given.

Chapter 8

Conclusions and outlook

In summary, this work has utilized condensed matter theories to engineer the dispersion of an optical ring resonator. The tight fabrication resolutions of CMOS-compatible lithography techniques have been leveraged to modify the ring's dispersion through precise design of its geometry. The proposed devices have been fabricated on the silicon-on-insulator and silicon nitride platforms, making them suitable for applications in optical communications, biosensing, non-linear optics, and optical metrology.

Through application of Bloch's theorem, it has been shown that a photonic crystal ring resonator possesses a non-linear dispersion relation near its photonic band edge. This effect can be used for the generation of slow-light resonances in rings. It has additionally been demonstrated that the unique characteristics of a photonic crystal ring resonator allow for direct experimental characterization of the device's underlying dispersion relation.

Dimerization of the photonic crystal lattice provides an additional degree of freedom for dispersion engineering. Tuning of the intra- and intercell spacing of the two PhC holes in the dimer unit cell provides control over the size of the resultant photonic band gap. This degree of freedom also enables the engineering of non-trivial topological geometric phases in dimer PhC lattices. It has been demonstrated computationally that PhC cavities can be formed in an optical ring resonator by interfacing two bulk dimer PhC lattices that possess different topological invariants. The resultant edge state is found precisely mid-photonic gap and is localized on a single sublattice of the photonic crystal, consistent with the predictions of the SSH model. Additionally, the degenerate edge states can be coupled by tuning the distance between the PhC cavities in the ring.

The intrinsic periodicity of the ring imposes an additional geometric constraint on the system which can be utilized for dispersion engineering. A theoretical model has

been proposed which relates the magnitude of coupling between a frequency-degenerate pair of resonances to the mode's corresponding coefficient in the Fourier expansion of the ring's dielectric function. This model can be utilized to engineer disorder into the system to selectively control modal coupling between an arbitrary pair of frequency-degenerate, counterpropagating resonances. This effect has been demonstrated both computationally and experimentally, opening the door for engineered ring resonances immune to disorder-induced resonance splitting.

The periodicity of the ring can also be utilized to project a synthetic axis in modal space. A weakly guiding optical ring resonator can be considered as a chain of coupled ring resonators in synthetic space, where the number of resonators in the chain is limited by the quality factor of the ring. The optical Schrödinger's equation implies that nearest-neighbor modal coupling of each ring's propagation constant, β , can be induced provided the ring is given a spatial modulation that matches the lattice constant of the system (i.e. $P = 2\pi R$). The synthetic modal dispersion relation of a 1D tight-bonding model for a chain of optical resonators has been demonstrated computationally and a proposal for the on-chip characterization of the dispersion relation has been offered.

The outlook for future research can be decomposed into several different areas. The concepts of Chapter 4 can easily be extended to design slow light ring resonators in the mid-IR. In particular, silicon nitride photonic crystal ring resonators could prove to be promising chemical or biosensors. Topologically-protected edge states in photonic crystal ring resonators may prove interesting candidates for exploration of non-linear optics or cavity quantum electrodynamics. The robustness of the cavity can be utilized to overcome current challenges related to fabricating high-Q photonic crystal cavities. The Hamiltonians of the trimer and tetramer lattices additionally possess unexplored parameters spaces that may possess non-trivial topological features.

Spatially modulated optical ring resonators have been realized on the silicon nitride platform due to its low refractive index contrast. To transfer this technology to the SOI platform, subwavelength grating ring resonators may be utilized. The effective index of the ring can be reduced using the SOI subwavelength gratings, which can potentially enable modulation dimensions that fall within the fabrication resolutions of current lithography techniques.

Finally, the concepts of synthetic dimensions in a spatially modulated optical ring resonator can be confirmed utilizing the experimental proposal given in Chapter 7. The dimensionality of the synthetic space can be increased by creating an array of evanescently coupled, spatially modulated ring resonators. This system could potentially be used to

engineer synthetic gauge fields by inducing a phase shift (i.e. relative rotation) between adjacent rings. Higher order modulations (e.g. $T = \frac{2\pi R}{2}$) can also be implemented in an optical ring resonator to consider more complex couplings in a 1D chain.

Bibliography

- [1] W. Bogaerts, R. Baets, P. Dumon, V. Wiaux, S. Beckx, D. Taillaert, B. Luyssaert, J. V. Campenhout, P. Bienstman, and D. V. Thourhout, “Nanophotonic Waveguides in Silicon-on-Insulator Fabricated With CMOS Technology,” *Journal of Lightwave Technology*, vol. 23, p. 401, Jan. 2005.
- [2] T. Shoji, T. Tsuchizawa, T. Watanabe, K. Yamada, and H. Morita, “Low loss mode size converter from 0.3 [micro sign]m square Si wire waveguides to singlemode fibres,” *Electronics Letters*, vol. 38, no. 25, p. 1669, 2002.
- [3] D. Taillaert, P. Bienstman, and R. Baets, “Compact efficient broadband grating coupler for silicon-on-insulator waveguides,” *Optics Letters*, vol. 29, p. 2749, Dec. 2004.
- [4] L. Liu, Y. Ding, K. Yvind, and J. M. Hvam, “Efficient and compact TE–TM polarization converter built on silicon-on-insulator platform with a simple fabrication process,” *Optics Letters*, vol. 36, p. 1059, Apr. 2011.
- [5] H. Yamada, Tao Chu, S. Ishida, and Y. Arakawa, “Optical directional coupler based on Si-wire waveguides,” *IEEE Photonics Technology Letters*, vol. 17, pp. 585–587, Mar. 2005.
- [6] M. Soltani, S. Yegnanarayanan, and A. Adibi, “Ultra-high Q planar silicon microdisk resonators for chip-scale silicon photonics,” *Optics Express*, vol. 15, no. 8, p. 4694, 2007.
- [7] D. K. Armani, T. J. Kippenberg, S. M. Spillane, and K. J. Vahala, “Ultra-high-Q toroid microcavity on a chip,” *Nature*, vol. 421, pp. 925–928, Feb. 2003.
- [8] G. S. Solomon, M. Pelton, and Y. Yamamoto, “Single-mode Spontaneous Emission from a Single Quantum Dot in a Three-Dimensional Microcavity,” *Physical Review Letters*, vol. 86, pp. 3903–3906, Apr. 2001.

- [9] D. G. Rabus, *Integrated Ring Resonators: The Compendium*. 2007. OCLC: 1120485927.
- [10] C. Vieu, F. Carcenac, A. Pépin, Y. Chen, M. Mejias, A. Lebib, L. Manin-Ferlazzo, L. Couraud, and H. Launois, “Electron beam lithography: resolution limits and applications,” *Applied Surface Science*, vol. 164, pp. 111–117, Sept. 2000.
- [11] M. Totzeck, W. Ulrich, A. Göhnermeier, and W. Kaiser, “Pushing deep ultraviolet lithography to its limits,” *Nature Photonics*, vol. 1, pp. 629–631, Nov. 2007.
- [12] W. Bogaerts, D. Taillaert, B. Luyssaert, P. Dumon, J. V. Campenhout, P. Bienstman, D. V. Thourhout, R. Baets, V. Wiaux, and S. Beckx, “Basic structures for photonic integrated circuits in Silicon-on-insulator,” *Optics Express*, vol. 12, pp. 1583–1591, Apr. 2004.
- [13] W. Bogaerts, P. De Heyn, T. Van Vaerenbergh, K. De Vos, S. Kumar Selvaraja, T. Claes, P. Dumon, P. Bienstman, D. Van Thourhout, and R. Baets, “Silicon microring resonators,” *Laser & Photonics Reviews*, vol. 6, pp. 47–73, Jan. 2012.
- [14] C. Reimer, M. Kues, P. Roztocki, B. Wetzels, F. Grazioso, B. E. Little, S. T. Chu, T. Johnston, Y. Bromberg, L. Caspani, D. J. Moss, and R. Morandotti, “Generation of multiphoton entangled quantum states by means of integrated frequency combs,” *Science*, vol. 351, pp. 1176–1180, Mar. 2016.
- [15] M. Hafezi, S. Mittal, J. Fan, A. Migdall, and J. M. Taylor, “Imaging topological edge states in silicon photonics,” *Nature Photonics*, vol. 7, pp. 1001–1005, Dec. 2013.
- [16] V. Brash, M. Geiselmann, T. Herr, G. Lihachev, M. H. P. Pfeiffer, M. L. Gorodetsky, and T. J. Kippenberg, “Photonic chip-based optical frequency comb using soliton Cherenkov radiation,” *Science*, vol. 351, pp. 357–360, Jan. 2016.
- [17] B. Little, S. Chu, H. Haus, J. Foresi, and J.-P. Laine, “Microring resonator channel dropping filters,” *Journal of Lightwave Technology*, vol. 15, pp. 998–1005, June 1997.
- [18] V. R. Almeida, C. A. Barrios, R. R. Panepucci, and M. Lipson, “All-optical control of light on a silicon chip,” *Nature*, vol. 431, pp. 1081–1084, Oct. 2004.

- [19] D. T. H. Tan, A. Grieco, and Y. Fainman, “Towards 100 channel dense wavelength division multiplexing with 100GHz spacing on silicon,” *Optics Express*, vol. 22, p. 10408, May 2014.
- [20] D.-X. Xu, M. Vachon, A. Densmore, R. Ma, A. Delâge, S. Janz, J. Lapointe, Y. Li, G. Lopinski, D. Zhang, Q. Y. Liu, P. Cheben, and J. H. Schmid, “Label-free biosensor array based on silicon-on-insulator ring resonators addressed using a WDM approach,” *Optics Letters*, vol. 35, p. 2771, Aug. 2010.
- [21] M. S. McClellan, L. L. Domier, and R. C. Bailey, “Label-free virus detection using silicon photonic microring resonators,” *Biosensors and Bioelectronics*, vol. 31, pp. 388–392, Jan. 2012.
- [22] C. E. Campanella, F. De Leonardis, L. Mastronardi, P. Malara, G. Gagliardi, and V. M. N. Passaro, “Investigation of refractive index sensing based on Fano resonance in fiber Bragg grating ring resonators,” *Optics Express*, vol. 23, p. 14301, June 2015.
- [23] Y. Okawachi, K. Saha, J. S. Levy, Y. H. Wen, M. Lipson, and A. L. Gaeta, “Octave-spanning frequency comb generation in a silicon nitride chip,” *Optics Letters*, vol. 36, p. 3398, Sept. 2011.
- [24] P. Del’Haye, T. Herr, E. Gavartin, M. L. Gorodetsky, R. Holzwarth, and T. J. Kippenberg, “Octave Spanning Tunable Frequency Comb from a Microresonator,” *Physical Review Letters*, vol. 107, p. 063901, Aug. 2011.
- [25] Q. Li, T. C. Briles, D. A. Westly, T. E. Drake, J. R. Stone, B. R. Ilic, S. A. Diddams, S. B. Papp, and K. Srinivasan, “Stably accessing octave-spanning microresonator frequency combs in the soliton regime,” *Optica*, vol. 4, p. 193, Feb. 2017.
- [26] K. Saha, Y. Okawachi, J. S. Levy, R. K. W. Lau, K. Luke, M. A. Foster, M. Lipson, and A. L. Gaeta, “Broadband parametric frequency comb generation with a 1- μm pump source,” *Optics Express*, vol. 20, p. 26935, Nov. 2012.
- [27] A. C. Turner, C. Manolatou, B. S. Schmidt, M. Lipson, M. A. Foster, J. E. Sharping, and A. L. Gaeta, “Tailored anomalous group-velocity dispersion in silicon channel waveguides,” *Optics Express*, vol. 14, no. 10, p. 4357, 2006.
- [28] K. Y. Yang, K. Beha, D. C. Cole, X. Yi, P. Del’Haye, H. Lee, J. Li, D. Y. Oh, S. A. Diddams, S. B. Papp, and K. J. Vahala, “Broadband dispersion-engineered microresonator on a chip,” *Nature Photonics*, vol. 10, pp. 316–320, May 2016.

- [29] I. S. Grudinin and N. Yu, “Dispersion engineering of crystalline resonators via microstructuring,” *Optica*, vol. 2, pp. 221–224, Mar. 2015.
- [30] X. Xue, Y. Xuan, P.-H. Wang, Y. Liu, D. E. Leaird, M. Qi, and A. M. Weiner, “Normal-dispersion microcombs enabled by controllable mode interactions,” *Laser & Photonics Reviews*, vol. 9, no. 4, pp. L23–L28, 2015.
- [31] S. Kim, K. Han, C. Wang, J. A. Jaramillo-Villegas, X. Xue, C. Bao, Y. Xuan, D. E. Leaird, A. M. Weiner, and M. Qi, “Dispersion engineering and frequency comb generation in thin silicon nitride concentric microresonators,” *Nature Communications*, vol. 8, p. 372, Dec. 2017.
- [32] Y. Liu, Y. Xuan, X. Xue, P.-H. Wang, S. Chen, A. J. Metcalf, J. Wang, D. E. Leaird, M. Qi, and A. M. Weiner, “Investigation of mode coupling in normal-dispersion silicon nitride microresonators for Kerr frequency comb generation,” *Optica*, vol. 1, p. 137, Sept. 2014.
- [33] Y. Li, J. Li, Y. Huo, M. Chen, S. Yang, and H. Chen, “Spatial-mode-coupling-based dispersion engineering for integrated optical waveguide,” *Optics Express*, vol. 26, p. 2807, Feb. 2018.
- [34] J. Riemensberger, K. Hartinger, T. Herr, V. Brash, R. Holzwarth, and T. J. Kippenberg, “Dispersion engineering of thick high-Q silicon nitride ring-resonators via atomic layer deposition,” *Optics Express*, vol. 20, p. 27661, Dec. 2012.
- [35] H. Liang, Y. He, R. Luo, and Q. Lin, “Ultra-broadband dispersion engineering of nanophotonic waveguides,” *Optics Express*, vol. 24, p. 29444, Dec. 2016.
- [36] M. Koshiba, *Optical waveguide analysis*. Advanced science and technology series, New York: McGraw-Hill, 1992.
- [37] *MODE*. Vancouver, Canada: Lumerical Inc., 2020. www.lumerical.com/products.
- [38] *COMSOL Multiphysics v5.4*. Stockholm, Sweden: COMSOL AB, 2020. www.comsol.com.
- [39] S. Feng, T. Lei, H. Chen, H. Cai, X. Luo, and A. W. Poon, “Silicon photonics: from a microresonator perspective,” *Laser & Photonics Reviews*, vol. 6, no. 2, pp. 145–177, 2012.

- [40] H. Lin, Z. Luo, T. Gu, L. C. Kimerling, K. Wada, A. Agarwal, and J. Hu, “Mid-infrared integrated photonics on silicon: a perspective,” *Nanophotonics*, vol. 7, Dec. 2017.
- [41] F. Xia, L. Sekaric, and Y. Vlasov, “Ultracompact optical buffers on a silicon chip,” *Nature Photonics*, vol. 1, pp. 65–71, Jan. 2007.
- [42] L.-W. Luo, N. Ophir, C. P. Chen, L. H. Gabrielli, C. B. Poitras, K. Bergmen, and M. Lipson, “WDM-compatible mode-division multiplexing on a silicon chip,” *Nature Communications*, vol. 5, p. 3069, May 2014.
- [43] H. Fukuda, K. Yamada, T. Shoji, M. Takahashi, T. Tsuchizawa, T. Watanabe, J.-i. Takahashi, and S.-i. Itabashi, “Four-wave mixing in silicon wire waveguides,” *Optics Express*, vol. 13, pp. 4629–4637, June 2005.
- [44] A. G. Griffith, R. K. Lau, J. Cardenas, Y. Okawachi, A. Mohanty, R. Fain, Y. H. D. Lee, M. Yu, C. T. Phare, C. B. Poitras, A. L. Gaeta, and M. Lipson, “Silicon-chip mid-infrared frequency comb generation,” *Nature Communications*, vol. 6, p. 6299, May 2015.
- [45] M. Yu, Y. Okawachi, A. G. Griffith, N. Picqué, M. Lipson, and A. L. Gaeta, “Silicon-chip-based mid-infrared dual-comb spectroscopy,” *Nature Communications*, vol. 9, p. 1869, Dec. 2018.
- [46] J. Gonzalo Wangüemert-Pérez, P. Cheben, A. Ortega-Moñux, C. Alonso-Ramos, D. Pérez-Galacho, R. Halir, I. Molina-Fernández, D.-X. Xu, and J. H. Schmid, “Evanescent field waveguide sensing with subwavelength grating structures in silicon-on-insulator,” *Optics Letters*, vol. 39, p. 4442, Aug. 2014.
- [47] J. Flueckiger, S. Schmidt, V. Donzella, A. Sherwali, D. M. Ratner, L. Chrostowski, and K. C. Cheung, “Sub-wavelength grating for enhanced ring resonator biosensor,” *Optics Express*, vol. 24, p. 15672, July 2016.
- [48] L. Huang, H. Yan, X. Xu, S. Chakravarty, N. Tang, H. Tian, and R. T. Chen, “Improving the detection limit for on-chip photonic sensors based on subwavelength grating racetrack resonators,” *Optics Express*, vol. 25, p. 10527, May 2017.
- [49] J. Cardenas, C. B. Poitras, J. T. Robinson, K. Preston, L. Chen, and M. Lipson, “Low loss etchless silicon photonic waveguides,” *Optics Express*, vol. 17, p. 4752, Mar. 2009.

- [50] K. Debnath, H. Arimoto, M. K. Husain, A. Prasmusinto, A. Al-Attili, R. Petra, H. M. H. Chong, G. T. Reed, and S. Saito, “Low-Loss Silicon Waveguides and Grating Couplers Fabricated Using Anisotropic Wet Etching Technique,” *Frontiers in Materials*, vol. 3, Feb. 2016.
- [51] M. Galli, D. Gerace, A. Politi, M. Liscidini, M. Patrini, L. C. Andreani, A. Canino, M. Miritello, R. L. Savio, A. Irrera, and F. Priolo, “Direct evidence of light confinement and emission enhancement in active silicon-on-insulator slot waveguides,” *Applied Physics Letters*, vol. 89, p. 241114, Dec. 2006.
- [52] C. Koos, P. Vorreau, T. Vallaitis, P. Dumon, W. Bogaerts, R. Baets, B. Esembeson, I. Biaggio, T. Michinobu, F. Diederich, W. Freude, and J. Leuthold, “All-optical high-speed signal processing with silicon–organic hybrid slot waveguides,” *Nature Photonics*, vol. 3, pp. 216–219, Apr. 2009.
- [53] W. Bogaerts, S. K. Selvaraja, P. Dumon, J. Brouckaert, K. De Vos, D. Van Thourhout, and R. Baets, “Silicon-on-Insulator Spectral Filters Fabricated With CMOS Technology,” *IEEE Journal of Selected Topics in Quantum Electronics*, vol. 16, no. 1, pp. 33–44, 2010.
- [54] E. Dulkeith, Y. A. Vlasov, X. Chen, N. C. Panoiu, and R. M. Osgood, “Self-phase-modulation in submicron silicon-on-insulator photonic wires,” *Optics Express*, vol. 14, pp. 5524–5534, June 2006.
- [55] M. Cazzanelli, F. Bianco, E. Borga, G. Pucker, M. Ghulinyan, E. Degoli, E. Luppi, V. Véniard, S. Ossicini, D. Modotto, S. Wabnitz, R. Pierobon, and L. Pavesi, “Second-harmonic generation in silicon waveguides strained by silicon nitride,” *Nature Materials*, vol. 11, pp. 148–154, Feb. 2012.
- [56] A. Rahim, E. Ryckeboer, A. Z. Subramanian, S. Clemmen, B. Kuyken, A. Dhakal, A. Raza, A. Hermans, M. Muneeb, S. Dhoore, Y. Li, U. Dave, P. Bienstman, N. Le Thomas, G. Roelkens, D. Van Thourhout, P. Helin, S. Severi, X. Rottenberg, and R. Baets, “Expanding the Silicon Photonics Portfolio With Silicon Nitride Photonic Integrated Circuits,” *Journal of Lightwave Technology*, vol. 35, pp. 639–649, Feb. 2017.
- [57] Z. Zhou, B. Yin, and J. Michel, “On-chip light sources for silicon photonics,” *Light: Science & Applications*, vol. 4, pp. e358–e358, Nov. 2015.

- [58] J. F. Bauters, M. J. R. Heck, D. D. John, J. S. Barton, C. M. Bruinink, A. Leinse, R. G. Heideman, D. J. Blumenthal, and J. E. Bowers, “Planar waveguides with less than 01 dB/m propagation loss fabricated with wafer bonding,” *Optics Express*, vol. 19, p. 24090, Nov. 2011.
- [59] K. Ikeda, R. E. Saperstein, N. Alic, and Y. Fainman, “Thermal and Kerr nonlinear properties of plasma-deposited silicon nitride/ silicon dioxide waveguides,” *Optics Express*, vol. 16, p. 12987, Aug. 2008.
- [60] H. K. Tsang and Y. Liu, “Nonlinear optical properties of silicon waveguides,” *Semiconductor Science and Technology*, vol. 23, p. 064007, June 2008.
- [61] A. Boskovic, L. Gruner-Nielsen, O. A. Levring, S. V. Chernikov, and J. R. Taylor, “Direct continuous-wave measurement of n_2 in various types of telecommunication fiber at $155\ \mu\text{m}$,” *Optics Letters*, vol. 21, p. 1966, Dec. 1996.
- [62] M. Zhang, C. Wang, R. Cheng, A. Shams-Ansari, and M. Lončar, “Monolithic ultra-high-Q lithium niobate microring resonator,” *Optica*, vol. 4, pp. 1536–1537, Dec. 2017.
- [63] R. DeSalvo, A. Said, D. Hagan, E. Van Stryland, and M. Sheik-Bahae, “Infrared to ultraviolet measurements of two-photon absorption and n_2 in wide bandgap solids,” *IEEE Journal of Quantum Electronics*, vol. 32, pp. 1324–1333, Aug. 1996.
- [64] M. Melchiorri, N. Daldosso, F. Sbrana, L. Pavesi, G. Pucker, C. Kompocholis, P. Bellutti, and A. Lui, “Propagation losses of silicon nitride waveguides in the near-infrared range,” *Applied Physics Letters*, vol. 86, p. 121111, Mar. 2005.
- [65] J. S. Levy, A. Gondarenko, M. A. Foster, A. C. Turner-Foster, A. L. Gaeta, and M. Lipson, “CMOS-compatible multiple-wavelength oscillator for on-chip optical interconnects,” *Nature Photonics*, vol. 4, pp. 37–40, Jan. 2010.
- [66] X. Ji, F. A. S. Barbosa, S. P. Roberts, A. Dutt, J. Cardenas, Y. Okawachi, A. Bryant, A. L. Gaeta, and M. Lipson, “Ultra-low-loss on-chip resonators with sub-milliwatt parametric oscillation threshold,” *Optica*, vol. 4, p. 619, June 2017.
- [67] E. Wooten, K. Kissa, A. Yi-Yan, E. Murphy, D. Lafaw, P. Hallemeier, D. Maack, D. Attanasio, D. Fritz, G. McBrien, and D. Bossi, “A review of lithium niobate modulators for fiber-optic communications systems,” *IEEE Journal of Selected Topics in Quantum Electronics*, vol. 6, pp. 69–82, Jan. 2000.

- [68] D. Janner, D. Tulli, M. García-Granda, M. Belmonte, and V. Pruneri, “Microstructured integrated electro-optic LiNbO₃ modulators,” *Laser & Photonics Review*, vol. 3, pp. 301–313, Apr. 2009.
- [69] L. Chen, Q. Xu, M. G. Wood, and R. M. Reano, “Hybrid silicon and lithium niobate electro-optical ring modulator,” *Optica*, vol. 1, p. 112, Aug. 2014.
- [70] A. Rao, A. Patil, P. Rabiei, A. Honardoost, R. DeSalvo, A. Paoella, and S. Fathpour, “High-performance and linear thin-film lithium niobate Mach–Zehnder modulators on silicon up to 50 GHz,” *Optics Letters*, vol. 41, p. 5700, Dec. 2016.
- [71] C. Wang, M. Zhang, M. Yu, R. Zhu, H. Hu, and M. Loncar, “Monolithic lithium niobate photonic circuits for Kerr frequency comb generation and modulation,” *Nature Communications*, vol. 10, p. 978, Dec. 2019.
- [72] M. Zhang, C. Wang, Y. Hu, A. Shams-Ansari, T. Ren, S. Fan, and M. Lončar, “Electronically programmable photonic molecule,” *Nature Photonics*, vol. 13, pp. 36–40, Jan. 2019.
- [73] J. D. Joannopoulos, ed., *Photonic crystals: molding the flow of light*. Princeton: Princeton University Press, 2nd ed ed., 2008. OCLC: ocn180190957.
- [74] S. John, “Strong localization of photons in certain disordered dielectric superlattices,” *PhRvL*, vol. 58, pp. 2486–2489, June 1987.
- [75] E. Yablonovitch, “Inhibited Spontaneous Emission in Solid-State Physics and Electronics,” *Physical Review Letters*, vol. 58, pp. 2059–2062, May 1987.
- [76] F. Bloch, “Über die Quantenmechanik der Elektronen in Kristallgittern,” *Zeitschrift für Physik*, vol. 52, pp. 555–600, July 1929.
- [77] N. W. Ashcroft and N. D. Mermin, *Solid state physics*. New York: Holt, Rinehart and Winston, 1976.
- [78] D. Goldring, U. Levy, and D. Mendlovic, “Highly dispersive micro-ring resonator based on one dimensional photonic crystal waveguide design and analysis,” *Optics Express*, vol. 15, pp. 3156–3168, Mar. 2007.
- [79] D. Goldring, U. Levy, I. E. Dotan, A. Tsukernik, M. Oksman, I. Rubin, Y. David, and D. Mendlovic, “Experimental measurement of quality factor enhancement using slow light modes in one dimensional photonic crystal,” *Optics Express*, vol. 16, pp. 5585–5595, Apr. 2008.

- [80] J. Y. Lee and P. M. Fauchet, “Slow-light dispersion in periodically patterned silicon microring resonators,” *Optics Letters*, vol. 37, pp. 58–60, Jan. 2012.
- [81] K. Jensen, M. Alam, B. Scherer, A. Lambrecht, and N. Mortensen, “Slow-light enhanced light–matter interactions with applications to gas sensing,” *Optics Communications*, vol. 281, pp. 5335–5339, Nov. 2008.
- [82] M. Soljačić, E. Lidorikis, L. V. Hau, and J. D. Joannopoulos, “Enhancement of microcavity lifetimes using highly dispersive materials,” *Physical Review E*, vol. 71, p. 026602, Feb. 2005.
- [83] K. McGarvey-Lechable and P. Bianucci, “Maximizing slow-light enhancement in one-dimensional photonic crystal ring resonators,” *Optics Express*, vol. 22, pp. 26032–26041, Oct. 2014.
- [84] S. G. Johnson and J. D. Joannopoulos, “Block-iterative frequency-domain methods for Maxwell’s equations in a planewave basis,” *Optics Express*, vol. 8, pp. 173–190, Jan. 2001.
- [85] A. F. Oskooi, D. Roundy, M. Ibanescu, P. Bermel, J. D. Joannopoulos, and S. G. Johnson, “Meep: A flexible free-software package for electromagnetic simulations by the FDTD method,” *Computer Physics Communications*, vol. 181, pp. 687–702, Mar. 2010.
- [86] G. Gao, Y. Zhang, H. Zhang, Y. Wang, Q. Huang, and J. Xia, “Air-mode photonic crystal ring resonator on silicon-on-insulator,” *Scientific Reports*, vol. 6, pp. 1–6, Jan. 2016.
- [87] K. McGarvey-Lechable, T. Hamidfar, D. Patel, L. Xu, D. V. Plant, and P. Bianucci, “Slow light in mass-produced, dispersion-engineered photonic crystal ring resonators,” *Optics Express*, vol. 25, pp. 3916–3926, Feb. 2017.
- [88] K. v. Klitzing, G. Dorda, and M. Pepper, “New Method for High-Accuracy Determination of the Fine-Structure Constant Based on Quantized Hall Resistance,” *Physical Review Letters*, vol. 45, pp. 494–497, Aug. 1980.
- [89] K. S. Novoselov, Z. Jiang, Y. Zhang, S. V. Morozov, H. L. Stormer, U. Zeitler, J. C. Maan, G. S. Boebinger, P. Kim, and A. K. Geim, “Room-Temperature Quantum Hall Effect in Graphene,” *Science*, vol. 315, pp. 1379–1379, Mar. 2007. Publisher: American Association for the Advancement of Science Section: Brevia.

- [90] F. D. M. Haldane and S. Raghu, “Possible Realization of Directional Optical Waveguides in Photonic Crystals with Broken Time-Reversal Symmetry,” *Physical Review Letters*, vol. 100, p. 013904, Jan. 2008.
- [91] S. Raghu and F. D. M. Haldane, “Analogues of quantum-Hall-effect edge states in photonic crystals,” *Physical Review A*, vol. 78, p. 033834, Sept. 2008.
- [92] Z. Wang, Y. D. Chong, J. D. Joannopoulos, and M. Soljačić, “Reflection-Free One-Way Edge Modes in a Gyromagnetic Photonic Crystal,” *Physical Review Letters*, vol. 100, p. 013905, Jan. 2008.
- [93] Z. Wang, Y. Chong, J. D. Joannopoulos, and M. Soljačić, “Observation of unidirectional backscattering-immune topological electromagnetic states,” *Nature*, vol. 461, pp. 772–775, Oct. 2009.
- [94] A. Blanco-Redondo, I. Andonegui, M. J. Collins, G. Harari, Y. Lumer, M. C. Rechtsman, B. J. Eggleton, and M. Segev, “Topological Optical Waveguiding in Silicon and the Transition between Topological and Trivial Defect States,” *Physical Review Letters*, vol. 116, p. 163901, Apr. 2016.
- [95] P. St-Jean, V. Goblot, E. Galopin, A. Lemaître, T. Ozawa, L. Le Gratiet, I. Sagnes, J. Bloch, and A. Amo, “Lasing in topological edge states of a one-dimensional lattice,” *Nature Photonics*, vol. 11, pp. 651–656, Oct. 2017.
- [96] S. Ryu, A. P. Schnyder, A. Furusaki, and A. W. W. Ludwig, “Topological insulators and superconductors: tenfold way and dimensional hierarchy,” *New Journal of Physics*, vol. 12, p. 065010, June 2010.
- [97] W. P. Su, J. R. Schrieffer, and A. J. Heeger, “Soliton excitations in polyacetylene,” *Physical Review B*, vol. 22, pp. 2099–2111, Aug. 1980.
- [98] J. K. Asbóth, L. Oroszlány, and A. Pályi, *A short course on topological insulators: band structure and edge states in one and two dimensions*. No. volume 919 in Lecture notes in physics, Cham Heidelberg New York Dordrecht London: Springer, 2016. OCLC: 942849465.
- [99] J. Zak, “Berry’s phase for energy bands in solids,” *Physical Review Letters*, vol. 62, pp. 2747–2750, June 1989.
- [100] P. Delplace, D. Ullmo, and G. Montambaux, “Zak phase and the existence of edge states in graphene,” *Physical Review B*, vol. 84, p. 195452, Nov. 2011.

- [101] J. Vučković and Y. Yamamoto, “Photonic crystal microcavities for cavity quantum electrodynamics with a single quantum dot,” *Applied Physics Letters*, vol. 82, pp. 2374–2376, Apr. 2003.
- [102] L. Sapienza, H. Thyrestrup, S. Stobbe, P. D. Garcia, S. Smolka, and P. Lodahl, “Cavity Quantum Electrodynamics with Anderson-Localized Modes,” *Science*, vol. 327, pp. 1352–1355, Mar. 2010.
- [103] Q. Quan and M. Loncar, “Deterministic design of wavelength scale, ultra-high Q photonic crystal nanobeam cavities,” *Optics Express*, vol. 19, pp. 18529–18542, Sept. 2011.
- [104] M. Gell-Mann, “Symmetries of Baryons and Mesons,” *Physical Review*, vol. 125, pp. 1067–1084, Feb. 1962.
- [105] V. M. Martinez Alvarez and M. D. Coutinho-Filho, “Edge states in trimer lattices,” *Physical Review A*, vol. 99, p. 013833, Jan. 2019.
- [106] H. Guo and S. Chen, “Kaleidoscope of symmetry-protected topological phases in one-dimensional periodically modulated lattices,” *Physical Review B*, vol. 91, p. 041402, Jan. 2015.
- [107] Z. Zhang, M. Dainese, L. Wosinski, and M. Qiu, “Resonance-splitting and enhanced notch depth in SOI ring resonators with mutual mode coupling,” *Optics Express*, vol. 16, pp. 4621–4630, Mar. 2008.
- [108] T. Wang, F. Liu, J. Wang, Y. Tian, Z. Zhang, T. Ye, M. Qiu, and Y. Su, “Pulse Delay and Advancement in SOI Microring Resonators With Mutual Mode Coupling,” *Journal of Lightwave Technology*, vol. 27, pp. 4734–4743, Nov. 2009.
- [109] G. C. Ballesteros, J. Matres, J. Martí, and C. J. Oton, “Characterizing and modeling backscattering in silicon microring resonators,” *Optics Express*, vol. 19, pp. 24980–24985, Dec. 2011.
- [110] Q. Li, T. Wang, Y. Su, M. Yan, and M. Qiu, “Coupled mode theory analysis of mode-splitting in coupled cavity system,” *Optics Express*, vol. 18, pp. 8367–8382, Apr. 2010.
- [111] A. Li, T. V. Vaerenbergh, P. D. Heyn, P. Bienstman, and W. Bogaerts, “Backscattering in silicon microring resonators: a quantitative analysis,” *Laser & Photonics Reviews*, vol. 10, no. 3, pp. 420–431, 2016.

- [112] B. E. Little, J.-P. Laine, and S. T. Chu, “Surface-roughness-induced contradirectional coupling in ring and disk resonators,” *Optics Letters*, vol. 22, pp. 4–6, Jan. 1997.
- [113] Y. M. Kang, A. Arbabi, and L. L. Goddard, “Engineering the spectral reflectance of microring resonators with integrated reflective elements,” *Optics Express*, vol. 18, pp. 16813–16825, Aug. 2010.
- [114] G. Gao, D. Li, Y. Zhang, S. Yuan, A. Armghan, Q. Huang, Y. Wang, J. Yu, and J. Xia, “Tuning of resonance spacing over whole free spectral range based on Autler-Townes splitting in a single microring resonator,” *Optics Express*, vol. 23, pp. 26895–26904, Oct. 2015.
- [115] K. McGarvey-Lechable and P. Bianucci, “Bloch-Floquet waves in optical ring resonators,” *Physical Review B*, vol. 97, p. 214204, June 2018.
- [116] K. Sakoda, *Optical Properties of Photonic Crystals*. 2001. OCLC: 1113638080.
- [117] L. Yuan, Q. Lin, M. Xiao, and S. Fan, “Synthetic dimension in photonics,” *Optica*, vol. 5, pp. 1396–1405, Nov. 2018.
- [118] A. Celi, P. Massignan, J. Ruseckas, N. Goldman, I. B. Spielman, G. Juzeliūnas, and M. Lewenstein, “Synthetic Gauge Fields in Synthetic Dimensions,” *Physical Review Letters*, vol. 112, p. 043001, Jan. 2014.
- [119] X.-W. Luo, X. Zhou, C.-F. Li, J.-S. Xu, G.-C. Guo, and Z.-W. Zhou, “Quantum simulation of 2D topological physics in a 1D array of optical cavities,” *Nature Communications*, vol. 6, p. 7704, Nov. 2015.
- [120] L. Yuan, Y. Shi, and S. Fan, “Photonic gauge potential in a system with a synthetic frequency dimension,” *Optics Letters*, vol. 41, pp. 741–744, Feb. 2016.
- [121] O. Boada, A. Celi, J. I. Latorre, and M. Lewenstein, “Quantum Simulation of an Extra Dimension,” *Physical Review Letters*, vol. 108, p. 133001, Mar. 2012.
- [122] Q. Lin, M. Xiao, L. Yuan, and S. Fan, “Photonic Weyl point in a two-dimensional resonator lattice with a synthetic frequency dimension,” *Nature Communications*, vol. 7, p. 13731, Dec. 2016.
- [123] I. D. Vatnik, A. Tikan, G. Onishchukov, D. V. Churkin, and A. A. Sukhorukov, “Anderson localization in synthetic photonic lattices,” *Scientific Reports*, vol. 7, p. 4301, Dec. 2017.

- [124] A. Dutt, Q. Lin, L. Yuan, M. Minkov, M. Xiao, and S. Fan, “A single photonic cavity with two independent physical synthetic dimensions,” *Science*, vol. 367, pp. 59–64, Jan. 2020.
- [125] A. Dutt, M. Minkov, Q. Lin, L. Yuan, D. A. B. Miller, and S. Fan, “Experimental band structure spectroscopy along a synthetic dimension,” *Nature Communications*, vol. 10, p. 3122, Dec. 2019.
- [126] M. C. Rechtsman, J. M. Zeuner, Y. Plotnik, Y. Lumer, D. Podolsky, F. Dreisow, S. Nolte, M. Segev, and A. Szameit, “Photonic Floquet topological insulators,” *Nature*, vol. 496, pp. 196–200, Apr. 2013.
- [127] E. Lustig, S. Weimann, Y. Plotnik, Y. Lumer, M. A. Bandres, A. Szameit, and M. Segev, “Photonic topological insulator in synthetic dimensions,” *Nature*, vol. 567, pp. 356–360, Mar. 2019.
- [128] A. Altland and B. D. Simons, *Condensed matter field theory*. 2010. OCLC: 651601524.
- [129] G. Brambilla, V. Finazzi, and D. J. Richardson, “Ultra-low-loss optical fiber nanotapers,” *Optics Express*, vol. 12, no. 10, p. 2258, 2004.
- [130] T. J. Kippenberg, S. M. Spillane, D. K. Armani, and K. J. Vahala, “Fabrication and coupling to planar high-Q silica disk microcavities,” *Applied Physics Letters*, vol. 83, pp. 797–799, July 2003.

Appendix A

Python scripts for frequency-domain eigenmode simulations

The following file can be used to simulate either a standard waveguide ($r = 0$), a photonic crystal waveguide ($d = 0$), or a dimerized photonic crystal ring resonator ($d = 1$).

Python files can be downloaded directly [here](#).

```
## Compute the band structure of a photonic crystal waveguide
## using the frequency-domain eigenmode solver MPB
## https://mpb.readthedocs.io/en/latest/    May 2020 KWM

import math
import multiprocessing as mp
from multiprocessing import mp
import numpy as np
import matplotlib.pyplot as plt

def main(args, sim_dir):

    # Simulation parameters
    resolution = args.res      # pixels/a
    plotfields = args.p        # Plot the fields (0 = off, 1 = on)
    num_bands = args.n         # Number of photonic bands to compute
    nks = args.nks             # Number of k-points to interpolate in the
                               ↪ FBZ
```

```

dimer = args.dimer          # Simulate a dimerized PhC unit cell (0 =
    ↪ off, 1 = on)
pol = args.P                # excitation polarization (0 = TE (Hz), 1
    ↪ = TM (Ez))

# Waveguide parameters
nwg = args.i               # Waveguide refractive index
kwg = 0                    # Waveguide extinction coefficient
w = args.w                 # Width of waveguide (in units of the lattice
    ↪ constant)
relem = args.r             # Radius of periodic elements (in units of the
    ↪ lattice constant)
h = args.d                 # Hopping parameter (in units of the lattice
    ↪ constant)
nelem = args.nelem         # Periodic element refractive index
kelem = 0                  # Periodic element extinction coefficient

# Define the ring material
re_eps_wg = (nwg ** 2) - (kwg ** 2)
im_eps_wg = 2 * nwg * kwg
mysigmad_wg = (2 * math.pi * fcen * im_eps_wg) / re_eps_wg
wg_material = mp.Medium(epsilon = re_eps_wg, D_conductivity =
    ↪ mysigmad_wg)

# Define the periodic element material
re_eps_elem = (nelem ** 2) - (kelem ** 2)
im_eps_elem = 2 * nelem * kelem
mysigmad_elem = (2 * math.pi * fcen * im_eps_elem) / re_eps_elem
elem_material = mp.Medium(epsilon = re_eps_elem, D_conductivity =
    ↪ mysigmad_elem)

# Define the lattice cell
if dimer == 0:
    sx = 1

```

```

else:
    sx = 2

sy = 5
sz = 0
cell = mp.Vector3(sx, sy)
geometry_lattice = mp.Lattice(size=cell)

# Define the cell's geometry
if dimer == 0:
    geometry = [mp.Block(center=mp.Vector3(), material=wg_material,
        ↪ size = mp.Vector3(1,w,0)),
        mp.Cylinder(center=mp.Vector3(), material=elem_material,
        ↪ radius=relem)]
else:
    geometry = [mp.Block(center=mp.Vector3(), material=wg_material,
        ↪ size = mp.Vector3(2,w,0)),
        mp.Cylinder(center=mp.Vector3(-0.5 + h),
        ↪ material=elem_material, radius=relem),
        mp.Cylinder(center=mp.Vector3(0.5 - h),
        ↪ material=elem_material, radius = relem)]

# Define the k-points in the FBZ
k_points = [mp.Vector3(), mp.Vector3(0.5)] # K-points of the
        ↪ first Brillouin zone
k_points = mp.interpolate(nks, k_points) # Number of k-points to
        ↪ interpolate in the first Brillouin zone

# Define the mode solver
ms = mpb.ModeSolver(num_bands=num_bands,
                    k_points=k_points,
                    geometry=geometry,
                    geometry_lattice=geometry_lattice,
                    resolution=resolution)

```

```

if pol == 0:
    if plotfields == 0:
        ms.run_te()
    else:
        ms.run_te(mpb.output_at_kpoint(mp.Vector3(0.5),
        ↪ mpb.output_hfield_z, mpb.output_dpwr)
else:
    if plotfields == 0:
        ms.run_tm()
    else:
        ms.run_tm(mpb.output_at_kpoint(mp.Vector3(0.5),
        ↪ mpb.output_efield_z, mpb.output_bpwr)

ms.output_epsilon()

if __name__ == '__main__':
    parser = argparse.ArgumentParser()
    parser.add_argument('-res', type=int, default=20, help='Simulation
    ↪ resolution (pixels/lattice constant) (default: 20)')
    parser.add_argument('-p', type=int, default=0, help='Plot the fields
    ↪ (0 = off, 1 = on) (default: 0)')
    parser.add_argument('-n', type=int, default=1, help='Number of bands
    ↪ to compute (default: 1)')
    parser.add_argument('-nks', type=int, default=4, help='Number of k
    ↪ points to interpolate (default: 4)')
    parser.add_argument('-dimer', type=int, default=0, help='Simulate a
    ↪ dimerized PhC unit cell (0 = off, 1 = on)')
    parser.add_argument('-P', type=int, default=0, help='(0 = TE, 1 = TM)
    ↪ (default: 0)')
    parser.add_argument('-i', type=float, default=2.0, help='Effective
    ↪ refractive index of the waveguide (default: 2.00)')
    parser.add_argument('-w', type=float, default=1, help='Width of the
    ↪ ring (units of the lattice constant) (default: 1.0)')

```

```

parser.add_argument('-r', type=float, default=0.3, help='Radius of
↳ periodic elements (units of the lattice constant) (default:
↳ 0.3)')
parser.add_argument('-nelem', type=float, default=1.00,
↳ help='Effective refractive index of the periodic elements
↳ (default: 1.00)')
parser.add_argument('-d', type=float, default=0.2, help='Hopping
↳ parameter (in units of the lattice constant) (default: 0.2)')
args = parser.parse_args()

# Create a directory name for the run
sim_dir = 'phc-wg-res_' + str(args.res) + '-num-bands_' +
↳ str(args.n) + '-nwg_' + str(args.i) + '-w_' + str(args.w) +
↳ '-relem_' + str(args.r) + '-hop_' + str(args.hop)

# Check to see if directory already exists
if os.path.isdir(sim_dir + '.old') == True:
    shutil.rmtree(sim_dir + '.old')

if os.path.isdir(sim_dir) == True:
    os.rename(sim_dir, sim_dir + '.old')

main(args, sim_dir)

# Print simulation parameters to a file
with open(sim_dir + '/cmdline.txt', 'w') as f:
    f.write(' '.join(sys.argv[1:]))

```

Appendix B

Python scripts for finite-difference-time-domain simulations

B.1 Photonic crystal ring resonator

The following file can be used to simulate either a standard ring resonator ($r = 0$), a photonic crystal ring resonator ($r \neq 0$, $\text{hop} = 0$), a dimerized photonic crystal ring resonator ($\text{hop} \neq 0$, $\text{topo} = 0$), or a dimerized PhCRR with topological cavities ($\text{topo} = 1$) Python files for the photonic crystal ring resonator can be downloaded directly [here](#).

```
## Compute the time response of a photonic crystal ring resonator  
## using the finite-difference-time-domain software MEEP  
## https://meep.readthedocs.io/en/latest/ KM Oct 2020  
  
import meep as mp  
import sys, os, shutil  
import argparse  
import math  
import numpy as np  
import matplotlib.pyplot as plt  
import sys  
import subprocess  
import random
```

```

def main(args, sim_dir):

    # Simulation parameters
    resolution = args.res      # pixels/um
    fixt = args.t              # Run the simulation as a function of time
    ↪ or field decay (0 = time, 1 = decay)
    runtime = args.T           # MEEP time units
    decayfrac = args.D         # Run the simulation until the absolute
    ↪ value squared of the field decays by 'decayfrac'
    plotfields = args.p        # Plot the fields after simulation (0 =
    ↪ off, 1 = on)

    # Ring parameters
    nring = args.i             # Ring refractive index
    kring = 0                  # Ring extinction coefficient
    r0 = args.R                # Center radius of ring (um)
    w = args.w                 # Width of ring (um)
    topo = args.topo           # Trivial (0) or topological (1) ring

    # Periodic element parameters
    N = args.N                 # Number of periodic elements
    nelem = 1                  # Periodic element refractive index
    kelem = 0                  # Periodic element extinction coefficient
    relem = args.r             # Radius of periodic elements
    dr = args.dr               # Standard deviation on the radius (um)
    seed = 142857              # Random seed
    h = args.hop               # Hopping parameter (in units of the lattice
    ↪ constant)
    reduc = args.u             # Number of lattice constants by which to reduce the
    ↪ spacing between topo defects

    # Ring surface roughness parameters
    rough = 0                  # Option for running simulation with surface roughness
    ↪ (0 = off, 1 = on)
    Ra = 0.003                 # Average radius of surface scatterer (um)

```

```

Rd = 100      # Linear surface scatterer density (um-1)

# Coupling waveguide parameters
coup = args.c      # Add a coupling waveguide for flux simulations (0
→ = off, 1 = on)
g = args.g         # Evanescent coupling gap width (um)
wgw = args.wgw     # Coupling waveguide width (um)
nwg = args.i       # Coupling waveguide refractive index
kwg = 0           # Coupling waveguide extinction coefficient

# Background material parameters
nback = 1         # Background material refractive index
kback = 0         # Background material extinction coefficient

# Excitation parameters
lcn = args.l              # pulse center wavelength (um)
dl = args.dl              # pulse width (um)
pol = args.P              # excitation polarization (0 =
→ TE (Hz), 1 = TM (Ez))
fcen = 1/lcn              # pulse center in frequency
→ (dimensionless)
df = ((1/lcn) - (1/(lcn + dl))) # pulse width in frequency
→ (dimensionless)
print("fcen: " + str(fcen) + ", df = " + str(df))

# Define the PMLs and padding
pad = 2 * lcn # Padding before PML (wavelengths in vacuum)
dpml = 3 * lcn # Thickness of PML (wavelengths in vacuum)
pml_layers = [mp.PML(dpml)]

# Define the cell geometry
sx = dpml + pad + wgw + g + (2 * r0) + pad + dpml
sy = dpml + pad + wgw + g + (2 * r0) + pad + dpml
sz = 0
cell = mp.Vector3(sx, sy)

```

```

# Define the ring material
re_eps_ring = (nring ** 2) - (kring ** 2)
im_eps_ring = 2 * nring * kring
mysigmat_ring = (2 * math.pi * fcen * im_eps_ring) / re_eps_ring
ring_material = mp.Medium(epsilon = re_eps_ring, D_conductivity =
    ↪ mysigmat_ring)

# Define the periodic element material
re_eps_elem = (nelem ** 2) - (kelem ** 2)
im_eps_elem = 2 * nelem * kelem
mysigmat_elem = (2 * math.pi * fcen * im_eps_elem) / re_eps_elem
elem_material = mp.Medium(epsilon = re_eps_elem, D_conductivity =
    ↪ mysigmat_elem)

# Define the background material
re_eps_back = (nback ** 2) - (kback ** 2)
im_eps_back = 2 * nback * kback
mysigmat_back = (2 * math.pi * fcen * im_eps_back) / re_eps_back
back_material = mp.Medium(epsilon = re_eps_back, D_conductivity =
    ↪ mysigmat_back)

# Geometry definitions
delta = 2 * math.pi / N      # angle of the period
hop = (h * delta) / 2       # angle of the hopping parameter
print("Length period: " + str(delta * r0) + " um")
random.seed(seed) # Random seed generator for radius variation

geometry_back = [mp.Block(size = mp.Vector3(mp.inf, mp.inf, mp.inf),
    ↪ material = back_material)]

geometry_ring = [mp.Cylinder(radius = r0 + (w/2), center =
    ↪ mp.Vector3(0, 0, 0), material = ring_material, height=mp.inf),

```

```

        mp.Cylinder(radius = r0 - (w/2), center
        ↪ =mp.Vector3(0, 0, 0), material = back_material,
        ↪ height=mp.inf)]

geometry_elem = []

if topo == 0:
    for i in range(0, N, 2):
        geometry_elem.append(mp.Cylinder(radius =
        ↪ random.normalvariate(relem, dr), height = mp.inf,
        ↪ material = elem_material, center =
        ↪ mp.Vector3(r0*math.cos((i*delta) - hop),
        ↪ r0*math.sin((i*delta) - hop), 0)))
    for i in range(1, N, 2):
        geometry_elem.append(mp.Cylinder(radius =
        ↪ random.normalvariate(relem, dr), height = mp.inf,
        ↪ material = elem_material, center =
        ↪ mp.Vector3(r0*math.cos((i*delta) + hop),
        ↪ r0*math.sin((i*delta) + hop), 0)))
else:
    for i in range(0, math.ceil(N/2) - reduc, 2):
        geometry_elem.append(mp.Cylinder(radius =
        ↪ random.normalvariate(relem, dr), height = mp.inf,
        ↪ material = elem_material, center =
        ↪ mp.Vector3(r0*math.cos((i*delta) + hop + np.pi/2),
        ↪ r0*math.sin((i*delta) + hop + np.pi/2), 0)))
    for i in range(1, math.ceil(N/2) - reduc, 2):
        geometry_elem.append(mp.Cylinder(radius =
        ↪ random.normalvariate(relem, dr), height = mp.inf,
        ↪ material = elem_material, center =
        ↪ mp.Vector3(r0*math.cos((i*delta) - hop + np.pi/2),
        ↪ r0*math.sin((i*delta) - hop + np.pi/2), 0)))
    for i in range((math.ceil(N/2) - (2 * reduc)), N, 2):

```

```

geometry_elem.append(mp.Cylinder(radius =
    ↪ random.normalvariate(relem, dr), height = mp.inf,
    ↪ material = elem_material, center =
    ↪ mp.Vector3(r0*math.cos((i*delta) - hop + np.pi/2),
    ↪ r0*math.sin((i*delta) - hop + np.pi/2), 0)))
for i in range(((math.ceil(N/2) - (2*reduc)) + 1), N, 2):
    geometry_elem.append(mp.Cylinder(radius =
        ↪ random.normalvariate(relem, dr), height = mp.inf,
        ↪ material = elem_material, center =
        ↪ mp.Vector3(r0*math.cos((i*delta) + hop + np.pi/2),
        ↪ r0*math.sin((i*delta) + hop + np.pi/2), 0)))

geometry_wg = [mp.Block(center = mp.Vector3(0, r0 + g + wgw/2 + w/2,
    ↪ 0), size = mp.Vector3(mp.inf, wgw, 0), material = ring_material)]

if coup == 0:      # Use this option to find the resonances of the
    ↪ ring
    geometry = geometry_back + geometry_ring + geometry_elem

if coup == 1:      # Use this option to calculate transmission
    ↪ spectrum of the ring
    geometry = geometry_back + geometry_ring + geometry_elem +
    ↪ geometry_wg

# Source definitions
disp = w / 20     # Small displacement from original coordinate to
    ↪ avoid field nodes
if pol == 0:
    my_component = mp.Hz
else:
    my_component = mp.Ez

if coup == 0:

```

```

sources = [mp.Source(mp.GaussianSource(fcen, fwidth = df),
↪ component = my_component, center =
↪ mp.Vector3(r0*math.cos(delta + disp),
↪ r0*math.sin(delta+disp), 0)),
           mp.Source(mp.GaussianSource(fcen, fwidth = df),
↪ component = my_component, center =
↪ mp.Vector3(r0*math.cos((delta*2) + disp),
↪ r0*math.sin((delta*2) + disp), 0))]

else:
sources = [mp.Source(mp.GaussianSource(fcen, fwidth = df),
↪ component = my_component, center = mp.Vector3((-sx/2) + dpml,
↪ r0 + g + (wgv/2) + (w/2), 0), size = mp.Vector3(0, wgv, 0))]

# Simulation definition
sim = mp.Simulation(cell_size=cell,
                    boundary_layers=pml_layers,
                    sources=sources,
                    geometry=geometry,
                    resolution=resolution)

sim.use_output_directory(sim_dir)

# Define a function to plot the dielectric function of the
↪ structure
def plot_epsilon():
    # Plot the dielectric function
    eps_data = sim.get_array(center=mp.Vector3(), size=cell,
↪ component=mp.Dielectric)
    plt.figure(dpi=1000)
    plt.imshow(eps_data, interpolation='spline36', cmap='binary')
    plt.axis('off')
    plt.savefig(sim_dir + '/epsilon_profile.png')

# Field measurement definitions

```

```

# Define the positions where the fields should be measured ! Must
↪ be placed far from the source position
meas1 = mp.Vector3(r0*math.cos(((N/2) * delta) + disp + np.pi/2),
↪ r0*math.sin(((N/2) * delta) + disp + np.pi/2), 0)
meas2 = mp.Vector3(r0*math.cos(((N/2) * delta) - (delta / 2) + disp +
↪ 2*np.pi/3), r0*math.sin(((N/2) * delta) - (delta / 2) + disp +
↪ 3*np.pi/2), 0)

```

```

# Define a function which measures the fields

```

```

def get_fields(sim):
    f = open(sim_dir + '/meas1.dat', "a+")
    f.write(str(sim.meep_time()) + ", " +
↪ str(np.real(sim.get_field_point(my_component, meas1))) +
↪ '\n')
    f.close()
    g = open(sim_dir + '/meas2.dat', "a+")
    g.write(str(sim.meep_time()) + ", " +
↪ str(np.real(sim.get_field_point(my_component, meas2))) +
↪ '\n')
    g.close()

```

```

# Define flux regions for transmission spectrum run

```

```

nfreq = 2000

```

```

# Incident flux

```

```

inc_flux = mp.FluxRegion(center = mp.Vector3((-sx/2) + dpml + 1, r0 +
↪ g + (w/w/2) + (w/2), 0), size = mp.Vector3(0, 2 * w/w, 0))
inc = sim.add_flux(fcen, df, nfreq, inc_flux)

```

```

# Transmitted flux

```

```

trans_flux = mp.FluxRegion(center = mp.Vector3((sx/2) - dpml - 1, r0
↪ + g + (w/w/2) + (w/2), 0), size = mp.Vector3(0, 2 * w/w, 0))

```

```

trans = sim.add_flux(fcen, df, nfreq, trans_flux)

# Run the simulation
if coup == 0 and fixt == 0: # Run simulation with no coupling
    ↪ waveguide for 'runtime' MEEP time units
    sim.run(mp.at_beginning(mp.output_epsilon),
            mp.after_sources(get_fields,
                             mp.Harminv(my_component, meas1, fcen,
                                         ↪ df),
                             mp.Harminv(my_component, meas2, fcen,
                                         ↪ df)),
            until_after_sources=runtime)

# Plot the fields
if plotfields == 1:
    sim.run(mp.at_every(1/fcen/10, mp.output_png(my_component,
    ↪ "-C $EPS -Zc dkbluered")), until = 1 /fcen)

if coup == 0 and fixt == 1: # Run simulation with no coupling
    ↪ waveguide until absolute value squared of fields have decayed to
    ↪ 'decayfrac' of original value
    sim.run(mp.at_beginning(mp.output_epsilon),
            mp.after_sources(get_fields,
                             mp.Harminv(my_component, meas1, fcen,
                                         ↪ df),
                             mp.Harminv(my_component, meas2, fcen,
                                         ↪ df)),
            ↪ until_after_sources=mp.stop_when_fields_decayed(
            ↪ my_component, meas1, decayfrac))

# Plot the fields
plot_epsilon()
if plotfields == 1:
    sim.run(mp.at_every(1/fcen/10, mp.output_png(my_component,
    ↪ "-C $EPS -Zc dkbluered")), until = 1 /fcen)

```

```

# Perform the Fourier transform of the fields
if coup == 0:
    # Load and sort data into structured arrays
    d1 = np.loadtxt(sim_dir + '/meas1.dat', dtype={'names': ('time',
    ↪ 'fields'), 'formats':(float, float)}, delimiter=", ")
    d2 = np.loadtxt(sim_dir + '/meas2.dat', dtype={'names': ('time',
    ↪ 'fields'), 'formats':(float, float)}, delimiter=", ")
    data1 = np.sort(np.unique(d1), order='time')
    data2 = np.sort(np.unique(d2), order='time')

    # Resave the sorted data to a compressed file
    np.savetxt(sim_dir + '/meas1.dat.gz', data1, delimiter=", ",
    ↪ newline='\n', header="MEEP time units, Field")
    np.savetxt(sim_dir + '/meas2.dat.gz', data2, delimiter=", ",
    ↪ newline='\n', header="MEEP time units, Field")
    os.remove(sim_dir + '/meas1.dat')
    os.remove(sim_dir + '/meas2.dat')

    # Compute the Fourier transform
    time = data1['time']
    field1 = data1['fields']
    field2 = data2['fields']

    fft1 = np.abs(np.fft.rfft(field1))
    fft2 = np.abs(np.fft.rfft(field2))
    n = fft1.size
    timestep = time[1] - time[0]
    freqs = np.fft.rfftfreq(n, timestep*2)

    # Plot the result

plt.clf()

```

```

plt.plot(freqs, fft1[0:math.ceil(n/2)]/n, 'k-', freqs,
↪  fft2[0:math.ceil(n/2)]/n, 'r-')
plt.xlabel("Dimensionless frequency (c/a)")
plt.ylabel("Arbitrary amplitude")
plt.axis('on')
plt.axis('tight')
plt.autoscale(axis='y')
plt.xlim(0.4, 0.8)
plt.savefig(sim_dir + '/fft.png')

if coup == 1 and fixt == 0: # Run simulation with coupling
↪  waveguide for 'runtime' MEEP time units
    sim.run(mp.at_beginning(mp.output_epsilon), until_after_sources =
↪  runtime)
    incident = mp.get_fluxes(inc)
    transmission = mp.get_fluxes(trans)

    # Plot the fields
    plot_epsilon()
    if plotfields == 1:
        sim.run(mp.at_every(1/fcen/10, mp.output_png(my_component,
↪  "-C $EPS -Zc dkbluered")), until = 1 /fcen)

    # Reinitialize the simulation region for normalization run
    sim.reset_meep()
    geometry = geometry_back + geometry_wg
    sim = mp.Simulation(cell_size=cell,
                        boundary_layers=pml_layers,
                        sources=sources,
                        geometry=geometry,
                        resolution=resolution)
    trans_norm_flux = sim.add_flux(fcen, df, nfreq, trans_flux)
    sim.run(until_after_sources = runtime)

```

```

trans_norm = mp.get_fluxes(trans_norm_flux)

if coup == 1 and fixt == 1: # Run simulation with coupling
    ↪ waveguide until absolute value squared of fields have decayed to
    ↪ 'decayfrac'
    sim.run(mp.at_beginning(mp.output_epsilon), until_after_sources =
        ↪ mp.stop_when_fields_decayed(25, my_component, meas1,
        ↪ decayfrac))
    incident = mp.get_fluxes(inc)
    transmission = mp.get_fluxes(trans)

    # Plot the fields
    plot_epsilon()
    if plotfields == 1:
        sim.run(mp.at_every(1/fcen/10, mp.output_png(my_component,
            ↪ "-C $EPS -Zc dkbluered")), until = 1 /fcen)

    # Reinitialize the simulation region for normalization run
    sim.reset_meep()
    geometry = geometry_back + geometry_wg
    sim = mp.Simulation(cell_size=cell,
                        boundary_layers=pml_layers,
                        sources=sources,
                        geometry=geometry,
                        resolution=resolution)
    trans_norm_flux = sim.add_flux(fcen, df, nfreq, trans_flux)
    sim.run(until_after_sources = runtime)
    trans_norm = mp.get_fluxes(trans_norm_flux)

    # Plot the transmission spectrum
    if coup == 1:
        T1 = []
        T2 = []

```

```

T_norm = []
lambda = []
flux_freqs = mp.get_flux_freqs(trans)

for i in range(nfreq):
    lambda = np.append(lambda, 1/flux_freqs[i])
    T1 = np.append(T1, transmission[i])
    T2 = np.append(T2, trans_norm[i])
    T_norm = np.append(T_norm, transmission[i]/trans_norm[i])

plt.clf()
plt.plot(lambda, T_norm, 'k-', label='Transmitted flux')
plt.legend(loc="upper right")
plt.xlabel("Wavelength (microns)")
plt.axis('on')
plt.axis('tight')
plt.savefig(sim_dir + '/transmission.png')
T1_zip = list(zip(lambda, T1))
T2_zip = list(zip(lambda, T2))
T_norm_zip = list(zip(lambda, T_norm))
np.savetxt(sim_dir + '/flux.dat.gz', T1_zip, fmt='%5e, %5e')
np.savetxt(sim_dir + '/flux_wg.dat.gz', T2_zip, fmt='%5e, %5e')
np.savetxt(sim_dir + '/flux_norm.dat.gz', T_norm_zip, fmt='%5e,
↪ %5e')

if __name__ == '__main__':
    parser = argparse.ArgumentParser()
    parser.add_argument('-res', type=int, default=20, help='Simulation
↪ resolution (pixels/um) (default: 20)')
    parser.add_argument('-t', type=int, default=0, help='Run a fixed time
↪ simulation (0 = on, 1 = off) (default: 0)')
    parser.add_argument('-T', type=int, default=100, help='Run the
↪ simulation for <<t>> MEEP time units (default: 100)')

```

```

parser.add_argument('-D', type=float, default=1e-5, help='Run the
↳ simulation until the fields have decayed to <<D>> of max value
↳ (default: 1e-5)')
parser.add_argument('-p', type=int, default=0, help='Plot the fields
↳ (0 = off, 1 = on) (default: 0)')
parser.add_argument('-i', type=float, default=2.0, help='Effective
↳ refractive index of the ring (default: 2.00)')
parser.add_argument('-R', type=float, default=2.5, help='Radius of
↳ the ring (um) (default: 2.5)')
parser.add_argument('-w', type=float, default=0.45, help='Width of
↳ the ring (um) (default: 0.45)')
parser.add_argument('-N', type=int, default=60, help='Number of
↳ periodic elements (default: 60)')
parser.add_argument('-r', type=float, default=0.075, help='Radius of
↳ periodic elements (um) (default: 0.075)')
parser.add_argument('-dr', type=float, default=0, help='Standard
↳ deviation variation on radius of periodic elements (default: 0)')
parser.add_argument('-hop', type=float, default=0.2, help='Hopping
↳ parameter (in units of the lattice constant) (default: 0.2)')
parser.add_argument('-c', type=int, default=0, help='Add coupling
↳ waveguide and calculate transmission spectrum of ring (0 = off, 1
↳ = on) (default: 0)')
parser.add_argument('-g', type=float, default=0.15, help='Evanescent
↳ coupling gap width (um) (default: 0.15)')
parser.add_argument('-wgw', type=float, default=0.45, help='Coupling
↳ waveguide width (um) (default: 0.45)')
parser.add_argument('-l', type=float, default=1.55, help='Center
↳ wavelength (um) (default: 1.55 um)')
parser.add_argument('-dl', type=float, default=1, help='Excitation
↳ linewidth (um) (default: 1.00 um)')
parser.add_argument('-P', type=int, default=0, help='Polarization (0
↳ = TE, 1 = TM) (default: 0)')
parser.add_argument('-topo', type=int, default=0, help='Trivial (0)
↳ or topological (1) ring (default: 0)')

```

```

parser.add_argument('-u', type=int, default=0, help='Number of
↳ lattice constants by which to reduce the spacing between topo
↳ defects (default: 0)')
args = parser.parse_args()

# Create a directory name for the run
if args.topo == 0:
    ring = 'triv'
else:
    ring = 'topo'

if args.c == 0:
    sim_dir = ring + '-dimer_ring-res_' + str(args.res) + '-r0_' +
↳ str(args.R) + '-lcn_' + str(args.l) + '-dl_' + str(args.dl)
↳ + '-nring_' + str(args.i) + '-w_' + str(args.w) + '-N_' +
↳ str(args.N) + '-rad_' + str(args.r) + '-dr_' + str(args.dr) +
↳ '-hop_' + str(args.hop)
else:
    sim_dir = ring + '-dimer_ring-res_' + str(args.res) + '-r0_' +
↳ str(args.R) + '-lcn_' + str(args.l) + '-dl_' + str(args.dl)
↳ + '-nring_' + str(args.i) + '-w_' + str(args.w) + '-N_' +
↳ str(args.N) + '-rad_' + str(args.r) + '-dr_' + str(args.dr) +
↳ '-hop_' + str(args.hop) + '-g_' + str(args.g) + '-wg_' +
↳ str(args.wgw)

# Check to see if directory already exists
if os.path.isdir(sim_dir + '.old') == True:
    shutil.rmtree(sim_dir + '.old')

if os.path.isdir(sim_dir) == True:
    os.rename(sim_dir, sim_dir + '.old')

```

```

main(args, sim_dir)

# Print simulation parameters to a file

with open(sim_dir + '/cmdline.txt', 'w') as f:
    f.write(' '.join(sys.argv[1:]))

```

B.2 Bloch waves in ring resonators

The following file can be used to simulate a spatially-modulated ring resonator with various different modulations. Python files for the Bloch rings can be downloaded directly [here](#).

```

## Compute the optical spectrum of a spatially modulated ring
→ resonator
## using the finite-difference-time-domain software MEEP
## https://meep.readthedocs.io/en/latest/    KM May 27, 2019

import meep as mp
import sys, os, shutil
import argparse
import math
import numpy as np
import matplotlib.pyplot as plt
import sys
import subprocess
import random

def main(args, sim_dir):

    # Simulation parameters
    resolution = args.res      # pixels/um
    fixt = args.t              # Run the simulation as a function of time
    → or field decay (0 = time, 1 = decay)
    runtime = args.T          # MEEP time units

```

```

decayfrac = args.D          # Run the simulation until the absolute
    ↪ value squared of the field decays by 'decayfrac'
plotfields = args.p        # Plot the fields after simulation (0 =
    ↪ off, 1 = on)

# Ring parameters
nring = args.i             # Ring refractive index
kring = 0                  # Ring extinction coefficient
r0 = args.R                # Center radius of ring (um)
w = args.w                 # Width of ring (um)

# Fourier coefficients
a1 = args.a1               # Define the order number of the Fourier
    ↪ coefficients
a2 = args.a2
a3 = args.a3
a4 = args.a4

a1mag = args.a1mag        # Magnitude of Fourier coefficients
a2mag = args.a2mag
a3mag = args.a3mag
a4mag = args.a4mag

# Coupling waveguide parameters
coup = args.c              # Add a coupling waveguide for flux simulations (0
    ↪ = off, 1 = on)
g = args.g                 # Evanescent coupling gap width (um)
wgw = args.wgw             # Coupling waveguide width (um)
nwg = args.i               # Coupling waveguide refractive index
kwg = 0                    # Coupling waveguide extinction coefficient

# Background material parameters
nback = 1                  # Background material refractive index
kback = 0                  # Background material extinction coefficient

```

```

# Excitation parameters
lcn = args.l # pulse center wavelength (um)
dl = args.dl # pulse width (um)
pol = args.P # excitation polarization (0 =
↳ TE (Hz), 1 = TM (Ez))
fcen = 1/lcn # pulse center in frequency
↳ (dimensionless)
df = ((1/lcn) - (1/(lcn + dl))) # pulse width in frequency
↳ (dimensionless)
print("fcen: " + str(fcen) + ", df = " + str(df))

# Define the PMLs and padding
pad = 2 * lcn # Padding before PML (wavelengths in vacuum)
dpml = 3 * lcn # Thickness of PML (wavelengths in vacuum)
pml_layers = [mp.PML(dpml)]

# Define the cell geometry
sx = dpml + pad + wgw + g + (2 * r0) + pad + dpml
sy = dpml + pad + wgw + g + (2 * r0) + pad + dpml
sz = 0
cell = mp.Vector3(sx, sy)

# Define the ring material
re_eps_ring = (nring ** 2) - (kring ** 2)
im_eps_ring = 2 * nring * kring
mysigmatd_ring = (2 * math.pi * fcen * im_eps_ring) / re_eps_ring
ring_material = mp.Medium(epsilon = re_eps_ring, D_conductivity =
↳ mysigmatd_ring)

# Define the background material
re_eps_back = (nback ** 2) - (kback ** 2)
im_eps_back = 2 * nback * kback
mysigmatd_back = (2 * math.pi * fcen * im_eps_back) / re_eps_back

```

```

back_material = mp.Medium(epsilon = re_eps_back, D_conductivity =
↳ mysigmatd_back)

# Define field measurement helpers
delta = 2*np.pi/a1
if coup == 0:
    disp = w / 50
    disp = dpml + 1

# Define a material function for the ring material
def ring_medium(p):
    index = mp.Medium(epsilon = re_eps_ring + a1mag*np.cos(a1*
↳ math.atan2(p.y, p.x))+ a2mag*np.cos(a2* math.atan2(p.y, p.x))
↳ + a3mag*np.cos(a3* math.atan2(p.y, p.x)) + a4mag*np.cos(a4*
↳ math.atan2(p.y, p.x)))
    return index

geometry_back = [mp.Block(size = mp.Vector3(mp.inf, mp.inf, mp.inf),
↳ material = back_material)]

geometry_ring = [mp.Cylinder(radius = r0 + (w/2), center =
↳ mp.Vector3(0, 0, 0), material = ring_medium, height=mp.inf),
    mp.Cylinder(radius = r0 - (w/2), center
↳ =mp.Vector3(0, 0, 0), material = back_material,
↳ height=mp.inf)]

geometry_wg = [mp.Block(center = mp.Vector3(0, r0 + g + wgw/2 + w/2,
↳ 0), size = mp.Vector3(mp.inf, wgw, 0), material = ring_material)]

if coup == 0:      # Use this option to find the resonances of the
↳ ring
    geometry = geometry_back + geometry_ring

```

```

if coup == 1:      # Use this option to calculate transmission
    ↪ spectrum of the ring
    geometry = geometry_back + geometry_ring + geometry_wg

# Source definitions
disp = w / 20     # Small displacement from original coordinate to
    ↪ avoid field nodes
if pol == 0:
    my_component = mp.Hz
else:
    my_component = mp.Ez

if coup == 0:
    sources = [mp.Source(mp.GaussianSource(fcen, fwidth = df),
        ↪ component = my_component, center =
        ↪ mp.Vector3(r0*math.cos(delta + disp),
        ↪ r0*math.sin(delta+disp), 0)),
                mp.Source(mp.GaussianSource(fcen, fwidth = df),
        ↪ component = my_component, center =
        ↪ mp.Vector3(r0*math.cos((delta/2) + disp),
        ↪ r0*math.sin((delta/2) + disp), 0))]
else:
    sources = [mp.Source(mp.GaussianSource(fcen, fwidth = df),
        ↪ component = my_component, center = mp.Vector3((-sx/2) + dpml,
        ↪ r0 + g + (w/wg/2) + (w/2), 0), size = mp.Vector3(0, w/wg, 0))]

# Simulation definition
sim = mp.Simulation(cell_size=cell,
                    boundary_layers=pml_layers,
                    sources=sources,
                    geometry=geometry,
                    resolution=resolution)

```

```

sim.use_output_directory(sim_dir)

# Define a function to plot the dielectric function of the
↪ structure
def plot_epsilon():
    # Plot the dielectric function
    eps_data = sim.get_array(center=mp.Vector3(), size=cell,
        ↪ component=mp.Dielectric)
    plt.figure(dpi=1000)
    plt.imshow(eps_data, interpolation='spline36', cmap='binary')
    plt.axis('off')
    plt.savefig(sim_dir + '/epsilon_profile.png')

# Field measurement definitions

# Define the positions where the fields should be measured ! Must
↪ be placed far from the source position
meas1 = mp.Vector3(r0*math.cos(((a1/4) * delta) + disp),
    ↪ r0*math.sin(((a1/4) * delta) + disp), 0)
meas2 = mp.Vector3(r0*math.cos(((a1/4) * delta) - (delta / 2) +
    ↪ disp), r0*math.sin(((a1/4) * delta) - (delta / 2) + disp), 0)
meas3 = mp.Vector3(r0*math.cos(((a1/2) * delta) + disp),
    ↪ r0*math.sin(((a1/2) * delta) + disp), 0)
meas4 = mp.Vector3(r0*math.cos(((a1/2) * delta) - (delta / 2) +
    ↪ disp), r0*math.sin(((a1/2) * delta) - (delta / 2) + disp), 0)

# Define a function which measures the fields
def get_fields(sim):
    f = open(sim_dir + '/meas1.dat', "a+")
    f.write(str(sim.meep_time()) + ", " +
        ↪ str(np.real(sim.get_field_point(my_component, meas1))) +
        ↪ '\n')
    f.close()
    g = open(sim_dir + '/meas2.dat', "a+")

```

```

g.write(str(sim.meep_time()) + ", " +
↳ str(np.real(sim.get_field_point(my_component, meas2))) +
↳ '\n')
g.close()
h = open(sim_dir + '/meas3.dat', "a+")
h.write(str(sim.meep_time()) + ", " +
↳ str(np.real(sim.get_field_point(my_component, meas3))) +
↳ '\n')
h.close()
j = open(sim_dir + '/meas4.dat', "a+")
j.write(str(sim.meep_time()) + ", " +
↳ str(np.real(sim.get_field_point(my_component, meas4))) +
↳ '\n')
j.close()

```

Define flux regions for transmission spectrum run

```
nfreq = 2000
```

Incident flux

```

inc_flux = mp.FluxRegion(center = mp.Vector3((-sx/2) + dpml + 1, r0 +
↳ g + (w/w/2) + (w/2), 0), size = mp.Vector3(0, 2 * w/w, 0))
inc = sim.add_flux(fcen, df, nfreq, inc_flux)

```

Transmitted flux

```

trans_flux = mp.FluxRegion(center = mp.Vector3((sx/2) - dpml - 1, r0
↳ + g + (w/w/2) + (w/2), 0), size = mp.Vector3(0, 2 * w/w, 0))
trans = sim.add_flux(fcen, df, nfreq, trans_flux)

```

Run the simulation

```

if coup == 0 and fixt == 0: # Run simulation with no coupling
↳ waveguide for 'runtime' MEEP time units
    sim.run(mp.at_beginning(mp.output_epsilon),
            mp.to_appended("hz", mp.at_every(1, mp.output_hfield_z)),
            mp.after_sources(get_fields,

```

```

        mp.Harminv(my_component, meas1, fcen,
        ↪ df),
        mp.Harminv(my_component, meas2, fcen,
        ↪ df)),
        until_after_sources=runtime)

    # Plot the fields
    # if plotfields == 1:
        #sim.run(mp.at_every(1/fcen/10, mp.output_png(my_component,
        ↪ "-C $EPS -Zc dkbluered")), until = 1 /fcen)
        #sim.run(mp.to_appended("hz", mp.at_every(1,
        ↪ mp.output_hfield_z)), until=runtime)

if coup == 0 and fixt == 1: # Run simulation with no coupling
    ↪ waveguide until absolute value squared of fields have decayed to
    ↪ 'decayfrac' of original value
    sim.run(mp.at_beginning(mp.output_epsilon),
            mp.after_sources(get_fields,
                            mp.Harminv(my_component, meas1, fcen,
                            ↪ df),
                            mp.Harminv(my_component, meas2, fcen,
                            ↪ df)),
            ↪ until_after_sources=mp.stop_when_fields_decayed(
            ↪ my_component, meas1, decayfrac))

    # Plot the fields
    plot_epsilon()
    if plotfields == 1:
        sim.run(mp.at_every(1/fcen/10, mp.output_png(my_component,
        ↪ "-C $EPS -Zc dkbluered")), until = 1 /fcen)

# Perform the Fourier transform of the fields
if coup == 0:
    # Load and sort data into structured arrays

```

```

d1 = np.loadtxt(sim_dir + '/meas1.dat', dtype={'names': ('time',
↳ 'fields'), 'formats':(float, float)}, delimiter=", ")
d2 = np.loadtxt(sim_dir + '/meas2.dat', dtype={'names': ('time',
↳ 'fields'), 'formats':(float, float)}, delimiter=", ")
d3 = np.loadtxt(sim_dir + '/meas3.dat', dtype={'names': ('time',
↳ 'fields'), 'formats':(float, float)}, delimiter=", ")
d4 = np.loadtxt(sim_dir + '/meas4.dat', dtype={'names': ('time',
↳ 'fields'), 'formats':(float, float)}, delimiter=", ")
data1 = np.sort(np.unique(d1), order='time')
data2 = np.sort(np.unique(d2), order='time')
data3 = np.sort(np.unique(d3), order='time')
data4 = np.sort(np.unique(d4), order='time')

```

Resave the sorted data to a compressed file

```

np.savetxt(sim_dir + '/meas1.dat.gz', data1, delimiter=", ",
↳ newline='\n', header="MEEP time units, Field")
np.savetxt(sim_dir + '/meas2.dat.gz', data2, delimiter=", ",
↳ newline='\n', header="MEEP time units, Field")
np.savetxt(sim_dir + '/meas3.dat.gz', data3, delimiter=", ",
↳ newline='\n', header="MEEP time units, Field")
np.savetxt(sim_dir + '/meas4.dat.gz', data4, delimiter=", ",
↳ newline='\n', header="MEEP time units, Field")
os.remove(sim_dir + '/meas1.dat')
os.remove(sim_dir + '/meas2.dat')
os.remove(sim_dir + '/meas3.dat')
os.remove(sim_dir + '/meas4.dat')

```

Compute the Fourier transform

```

time = data1['time']
field1 = data1['fields']
field2 = data2['fields']
field3 = data3['fields']
field4 = data4['fields']

```

```

fft1 = np.abs(np.fft.rfft(field1))
fft2 = np.abs(np.fft.rfft(field2))
fft3 = np.abs(np.fft.rfft(field3))
fft4 = np.abs(np.fft.rfft(field4))
n = fft1.size
timestep = time[1] - time[0]
freqs = np.fft.rfftfreq(n, timestep*2)

# Plot the result

plt.clf()
plt.plot(freqs, fft1[0:math.ceil(n/2)]/n, 'k-', freqs,
↪ fft2[0:math.ceil(n/2)]/n, 'r-', fft3[0:math.ceil(n/2)]/n,
↪ 'b', fft4[0:math.ceil(n/2)]/n, 'g')
plt.xlabel("Dimensionless frequency (c/a)")
plt.ylabel("Arbitrary amplitude")
plt.axis('on')
plt.axis('tight')
plt.autoscale(axis='y')
plt.xlim(0.4, 0.8)
plt.savefig(sim_dir + '/fft.png')

if coup == 1 and fixt == 0: # Run simulation with coupling
↪ waveguide for 'runtime' MEEP time units
    sim.run(mp.at_beginning(mp.output_epsilon), until_after_sources =
↪ runtime)
    incident = mp.get_fluxes(inc)
    transmission = mp.get_fluxes(trans)

# Plot the fields
plot_epsilon()
if plotfields == 1:

```

```

sim.run(mp.at_every(1/fcen/10, mp.output_png(my_component,
↪ "-C $EPS -Zc dkbluered")), until = 1 /fcen)

# Reinitialize the simulation region for normalization run
sim.reset_meep()
geometry = geometry_back + geometry_wg
sim = mp.Simulation(cell_size=cell,
                    boundary_layers=pml_layers,
                    sources=sources,
                    geometry=geometry,
                    resolution=resolution)
trans_norm_flux = sim.add_flux(fcen, df, nfreq, trans_flux)
sim.run(until_after_sources = runtime)
trans_norm = mp.get_fluxes(trans_norm_flux)

if coup == 1 and fixt == 1: # Run simulation with coupling
↪ waveguide until absolute value squared of fields have decayed to
↪ 'decayfrac'
sim.run(mp.at_beginning(mp.output_epsilon), until_after_sources =
↪ mp.stop_when_fields_decayed(25, my_component, meas1,
↪ decayfrac))
incident = mp.get_fluxes(inc)
transmission = mp.get_fluxes(trans)

# Plot the fields
plot_epsilon()
if plotfields == 1:
    sim.run(mp.at_every(1/fcen/10, mp.output_png(my_component,
↪ "-C $EPS -Zc dkbluered")), until = 1 /fcen)

# Reinitialize the simulation region for normalization run
sim.reset_meep()
geometry = geometry_back + geometry_wg
sim = mp.Simulation(cell_size=cell,

```

```

        boundary_layers=pml_layers,
        sources=sources,
        geometry=geometry,
        resolution=resolution)
trans_norm_flux = sim.add_flux(fcen, df, nfreq, trans_flux)
sim.run(until_after_sources = runtime)
trans_norm = mp.get_fluxes(trans_norm_flux)

# Plot the transmission spectrum
if coup == 1:
    T1 = []
    T2 = []
    T_norm = []
    lambda = []
    flux_freqs = mp.get_flux_freqs(trans)

    for i in range(nfreq):
        lambda = np.append(lambda, 1/flux_freqs[i])
        T1 = np.append(T1, transmission[i])
        T2 = np.append(T2, trans_norm[i])
        T_norm = np.append(T_norm, transmission[i]/trans_norm[i])

plt.clf()
plt.plot(lambda, T_norm, 'k-', label='Transmitted flux')
plt.legend(loc="upper right")
plt.xlabel("Wavelength (microns)")
plt.axis('on')
plt.axis('tight')
plt.savefig(sim_dir + '/transmission.png')
T1_zip = list(zip(lambda, T1))
T2_zip = list(zip(lambda, T2))
T_norm_zip = list(zip(lambda, T_norm))
np.savetxt(sim_dir + '/flux.dat.gz', T1_zip, fmt='%5e, %5e')
np.savetxt(sim_dir + '/flux_wg.dat.gz', T2_zip, fmt='%5e, %5e')

```

```

    np.savetxt(sim_dir + '/flux_norm.dat.gz', T_norm_zip, fmt='%5e,
    ↪ %5e')

if __name__ == '__main__':
    parser = argparse.ArgumentParser()
    parser.add_argument('-res', type=int, default=20, help='Simulation
    ↪ resolution (pixels/um) (default: 20)')
    parser.add_argument('-t', type=int, default=0, help='Run a fixed time
    ↪ simulation (0 = on, 1 = off) (default: 0)')
    parser.add_argument('-T', type=int, default=100, help='Run the
    ↪ simulation for <<t>> MEEP time units (default: 100)')
    parser.add_argument('-D', type=float, default=1e-5, help='Run the
    ↪ simulation until the fields have decayed to <<D>> of max value
    ↪ (default: 1e-5)')
    parser.add_argument('-p', type=int, default=0, help='Plot the fields
    ↪ (0 = off, 1 = on) (default: 0)')
    parser.add_argument('-i', type=float, default=2.0, help='Effective
    ↪ refractive index of the ring (default: 2.00)')
    parser.add_argument('-R', type=float, default=2.5, help='Radius of
    ↪ the ring (um) (default: 2.5)')
    parser.add_argument('-w', type=float, default=0.45, help='Width of
    ↪ the ring (um) (default: 0.45)')
    parser.add_argument('-a1', type=int, default=122, help='Order of
    ↪ first Fourier coefficient (default: 122)')
    parser.add_argument('-a2', type=int, default=124, help='Order of
    ↪ second Fourier coefficient (default: 124)')
    parser.add_argument('-a3', type=int, default=126, help='Order of
    ↪ third Fourier coefficient (default: 126)')
    parser.add_argument('-a4', type=int, default=128, help='Order of
    ↪ fourth Fourier coefficient (default: 128)')
    parser.add_argument('-a1mag', type=float, default=0, help='Magnitude
    ↪ of first Fourier coefficient (default: 0)')
    parser.add_argument('-a2mag', type=float, default=0, help='Magnitude
    ↪ of first Fourier coefficient (default: 0)')

```

```

parser.add_argument('-a3mag', type=float, default=0, help='Magnitude
↳ of first Fourier coefficient (default: 0)')
parser.add_argument('-a4mag', type=float, default=0, help='Magnitude
↳ of first Fourier coefficient (default: 0)')
parser.add_argument('-c', type=int, default=0, help='Add coupling
↳ waveguide and calculate transmission spectrum of ring (0 = off, 1
↳ = on) (default: 0)')
parser.add_argument('-g', type=float, default=0.15, help='Evanescent
↳ coupling gap width (um) (default: 0.15)')
parser.add_argument('-wgw', type=float, default=0.45, help='Coupling
↳ waveguide width (um) (default: 0.45)')
parser.add_argument('-l', type=float, default=1.55, help='Center
↳ wavelength (um) (default: 1.55 um)')
parser.add_argument('-dl', type=float, default=1, help='Excitation
↳ linewidth (um) (default: 1.00 um)')
parser.add_argument('-P', type=int, default=0, help='Polarization (0
↳ = TE, 1 = TM) (default: 0)')
args = parser.parse_args()

```

```

# Create a directory name for the run

```

```

sim_dir = 'floquet_ring-res_' + str(args.res) + '-r0_' + str(args.R) +
↳ '-lcn_' + str(args.l) + '-dl_' + str(args.dl) + '-nring_' +
↳ str(args.i) + '-w_' + str(args.w) + '-a1_' + str(args.a1) +
↳ '-mag_' + str(args.a1mag) + '-a2_' + str(args.a2) + '-mag_' +
↳ str(args.a2mag) + '-a3_' + str(args.a3) + '-mag_' +
↳ str(args.a3mag)

```

```

# Check to see if directory already exists

```

```

if os.path.isdir(sim_dir + '.old') == True:
    shutil.rmtree(sim_dir + '.old')

if os.path.isdir(sim_dir) == True:
    os.rename(sim_dir, sim_dir + '.old')

```

```
main(args, sim_dir)

# Print simulation parameters to a file

with open(sim_dir + '/cmdline.txt', 'w') as f:
    f.write(' '.join(sys.argv[1:]))
```

Appendix C

Photonic crystal rings GDS library

The GDS files for the devices used for the experimental data in Chapter 4 can be found [here](#). The library contains the following files:

- Row 1:
 - 5.096- μm -radius photonic crystal ring resonator: $g = 150 \text{ nm}$, $W = 450 \text{ nm}$, $w = 462 \text{ nm}$, $l = 348 \text{ nm}$, $r = 120 \text{ nm}$
 - 9.970- μm -radius photonic crystal ring resonator: $g = 150 \text{ nm}$, $W = 450 \text{ nm}$, $w = 462 \text{ nm}$, $l = 348 \text{ nm}$, $r = 120 \text{ nm}$
 - 20.162- μm -radius photonic crystal ring resonator: $g = 150 \text{ nm}$, $W = 450 \text{ nm}$, $w = 462 \text{ nm}$, $l = 348 \text{ nm}$, $r = 120 \text{ nm}$
 - 30.132- μm -radius photonic crystal ring resonator: $g = 150 \text{ nm}$, $W = 450 \text{ nm}$, $w = 462 \text{ nm}$, $l = 348 \text{ nm}$, $r = 120 \text{ nm}$
 - 40.102- μm -radius photonic crystal ring resonator: $g = 150 \text{ nm}$, $W = 450 \text{ nm}$, $w = 462 \text{ nm}$, $l = 348 \text{ nm}$, $r = 120 \text{ nm}$
 - 5.096- μm -radius photonic crystal ring resonator: $g = 150 \text{ nm}$, $W = 450 \text{ nm}$, $w = 462 \text{ nm}$, $l = 348 \text{ nm}$, $r = 120 \text{ nm}$
 - 9.970- μm -radius photonic crystal ring resonator: $g = 150 \text{ nm}$, $W = 450 \text{ nm}$, $w = 462 \text{ nm}$, $l = 348 \text{ nm}$, $r = 120 \text{ nm}$
 - 20.162- μm -radius photonic crystal ring resonator: $g = 150 \text{ nm}$, $W = 450 \text{ nm}$, $w = 462 \text{ nm}$, $l = 348 \text{ nm}$, $r = 120 \text{ nm}$
 - 30.132- μm -radius photonic crystal ring resonator: $g = 150 \text{ nm}$, $W = 450 \text{ nm}$, $w = 462 \text{ nm}$, $l = 348 \text{ nm}$, $r = 120 \text{ nm}$

- 40.102- μm -radius photonic crystal ring resonator: $g = 150 \text{ nm}$, $W = 450 \text{ nm}$, $w = 462 \text{ nm}$, $l = 348 \text{ nm}$, $r = 120 \text{ nm}$
- Row 2:
 - 5.096- μm -radius standard ring resonator: $g = 150 \text{ nm}$, $W = 450 \text{ nm}$, $w = 462 \text{ nm}$
 - 9.970- μm -radius standard ring resonator: $g = 150 \text{ nm}$, $W = 450 \text{ nm}$, $w = 462 \text{ nm}$
 - 20.162- μm -radius standard ring resonator: $g = 150 \text{ nm}$, $W = 450 \text{ nm}$, $w = 462 \text{ nm}$
 - 30.132- μm -radius standard ring resonator: $g = 150 \text{ nm}$, $W = 450 \text{ nm}$, $w = 462 \text{ nm}$
 - 40.102- μm -radius standard ring resonator: $g = 150 \text{ nm}$, $W = 450 \text{ nm}$, $w = 462 \text{ nm}$
 - 5.096- μm -radius standard ring resonator: $g = 150 \text{ nm}$, $W = 450 \text{ nm}$, $w = 462 \text{ nm}$
 - 9.970- μm -radius standard ring resonator: $g = 150 \text{ nm}$, $W = 450 \text{ nm}$, $w = 462 \text{ nm}$
 - 20.162- μm -radius standard ring resonator: $g = 150 \text{ nm}$, $W = 450 \text{ nm}$, $w = 462 \text{ nm}$
 - 30.132- μm -radius standard ring resonator: $g = 150 \text{ nm}$, $W = 450 \text{ nm}$, $w = 462 \text{ nm}$
 - 40.102- μm -radius standard ring resonator: $g = 150 \text{ nm}$, $W = 450 \text{ nm}$, $w = 462 \text{ nm}$
- Row 3:
 - 5.096- μm -radius photonic crystal ring resonator: $g = 150 \text{ nm}$, $W = 450 \text{ nm}$, $w = 462 \text{ nm}$, $l = 348 \text{ nm}$, $r = 117 \text{ nm}$
 - 9.970- μm -radius photonic crystal ring resonator: $g = 150 \text{ nm}$, $W = 450 \text{ nm}$, $w = 462 \text{ nm}$, $l = 348 \text{ nm}$, $r = 117 \text{ nm}$
 - 20.162- μm -radius photonic crystal ring resonator: $g = 150 \text{ nm}$, $W = 450 \text{ nm}$, $w = 462 \text{ nm}$, $l = 348 \text{ nm}$, $r = 117 \text{ nm}$

- 30.132- μm -radius photonic crystal ring resonator: $g = 150 \text{ nm}$, $W = 450 \text{ nm}$,
 $w = 462 \text{ nm}$, $l = 348 \text{ nm}$, $r = 117 \text{ nm}$
- 40.102- μm -radius photonic crystal ring resonator: $g = 150 \text{ nm}$, $W = 450 \text{ nm}$,
 $w = 462 \text{ nm}$, $l = 348 \text{ nm}$, $r = 117 \text{ nm}$
- 5.096- μm -radius photonic crystal ring resonator: $g = 150 \text{ nm}$, $W = 450 \text{ nm}$,
 $w = 462 \text{ nm}$, $l = 348 \text{ nm}$, $r = 117 \text{ nm}$
- 9.970- μm -radius photonic crystal ring resonator: $g = 150 \text{ nm}$, $W = 450 \text{ nm}$,
 $w = 462 \text{ nm}$, $l = 348 \text{ nm}$, $r = 117 \text{ nm}$
- 20.162- μm -radius photonic crystal ring resonator: $g = 150 \text{ nm}$, $W = 450 \text{ nm}$,
 $w = 462 \text{ nm}$, $l = 348 \text{ nm}$, $r = 117 \text{ nm}$
- 30.132- μm -radius photonic crystal ring resonator: $g = 150 \text{ nm}$, $W = 450 \text{ nm}$,
 $w = 462 \text{ nm}$, $l = 348 \text{ nm}$, $r = 117 \text{ nm}$
- 40.102- μm -radius photonic crystal ring resonator: $g = 150 \text{ nm}$, $W = 450 \text{ nm}$,
 $w = 462 \text{ nm}$, $l = 348 \text{ nm}$, $r = 117 \text{ nm}$
- Row 4:
 - 5.096- μm -radius standard ring resonator: $g = 150 \text{ nm}$, $W = 450 \text{ nm}$, $w = 462$
 nm
 - 9.970- μm -radius standard ring resonator: $g = 150 \text{ nm}$, $W = 450 \text{ nm}$, $w = 462$
 nm
 - 20.162- μm -radius standard ring resonator: $g = 150 \text{ nm}$, $W = 450 \text{ nm}$, $w = 462$
 nm
 - 30.132- μm -radius standard ring resonator: $g = 150 \text{ nm}$, $W = 450 \text{ nm}$, $w = 462$
 nm
 - 40.102- μm -radius standard ring resonator: $g = 150 \text{ nm}$, $W = 450 \text{ nm}$, $w = 462$
 nm
 - 5.096- μm -radius standard ring resonator: $g = 150 \text{ nm}$, $W = 450 \text{ nm}$, $w = 462$
 nm
 - 9.970- μm -radius standard ring resonator: $g = 150 \text{ nm}$, $W = 450 \text{ nm}$, $w = 462$
 nm
 - 20.162- μm -radius standard ring resonator: $g = 150 \text{ nm}$, $W = 450 \text{ nm}$, $w = 462$
 nm

- 30.132- μm -radius standard ring resonator: $g = 150 \text{ nm}$, $W = 450 \text{ nm}$, $w = 462 \text{ nm}$
- 40.102- μm -radius standard ring resonator: $g = 150 \text{ nm}$, $W = 450 \text{ nm}$, $w = 462 \text{ nm}$
- Row 5:
 - 5.096- μm -radius photonic crystal ring resonator: $g = 150 \text{ nm}$, $W = 450 \text{ nm}$, $w = 462 \text{ nm}$, $l = 348 \text{ nm}$, $r = 123 \text{ nm}$
 - 9.970- μm -radius photonic crystal ring resonator: $g = 150 \text{ nm}$, $W = 450 \text{ nm}$, $w = 462 \text{ nm}$, $l = 348 \text{ nm}$, $r = 123 \text{ nm}$
 - 20.162- μm -radius photonic crystal ring resonator: $g = 150 \text{ nm}$, $W = 450 \text{ nm}$, $w = 462 \text{ nm}$, $l = 348 \text{ nm}$, $r = 123 \text{ nm}$
 - 30.132- μm -radius photonic crystal ring resonator: $g = 150 \text{ nm}$, $W = 450 \text{ nm}$, $w = 462 \text{ nm}$, $l = 348 \text{ nm}$, $r = 123 \text{ nm}$
 - 40.102- μm -radius photonic crystal ring resonator: $g = 150 \text{ nm}$, $W = 450 \text{ nm}$, $w = 462 \text{ nm}$, $l = 348 \text{ nm}$, $r = 123 \text{ nm}$
 - 5.096- μm -radius photonic crystal ring resonator: $g = 150 \text{ nm}$, $W = 450 \text{ nm}$, $w = 462 \text{ nm}$, $l = 348 \text{ nm}$, $r = 123 \text{ nm}$
 - 9.970- μm -radius photonic crystal ring resonator: $g = 150 \text{ nm}$, $W = 450 \text{ nm}$, $w = 462 \text{ nm}$, $l = 348 \text{ nm}$, $r = 123 \text{ nm}$
 - 20.162- μm -radius photonic crystal ring resonator: $g = 150 \text{ nm}$, $W = 450 \text{ nm}$, $w = 462 \text{ nm}$, $l = 348 \text{ nm}$, $r = 123 \text{ nm}$
 - 30.132- μm -radius photonic crystal ring resonator: $g = 150 \text{ nm}$, $W = 450 \text{ nm}$, $w = 462 \text{ nm}$, $l = 348 \text{ nm}$, $r = 123 \text{ nm}$
 - 40.102- μm -radius photonic crystal ring resonator: $g = 150 \text{ nm}$, $W = 450 \text{ nm}$, $w = 462 \text{ nm}$, $l = 348 \text{ nm}$, $r = 123 \text{ nm}$
- Row 6:
 - 5.096- μm -radius standard ring resonator: $g = 150 \text{ nm}$, $W = 450 \text{ nm}$, $w = 462 \text{ nm}$
 - 9.970- μm -radius standard ring resonator: $g = 150 \text{ nm}$, $W = 450 \text{ nm}$, $w = 462 \text{ nm}$

- 20.162- μm -radius standard ring resonator: $g = 150 \text{ nm}$, $W = 450 \text{ nm}$, $w = 462 \text{ nm}$
 - 30.132- μm -radius standard ring resonator: $g = 150 \text{ nm}$, $W = 450 \text{ nm}$, $w = 462 \text{ nm}$
 - 40.102- μm -radius standard ring resonator: $g = 150 \text{ nm}$, $W = 450 \text{ nm}$, $w = 462 \text{ nm}$
 - 5.096- μm -radius standard ring resonator: $g = 150 \text{ nm}$, $W = 450 \text{ nm}$, $w = 462 \text{ nm}$
 - 9.970- μm -radius standard ring resonator: $g = 150 \text{ nm}$, $W = 450 \text{ nm}$, $w = 462 \text{ nm}$
 - 20.162- μm -radius standard ring resonator: $g = 150 \text{ nm}$, $W = 450 \text{ nm}$, $w = 462 \text{ nm}$
 - 30.132- μm -radius standard ring resonator: $g = 150 \text{ nm}$, $W = 450 \text{ nm}$, $w = 462 \text{ nm}$
 - 40.102- μm -radius standard ring resonator: $g = 150 \text{ nm}$, $W = 450 \text{ nm}$, $w = 462 \text{ nm}$
- Row 7:
 - 5.096- μm -radius photonic crystal ring resonator: $g = 150 \text{ nm}$, $W = 450 \text{ nm}$, $w = 462 \text{ nm}$, $l = 348 \text{ nm}$, $r = 115 \text{ nm}$
 - 9.970- μm -radius photonic crystal ring resonator: $g = 150 \text{ nm}$, $W = 450 \text{ nm}$, $w = 462 \text{ nm}$, $l = 348 \text{ nm}$, $r = 115 \text{ nm}$
 - 20.162- μm -radius photonic crystal ring resonator: $g = 150 \text{ nm}$, $W = 450 \text{ nm}$, $w = 462 \text{ nm}$, $l = 348 \text{ nm}$, $r = 115 \text{ nm}$
 - 30.132- μm -radius photonic crystal ring resonator: $g = 150 \text{ nm}$, $W = 450 \text{ nm}$, $w = 462 \text{ nm}$, $l = 348 \text{ nm}$, $r = 115 \text{ nm}$
 - 40.102- μm -radius photonic crystal ring resonator: $g = 150 \text{ nm}$, $W = 450 \text{ nm}$, $w = 462 \text{ nm}$, $l = 348 \text{ nm}$, $r = 115 \text{ nm}$
 - 5.096- μm -radius photonic crystal ring resonator: $g = 150 \text{ nm}$, $W = 450 \text{ nm}$, $w = 462 \text{ nm}$, $l = 348 \text{ nm}$, $r = 115 \text{ nm}$
 - 9.970- μm -radius photonic crystal ring resonator: $g = 150 \text{ nm}$, $W = 450 \text{ nm}$, $w = 462 \text{ nm}$, $l = 348 \text{ nm}$, $r = 115 \text{ nm}$

- 20.162- μm -radius photonic crystal ring resonator: $g = 150 \text{ nm}$, $W = 450 \text{ nm}$,
 $w = 462 \text{ nm}$, $l = 348 \text{ nm}$, $r = 115 \text{ nm}$
 - 30.132- μm -radius photonic crystal ring resonator: $g = 150 \text{ nm}$, $W = 450 \text{ nm}$,
 $w = 462 \text{ nm}$, $l = 348 \text{ nm}$, $r = 115 \text{ nm}$
 - 40.102- μm -radius photonic crystal ring resonator: $g = 150 \text{ nm}$, $W = 450 \text{ nm}$,
 $w = 462 \text{ nm}$, $l = 348 \text{ nm}$, $r = 115 \text{ nm}$
- Row 8:
 - 5.096- μm -radius standard ring resonator: $g = 150 \text{ nm}$, $W = 450 \text{ nm}$, $w = 462$
nm
 - 9.970- μm -radius standard ring resonator: $g = 150 \text{ nm}$, $W = 450 \text{ nm}$, $w = 462$
nm
 - 20.162- μm -radius standard ring resonator: $g = 150 \text{ nm}$, $W = 450 \text{ nm}$, $w = 462$
nm
 - 30.132- μm -radius standard ring resonator: $g = 150 \text{ nm}$, $W = 450 \text{ nm}$, $w = 462$
nm
 - 40.102- μm -radius standard ring resonator: $g = 150 \text{ nm}$, $W = 450 \text{ nm}$, $w = 462$
nm
 - 5.096- μm -radius standard ring resonator: $g = 150 \text{ nm}$, $W = 450 \text{ nm}$, $w = 462$
nm
 - 9.970- μm -radius standard ring resonator: $g = 150 \text{ nm}$, $W = 450 \text{ nm}$, $w = 462$
nm
 - 20.162- μm -radius standard ring resonator: $g = 150 \text{ nm}$, $W = 450 \text{ nm}$, $w = 462$
nm
 - 30.132- μm -radius standard ring resonator: $g = 150 \text{ nm}$, $W = 450 \text{ nm}$, $w = 462$
nm
 - 40.102- μm -radius standard ring resonator: $g = 150 \text{ nm}$, $W = 450 \text{ nm}$, $w = 462$
nm
 - Row 9:
 - 5.096- μm -radius photonic crystal ring resonator: $g = 150 \text{ nm}$, $W = 450 \text{ nm}$,
 $w = 462 \text{ nm}$, $l = 348 \text{ nm}$, $r = 125 \text{ nm}$

- 9.970- μm -radius photonic crystal ring resonator: $g = 150 \text{ nm}$, $W = 450 \text{ nm}$,
 $w = 462 \text{ nm}$, $l = 348 \text{ nm}$, $r = 125 \text{ nm}$
- 20.162- μm -radius photonic crystal ring resonator: $g = 150 \text{ nm}$, $W = 450 \text{ nm}$,
 $w = 462 \text{ nm}$, $l = 348 \text{ nm}$, $r = 125 \text{ nm}$
- 30.132- μm -radius photonic crystal ring resonator: $g = 150 \text{ nm}$, $W = 450 \text{ nm}$,
 $w = 462 \text{ nm}$, $l = 348 \text{ nm}$, $r = 125 \text{ nm}$
- 40.102- μm -radius photonic crystal ring resonator: $g = 150 \text{ nm}$, $W = 450 \text{ nm}$,
 $w = 462 \text{ nm}$, $l = 348 \text{ nm}$, $r = 125 \text{ nm}$
- 5.096- μm -radius photonic crystal ring resonator: $g = 150 \text{ nm}$, $W = 450 \text{ nm}$,
 $w = 462 \text{ nm}$, $l = 348 \text{ nm}$, $r = 125 \text{ nm}$
- 9.970- μm -radius photonic crystal ring resonator: $g = 150 \text{ nm}$, $W = 450 \text{ nm}$,
 $w = 462 \text{ nm}$, $l = 348 \text{ nm}$, $r = 125 \text{ nm}$
- 20.162- μm -radius photonic crystal ring resonator: $g = 150 \text{ nm}$, $W = 450 \text{ nm}$,
 $w = 462 \text{ nm}$, $l = 348 \text{ nm}$, $r = 125 \text{ nm}$
- 30.132- μm -radius photonic crystal ring resonator: $g = 150 \text{ nm}$, $W = 450 \text{ nm}$,
 $w = 462 \text{ nm}$, $l = 348 \text{ nm}$, $r = 125 \text{ nm}$
- 40.102- μm -radius photonic crystal ring resonator: $g = 150 \text{ nm}$, $W = 450 \text{ nm}$,
 $w = 462 \text{ nm}$, $l = 348 \text{ nm}$, $r = 125 \text{ nm}$
- Row 10:
 - 5.096- μm -radius standard ring resonator: $g = 150 \text{ nm}$, $W = 450 \text{ nm}$, $w = 462$
 nm
 - 9.970- μm -radius standard ring resonator: $g = 150 \text{ nm}$, $W = 450 \text{ nm}$, $w = 462$
 nm
 - 20.162- μm -radius standard ring resonator: $g = 150 \text{ nm}$, $W = 450 \text{ nm}$, $w = 462$
 nm
 - 30.132- μm -radius standard ring resonator: $g = 150 \text{ nm}$, $W = 450 \text{ nm}$, $w = 462$
 nm
 - 40.102- μm -radius standard ring resonator: $g = 150 \text{ nm}$, $W = 450 \text{ nm}$, $w = 462$
 nm
 - 5.096- μm -radius standard ring resonator: $g = 150 \text{ nm}$, $W = 450 \text{ nm}$, $w = 462$
 nm

- 9.970- μm -radius standard ring resonator: $g = 150 \text{ nm}$, $W = 450 \text{ nm}$, $w = 462 \text{ nm}$
- 20.162- μm -radius standard ring resonator: $g = 150 \text{ nm}$, $W = 450 \text{ nm}$, $w = 462 \text{ nm}$
- 30.132- μm -radius standard ring resonator: $g = 150 \text{ nm}$, $W = 450 \text{ nm}$, $w = 462 \text{ nm}$
- 40.102- μm -radius standard ring resonator: $g = 150 \text{ nm}$, $W = 450 \text{ nm}$, $w = 462 \text{ nm}$
- Stand-alone rings:
 - I-: 5.096- μm -radius standard ring resonator: $w = 462 \text{ nm}$
 - II-: 5.096- μm -radius photonic crystal ring resonator: $w = 462 \text{ nm}$, $l = 348 \text{ nm}$, $r = 120 \text{ nm}$
 - III-: 5.096- μm -radius photonic crystal ring resonator: $w = 462 \text{ nm}$, $l = 348 \text{ nm}$, $r = 117 \text{ nm}$
 - IIII-: 5.096- μm -radius photonic crystal ring resonator: $w = 462 \text{ nm}$, $l = 348 \text{ nm}$, $r = 123 \text{ nm}$
 - T-: 5.096- μm -radius photonic crystal ring resonator: $w = 462 \text{ nm}$, $l = 348 \text{ nm}$, $r = 115 \text{ nm}$
 - TI-: 5.096- μm -radius photonic crystal ring resonator: $w = 462 \text{ nm}$, $l = 348 \text{ nm}$, $r = 125 \text{ nm}$
 - TII-: 9.970- μm -radius standard ring resonator: $w = 462 \text{ nm}$
 - TIII-: 9.970- μm -radius photonic crystal ring resonator: $w = 462 \text{ nm}$, $l = 348 \text{ nm}$, $r = 120 \text{ nm}$
 - IX-: 9.970- μm -radius photonic crystal ring resonator: $w = 462 \text{ nm}$, $l = 348 \text{ nm}$, $r = 117 \text{ nm}$
 - X-: 9.970- μm -radius photonic crystal ring resonator: $w = 462 \text{ nm}$, $l = 348 \text{ nm}$, $r = 123 \text{ nm}$
 - XI-: 9.970- μm -radius photonic crystal ring resonator: $w = 462 \text{ nm}$, $l = 348 \text{ nm}$, $r = 115 \text{ nm}$
 - XII-: 9.970- μm -radius photonic crystal ring resonator: $w = 462 \text{ nm}$, $l = 348 \text{ nm}$, $r = 125 \text{ nm}$

- XIII-: 20.162- μm -radius standard ring resonator: $w = 462$ nm
- XIT-: 20.162- μm -radius photonic crystal ring resonator: $w = 462$ nm, $l = 348$ nm, $r = 120$ nm
- XT-: 20.162- μm -radius photonic crystal ring resonator: $w = 462$ nm, $l = 348$ nm, $r = 117$ nm
- XTI-: 20.162- μm -radius photonic crystal ring resonator: $w = 462$ nm, $l = 348$ nm, $r = 123$ nm
- XTII-: 20.162- μm -radius photonic crystal ring resonator: $w = 462$ nm, $l = 348$ nm, $r = 115$ nm
- XTIII-: 20.162- μm -radius photonic crystal ring resonator: $w = 462$ nm, $l = 348$ nm, $r = 125$ nm
- XIX-: 30.132- μm -radius standard ring resonator: $w = 462$ nm
- XX-: 30.132- μm -radius photonic crystal ring resonator: $w = 462$ nm, $l = 348$ nm, $r = 120$ nm
- XXI-: 30.132- μm -radius photonic crystal ring resonator: $w = 462$ nm, $l = 348$ nm, $r = 117$ nm
- XXII-: 30.132- μm -radius photonic crystal ring resonator: $w = 462$ nm, $l = 348$ nm, $r = 123$ nm
- XXIII-: 30.132- μm -radius photonic crystal ring resonator: $w = 462$ nm, $l = 348$ nm, $r = 115$ nm
- XXIT-: 30.132- μm -radius photonic crystal ring resonator: $w = 462$ nm, $l = 348$ nm, $r = 125$ nm
- XXT-: 40.102- μm -radius standard ring resonator: $w = 462$ nm
- XXTI-: 40.102- μm -radius photonic crystal ring resonator: $w = 462$ nm, $l = 348$ nm, $r = 120$ nm
- XXTII-: 40.102- μm -radius photonic crystal ring resonator: $w = 462$ nm, $l = 348$ nm, $r = 117$ nm
- XXTIII-: 40.102- μm -radius photonic crystal ring resonator: $w = 462$ nm, $l = 348$ nm, $r = 123$ nm
- XXIX-: 40.102- μm -radius photonic crystal ring resonator: $w = 462$ nm, $l = 348$ nm, $r = 115$ nm

- XXX-: 40.102- μm -radius photonic crystal ring resonator: $w = 462 \text{ nm}$, $l = 348 \text{ nm}$, $r = 125 \text{ nm}$

Appendix D

Dimerized photonic crystal rings GDS library

The GDS files for the dimerized photonic crystal ring resonators discussed in Chapter 5 can be found [here](#). Additionally, spatially modulated optical ring resonators are included in the layout. The GDS file contains the following devices:

- Row 1:
 - 20- μm -radius standard ring resonator: $g = 200 \text{ nm}$, $W = 700 \text{ nm}$, $w = 1.0 \mu\text{m}$
 - 20- μm -radius ring resonator: $g = 200 \text{ nm}$, $W = 700 \text{ nm}$, $w = 1.0 \mu\text{m}$, $\kappa_{126} = 70 \text{ nm}$
 - 20- μm -radius ring resonator: $g = 200 \text{ nm}$, $W = 700 \text{ nm}$, $w = 1.0 \mu\text{m}$, $\kappa_{126} = 80 \text{ nm}$
 - 20- μm -radius ring resonator: $g = 200 \text{ nm}$, $W = 700 \text{ nm}$, $w = 1.0 \mu\text{m}$, $\kappa_{126} = 90 \text{ nm}$
 - 20- μm -radius standard ring resonator: $g = 175 \text{ nm}$, $W = 700 \text{ nm}$, $w = 1.0 \mu\text{m}$
 - 20- μm -radius ring resonator: $g = 175 \text{ nm}$, $W = 700 \text{ nm}$, $w = 1.0 \mu\text{m}$, $\kappa_{126} = 70 \text{ nm}$
 - 20- μm -radius ring resonator: $g = 175 \text{ nm}$, $W = 700 \text{ nm}$, $w = 1.0 \mu\text{m}$, $\kappa_{126} = 80 \text{ nm}$
 - 20- μm -radius ring resonator: $g = 175 \text{ nm}$, $W = 700 \text{ nm}$, $w = 1.0 \mu\text{m}$, $\kappa_{126} = 90 \text{ nm}$
 - 20- μm -radius standard ring resonator: $g = 150 \text{ nm}$, $W = 700 \text{ nm}$, $w = 1.0 \mu\text{m}$

- 20- μm -radius ring resonator: $g = 175 \text{ nm}$, $W = 700 \text{ nm}$, $w = 1.0 \mu\text{m}$, $\kappa_{127} = 80 \text{ nm}$
 - 20- μm -radius ring resonator: $g = 175 \text{ nm}$, $W = 700 \text{ nm}$, $w = 1.0 \mu\text{m}$, $\kappa_{127} = 90 \text{ nm}$
 - 20- μm -radius ring resonator: $g = 150 \text{ nm}$, $W = 700 \text{ nm}$, $w = 1.0 \mu\text{m}$, $\kappa_{127} = 70 \text{ nm}$
 - 20- μm -radius ring resonator: $g = 150 \text{ nm}$, $W = 700 \text{ nm}$, $w = 1.0 \mu\text{m}$, $\kappa_{127} = 80 \text{ nm}$
 - 20- μm -radius ring resonator: $g = 150 \text{ nm}$, $W = 700 \text{ nm}$, $w = 1.0 \mu\text{m}$, $\kappa_{127} = 90 \text{ nm}$
- Row 2:
- 20- μm -radius ring resonator: $g = 200 \text{ nm}$, $W = 700 \text{ nm}$, $w = 1.0 \mu\text{m}$, $\kappa_{125} = 70 \text{ nm}$, $\kappa_{126} = 70 \text{ nm}$
 - 20- μm -radius ring resonator: $g = 175 \text{ nm}$, $W = 700 \text{ nm}$, $w = 1.0 \mu\text{m}$, $\kappa_{125} = 70 \text{ nm}$, $\kappa_{126} = 70 \text{ nm}$
 - 20- μm -radius ring resonator: $g = 150 \text{ nm}$, $W = 700 \text{ nm}$, $w = 1.0 \mu\text{m}$, $\kappa_{125} = 70 \text{ nm}$, $\kappa_{126} = 70 \text{ nm}$
 - 20- μm -radius ring resonator: $g = 200 \text{ nm}$, $W = 700 \text{ nm}$, $w = 1.0 \mu\text{m}$, $\kappa_{125} = 80 \text{ nm}$, $\kappa_{126} = 80 \text{ nm}$
 - 20- μm -radius ring resonator: $g = 175 \text{ nm}$, $W = 700 \text{ nm}$, $w = 1.0 \mu\text{m}$, $\kappa_{125} = 80 \text{ nm}$, $\kappa_{126} = 80 \text{ nm}$
 - 20- μm -radius ring resonator: $g = 150 \text{ nm}$, $W = 700 \text{ nm}$, $w = 1.0 \mu\text{m}$, $\kappa_{125} = 80 \text{ nm}$, $\kappa_{126} = 80 \text{ nm}$
 - 20- μm -radius ring resonator: $g = 200 \text{ nm}$, $W = 700 \text{ nm}$, $w = 1.0 \mu\text{m}$, $\kappa_{125} = 90 \text{ nm}$, $\kappa_{126} = 90 \text{ nm}$
 - 20- μm -radius ring resonator: $g = 175 \text{ nm}$, $W = 700 \text{ nm}$, $w = 1.0 \mu\text{m}$, $\kappa_{125} = 90 \text{ nm}$, $\kappa_{126} = 90 \text{ nm}$
 - 20- μm -radius ring resonator: $g = 150 \text{ nm}$, $W = 700 \text{ nm}$, $w = 1.0 \mu\text{m}$, $\kappa_{125} = 90 \text{ nm}$, $\kappa_{126} = 90 \text{ nm}$
 - 20- μm -radius ring resonator: $g = 200 \text{ nm}$, $W = 700 \text{ nm}$, $w = 1.0 \mu\text{m}$, $\kappa_{126} = 70 \text{ nm}$, $\kappa_{127} = 70 \text{ nm}$

- 20- μm -radius ring resonator: $g = 150 \text{ nm}$, $W = 700 \text{ nm}$, $w = 1.0 \mu\text{m}$, $\kappa_{124} = 90 \text{ nm}$, $\kappa_{125} = 90 \text{ nm}$
 - 20- μm -radius standard ring resonator: $g = 200 \text{ nm}$, $W = 700 \text{ nm}$, $w = 1.0 \mu\text{m}$
 - 20- μm -radius standard ring resonator: $g = 175 \text{ nm}$, $W = 700 \text{ nm}$, $w = 1.0 \mu\text{m}$
 - 20- μm -radius standard ring resonator: $g = 150 \text{ nm}$, $W = 700 \text{ nm}$, $w = 1.0 \mu\text{m}$
- Row 3:
- 20- μm -radius standard ring resonator: $g = 200 \text{ nm}$, $W = 600 \text{ nm}$, $w = 1.0 \mu\text{m}$
 - 20- μm -radius ring resonator: $g = 200 \text{ nm}$, $W = 600 \text{ nm}$, $w = 1.0 \mu\text{m}$, $\kappa_{126} = 70 \text{ nm}$
 - 20- μm -radius ring resonator: $g = 200 \text{ nm}$, $W = 600 \text{ nm}$, $w = 1.0 \mu\text{m}$, $\kappa_{126} = 80 \text{ nm}$
 - 20- μm -radius ring resonator: $g = 200 \text{ nm}$, $W = 600 \text{ nm}$, $w = 1.0 \mu\text{m}$, $\kappa_{126} = 90 \text{ nm}$
 - 20- μm -radius standard ring resonator: $g = 175 \text{ nm}$, $W = 600 \text{ nm}$, $w = 1.0 \mu\text{m}$
 - 20- μm -radius ring resonator: $g = 175 \text{ nm}$, $W = 600 \text{ nm}$, $w = 1.0 \mu\text{m}$, $\kappa_{126} = 70 \text{ nm}$
 - 20- μm -radius ring resonator: $g = 175 \text{ nm}$, $W = 600 \text{ nm}$, $w = 1.0 \mu\text{m}$, $\kappa_{126} = 80 \text{ nm}$
 - 20- μm -radius ring resonator: $g = 175 \text{ nm}$, $W = 600 \text{ nm}$, $w = 1.0 \mu\text{m}$, $\kappa_{126} = 90 \text{ nm}$
 - 20- μm -radius standard ring resonator: $g = 150 \text{ nm}$, $W = 600 \text{ nm}$, $w = 1.0 \mu\text{m}$
 - 20- μm -radius ring resonator: $g = 150 \text{ nm}$, $W = 600 \text{ nm}$, $w = 1.0 \mu\text{m}$, $\kappa_{126} = 70 \text{ nm}$
 - 20- μm -radius ring resonator: $g = 150 \text{ nm}$, $W = 600 \text{ nm}$, $w = 1.0 \mu\text{m}$, $\kappa_{126} = 80 \text{ nm}$
 - 20- μm -radius ring resonator: $g = 150 \text{ nm}$, $W = 600 \text{ nm}$, $w = 1.0 \mu\text{m}$, $\kappa_{126} = 90 \text{ nm}$
 - 20- μm -radius ring resonator: $g = 200 \text{ nm}$, $W = 600 \text{ nm}$, $w = 1.0 \mu\text{m}$, $\kappa_{125} = 70 \text{ nm}$
 - 20- μm -radius ring resonator: $g = 200 \text{ nm}$, $W = 600 \text{ nm}$, $w = 1.0 \mu\text{m}$, $\kappa_{125} = 80 \text{ nm}$

- 20- μm -radius ring resonator: $g = 200 \text{ nm}$, $W = 600 \text{ nm}$, $w = 1.0 \mu\text{m}$, $\kappa_{125} = 90 \text{ nm}$
- 20- μm -radius ring resonator: $g = 175 \text{ nm}$, $W = 600 \text{ nm}$, $w = 1.0 \mu\text{m}$, $\kappa_{125} = 70 \text{ nm}$
- 20- μm -radius ring resonator: $g = 175 \text{ nm}$, $W = 600 \text{ nm}$, $w = 1.0 \mu\text{m}$, $\kappa_{125} = 80 \text{ nm}$
- 20- μm -radius ring resonator: $g = 175 \text{ nm}$, $W = 600 \text{ nm}$, $w = 1.0 \mu\text{m}$, $\kappa_{125} = 90 \text{ nm}$
- 20- μm -radius ring resonator: $g = 150 \text{ nm}$, $W = 600 \text{ nm}$, $w = 1.0 \mu\text{m}$, $\kappa_{125} = 70 \text{ nm}$
- 20- μm -radius ring resonator: $g = 150 \text{ nm}$, $W = 600 \text{ nm}$, $w = 1.0 \mu\text{m}$, $\kappa_{125} = 80 \text{ nm}$
- 20- μm -radius ring resonator: $g = 150 \text{ nm}$, $W = 600 \text{ nm}$, $w = 1.0 \mu\text{m}$, $\kappa_{125} = 90 \text{ nm}$
- 20- μm -radius ring resonator: $g = 200 \text{ nm}$, $W = 600 \text{ nm}$, $w = 1.0 \mu\text{m}$, $\kappa_{127} = 70 \text{ nm}$
- 20- μm -radius ring resonator: $g = 200 \text{ nm}$, $W = 600 \text{ nm}$, $w = 1.0 \mu\text{m}$, $\kappa_{127} = 80 \text{ nm}$
- 20- μm -radius ring resonator: $g = 200 \text{ nm}$, $W = 600 \text{ nm}$, $w = 1.0 \mu\text{m}$, $\kappa_{127} = 90 \text{ nm}$
- 20- μm -radius ring resonator: $g = 175 \text{ nm}$, $W = 600 \text{ nm}$, $w = 1.0 \mu\text{m}$, $\kappa_{127} = 70 \text{ nm}$
- 20- μm -radius ring resonator: $g = 175 \text{ nm}$, $W = 600 \text{ nm}$, $w = 1.0 \mu\text{m}$, $\kappa_{127} = 80 \text{ nm}$
- 20- μm -radius ring resonator: $g = 175 \text{ nm}$, $W = 600 \text{ nm}$, $w = 1.0 \mu\text{m}$, $\kappa_{127} = 90 \text{ nm}$
- 20- μm -radius ring resonator: $g = 150 \text{ nm}$, $W = 600 \text{ nm}$, $w = 1.0 \mu\text{m}$, $\kappa_{127} = 70 \text{ nm}$
- 20- μm -radius ring resonator: $g = 150 \text{ nm}$, $W = 600 \text{ nm}$, $w = 1.0 \mu\text{m}$, $\kappa_{127} = 80 \text{ nm}$
- 20- μm -radius ring resonator: $g = 150 \text{ nm}$, $W = 600 \text{ nm}$, $w = 1.0 \mu\text{m}$, $\kappa_{127} = 90 \text{ nm}$

- 20- μm -radius ring resonator: $g = 200 \text{ nm}$, $W = 600 \text{ nm}$, $w = 1.0 \mu\text{m}$, $\kappa_{126} = 90 \text{ nm}$, $\kappa_{127} = 90 \text{ nm}$
- 20- μm -radius ring resonator: $g = 175 \text{ nm}$, $W = 600 \text{ nm}$, $w = 1.0 \mu\text{m}$, $\kappa_{126} = 90 \text{ nm}$, $\kappa_{127} = 90 \text{ nm}$
- 20- μm -radius ring resonator: $g = 150 \text{ nm}$, $W = 600 \text{ nm}$, $w = 1.0 \mu\text{m}$, $\kappa_{126} = 90 \text{ nm}$, $\kappa_{127} = 90 \text{ nm}$
- 20- μm -radius ring resonator: $g = 200 \text{ nm}$, $W = 600 \text{ nm}$, $w = 1.0 \mu\text{m}$, $\kappa_{124} = 70 \text{ nm}$, $\kappa_{125} = 70 \text{ nm}$
- 20- μm -radius ring resonator: $g = 175 \text{ nm}$, $W = 600 \text{ nm}$, $w = 1.0 \mu\text{m}$, $\kappa_{124} = 70 \text{ nm}$, $\kappa_{125} = 70 \text{ nm}$
- 20- μm -radius ring resonator: $g = 150 \text{ nm}$, $W = 600 \text{ nm}$, $w = 1.0 \mu\text{m}$, $\kappa_{124} = 70 \text{ nm}$, $\kappa_{125} = 70 \text{ nm}$
- 20- μm -radius ring resonator: $g = 200 \text{ nm}$, $W = 600 \text{ nm}$, $w = 1.0 \mu\text{m}$, $\kappa_{124} = 80 \text{ nm}$, $\kappa_{125} = 80 \text{ nm}$
- 20- μm -radius ring resonator: $g = 175 \text{ nm}$, $W = 600 \text{ nm}$, $w = 1.0 \mu\text{m}$, $\kappa_{124} = 80 \text{ nm}$, $\kappa_{125} = 80 \text{ nm}$
- 20- μm -radius ring resonator: $g = 150 \text{ nm}$, $W = 600 \text{ nm}$, $w = 1.0 \mu\text{m}$, $\kappa_{124} = 80 \text{ nm}$, $\kappa_{125} = 80 \text{ nm}$
- 20- μm -radius ring resonator: $g = 200 \text{ nm}$, $W = 600 \text{ nm}$, $w = 1.0 \mu\text{m}$, $\kappa_{124} = 90 \text{ nm}$, $\kappa_{125} = 90 \text{ nm}$
- 20- μm -radius ring resonator: $g = 175 \text{ nm}$, $W = 600 \text{ nm}$, $w = 1.0 \mu\text{m}$, $\kappa_{124} = 90 \text{ nm}$, $\kappa_{125} = 90 \text{ nm}$
- 20- μm -radius ring resonator: $g = 150 \text{ nm}$, $W = 600 \text{ nm}$, $w = 1.0 \mu\text{m}$, $\kappa_{124} = 90 \text{ nm}$, $\kappa_{125} = 90 \text{ nm}$
- 20- μm -radius standard ring resonator: $g = 200 \text{ nm}$, $W = 600 \text{ nm}$, $w = 1.0 \mu\text{m}$
- 20- μm -radius standard ring resonator: $g = 175 \text{ nm}$, $W = 600 \text{ nm}$, $w = 1.0 \mu\text{m}$
- 20- μm -radius standard ring resonator: $g = 150 \text{ nm}$, $W = 600 \text{ nm}$, $w = 1.0 \mu\text{m}$

- Row 5:

- 19.745- μm -radius photonic crystal ring resonator: $g = 120 \text{ nm}$, $W = 400 \text{ nm}$, $w = 465 \text{ nm}$, $a = 326 \text{ nm}$, $f = 0.22a$

- 21.008- μm -radius dimerized photonic crystal ring resonator: $g = 120 \text{ nm}$, $W = 430 \text{ nm}$, $w = 495 \text{ nm}$, $a = 330 \text{ nm}$, $f = 0.24a$, $dd = 0.1a$
 - 18.398- μm -radius photonic crystal ring resonator: $g = 120 \text{ nm}$, $W = 400 \text{ nm}$, $w = 434 \text{ nm}$, $a = 300 \text{ nm}$, $f = 0.23a$
 - 18.398- μm -radius dimerized photonic crystal ring resonator: $g = 120 \text{ nm}$, $W = 400 \text{ nm}$, $w = 434 \text{ nm}$, $a = 300 \text{ nm}$, $f = 0.23a$, $dd = 0.02a$
 - 18.398- μm -radius dimerized photonic crystal ring resonator: $g = 120 \text{ nm}$, $W = 400 \text{ nm}$, $w = 434 \text{ nm}$, $a = 300 \text{ nm}$, $f = 0.23a$, $dd = 0.04a$
 - 18.398- μm -radius dimerized photonic crystal ring resonator: $g = 120 \text{ nm}$, $W = 400 \text{ nm}$, $w = 434 \text{ nm}$, $a = 300 \text{ nm}$, $f = 0.23a$, $dd = 0.06a$
 - 18.398- μm -radius dimerized photonic crystal ring resonator: $g = 120 \text{ nm}$, $W = 400 \text{ nm}$, $w = 434 \text{ nm}$, $a = 300 \text{ nm}$, $f = 0.23a$, $dd = 0.08a$
 - 18.398- μm -radius dimerized photonic crystal ring resonator: $g = 120 \text{ nm}$, $W = 400 \text{ nm}$, $w = 434 \text{ nm}$, $a = 300 \text{ nm}$, $f = 0.23a$, $dd = 0.1a$
 - 21.008- μm -radius photonic crystal ring resonator: $g = 150 \text{ nm}$, $W = 430 \text{ nm}$, $w = 495 \text{ nm}$, $a = 330 \text{ nm}$, $f = 0.24a$
 - 21.008- μm -radius dimerized photonic crystal ring resonator: $g = 150 \text{ nm}$, $W = 430 \text{ nm}$, $w = 495 \text{ nm}$, $a = 330 \text{ nm}$, $f = 0.24a$, $dd = 0.05a$
 - 21.008- μm -radius dimerized photonic crystal ring resonator: $g = 150 \text{ nm}$, $W = 430 \text{ nm}$, $w = 495 \text{ nm}$, $a = 330 \text{ nm}$, $f = 0.24a$, $dd = 0.1a$
 - 18.398- μm -radius photonic crystal ring resonator: $g = 150 \text{ nm}$, $W = 400 \text{ nm}$, $w = 434 \text{ nm}$, $a = 300 \text{ nm}$, $f = 0.23a$
 - 18.398- μm -radius dimerized photonic crystal ring resonator: $g = 150 \text{ nm}$, $W = 400 \text{ nm}$, $w = 434 \text{ nm}$, $a = 300 \text{ nm}$, $f = 0.23a$, $dd = 0.05a$
 - 18.398- μm -radius dimerized photonic crystal ring resonator: $g = 150 \text{ nm}$, $W = 400 \text{ nm}$, $w = 434 \text{ nm}$, $a = 300 \text{ nm}$, $f = 0.23a$, $dd = 0.1a$
- Row 6:
- 29.603- μm -radius photonic crystal ring resonator: $g = 120 \text{ nm}$, $W = 400 \text{ nm}$, $w = 465 \text{ nm}$, $a = 326 \text{ nm}$, $f = 0.22a$
 - 29.603- μm -radius photonic crystal ring resonator: $g = 120 \text{ nm}$, $W = 400 \text{ nm}$, $w = 465 \text{ nm}$, $a = 326 \text{ nm}$, $f = 0.22a$, $dd = 0.02a$

- 29.603- μm -radius photonic crystal ring resonator: $g = 150 \text{ nm}$, $W = 400 \text{ nm}$, $w = 465 \text{ nm}$, $a = 326 \text{ nm}$, $f = 0.22a$
- 29.603- μm -radius photonic crystal ring resonator: $g = 150 \text{ nm}$, $W = 400 \text{ nm}$, $w = 465 \text{ nm}$, $a = 326 \text{ nm}$, $f = 0.22a$, $dd = 0.02a$
- 29.603- μm -radius photonic crystal ring resonator: $g = 150 \text{ nm}$, $W = 400 \text{ nm}$, $w = 465 \text{ nm}$, $a = 326 \text{ nm}$, $f = 0.22a$, $dd = 0.04a$
- 29.603- μm -radius photonic crystal ring resonator: $g = 150 \text{ nm}$, $W = 400 \text{ nm}$, $w = 465 \text{ nm}$, $a = 326 \text{ nm}$, $f = 0.22a$, $dd = 0.06a$
- 29.603- μm -radius photonic crystal ring resonator: $g = 150 \text{ nm}$, $W = 400 \text{ nm}$, $w = 465 \text{ nm}$, $a = 326 \text{ nm}$, $f = 0.22a$, $dd = 0.08a$
- 29.603- μm -radius photonic crystal ring resonator: $g = 150 \text{ nm}$, $W = 400 \text{ nm}$, $w = 465 \text{ nm}$, $a = 326 \text{ nm}$, $f = 0.22a$, $dd = 0.1a$
- 31.513- μm -radius dimerized photonic crystal ring resonator: $g = 150 \text{ nm}$, $W = 430 \text{ nm}$, $w = 495 \text{ nm}$, $a = 330 \text{ nm}$, $f = 0.24a$
- 31.513- μm -radius dimerized photonic crystal ring resonator: $g = 150 \text{ nm}$, $W = 430 \text{ nm}$, $w = 495 \text{ nm}$, $a = 330 \text{ nm}$, $f = 0.24a$, $dd = 0.05a$
- 31.513- μm -radius dimerized photonic crystal ring resonator: $g = 150 \text{ nm}$, $W = 430 \text{ nm}$, $w = 495 \text{ nm}$, $a = 330 \text{ nm}$, $f = 0.24a$, $dd = 0.1a$
- 27.597- μm -radius photonic crystal ring resonator: $g = 150 \text{ nm}$, $W = 400 \text{ nm}$, $w = 434 \text{ nm}$, $a = 300 \text{ nm}$, $f = 0.23a$
- 27.597- μm -radius photonic crystal ring resonator: $g = 150 \text{ nm}$, $W = 400 \text{ nm}$, $w = 434 \text{ nm}$, $a = 300 \text{ nm}$, $f = 0.23a$, $dd = 0.05a$
- 27.597- μm -radius photonic crystal ring resonator: $g = 150 \text{ nm}$, $W = 400 \text{ nm}$, $w = 434 \text{ nm}$, $a = 300 \text{ nm}$, $f = 0.23a$, $dd = 0.1a$

• Row 7:

- 19.745- μm -radius dimerized PhCRR with topological cavities, $g = 120 \text{ nm}$, $W = 400 \text{ nm}$, $w = 465 \text{ nm}$, $a = 326 \text{ nm}$, $f = 0.22a$, $dd = 0.1a$, $reduc = 0$
- 19.745- μm -radius dimerized PhCRR with topological cavities, $g = 150 \text{ nm}$, $W = 400 \text{ nm}$, $w = 465 \text{ nm}$, $a = 326 \text{ nm}$, $f = 0.22a$, $dd = 0.1a$, $reduc = 0$
- 21.008- μm -radius dimerized PhCRR with topological cavities: $g = 120 \text{ nm}$, $W = 430 \text{ nm}$, $w = 495 \text{ nm}$, $a = 330 \text{ nm}$, $f = 0.24a$, $dd = 0.1a$, $reduc = 0$

- 21.008- μm -radius dimerized PhCRR with topological cavities: $g = 150 \text{ nm}$, $W = 430 \text{ nm}$, $w = 495 \text{ nm}$, $a = 330 \text{ nm}$, $f = 0.24a$, $dd = 0.1a$, $reduc = 0$
- 18.398- μm -radius dimerized PhCRR with topological cavities: $g = 120 \text{ nm}$, $W = 400 \text{ nm}$, $w = 434 \text{ nm}$, $a = 300 \text{ nm}$, $f = 0.23a$, $dd = 0.1a$, $reduc = 0$
- 18.398- μm -radius dimerized PhCRR with topological cavities: $g = 150 \text{ nm}$, $W = 400 \text{ nm}$, $w = 434 \text{ nm}$, $a = 300 \text{ nm}$, $f = 0.23a$, $dd = 0.1a$, $reduc = 0$
- 29.603- μm -radius dimerized PhCRR with topological cavities: $g = 120 \text{ nm}$, $W = 400 \text{ nm}$, $w = 465 \text{ nm}$, $a = 326 \text{ nm}$, $f = 0.22a$, $dd = 0.1a$, $reduc = 0$
- 29.603- μm -radius dimerized PhCRR with topological cavities: $g = 150 \text{ nm}$, $W = 400 \text{ nm}$, $w = 465 \text{ nm}$, $a = 326 \text{ nm}$, $f = 0.22a$, $dd = 0.1a$, $reduc = 0$
- 31.513- μm -radius dimerized PhCRR with topological cavities: $g = 120 \text{ nm}$, $W = 430 \text{ nm}$, $w = 495 \text{ nm}$, $a = 330 \text{ nm}$, $f = 0.24a$, $dd = 0.1a$, $reduc = 0$
- 31.513- μm -radius dimerized PhCRR with topological cavities: $g = 150 \text{ nm}$, $W = 430 \text{ nm}$, $w = 495 \text{ nm}$, $a = 330 \text{ nm}$, $f = 0.24a$, $dd = 0.1a$, $reduc = 0$
- 27.597- μm -radius dimerized PhCRR with topological cavities: $g = 120 \text{ nm}$, $W = 400 \text{ nm}$, $w = 434 \text{ nm}$, $a = 300 \text{ nm}$, $f = 0.23a$, $dd = 0.1a$, $reduc = 0$
- 39.470- μm -radius dimerized PhCRR with topological cavities: $g = 120 \text{ nm}$, $W = 400 \text{ nm}$, $w = 465 \text{ nm}$, $a = 326 \text{ nm}$, $f = 0.22a$, $dd = 0.1a$, $reduc = 0$
- 39.470- μm -radius dimerized PhCRR with topological cavities: $g = 150 \text{ nm}$, $W = 400 \text{ nm}$, $w = 465 \text{ nm}$, $a = 326 \text{ nm}$, $f = 0.22a$, $dd = 0.1a$, $reduc = 0$
- 42.017- μm -radius dimerized PhCRR with topological cavities: $g = 120 \text{ nm}$, $W = 430 \text{ nm}$, $w = 495 \text{ nm}$, $a = 330 \text{ nm}$, $f = 0.24a$, $dd = 0.1a$, $reduc = 0$
- 42.017- μm -radius dimerized PhCRR with topological cavities: $g = 150 \text{ nm}$, $W = 430 \text{ nm}$, $w = 495 \text{ nm}$, $a = 330 \text{ nm}$, $f = 0.24a$, $dd = 0.1a$, $reduc = 0$
- 36.797- μm -radius dimerized PhCRR with topological cavities: $g = 120 \text{ nm}$, $W = 400 \text{ nm}$, $w = 434 \text{ nm}$, $a = 300 \text{ nm}$, $f = 0.23a$, $dd = 0.1a$, $reduc = 0$
- 36.797- μm -radius dimerized PhCRR with topological cavities: $g = 150 \text{ nm}$, $W = 400 \text{ nm}$, $w = 434 \text{ nm}$, $a = 300 \text{ nm}$, $f = 0.23a$, $dd = 0.1a$, $reduc = 0$

• Row 8:

- 19.745- μm -radius dimerized PhCRR with trivial cavities: $g = 120 \text{ nm}$, $W = 400 \text{ nm}$, $w = 465 \text{ nm}$, $a = 326 \text{ nm}$, $f = 0.22a$, $dd = 0.1a$, $defect = 0.25a$

- 36.797- μm -radius dimerized PhCRR with trivial cavities: $g = 150 \text{ nm}$, $W = 400 \text{ nm}$, $w = 434 \text{ nm}$, $a = 300 \text{ nm}$, $f = 0.23a$, $dd = 0.1a$, $defect = 0.25a$
- Row 9:
 - 19.745- μm -radius dimerized PhCRR with topological cavities - homodyne coupler: $g = 120 \text{ nm}$, $W = 400 \text{ nm}$, $w = 465 \text{ nm}$, $a = 326 \text{ nm}$, $f = 0.22a$, $dd = 0.1a$, $reduc = 0$
 - 19.745- μm -radius dimerized PhCRR with topological cavities - homodyne coupler: $g = 150 \text{ nm}$, $W = 400 \text{ nm}$, $w = 465 \text{ nm}$, $a = 326 \text{ nm}$, $f = 0.22a$, $dd = 0.1a$, $reduc = 0$
 - 21.008- μm -radius dimerized PhCRR with topological cavities - homodyne coupler: $g = 120 \text{ nm}$, $W = 430 \text{ nm}$, $w = 495 \text{ nm}$, $a = 330 \text{ nm}$, $f = 0.24a$, $dd = 0.1a$, $reduc = 0$
 - 21.008- μm -radius dimerized PhCRR with topological cavities - homodyne coupler: $g = 150 \text{ nm}$, $W = 430 \text{ nm}$, $w = 495 \text{ nm}$, $a = 330 \text{ nm}$, $f = 0.24a$, $dd = 0.1a$, $reduc = 0$
 - 18.398- μm -radius dimerized PhCRR with topological cavities - homodyne coupler: $g = 120 \text{ nm}$, $W = 400 \text{ nm}$, $w = 434 \text{ nm}$, $a = 300 \text{ nm}$, $f = 0.23a$, $dd = 0.1a$, $reduc = 0$
 - 18.398- μm -radius dimerized PhCRR with topological cavities - homodyne coupler: $g = 150 \text{ nm}$, $W = 400 \text{ nm}$, $w = 434 \text{ nm}$, $a = 300 \text{ nm}$, $f = 0.23a$, $dd = 0.1a$, $reduc = 0$
 - 29.603- μm -radius dimerized PhCRR with topological cavities - homodyne coupler: $g = 120 \text{ nm}$, $W = 400 \text{ nm}$, $w = 465 \text{ nm}$, $a = 326 \text{ nm}$, $f = 0.22a$, $dd = 0.1a$, $reduc = 0$
 - 29.603- μm -radius dimerized PhCRR with topological cavities - homodyne coupler: $g = 150 \text{ nm}$, $W = 400 \text{ nm}$, $w = 465 \text{ nm}$, $a = 326 \text{ nm}$, $f = 0.22a$, $dd = 0.1a$, $reduc = 0$
 - 31.513- μm -radius dimerized PhCRR with topological cavities - homodyne coupler: $g = 120 \text{ nm}$, $W = 430 \text{ nm}$, $w = 495 \text{ nm}$, $a = 330 \text{ nm}$, $f = 0.24a$, $dd = 0.1a$, $reduc = 0$
 - 31.513- μm -radius dimerized PhCRR with topological cavities - homodyne coupler: $g = 150 \text{ nm}$, $W = 430 \text{ nm}$, $w = 495 \text{ nm}$, $a = 330 \text{ nm}$, $f = 0.24a$, $dd = 0.1a$, $reduc = 0$

- 27.597- μm -radius dimerized PhCRR with topological cavities - homodyne coupler: $g = 120 \text{ nm}$, $W = 400 \text{ nm}$, $w = 434 \text{ nm}$, $a = 300 \text{ nm}$, $f = 0.23a$, $dd = 0.1a$, $reduc = 0$
- 27.597- μm -radius dimerized PhCRR with topological cavities - homodyne coupler: $g = 150 \text{ nm}$, $W = 400 \text{ nm}$, $w = 434 \text{ nm}$, $a = 300 \text{ nm}$, $f = 0.23a$, $dd = 0.1a$, $reduc = 0$
- 39.470- μm -radius dimerized PhCRR with topological cavities - homodyne coupler: $g = 120 \text{ nm}$, $W = 400 \text{ nm}$, $w = 465 \text{ nm}$, $a = 326 \text{ nm}$, $f = 0.22a$, $dd = 0.1a$, $reduc = 0$
- 42.017- μm -radius dimerized PhCRR with topological cavities - homodyne coupler: $g = 120 \text{ nm}$, $W = 430 \text{ nm}$, $w = 495 \text{ nm}$, $a = 330 \text{ nm}$, $f = 0.24a$, $dd = 0.1a$, $reduc = 0$
- 36.797- μm -radius dimerized PhCRR with topological cavities - homodyne coupler: $g = 120 \text{ nm}$, $W = 400 \text{ nm}$, $w = 434 \text{ nm}$, $a = 300 \text{ nm}$, $f = 0.23a$, $dd = 0.1a$, $reduc = 0$
- Row 10:
 - 19.745- μm -radius dimerized PhCRR with trivial cavities - homodyne coupler: $g = 120 \text{ nm}$, $W = 400 \text{ nm}$, $w = 465 \text{ nm}$, $a = 326 \text{ nm}$, $f = 0.22a$, $dd = 0.1a$, $defect = 0.25a$
 - 19.745- μm -radius dimerized PhCRR with trivial cavities - homodyne coupler: $g = 150 \text{ nm}$, $W = 400 \text{ nm}$, $w = 465 \text{ nm}$, $a = 326 \text{ nm}$, $f = 0.22a$, $dd = 0.1a$, $defect = 0.25a$
 - 21.008- μm -radius dimerized PhCRR with trivial cavities - homodyne coupler: $g = 120 \text{ nm}$, $W = 430 \text{ nm}$, $w = 495 \text{ nm}$, $a = 330 \text{ nm}$, $f = 0.24a$, $dd = 0.1a$, $defect = 0.25a$
 - 21.008- μm -radius dimerized PhCRR with trivial cavities - homodyne coupler: $g = 150 \text{ nm}$, $W = 430 \text{ nm}$, $w = 495 \text{ nm}$, $a = 330 \text{ nm}$, $f = 0.24a$, $dd = 0.1a$, $defect = 0.25a$
 - 18.398- μm -radius dimerized PhCRR with trivial cavities - homodyne coupler: $g = 120 \text{ nm}$, $W = 400 \text{ nm}$, $w = 434 \text{ nm}$, $a = 300 \text{ nm}$, $f = 0.23a$, $dd = 0.1a$, $defect = 0.25a$
 - 18.398- μm -radius dimerized PhCRR with trivial cavities - homodyne coupler:

- $g = 150 \text{ nm}$, $W = 400 \text{ nm}$, $w = 434 \text{ nm}$, $a = 300 \text{ nm}$, $f = 0.23a$, $dd = 0.1a$,
 $defect = 0.25a$
- 29.603- μm -radius dimerized PhCRR with trivial cavities - homodyne coupler:
 $g = 120 \text{ nm}$, $W = 400 \text{ nm}$, $w = 465 \text{ nm}$, $a = 326 \text{ nm}$, $f = 0.22a$, $dd = 0.1a$,
 $defect = 0.25a$
 - 29.603- μm -radius dimerized PhCRR with trivial cavities - homodyne coupler:
 $g = 150 \text{ nm}$, $W = 400 \text{ nm}$, $w = 465 \text{ nm}$, $a = 326 \text{ nm}$, $f = 0.22a$, $dd = 0.1a$,
 $defect = 0.25a$
 - 31.513- μm -radius dimerized PhCRR with trivial cavities - homodyne coupler:
 $g = 120 \text{ nm}$, $W = 430 \text{ nm}$, $w = 495 \text{ nm}$, $a = 330 \text{ nm}$, $f = 0.24a$, $dd = 0.1a$,
 $defect = 0.25a$
 - 31.513- μm -radius dimerized PhCRR with trivial cavities - homodyne coupler:
 $g = 150 \text{ nm}$, $W = 430 \text{ nm}$, $w = 495 \text{ nm}$, $a = 330 \text{ nm}$, $f = 0.24a$, $dd = 0.1a$,
 $defect = 0.25a$
 - 27.597- μm -radius dimerized PhCRR with trivial cavities - homodyne coupler:
 $g = 120 \text{ nm}$, $W = 400 \text{ nm}$, $w = 434 \text{ nm}$, $a = 300 \text{ nm}$, $f = 0.23a$, $dd = 0.1a$,
 $defect = 0.25a$
 - 27.597- μm -radius dimerized PhCRR with trivial cavities - homodyne coupler:
 $g = 150 \text{ nm}$, $W = 400 \text{ nm}$, $w = 434 \text{ nm}$, $a = 300 \text{ nm}$, $f = 0.23a$, $dd = 0.1a$,
 $defect = 0.25a$
 - 39.470- μm -radius dimerized PhCRR with trivial cavities - homodyne coupler:
 $g = 120 \text{ nm}$, $W = 400 \text{ nm}$, $w = 465 \text{ nm}$, $a = 326 \text{ nm}$, $f = 0.22a$, $dd = 0.1a$,
 $defect = 0.25a$
 - 42.017- μm -radius dimerized PhCRR with trivial cavities - homodyne coupler:
 $g = 120 \text{ nm}$, $W = 430 \text{ nm}$, $w = 495 \text{ nm}$, $a = 330 \text{ nm}$, $f = 0.24a$, $dd = 0.1a$,
 $defect = 0.25a$
 - 36.797- μm -radius dimerized PhCRR with trivial cavities - homodyne coupler:
 $g = 120 \text{ nm}$, $W = 400 \text{ nm}$, $w = 434 \text{ nm}$, $a = 300 \text{ nm}$, $f = 0.23a$, $dd = 0.1a$,
 $defect = 0.25a$

Appendix E

Python scripts for the SSH model

E.1 Dimerized lattice

```
##Plot the energy band structure of a dimerized one-dimensional  
→ lattice.  
##Derived using the SSH model. KML Nov 23, 2018  
  
import numpy as np  
import scipy as sp  
import sympy as sym  
import matplotlib.pyplot as plt  
  
plt.rcParams['font.family'] = 'serif'  
  
# Define the strength of the dimer unit cell hopping parameters  
a = 1.0  
b = 1.0  
  
# Define the eigenvalues of the dimer bulk momentum space Hamiltonian  
→ as a function of the wavevector, k:  
def A(k):
```

```

return -np.sqrt((a + b*np.exp(1j*k))*(a*np.exp(1j*k) +
↪ b)*np.exp(-1j*k))

def B(k):
return np.sqrt((a + b*np.exp(1j*k))*(a*np.exp(1j*k) +
↪ b)*np.exp(-1j*k))

# Plot the eigenvalues over the first Brillouin zone ( $-\pi < k < \pi$ ) of
↪ the dimerized lattice:
k1 = np.linspace(start = -np.pi, stop = np.pi, num = 50)
fig = plt.figure()
disp = fig.add_axes([0.15,0.15,0.8,0.8])
disp.plot(k1/np.pi, A(k1), 'ko-', k1/np.pi, B(k1), 'ko-', linewidth=1.5,
↪ markersize=4)
disp.set_xlabel('Wavevector,  $k_x$  ( $\pi / \ell$ )')
disp.set_ylabel('Energy, E')
disp.set_xticks([-1.0, 0, 1.0])
disp.set_yticks([-1.5, 0, 1.5])
for item in ([disp.title, disp.xaxis.label, disp.yaxis.label] +
↪ disp.get_xticklabels() + disp.get_yticklabels()):
item.set_fontsize(15)
plt.show()

```

E.2 Trimer lattice

```

##Plot the energy band structure of a trimerized one-dimensional
↪ lattice.
##KML Nov 23, 2018

import numpy as np
import scipy as sp
import sympy as sym
import matplotlib.pyplot as plt

```

```

# Define the strength of the trimer unit cell hopping parameters
a = 1.0
b = 0.8
c = 0.8

# Define the eigenvalues of the trimer bulk momentum space Hamiltonian
→ as a function of the wavevector, k:
def A(k):
    return -(np.sqrt(729*(-a*b*c*np.exp(2*1j*k) -
    → a*b*c)**2*np.exp(-2*1j*k) - 4*(3*a**2 + 3*b**2 + 3*c**2)**3)/2 +
    → 27*(-a*b*c*np.exp(2*1j*k) - a*b*c)*np.exp(-1j*k)/2)**(1/3)/3 -
    → (3*a**2 + 3*b**2 + 3*c**2)/(3*(np.sqrt(729*(-a*b*c*np.exp(2*1j*k)
    → - a*b*c)**2*np.exp(-2*1j*k) - 4*(3*a**2 + 3*b**2 + 3*c**2)**3)/2
    → + 27*(-a*b*c*np.exp(2*1j*k) - a*b*c)*np.exp(-1j*k)/2)**(1/3))

def B(k):
    return -(-1/2 + np.sqrt(3)*1j/2)*(np.sqrt(729*(-a*b*c*np.exp(2*1j*k)
    → - a*b*c)**2*np.exp(-2*1j*k) - 4*(3*a**2 + 3*b**2 + 3*c**2)**3)/2
    → + 27*(-a*b*c*np.exp(2*1j*k) - a*b*c)*np.exp(-1j*k)/2)**(1/3)/3 -
    → (3*a**2 + 3*b**2 + 3*c**2)/(3*(-1/2 +
    → np.sqrt(3)*1j/2)*(np.sqrt(729*(-a*b*c*np.exp(2*1j*k) -
    → a*b*c)**2*np.exp(-2*1j*k) - 4*(3*a**2 + 3*b**2 + 3*c**2)**3)/2 +
    → 27*(-a*b*c*np.exp(2*1j*k) - a*b*c)*np.exp(-1j*k)/2)**(1/3))

def C(k):
    return -(-1/2 - np.sqrt(3)*1j/2)*(np.sqrt(729*(-a*b*c*np.exp(2*1j*k)
    → - a*b*c)**2*np.exp(-2*1j*k) - 4*(3*a**2 + 3*b**2 + 3*c**2)**3)/2
    → + 27*(-a*b*c*np.exp(2*1j*k) - a*b*c)*np.exp(-1j*k)/2)**(1/3)/3 -
    → (3*a**2 + 3*b**2 + 3*c**2)/(3*(-1/2 -
    → np.sqrt(3)*1j/2)*(np.sqrt(729*(-a*b*c*np.exp(2*1j*k) -
    → a*b*c)**2*np.exp(-2*1j*k) - 4*(3*a**2 + 3*b**2 + 3*c**2)**3)/2 +
    → 27*(-a*b*c*np.exp(2*1j*k) - a*b*c)*np.exp(-1j*k)/2)**(1/3))

# Plot the eigenvalues over the first Brillouin zone (-pi < k < pi) of
→ the trimerized lattice:

```

```

k1 = np.linspace(start = -np.pi, stop = np.pi, num = 50)
fig = plt.figure()
disp = fig.add_axes([0.15, 0.15, 0.8, 0.8])
disp.plot(k1/np.pi, A(k1), 'ko', k1/np.pi, B(k1), 'ko', k1/np.pi, C(k1),
→ 'ko', linewidth=1.5, markersize=4)
disp.set_xlabel('Wavevector, $k_x$ $(\pi / \ell)$')
disp.set_ylabel('Energy, E')
disp.set_xticks([-1.0, 0, 1.0])
disp.set_yticks([-1.5, 0, 1.5])
for item in ([disp.title, disp.xaxis.label, disp.yaxis.label] +
→ disp.get_xticklabels() + disp.get_yticklabels()):
    item.set_fontsize(15)
plt.show()

```

E.3 Tetramer lattice

```

##Plot the energy band structure of a tetramized one-dimensional
→ lattice.
##KML Nov 23, 2018

import numpy as np
import scipy as sp
import sympy as sym
import matplotlib.pyplot as plt

# Define the strength of the tetramer unit cell hopping parameters
a = 1.0
b = 0.7
c = 0.7
d = 0.7

# Define the eigenvalues of the tetramer bulk momentum space
→ Hamiltonian as a function of the wavevector, k:
def A(k):

```

```

return -np.sqrt(2)*np.sqrt(a**2 + b**2 + c**2 + d**2 -
↳ np.sqrt(a**4*np.exp(2*1j*k) + 2*a**2*b**2*np.exp(2*1j*k) -
↳ 2*a**2*c**2*np.exp(2*1j*k) + 2*a**2*d**2*np.exp(2*1j*k) +
↳ 4*a*b*c*d*np.exp(3*1j*k) + 4*a*b*c*d*np.exp(1j*k) +
↳ b**4*np.exp(2*1j*k) + 2*b**2*c**2*np.exp(2*1j*k) -
↳ 2*b**2*d**2*np.exp(2*1j*k) + c**4*np.exp(2*1j*k) +
↳ 2*c**2*d**2*np.exp(2*1j*k) +
↳ d**4*np.exp(2*1j*k))*np.exp(-1j*k))/2

```

```
def B(k):
```

```

return np.sqrt(2)*np.sqrt(a**2 + b**2 + c**2 + d**2 -
↳ np.sqrt(a**4*np.exp(2*1j*k) + 2*a**2*b**2*np.exp(2*1j*k) -
↳ 2*a**2*c**2*np.exp(2*1j*k) + 2*a**2*d**2*np.exp(2*1j*k) +
↳ 4*a*b*c*d*np.exp(3*1j*k) + 4*a*b*c*d*np.exp(1j*k) +
↳ b**4*np.exp(2*1j*k) + 2*b**2*c**2*np.exp(2*1j*k) -
↳ 2*b**2*d**2*np.exp(2*1j*k) + c**4*np.exp(2*1j*k) +
↳ 2*c**2*d**2*np.exp(2*1j*k) +
↳ d**4*np.exp(2*1j*k))*np.exp(-1j*k))/2

```

```
def C(k):
```

```

return -np.sqrt(2)*np.sqrt(a**2 + b**2 + c**2 + d**2 +
↳ np.sqrt(a**4*np.exp(2*1j*k) + 2*a**2*b**2*np.exp(2*1j*k) -
↳ 2*a**2*c**2*np.exp(2*1j*k) + 2*a**2*d**2*np.exp(2*1j*k) +
↳ 4*a*b*c*d*np.exp(3*1j*k) + 4*a*b*c*d*np.exp(1j*k) +
↳ b**4*np.exp(2*1j*k) + 2*b**2*c**2*np.exp(2*1j*k) -
↳ 2*b**2*d**2*np.exp(2*1j*k) + c**4*np.exp(2*1j*k) +
↳ 2*c**2*d**2*np.exp(2*1j*k) +
↳ d**4*np.exp(2*1j*k))*np.exp(-1j*k))/2

```

```
def D(k):
```

```

return np.sqrt(2)*np.sqrt(a**2 + b**2 + c**2 + d**2 +
↪ np.sqrt(a**4*np.exp(2*1j*k) + 2*a**2*b**2*np.exp(2*1j*k) -
↪ 2*a**2*c**2*np.exp(2*1j*k) + 2*a**2*d**2*np.exp(2*1j*k) +
↪ 4*a*b*c*d*np.exp(3*1j*k) + 4*a*b*c*d*np.exp(1j*k) +
↪ b**4*np.exp(2*1j*k) + 2*b**2*c**2*np.exp(2*1j*k) -
↪ 2*b**2*d**2*np.exp(2*1j*k) + c**4*np.exp(2*1j*k) +
↪ 2*c**2*d**2*np.exp(2*1j*k) +
↪ d**4*np.exp(2*1j*k))*np.exp(-1j*k))/2

```

*# Plot the eigenvalues over the first Brillouin zone ($-\pi < k < \pi$) of
↪ the tetramer lattice:*

```

k1 = np.linspace(start = -np.pi, stop = np.pi, num = 50)
fig = plt.figure()
disp = fig.add_axes([0.15,0.15,0.8,0.8])
disp.plot(k1/np.pi, A(k1), 'ko', k1/np.pi, B(k1), 'ko', k1/np.pi, C(k1),
↪ 'ko', k1/np.pi, D(k1), 'ko', linewidth=1.5, markersize=4)
disp.set_xlabel('Wavevector, $k_x$ $(\pi / \ell)$')
disp.set_ylabel('Energy, E')
disp.set_xticks([-1.0, 0, 1.0])
disp.set_yticks([-1.5, 0, 1.5])
for item in ([disp.title, disp.xaxis.label, disp.yaxis.label] +
↪ disp.get_xticklabels() + disp.get_yticklabels()):
    item.set_fontsize(15)
plt.show()

```

Appendix F

Bloch-Floquet rings GDS library

The GDS files for the devices used for the experimental data in Chapter 6 can be found [here](#). The library contains the following files:

- 10- μm -radius standard ring resonator
- 10- μm -radius ring resonator: $\kappa_{61} = 120 \text{ nm}$, $\kappa_{62} = 100 \text{ nm}$
- 10- μm -radius ring resonator: $\kappa_{61} = 130 \text{ nm}$, $\kappa_{62} = 110 \text{ nm}$
- 10- μm -radius ring resonator: $\kappa_{61} = 140 \text{ nm}$, $\kappa_{62} = 120 \text{ nm}$
- 10- μm -radius ring resonator: $\kappa_{61} = 150 \text{ nm}$, $\kappa_{62} = 130 \text{ nm}$
- 10- μm -radius ring resonator: $\kappa_{61} = 160 \text{ nm}$, $\kappa_{62} = 140 \text{ nm}$
- 10- μm -radius ring resonator: $\kappa_{62} = 165 \text{ nm}$
- 10- μm -radius ring resonator: $\kappa_{62} = 175 \text{ nm}$
- 10- μm -radius ring resonator: $\kappa_{62} = 185 \text{ nm}$

- 20- μm -radius standard ring resonator
- 20- μm -radius ring resonator: $\kappa_{122} = 70 \text{ nm}$, $\kappa_{123} = 60 \text{ nm}$, $\kappa_{124} = 60 \text{ nm}$
- 20- μm -radius ring resonator: $\kappa_{122} = 80 \text{ nm}$, $\kappa_{123} = 70 \text{ nm}$, $\kappa_{124} = 70 \text{ nm}$
- 20- μm -radius ring resonator: $\kappa_{122} = 90 \text{ nm}$, $\kappa_{123} = 80 \text{ nm}$, $\kappa_{124} = 80 \text{ nm}$
- 20- μm -radius ring resonator: $\kappa_{122} = 100 \text{ nm}$, $\kappa_{123} = 90 \text{ nm}$, $\kappa_{124} = 90 \text{ nm}$

- 20- μm -radius ring resonator: $\kappa_{123} = 70$ nm
- 20- μm -radius ring resonator: $\kappa_{123} = 80$ nm
- 20- μm -radius ring resonator: $\kappa_{123} = 90$ nm

Appendix G

Synthetic dimensions rings GDS library

The GDS files for the spatially modulated optical ring resonators proposed in Chapter 7 can be found [here](#). The library contains the following files:

- 100 μm -radius standard ring resonator
- 100- μm -radius ring resonator: $\kappa_1 = 100$ nm
- 100- μm -radius ring resonator: $\kappa_1 = 150$ nm
- 100- μm -radius ring resonator: $\kappa_1 = 200$ nm
- 100- μm -radius ring resonator: $\kappa_1 = 250$ nm
- 100- μm -radius ring resonator: $\kappa_1 = 300$ nm
- 100- μm -radius ring resonator: $\kappa_1 = 350$ nm
- 100- μm -radius ring resonator: $\kappa_1 = 400$ nm
- 100- μm -radius ring resonator: $\kappa_1 = 450$ nm
- 100- μm -radius ring resonator: $\kappa_1 = 500$ nm
- 100- μm -radius ring resonator: $\kappa_1 = 550$ nm
- 100- μm -radius ring resonator: $\kappa_1 = 600$ nm
- 100- μm -radius ring resonator: $\kappa_1 = 650$ nm

- 100- μm -radius ring resonator: $\kappa_1 = 700 \text{ nm}$
- 100- μm -radius ring resonator: $\kappa_1 = 750 \text{ nm}$
- 100- μm -radius ring resonator: $\kappa_1 = 800 \text{ nm}$
- 100- μm -radius ring resonator: $\kappa_1 = 850 \text{ nm}$
- 100- μm -radius ring resonator: $\kappa_1 = 900 \text{ nm}$
- 100- μm -radius ring resonator: $\kappa_1 = 950 \text{ nm}$
- 100- μm -radius ring resonator: $\kappa_1 = 1 \mu\text{m}$